# Exciton Polariton Modes in Nanostructures

---

Submitted by

**Martin James Gentile**

to the University of Exeter as a thesis for the degree of

**Doctor of Philosophy in Physics,**

April 2016.

---



---

I certify that all material in this thesis which is not my own work has been identified and that no material has previously been submitted and approved for the award of a degree by this or any other University.

Martin J. Gentile

Martin James Gentile

# Abstract

In this thesis, original theoretical and numerical investigations into the interaction of light with excitonic nanostructures are presented, in a bid to demonstrate that excitonic nanostructures are viable alternatives to the use of plasmonic nanostructures where electric field enhancement and confinement are sought. In particular, the field enhancement and confinement around excitonic nanostructures on resonance is shown to be comparable if not in excess of that around noble metal nanoparticles such as gold and silver. These excitonic modes, when set in the context of a core-shell geometry, are shown to offer tunability through nanoparticle design and through the index of the environment. In addition, hybrid 'hyperbolic' and 'plexcitonic' modes are shown to offer similar properties in metallic-excitonic nanostructures. Altogether, these excitonic and hybrid excitonic modes are shown to have potential in nanophotonic applications.

*To my father,*

*who first inspired me to*

*pursue an interest in science.*

# ACKNOWLEDGEMENTS

I would like to acknowledge the influence of several people in particular in the completion of this, my thesis.

Firstly, I thank my Ph.D. supervisor, Prof. W. L. Barnes, for accommodating me on this research project with such a flexible initial objective. I will always be grateful to Bill for his unwavering dedication, encouragement and advice throughout. I also thank Bill for providing me with the opportunity to present my work to a wider audience at domestic and international conferences, which has been invaluable experience for me. Finally, I thank Bill for taking his time to read and critically evaluate several versions of this thesis.

Fellow members of the electromagnetic and acoustic materials group in Exeter have helped to make it a stimulating research group to work in. In particular, thanks go to Dr. Simon Horsley for his patience and communication when it came to conveying advanced theoretical quantum mechanics. Thanks also go to Dr. Sara Nuñez Sánchez for her collaboration on the work to do with surface exciton polaritons in excitonic dye films: specifically, for her fabrication and measurement of reflectance and transmittance spectra through excitonic dye-doped thin films, and for her fabrication and measurement of transmittance spectra through arrays of excitonic dye-doped nanospheroids.

I thank Dr. Misha Portnoi for agreeing to be my Ph.D. research mentor. Misha has always managed to catch me off-guard when I have needed it the most by asking the right questions at the right time. This ensured that I was able to engage fully with the Ph.D. program throughout the course.

Outside the university, I thank the support of my wife Vicky, who has been my constant companion and source of moral support from the outset of starting my Ph.D. back in 2012. I also acknowledge the proofreaders of this thesis, whose work has helped towards the ironing out of spelling and grammatical errors.

Lastly, special thanks go to the many baristas involved in producing the many cups of coffee I have consumed over the course of my research.

# Contents

# List of Tables

# List of Figures

# Introduction

The nanophotonic applications of plasmon-based (plasmonic) devices is wide ranging: the field enhancement associated with surface plasmon polariton[1–3] (SPP) and particle plasmon polariton[4–7] (PPP) modes has been exploited to induce non-linear effects in non-linear materials,[8] and to increase the photoluminesence of molecules[9–11] enabling nanoscale microscopy.[12] These properties are highly medium dependent, and naturally lead to applications within environmental sensing,[13–17] including biosensing[18,19] and material characterisation.[20,21]

With the advent of modern fabrication techniques,[16,22] the nanoscale control of light[23,24] offered by plasmonic nanostructures has been of interest, with a view towards applications in optical computing[25] and optical communication.[26,27] SPPs have been explored within a waveguide context[28–32] and PPPs in lattices have been researched for their potential as nanoantennae with relatively high quality factors.[33]

In a departure from traditional plasmonics, outlined in this thesis is original theoretical and numerical investigation into whether excitonic nanostructures can exhibit the properties normally associated with plasmonic nanostructures: electric field enhancement and electric field confinement. If these properties can be demonstrated for excitonic nanostructures, this research may prove key towards demonstrating excitonic nanostructures as alternatives to plasmonic nanostructures for applications such as nanoscale microscopy, optical communication, environmental sensing, or material characterisation. Within this thesis, polariton modes in excitonic nanostructures are termed 'exciton polaritons' as compared to 'plasmon polaritons' in metallic nanostructures, indicating the origin of the modes. It is shown in this thesis that the properties of excitonic materials may be exploited in conjunction with plasmonic materials to tailor bespoke absorption properties within either artificially-constructed two-dimensional materials (metamaterials) or nanoparticles with a core-shell geometry, thereby expanding the potential of such modes.

This thesis is organised as follows:

In Ch. 1, the concepts of complex refractive index and permittivity are introduced, and an experimental technique utilising the Fresnel coefficients[34] and the Kramers-Kronig relations[35] to determine these quantities for thin films is outlined. Next, experimental results in the optical range for several thin films of plastic doped with the excitonic dye molecule TDBC are given; these results were obtained using this technique. Lastly, a method for relating reflectance and transmittance spectra to the colour seen by the human eye is related.

In Ch. 2, the permittivities of the excitonic thin films as determined in Ch. 1 are used in order to evaluate classical and quantum-mechanical models for the permittivity of TDBC:PVA films. In addition, classical models for metals are evaluated against published experimental data. It is shown that the quantum models for the permittivity of excitonic films are superior to that of the classical model, but the classical model suffices to describe the permittivity of metals.

In Ch. 3, surface exciton polaritons (SEP) modes are introduced and explored in the context of TDBC:PVA films. The models for the permittivity evaluated in Ch. 2 are used in order to quantify the skin depths and propagation lengths of SEPs in TDBC:PVA films, and compared with SPPs in metal films. The reflectance and absorption properties of TDBC:PVA thin films are then quantified. The colours predicted from the calculated reflectance and transmittance spectra are then evaluated against photographs of experimental TDBC:PVA films, and the features of the calculated absorption spectra are analysed. Next, multilayer stacks comprising excitonic and plasmonic materials are investigated in a bid to explore the properties of so-called hyperbolic metamaterials,[36] and whether absorption spectra can be controlled by careful design of these multilayers.

In Ch. 4, the focus lies upon particle polariton modes. Particle exciton polariton (PEP) and epsilon near zero (ENZ) modes are introduced and explored in the context of nanospheres and nanospheroids of TDBC:PVA. The Mie scattering and absorption spectra of these nanoparticles are compared against those of metallic nanoparticles, and the spectral positions of the resonances are evaluated by use of quasistatic theory. The power flow and electric field enhancement in the vicinity of TDBC:PVA nanospheres is examined in order to characterise the PEP and ENZ modes. An experimental method for measurements of these properties is outlined, and the initial results of such an experiment are detailed for nanospheroids. Lastly, a proposal for an extension to this work is related.

Ch. 5 builds upon the findings of Ch. 4, and explores particle polariton modes in the context of coated nanospheres. Through a combination of quasistatic considerations with a scattering theory for coated nanoparticles based upon Mie theory, several nanoparticle geometries are explored. First, the tunability of the modes for nanospheres with metallic and excitonic cores are contrasted against each other. Second, it is shown that for excitonic nanoshells, hybridised exciton polariton modes can be obtained. Third, the nanosphere with both an excitonic core and shell is explored and the effect of an increase in dye concentration of the shell determined. Lastly, it is shown that by fabrication of an excitonic-plasmonic nanosphere in a core-shell geometry, particle exciton and particle plasmon modes can hybridise to form ‘plexciton’ modes. The tunability of these plexciton modes is then explored *via* changes in geometry, choice of dye molecule, and dye concentration.

The findings of the work outlined in this thesis are summarised in Ch. 6, along with suggestions for future work that could build upon the research themes in this thesis.

# 1

# Determination of the Permittivity of Excitonic Thin Films

*In this chapter, the concept of complex permittivity is introduced and developed. A method for determination of this quantity for thin films over a range of wavelengths is outlined. The excitonic dye molecule TDBC is introduced, and the complex permittivity of TDBC-doped thin films of inert material is extracted, and examined for several dopant concentrations.*

## 1.1 Introduction

In order to perform calculations to describe the optical response of nanostructures, the response of the material to an electromagnetic wave must first be determined. The most useful quantity used to describe how a specific material responds to light is its complex permittivity; this quantity is now derived, starting with Maxwell's equations.[37,38] These are written in current-free form as,

$$\nabla \cdot \boldsymbol{B} = 0 \tag{1.1}$$

$$\nabla \cdot \boldsymbol{E} = \frac{\rho}{\epsilon} \tag{1.2}$$

$$\nabla \times \boldsymbol{B} = \frac{1}{c^2}\frac{\partial \boldsymbol{E}}{\partial t} \tag{1.3}$$

$$\nabla \times \boldsymbol{E} = -\frac{\partial \boldsymbol{B}}{\partial t}, \tag{1.4}$$

where $\boldsymbol{E}$ is the electric field, $\boldsymbol{B}$ is the magnetic flux density, $c$ is the speed of light in the material and $\epsilon = \varepsilon_0 \varepsilon$ is the complex permittivity of the material. The magnetic flux density is related to the magnetic field by $\boldsymbol{B} = \mu \boldsymbol{H}$, where $\mu = \mu_0 \mu_r$ is the magnetic permeability of the material. These fundamental equations governing electric and

magnetic fields can be used to derive wave equations for electric and magnetic fields by substitution of Eq. 1.1-1.4 into each other,

$$\left(\nabla^2 - \frac{1}{c^2}\frac{\partial^2}{\partial t^2}\right)\boldsymbol{E} = 0 \tag{1.5}$$

$$\left(\nabla^2 - \frac{1}{c^2}\frac{\partial^2}{\partial t^2}\right)\boldsymbol{B} = 0, \tag{1.6}$$

which are Maxwell's electromagnetic wave equations. Given that the speed of the waves implied by solutions to these equations is the speed of light, these equations describe the wave nature of light. Hence, light is demonstrably an electromagnetic wave and these wave equations can be used to mathematically describe light within the field of optics. One-dimensional solutions to Eq. 1.5 are of the form $\boldsymbol{E} = \boldsymbol{E}_0 e^{ikx+i\omega t}$. Putting this solution into Eq. 1.5 procures a relationship between the wavenumber $k$ and the angular frequency $\omega$,

$$\begin{aligned}\omega &= kc \\ &= \frac{k}{\sqrt{\mu\epsilon}},\end{aligned} \tag{1.7}$$

where the relationship $1/c^2 \equiv \mu\epsilon$ has been used to write Eq. 1.7. This relationship is applied to determine that $k = \omega\sqrt{\mu\epsilon}$. In this thesis, the materials under consideration have a relative permeability of unity ($\mu = \mu_0$). In this case, the magnetic fields are not modified by the material and,

$$\begin{aligned}k &= \omega\sqrt{\mu_0\varepsilon_0}\sqrt{\varepsilon} \\ &= \frac{\tilde{n}\omega}{c_0},\end{aligned} \tag{1.8}$$

where $\tilde{n} = n + i\kappa$ is the complex refractive index of the material and $c_0$ is the speed of light in free space. The importance of the quantity $\tilde{n}$ on the response of the material is evident when the one-dimensional solution to the wave equation is decomposed as a product of its time and spatially-dependent parts,

$$\begin{aligned}\boldsymbol{E} &= \boldsymbol{E}_0 e^{i(\omega/c_0)\tilde{n}x+i\omega t} \\ &= \boldsymbol{E}_0 e^{i\omega t} e^{i(\omega/c_0)nx} e^{-(\omega/c_0)\kappa x}.\end{aligned} \tag{1.9}$$

Eq. 1.9 implies that for $\kappa > 0$ ($\kappa < 0$), the amplitude of the electric field dies away (is enhanced) exponentially with propagation inside the material. Therefore, this

imaginary part of the refractive index accounts for energy dissipation (or enhancement) within the material. A definition for the real part of the refractive index of a material ($\mathbb{R}\mathrm{e}(\tilde{n}) = n$) is the ratio of the speed of light in free space to the speed of light in the material[39] (the phase velocity): this can be seen by substitution of Eq. 1.7 into Eq. 1.8. $n$ is therefore inversely related to the phase velocity, and $n$ is always positive.

In this thesis, the relative permittivity of a material is given the symbol $\varepsilon$. This quantity is complex and is written in terms of its real and imaginary parts in this thesis as $\varepsilon = \varepsilon' + i\varepsilon''$. The relative permittivity (henceforth referred to as 'permittivity' unless otherwise stated) of a material is related to the material's complex refractive index by $\tilde{n} = \sqrt{\varepsilon}$. From this relationship, the following two equations can be derived,

$$\varepsilon' = n^2 - \kappa^2 \tag{1.10}$$

$$\varepsilon'' = 2n\kappa. \tag{1.11}$$

From Eq. 1.10 & 1.11 and by inspection of Eq. 1.9, a set of eight distinct classes of materials can be identified, as summarised in Tab. 1.1.

| $\varepsilon$ | $n$ | $\kappa$ | Type |
|---|---|---|---|
| $\varepsilon'$ | $> 0$ | $0$ | Translucent material |
| $\varepsilon' + i\varepsilon''$ | $> 0$ | $0 < \kappa < n$ | Lossy dielectric |
| $\varepsilon' - i\varepsilon''$ | $> 0$ | $-n < \kappa < 0$ | Gain material |
| $i\varepsilon''$ | $\kappa$ | $n$ | Epsilon Near Zero (ENZ) material |
| $-i\varepsilon''$ | $\kappa$ | $-n$ | ENZ gain material |
| $-\varepsilon' + i\varepsilon''$ | $> 0$ | $> n$ | Metallic |
| $-\varepsilon' - i\varepsilon''$ | $> 0$ | $< -n$ | Highly reflective gain material |
| $-\varepsilon'$ | $0$ | $> 0$ | Index Near Zero (INZ) metamaterial |

**Table 1.1:** A summary of several classes of materials, where $\varepsilon'$ and $\varepsilon''$ are real and positive.

The differences between each of these classes are best observed by comparison of the reflection and transmission coefficients across a boundary for each of them at normal incidence. Solutions for the electric field of the form Eq. 1.9 are assumed. By applying wave amplitude continuity boundary conditions across each interface, the (generally complex) amplitude reflection and transmission coefficients from material $i$ to material $j$ ($r_{ij}$ and $t_{ij}$) can be derived by elementary algebra as,

$$r_{ij} = \frac{\tilde{n}_i - \tilde{n}_j}{\tilde{n}_i + \tilde{n}_j} \equiv \frac{k_i - k_j}{k_i + k_j} \tag{1.12}$$

$$t_{ij} = \frac{2\tilde{n}_i}{\tilde{n}_i + \tilde{n}_j} \equiv \frac{2k_i}{k_i + k_j}, \tag{1.13}$$

where $k_i$ and $k_j$ are the complex wavenumbers in the $i^{\text{th}}$ and $j^{\text{th}}$ media respectively. The two general expressions in Eq. 1.12 & 1.13 relate the wave amplitude reflected

and transmitted at a boundary. The fraction of light reflected (transmitted) is given by $R = |r|^2$ ($T = |t|^2/n_j$). With air on one side of the boundary these become,

$$R = \left|\frac{\tilde{n}-1}{\tilde{n}+1}\right|^2 = \frac{n^2+\kappa^2-2n+1}{n^2+\kappa^2+2n+1} \tag{1.14}$$

$$T = \frac{1}{n}\frac{4(n^2+\kappa^2)}{(\tilde{n}+1)^2} = \frac{4(n^2+\kappa^2)}{n^2+\kappa^2+2n+1}. \tag{1.15}$$

These relations show that the complex refractive index (and hence the permittivity) governs the fraction of incident light a material will reflect or transmit at a given wavelength *i.e.* the reflectance and transmittance spectra, and by extension, the optical properties of the material. The dependence of $R$ upon $n$ and $\kappa$ is illustrated in Fig. 1.1. The minimum in $R$ occurs at $n = \sqrt{\kappa^2+1}$. It can be seen that $R = 1$ for INZ materials,

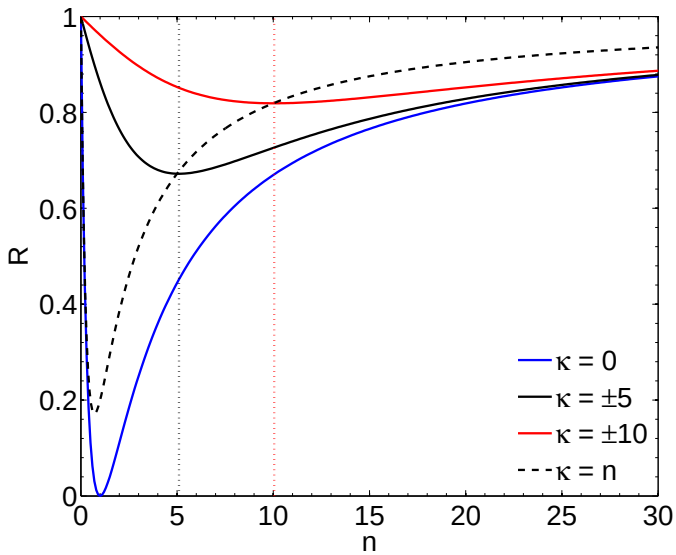


**Figure 1.1:** Reflectance ($R$) as a function of $n$ for three different values of $\kappa$, and for $\kappa = n$. The dotted lines indicate the values $n$ which minimise $R$.

irrespective of the value of $\kappa$. For metallic materials (where $n^2 < \kappa^2$, indicated by the region to the left of the respective dotted lines in Fig. 1.1) $R$ is high-valued, as expected. This boundary is also demarcated by the curve for an ENZ material ($\kappa = n$). In the case where $\kappa = 0$ (corresponding to a translucent dielectric), $R < 0.5$ for $1 < n < 5.8$. For the case where $n \to \infty$, $R \to 1$, albeit more slowly in relation to ENZ materials, for all values of $\kappa$.

This analysis can be generalised by calculation of $R$ for a range of $\varepsilon'$ and $\varepsilon''$, and plotting the results in a Cole-Cole plot[40] ($\varepsilon'$ *vs.* $\varepsilon''$). The Cole-Cole plot in Fig. 1.2 shows that $R$ increases as $\varepsilon'$ becomes more negative. Also plotted in Fig. 1.2 are $\varepsilon'$ and

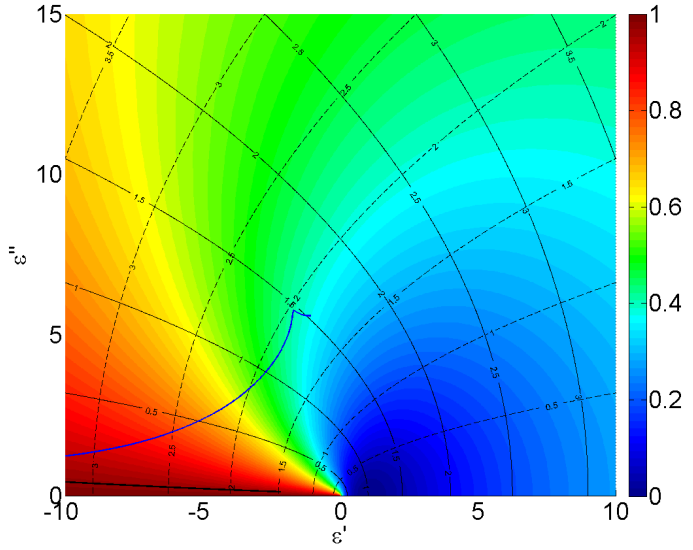


**Figure 1.2:** Reflectance as a function of both $\varepsilon'$ and $\varepsilon''$, with lines of constant $n$ (solid) and $\kappa$ (dashed). Gold (silver) for optical frequencies is indicated by the thick blue (black) line.

$\varepsilon''$ for gold and silver at optical frequencies. It can be seen that these two curves lie in the region of negative $\varepsilon'$, where $R$ is high-valued. Fig. 1.2 therefore demonstrates that a negative real permittivity enables metals such as silver to be used in the manufacture of high-quality mirrors. Fig. 1.2 also shows that there is a region of low $|\varepsilon|$ within which $R$ is suppressed. This region can be described as a low loss tangent region, where the loss tangent is defined as $\delta = \varepsilon''/\varepsilon'$, when $\{\varepsilon', \varepsilon''\} > 0$. Fig. 1.2 therefore demonstrates why balls of polyethylene and large quartz crystals (both materials with low loss tangents[41,42]) are relatively transparent.

From this analysis, it can be seen that the eight classes of materials in Tab. 1.1 are sorted in ascending order by the amount they reflect at normal incidence. In this chapter, it is shown that a single material may exhibit many of these different properties: for instance, a material may behave as a dielectric at one wavelength, and yet metallic behaviour at another.

## 1.2 Fresnel Approach

The complex refractive index of a thin film of material can be extracted by comparison of experimental measurements for reflectance and transmittance with theoretical values. The theoretical values are obtained by modelling the film as a homogeneous thin film of thickness $t_1$ with complex refractive index $\tilde{n}_1$, surrounded by two semi-infinite non-absorbing media with frequency-independent refractive indices $n_0$ and $n_2$, as

shown in Fig. 1.3. The effective (amplitude) reflection and transmission coefficients

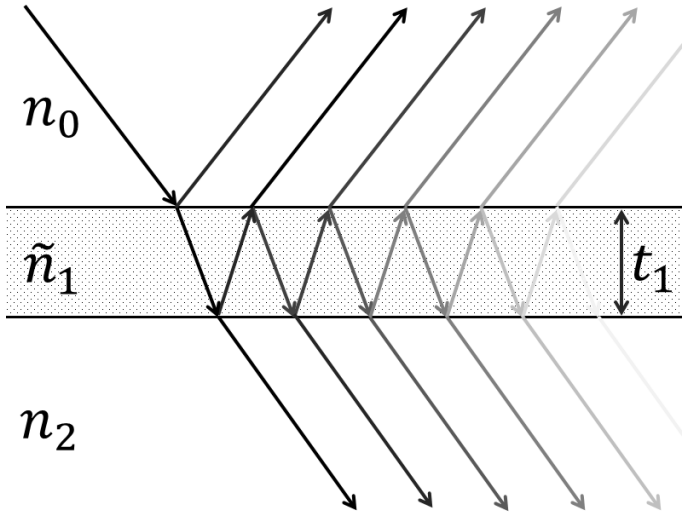


**Figure 1.3:** A schematic showing the notation used and the physical picture for reflectance and transmittance through a thin film.

($r$ and $t$) for a film in terms of the coefficients at each interface ($r_{ij}$ and $t_{ij}$) can be obtained by summation of the infinite geometric series of the reflections within the film.[34,35] The final result is,

$$r = r_{01} + \frac{r_{12}t_{01}t_{10}e^{-2\tilde{n}_1 k_1 t_1}}{1 + r_{12}r_{01}e^{-2\tilde{n}_1 k_1 t_1}} \tag{1.16}$$

$$t = \frac{t_{01}t_{12}e^{-ik_1 t_1}}{1 + r_{12}r_{10}e^{-2ik_1 t_1}}. \tag{1.17}$$

The (intensity) reflectance and transmittance values as measured in experiment are the absolute magnitude squared of these expressions, *i.e.* $R = |r|^2$ and $T = |t|^2$. Written out in full in terms of $n_0$, $\tilde{n}_1$ and $n_2$, $R$ and $T$ assume the following form[34,43,44],

$$R(n_1, \kappa_1) = R_{num}(n_1, \kappa_1)/D(n_1, \kappa_1), \tag{1.18}$$
$$T(n_1, \kappa_1) = T_{num}(n_1, \kappa_1)/D(n_1, \kappa_1), \tag{1.19}$$

where,

$$\begin{aligned} R_{num}(n_1,\kappa_1) = e^{2\kappa_1 qt_1}(n_0^2 - 2n_0n_1 + |\tilde{n_1}|^2)(|n_1|^2 + 2n_1n_2 + n_2^2) \\ +e^{-2\kappa_1 qt_1}(n_0^2 + 2n_0n_1 + |\tilde{n_1}|^2)(|n_1|^2 - 2nn_2 + n_2^2) \\ +2cos(2n_1qt_1)[(n_0^2 - |\tilde{n_1}|^2)(|\tilde{n_1}|^2 - n_2^2) - 4n_0n_2\kappa_1^2] \\ -4k_1 sin(2n_1qt_1)[(n_0 - n_2)|\tilde{n_1}|^2 - n_0n_2(n_2 - n_0)], \end{aligned} \tag{1.20}$$

$$T_{num}(n_1,\kappa_1) = 16n_0n_2|\tilde{n_1}|^2, \tag{1.21}$$

$$\begin{aligned} D(n_1,\kappa_1) = e^{2\kappa_1 qt_1}(n_0^2 + 2n_0n_1 + |\tilde{n_1}|^2)(|n_1|^2 + 2n_1n_2 + n_2^2) \\ +e^{-2\kappa_1 qt_1}(n_0^2 - 2n_0n_1 + |\tilde{n_1}|^2)(|n_1|^2 - 2nn_2 + n_2^2) \\ +2cos(2n_1qt_1)[(n_0^2 - |\tilde{n_1}|^2)(|\tilde{n_1}|^2 - n_2^2) + 4n_0n_2\kappa_1^2] \\ +4k_1 sin(2n_1qt_1)[(n_0 + n_2)|\tilde{n_1}|^2 - n_0n_2(n_0 + n_2)]. \end{aligned} \tag{1.22}$$

Here, $q = k_0/n_0$ where $k_0 = 2\pi/\lambda_0$, *i.e.* the wavenumber in the incident medium. The explicit dependency of $\tilde{n}_1$ upon $\omega$ has been omitted here for clarity.

Now that expressions for $R$ and $T$ of a thin film have been arrived at, the next step is to formulate a function which, when minimised, will yield $\tilde{n}_1$. If the complex value for $\tilde{n}_1$ is found exactly (given the film thickness and the indices of the surrounding media), the two equations $R(n_1,\kappa_1) = R_e$ and $T(n_1,\kappa_1) = T_e$ will be satisfied, where $R_e$ and $T_e$ are the values of reflectance and transmittance measured in experiment. Given these two equations, the following function can be defined,

$$f(n_1,\kappa_1) = |R(n_1,\kappa_1,\omega) - R_e(\omega)| + |T(n_1,\kappa_1,\omega) - T_e(\omega)|, \tag{1.23}$$

which is termed here the 'Fresnel residual function'. When minimised, this function will give $\tilde{n}_1$ at frequency $\omega$. To perform this minimisation, suitable trial ranges for $n_1$ and $\kappa_1$ must be established for each wavelength in which $n_1$ and $\kappa_1$ are expected to lie. Computations for $R$ and $T$ using these 'guessed' values are made for the values of $n_1$ and $\kappa_1$ across these ranges and substituted into Eq. 1.23. Given that there are two variables ($n_1$ and $\kappa_1$) which must be determined, the computational cost of the process increases with the square of the number of trials taken in the range - therefore, restriction of the range of guessed values to a physically plausible range is recommended.

## 1.3 Kramers-Kronig Relations

Once the complex permittivity of a material has been extracted for all wavelengths, the solutions need to be checked for physical plausibility. This can be done using the Kramers-Kronig (KK) relations. These relations arise from causality arguments and are defined as,[35]

$$\varepsilon'(\omega) = 1 + \frac{2}{\pi}\mathcal{P}\int_0^\infty \frac{\omega'\varepsilon''(\omega')}{\omega'^2 - \omega^2}d\omega' \tag{1.24}$$

$$\varepsilon''(\omega) = -\frac{2\omega}{\pi}\mathcal{P}\int_0^\infty \frac{\varepsilon'(\omega') - \varepsilon_b}{\omega'^2 - \omega^2}d\omega'. \tag{1.25}$$

Here, $\mathcal{P}$ symbolises the Cauchy principal value and $\varepsilon_b$ is a constant background contribution to $\varepsilon'$. The infinite range stipulated in Eq. 1.24 & 1.25 imply that $\varepsilon(\omega)$ must be known over the entire spectrum, or at least over the range where $\varepsilon(\omega)$ in non-zero. The Kramers-Kronig relations also apply to $n$ and $\kappa$ and can be written in the following form,

$$n(\omega) = \frac{1}{\pi}\mathcal{P}\int_{-\infty}^\infty \frac{\kappa(\omega')}{\omega' - \omega}d\omega' \tag{1.26}$$

$$\kappa(\omega) = -\frac{1}{\pi}\mathcal{P}\int_{-\infty}^\infty \frac{n(\omega')}{\omega' - \omega}d\omega'. \tag{1.27}$$

Eq. 1.26 & 1.27 enable one to obtain $n$ from $\kappa$ or *vice versa* by a relatively simple Hilbert transform on $\kappa$ or $n$. The former of these transforms can be aided by identifying that the Fourier transform $\kappa(t) = \mathcal{F}\{\kappa(\omega)\}$ is real-valued for all times $t$, *i.e.*,

$$\begin{aligned}\mathbb{I}\mathrm{m}\int_{-\infty}^\infty \kappa(\omega)e^{i\omega t}d\omega &= 0 \\ &= \mathbb{I}\mathrm{m}\int_0^\infty (\kappa(-\omega) + \kappa(\omega))e^{i\omega t}d\omega \\ &= \int_0^\infty (\kappa(-\omega) + \kappa(\omega))\sin(\omega t)d\omega. \end{aligned}\tag{1.28}$$

This implies that $\kappa(\omega) = -\kappa(-\omega)$ *i.e.* that $\kappa$ is odd under time-reversal symmetry.[45] Using $\kappa(\omega) = -\kappa(-\omega)$ in Eq. 1.26 produces a more accurate result for $n$ and is slightly more convenient than using Eq. 1.24, since Eq. 1.24 requires the data points for $\kappa$ to be linearly spaced in $\omega^2$, which is often not the case for experimental data.

## 1.4 Permittivity of Excitonic Films

The permittivities of poly(vinyl alcohol) (PVA) thin films doped with excitonic dye molecules are now procured using the procedure detailed above on experimental reflectance and transmittance data. Here, 'excitonic' refers to the ability of the molecules to host excitons, and 'dye' indicates the strong colour obtainable arising from the affinity between the molecules and the PVA substrate. The dye molecule used is *5,6-dichloro-2-[[5,6-dichloro-1-ethyl-3-(4-sulphobutyl)-benzimidazol-2-ylidene]-propenyl]-1-ethyl-3 -(4-sulphobutyl)-benzimidazolium hydroxide*, sodium salt, inner salt (herein referred to as TDBC). With a sufficient dopant concentration, the dye molecules form aggregates of $10 - 10^2$ molecules, and the film exhibits a metallic appearance in a narrow optical frequency range when illuminated with white light (the microscopic origin of this metallic appearance is detailed in Ch. 2). Outside this range, the film behaves like a transparent dielectric. Four such TDBC:PVA films are considered in this section, each produced *via* a spin-coating procedure[46] in collaboration with Sara Núñez-Sánchez, whose practical work on fabricating and measuring the reflectance and transmittance spectra of these films is acknowledged. It is implicit from here on in this thesis that any original experimentally-determined values for the permittivity derive from Sara's measured reflectance and transmittance spectra for these samples. Each of the films in question were fabricated to thicknesses of approximately 70 *nm*, and supported by a one millimetre thick glass substrate. A photograph of the most highly-doped of these (with a dye concentration of 1.46 *wt%*) is shown in Fig. 1.4, alongside a 70 *nm* gold film for comparison. In order to show

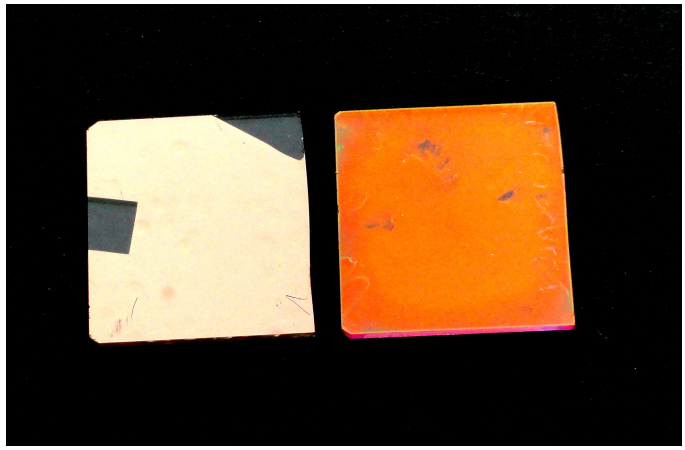

**Figure 1.4:** A 70 *nm* gold film (left) and a 70 *nm* 1.46 *wt%* TDBC:PVA film (right, as fabricated by Sara Núñez-Sánchez) illuminated with (unpolarised) sunlight.

clearly the steps involved and the challenges faced in extracting the permittivity of these films from reflectance and transmittance data, the focus of this section is upon

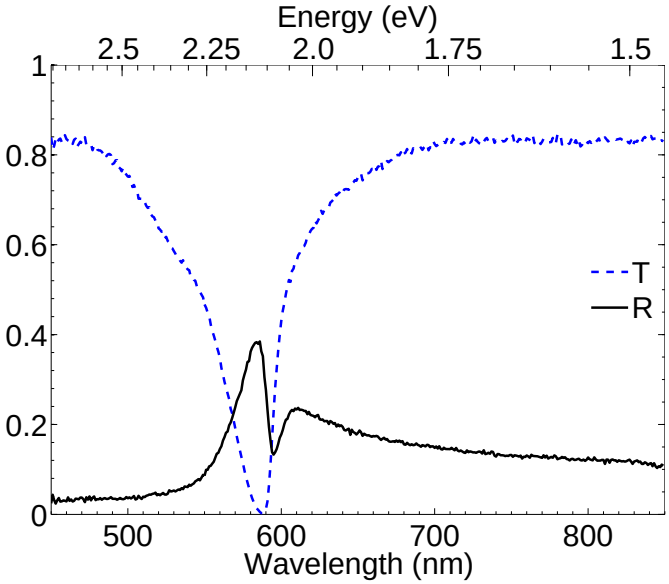


**Figure 1.5:** Reflectance ($R$) and transmittance ($T$) as a function of wavelength at normal incidence for the 1.46 *wt%* TDBC:PVA film shown in Fig. 1.4. Data credit: Sara Núñez-Sánchez.

the 1.46 *wt%* film. The final results for the other three films are then displayed.

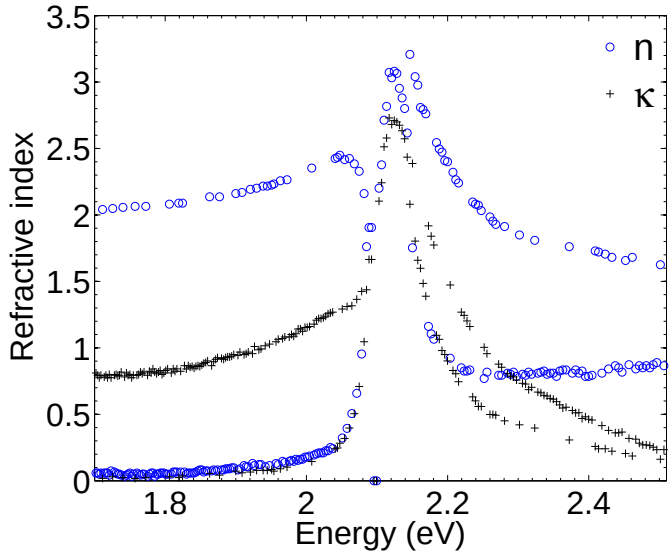


**Figure 1.6:** Complex refractive index for a 70 *nm* film of 1.46*wt%* TDBC:PVA as determined with the Fresnel procedure.

As a first step in the extraction process, reflectance and transmittance spectra for each film were measured at normal incidence; the measured spectra for the 1.46 *wt%* film are displayed in Fig. 1.5. These data were measured in nanometres (*nm*), but in this thesis electron-volts (*eV*) are used predominantly; these two units are related by the relationship $eV = 1270.7/nm$ (5 *s.f.*). By application of the Fresnel approach detailed above, initial results for $\tilde{n}(\omega)$, and hence $\varepsilon(\omega)$, obtained from these reflectance and transmittance spectra are plotted in Fig. 1.6. It can be seen from Fig. 1.6 that the results show two solutions for both $n$ and $\kappa$: the physical solution, and a spurious solution. The spurious solution emerges from the following limitations in the Fresnel approach: inaccuracies in the measured reflectance and transmittance values;[44] rounding errors in the 'guessed' values for $n$ and $\kappa$; and errors in the film thickness.[47] The method used to determine the film thickness is destructive to the film, and the value obtained here is accurate to within 12%, giving a film thickness of $t = 69.6 \pm 8.1$ *nm*.

In spite of these failings, the results in Fig. 1.6 demonstrate that there is less uncertainty in $\kappa$ than in $n$. Therefore, by application of KK analysis on $\kappa$, a physically plausible solution for $n$ (and hence $\tilde{n}$) can be obtained. This requires extraction of the physical solution for $\kappa$ for all energies considered. In order to do this, and to reduce the uncertainty in $\kappa$ introduced by the uncertainty in the film thickness, the Fresnel procedure can be re-run for many thicknesses across the confidence interval for the film thickness. The results from these calculations for twenty different film thicknesses are displayed in Fig. 1.7a (overleaf). In this figure, a continuum of data points for the physically-plausible solution for $\kappa$ is now evident, along with a band of erroneous results. In order to improve upon these values further, the transmittance through the film can be assumed to have the following dependency (for a given thickness $t$),

$$T \approx e^{-\kappa t} = e^{-\kappa' t'}. \tag{1.29}$$

This leads to,

$$\kappa' = \frac{t}{t'}\kappa. \tag{1.30}$$

By application of Eq. 1.30 (with $t = 69.6$ *nm*) to the data in Fig. 1.7a, the plot in Fig. 1.7b is achieved, where in effect, the data have been deconvoluted.

The final results for $n$ determined using Eq. 1.26 to perform KK analysis on the deconvoluted physical solution of $\kappa$ are displayed in Fig. 1.8a. $\varepsilon'$ and $\varepsilon''$ are shown in Fig. 1.8b, by use of Eq. 1.10 & 1.11.

From Fig. 1.8b, $\varepsilon' < 0$ and $\varepsilon'' > 0$ for the energy range $2.10\ eV < E < 2.25\ eV$. This indicates that for this range of energies, the 1.46 *wt%* TDBC:PVA film is metallic in nature. This accounts for the metallic appearance of the TDBC:PVA film in Fig. 1.4. Outside this range, the film behaves either as a lossy dielectric ($E \approx \{2.04, 2.10\}\ eV$) or as a translucent material: indeed, the value of $n$ approaches that of the PVA host ($n_{\mathrm{PVA}} = 1.52$) at the edges of the range of energies shown in the plot.

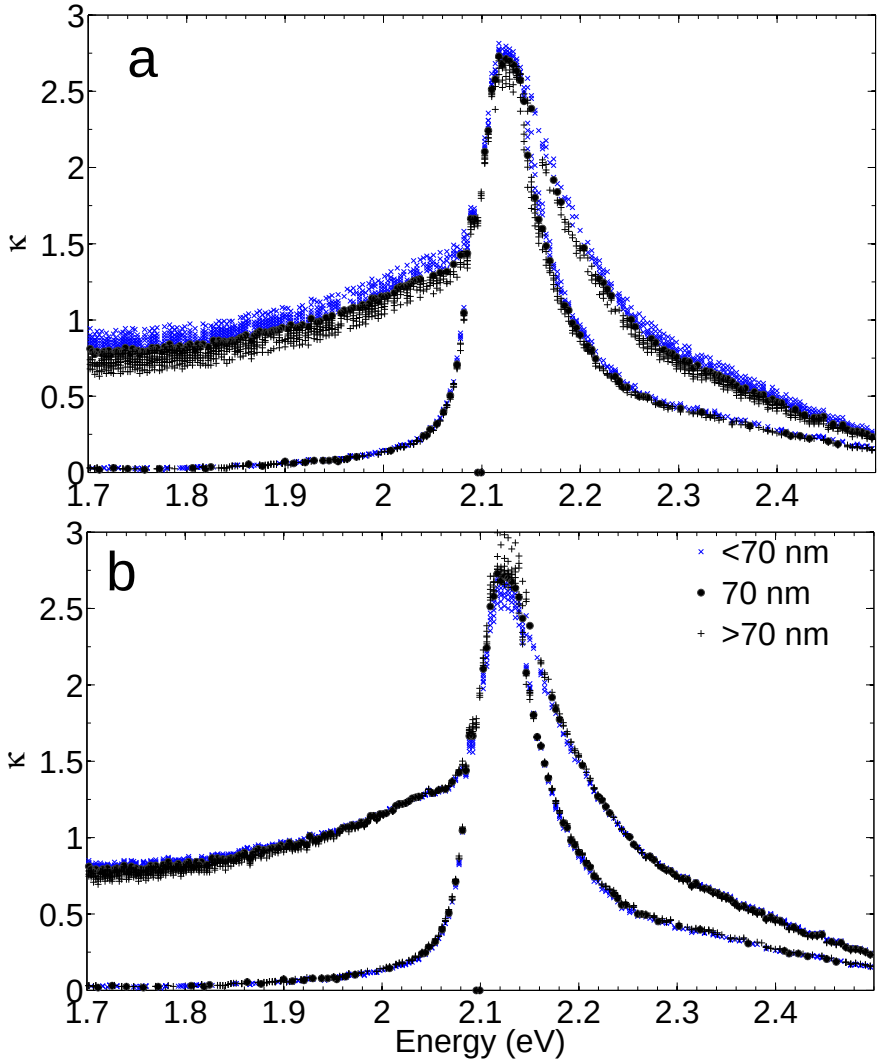


**Figure 1.7:** $\kappa$ for a 1.46 *wt%* TDBC:PVA film, assuming a range of thicknesses before (a) and after (b) adjustment for these thicknesses.

The concentrations and thicknesses of the four TDBC:PVA films studied in this thesis are summarised in Tab. 1.2. The distribution of thicknesses is a limitation of the manufacturing procedure used. The results obtained by repetition of the extraction procedure for permittivity on the three remaining TDBC:PVA films are displayed in Fig. 1.9 (overleaf).

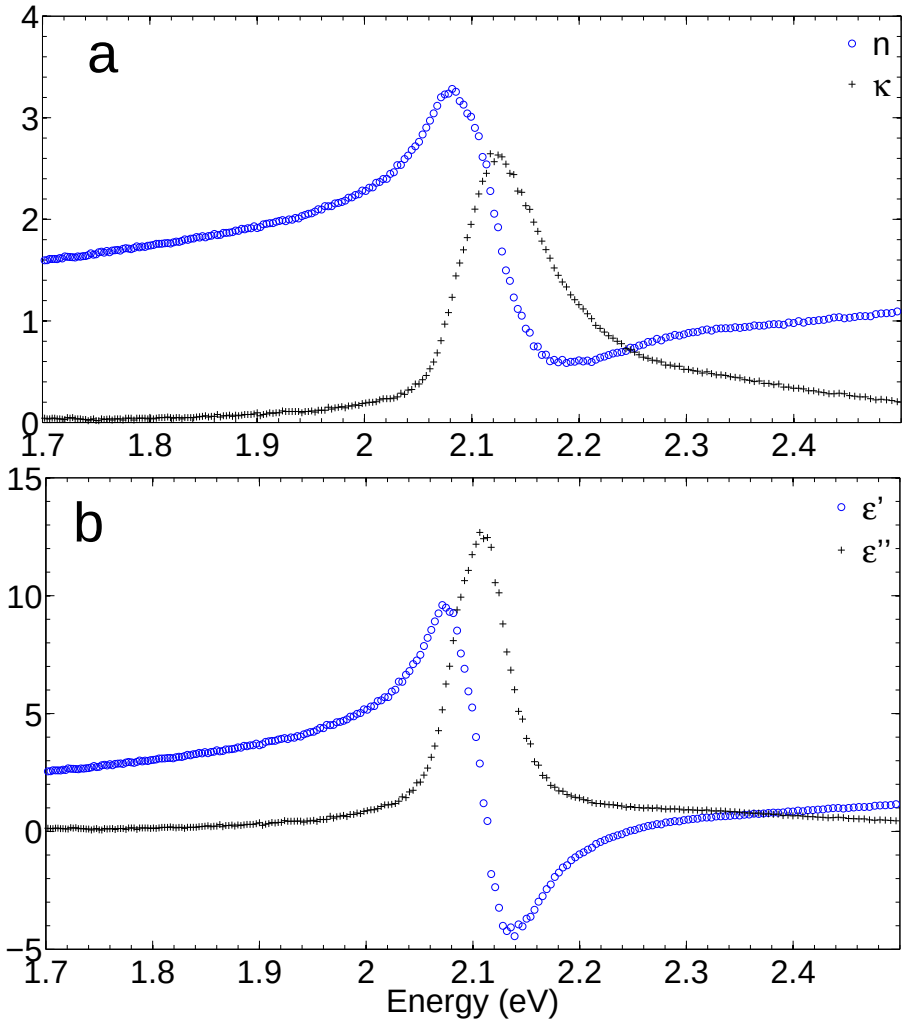


**Figure 1.8:** The retrieved refractive index (a) and permittivity (b) for a 70 *nm* 1.46 *wt%* TDBC:PVA film after KK analysis on $\kappa$.

| **Dye Concentration** (*wt %*) | **Film thickness** (*nm*) |
|---|---|
| 0.12 | 64.9 ± 3.9 |
| 0.48 | 76.6 ± 5.9 |
| 1.00 | 69.7 ± 4.9 |
| 1.46 | 69.6 ± 8.1 |

**Table 1.2:** Dye concentration and thickness for each of the TDBC:PVA films studied in this thesis. Data credit: Sara Núñez-Sánchez.

One general trend seen in Fig. 1.9 is that the minimum value of the real part of

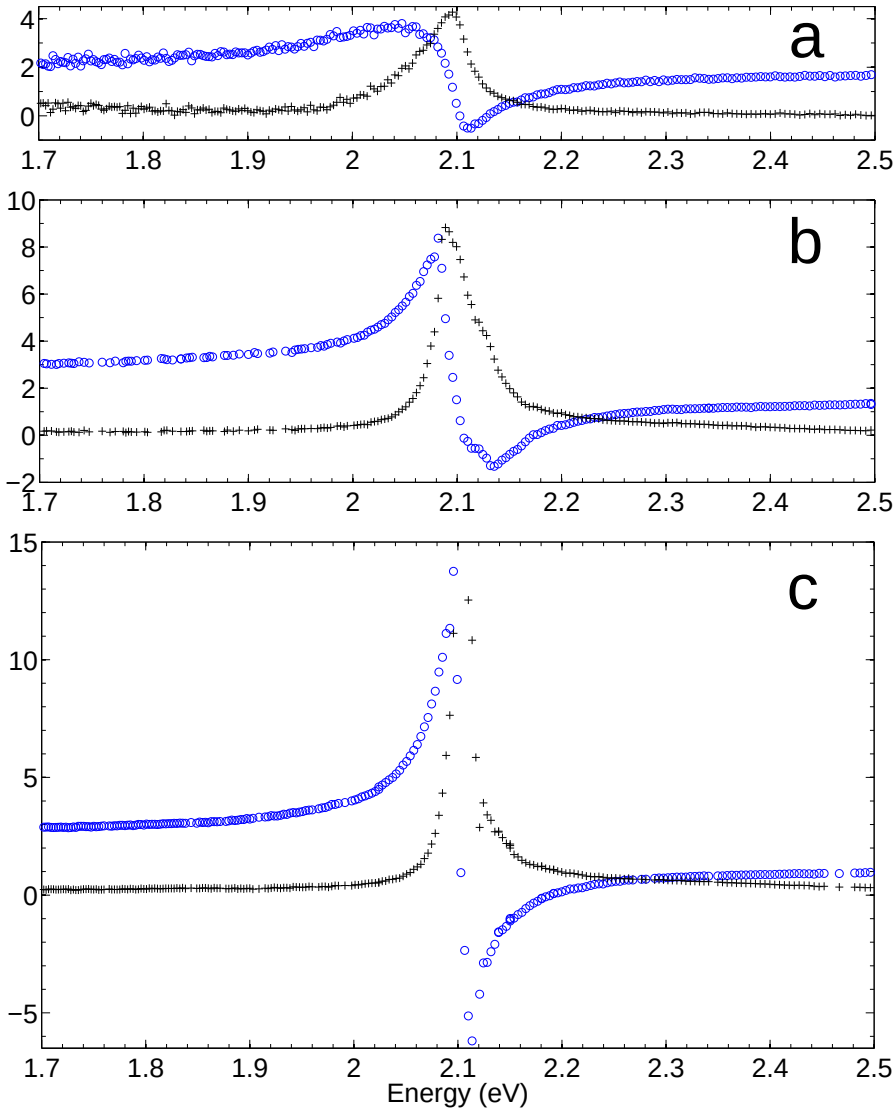


**Figure 1.9:** Experimentally-determined $\varepsilon'$ (blue circles) and $\varepsilon''$ (black crosses) for TDBC:PVA films with concentrations (a-c) 0.12 *wt%*, 0.48 *wt%* and 1.00 *wt%*, with thicknesses 64.9 ± 3.9 *nm*, 76.6 ± 5.9 *nm* and 69.7 ± 4.9 *nm* respectively.

the permittivity decreases with concentration. If the dye were absent from the PVA completely, the permittivity would be equal to $\varepsilon = (1.52)^2 = 2.31$ for all photon energies. Therefore, it is expected that a threshold concentration exists for which the real part of the permittivity of the film dips below zero, and the film takes on quasi-metallic optical properties. From the data shown in Fig. 1.9a, it is deduced that this concentration is less than 0.12 *wt%*, since the minimum value of $\varepsilon'$ for the

0.12 *wt%* sample is approximately equal to $\varepsilon' = -0.51$.

The minimum in the real part of the permittivity decreases to $\varepsilon' = -1.3$ for the 0.48 *wt%* TDBC:PVA film, and to $\varepsilon' = -4.2$ for the 1.00 *wt%* TDBC:PVA film. The lowest data point for the $\varepsilon'$ for the 1.00 *wt%* film as calculated is even less than this, but the data points around the peak in $\kappa$ from which $\tilde{n}$ was deduced have the most amount of noise for any of the samples tested. Therefore, the values shown for $\varepsilon'$ around this point are assumed to be subject to this experimental error. Indeed, given the general trend of the evolution of $\varepsilon'$ from the other three samples (including the minimum of $\varepsilon' = -5.6$ for the 1.46 *wt%* sample), the evidence for this presumption is bolstered.

Another observation drawn from Fig. 1.9 is that the energy range over which the real part of the permittivity is negative increases with dye concentration. For the 0.12 *wt%* TDBC:PVA film, this range is $2.10\ eV < E < 2.12\ eV$. As shown above, this range increases to $2.10\ eV < E < 2.25\ eV$ for the 1.46 *wt%* TDBC:PVA film. This range of energies is sometimes referred to as the 'polariton gap'.[48]

## 1.5 Computing the Apparent Colour of Materials

All structures (be they bulk, planar, or nanoparticle structures) have reflectance and transmittance spectra associated with them. Some structures, such as balls of strongly water-absorbing polymers[49] in aqueous environments, or materials coated with VANTA black,[50] reflect relatively little in the visible range; whereas others, such as bulk silver, reflect strongly in the visible range. The visible spectra give rise to colours as seen by the human eye. The human eye itself possesses three types of cone cells embedded in the retina, with each cone type containing a different light-sensitive pigment.[51] These different pigments have different peak absorption wavelengths and different sensitivities, as shown in Fig. 1.10 (overleaf). It is the relative amount of each of the three cone cells stimulated which produces the colours observed by the human eye.

In order to verify the reflectance and transmittance calculations made in this thesis, a function was developed to compute the RGB values which best represent the colours that would be observed by the human eye, taking the reflectance (or transmittance) spectra as inputs. This code is detailed in App. A.1. To illustrate the range of colours produced by the function, the visible spectrum is plotted alongside the three curves in Fig. 1.10. The spectrum was produced using 200 roughly monochromatic square spectra, each with equal intensity, across the visible range.

Colour calculations for the measured spectra of the 70 *nm* 1.46 *wt%* TDBC:PVA film at normal incidence are shown in Fig. 1.11. The orange colour as observed in reality for reflection (*cf.* the photograph of the same system in Fig. 1.4) is recovered. Therefore, given that the code can be used to reproduce an experimentally-observed colour, it can by extension be applied to predict the colour observed given a particular spectrum. This is explored in the context of thin films and multilayer stacks in Ch. 3.

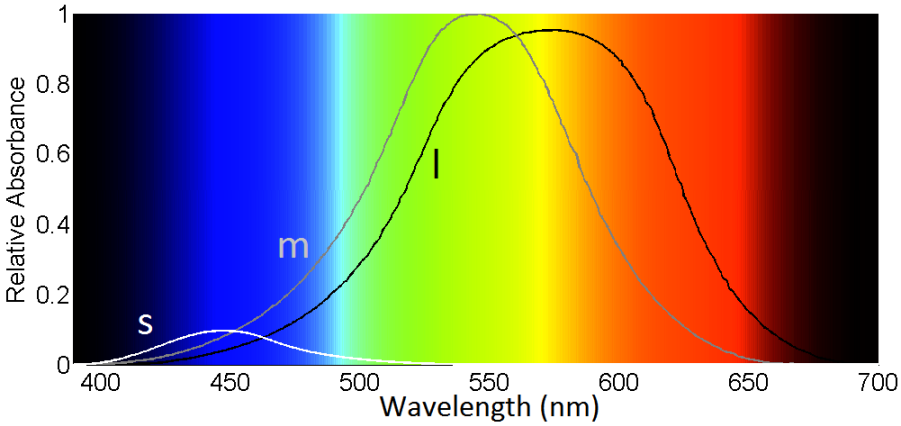


**Figure 1.10:** Curves: Relative absorbance (sensitivities) for the s (short, or blue) m (medium, or green) and l (long, or red) cones in the typical human eye. The spectrum shown is computed using the data from these three curves.

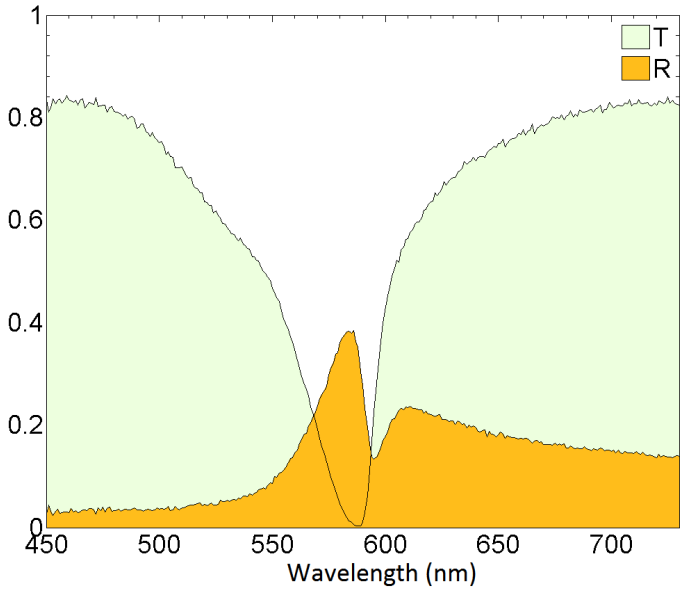


**Figure 1.11:** The calculated colours from reflectance (orange) and transmittance (greenish) spectra for a 70 *nm* 1.46*wt%* TDBC:PVA film.

One current limitation of the colour produced is that the range of wavelengths for which experimental data is available in Fig. 1.11 is not inclusive of the visible wavelength range 400 $nm < \lambda < 450$ *nm*: this range is dominated by the *s* (or blue) cone, seen in Fig. 1.10. The omission of this range means that the RGB colours calculated may suffer from an underestimate in the B (blue) channel, and consequently, the colours plotted in Fig. 1.11 may not be as blue as they might be in reality. Given that the

reflectance of the TDBC:PVA film is dominated by the peak at around $\lambda = 580\ nm$, and that $R$ is expected to be low-valued for this range of wavelengths, the orange colour observed in reflectance is recovered regardless of this omission. However, the green colour plotted for transmittance in Fig. 1.11 is almost certainly in need of adjustment: this is seen by continuation of the line for transmittance in Fig. 1.11 to shorter wavelengths, where it is expected that $T$ should be high-valued.

## 1.6 Conclusions

The optical properties of a material such as its colour, the fraction of light it reflects and the fraction it transmits are governed by its complex permittivity, $\varepsilon$. In order to extract the permittivity of a thin film from its reflectance and transmittance spectra, the thickness of the film must be determined with as much accuracy as possible. Fresnel calculations over a range of film thicknesses can help to achieve smoother numerical solutions for the imaginary part of the refractive index, $\kappa$. These results can be deconvoluted and subsequently analysed using the Kramers-Kronig (KK) relations to find the real part of the refractive index $n$. The KK relations themselves are best used in the form where one integrates over all frequencies ($-\infty < \omega < \infty$), with the application of time-reversal symmetry on $\kappa$. Once $n$ and $\kappa$ are established, $\varepsilon = \varepsilon' + i\varepsilon''$ can be found easily.

The metallic appearance of plastic films doped with sufficient concentration of the excitonic dye TDBC is no coincidence: the permittivity of such films within a narrow range of photon energies is like that of a metal, with a negative real part. This range of energies increases with dye concentration. The question remains as to what extent TDBC-doped nanostructures exhibit metallic properties; this question is addressed in the following chapters. For the moment, this negative permittivity causes such films to be highly reflective in this range, and they appear orange as a result. This colour is recovered by use of a computer program operating on experimental reflectance data. The lack of experimental data at the blue end of the visible spectrum for the samples considered within this chapter means that the calculated colours are not completely accurate. In order to calculate more accurate colours, a model for $\varepsilon$ is needed. Development of such a model is the central topic of Ch. 2.

# 2

# Modelling the Permittivity of Excitonic Materials

*In this chapter, semi-classical and quantum-mechanical models for the permittivity of excitonic materials are introduced and evaluated against experimental data. Models to describe metals are also examined.*

## 2.1 Introduction

As seen in Ch. 1, permittivity $\varepsilon$ governs the response of a material to incident light. So far, the microscopic origin of $\varepsilon$ has been left undiscussed. In this chapter, the microscopic origin of $\varepsilon$ is explored, and several models (semi-classical and quantum mechanical) are evaluated against experimental data for metals and excitonic TDBC:PVA films. It is implicit in this chapter that the materials considered are linear and non-magnetic.

As a starting point for the interaction of a non-magnetic isotropic material with an incident optical field, the electric displacement vector $\boldsymbol{D}$ is defined,

$$\boldsymbol{D} = \varepsilon_0 \varepsilon \boldsymbol{E}, \tag{2.1}$$

where $\boldsymbol{E}$ is the electric field strength of the optical field. For linear materials, $\boldsymbol{D}$ is written as a linear function[52] of the polarisation density induced in the material ($\boldsymbol{P} = \varepsilon_0 \chi \boldsymbol{E}$) as,

$$\begin{aligned} \boldsymbol{D} &= \varepsilon_0 \boldsymbol{E} + \boldsymbol{P} \\ &= \varepsilon_0 (1 + \chi) \boldsymbol{E}, \end{aligned} \tag{2.2}$$

where $\chi$ is the linear electric susceptibility of the material. Comparison of Eq. 2.2 with Eq. 2.1 gives the relationship $\varepsilon = 1 + \chi$.

These fundamental macroscopic relationships enable models (either semi-classical or quantum) to be built mathematically in order to calculate $\varepsilon$.

## 2.2 Semi-Classical Models for Permittivity

In this section, two semi-classical theoretical models for material permittivity - the Lorentz model and the Drude model - are reviewed and evaluated. The Lorentz model is more suited to modelling insulators, and the Drude model is more suited to modelling metals. Mathematical expressions for both the steady-state and temporal responses of each are examined, and their applicability to modelling the permittivity of silver, gold and TDBC:PVA is quantified.

### 2.2.1 The Lorentz model

Since the advent of the Bohr model[53] of the atom it has been known that electrons do not orbit their nuclei at arbitrary distances, but instead occupy discrete shells - a fact explained by application of De Broglie's postulate of wave-particle duality[54] to the electron. With application of an electric field provided by a light source, a driving force is imparted upon these bound electrons, distorting the positions of the electrons from the orbitals in which they sit. Therefore, the starting point for a semi-classical frequency-dependent model of permittivity for a general material is to assume that the electrons in the material can be modelled as point particles, each with mass $m$, bound to their electron orbitals by a harmonic potential with resonant frequency $\omega_0$. The motion of the electrons is assumed to be damped; in practice, this damping can arise from processes such as electron-phonon,[55,56] electron-defect[57,58] and (to a lesser extent) electron-electron[59] scattering. In the Lorentz model, all of these processes are accounted for phenomenologically by a single (real) constant damping term, $\gamma$. In general, this damping term is a function of temperature,[55] but room temperature is assumed throughout this thesis.

The response of the system to a uniform electric field $\boldsymbol{E}$ is considered as follows: first, the force law $\boldsymbol{F} = e\boldsymbol{E}$ is assumed. This force induces a separation of charge of length $x$ between the electrons and the unperturbed orbitals, and as a result, the potential $U = e\boldsymbol{E} \cdot \boldsymbol{x}$ is established. The Lagrangian for the system is written as,

$$L(x, \dot{x}, t) = \frac{m}{2} e^{-\gamma t} \left( \dot{x}^2 - \omega_0^2 x^2 - \frac{2e}{m} \boldsymbol{E} \cdot \boldsymbol{x} \right), \tag{2.3}$$

from which the following equation of motion can be derived using the Euler-Lagrange equation,[60]

$$m(\ddot{x} - \gamma\dot{x} + \omega_0^2 x) = eE(t). \tag{2.4}$$

Solving this classical forced damped harmonic equation of motion in the time domain assuming that the magnitude of the applied field takes the form $E(t) = E_0 exp(-i\omega t)$ gives the following solution,

$$x(t) = x_c(t) + x_p(t). \tag{2.5}$$

Here,

$$x_c(t) = e^{-\gamma t/2}\left(Ae^{ibt} + Be^{-ibt}\right), \tag{2.6}$$

$$x_p(t) = x_0 e^{-i\omega t}. \tag{2.7}$$

The constants $A$, $B$ and $x_0$ are complex and $b^2 = \omega_0^2 - (\gamma/2)^2$. The solution for $x_c(t)$ is transient, and the steady-state solution is therefore wholly dependent upon $x_p(t)$. The amplitude $x_0$ is written as,

$$x_0 = \left(\frac{eE_0}{m}\right)\frac{1}{\omega_0^2 - \omega^2 - i\gamma\omega}, \tag{2.8}$$

which can be found by substitution of $x_p(t)$ into the equation of motion (Eq. 2.4). This separation of charge length is related to permittivity in the following way: polarisation of a material per unit volume is defined as,[61]

$$\begin{aligned} \boldsymbol{P} &= \varepsilon_0\chi(\omega)\boldsymbol{E} \\ &= Ne\boldsymbol{x}, \end{aligned} \tag{2.9}$$

where $N$ is the number of oscillators per unit volume and $\chi$ the electric susceptibility. From Eq. 2.9, the permittivity contribution $\varepsilon = 1 + \chi$ arising from these oscillators can be found as,

$$\varepsilon(t) = 1 + \frac{Nex(t)}{\varepsilon_0 E(t)}. \tag{2.10}$$

The division of $x$ by $E$ in Eq. 2.10 causes $\varepsilon$ to approach a constant value as $t \to \infty$,

$$\varepsilon(\omega) = \varepsilon_b(\omega) + \left(\frac{Ne^2}{\varepsilon_0 m}\right)\frac{1}{\omega_0^2 - \omega^2 - i\gamma\omega}, \tag{2.11}$$

where $\varepsilon_b$ is the background contribution to the permittivity arising from the lattice.[62] This result is known as the Drude-Lorentz model[63] (p.251). Its applicability can be extended to general dielectric materials by taking the assumption that there exist a number of resonant frequencies, $\omega_i$. The relative strength of the $i^{\text{th}}$ oscillator is accounted for by a reduced oscillator strength[64] $f_i$ (where $\sum_i f_i = 1$) so $\varepsilon$ becomes,

$$\varepsilon(\omega) = \varepsilon_b(\omega) + \sum_n \frac{f_n \omega_p^2}{\omega_n^2 - \omega^2 - i\omega\gamma_n}, \tag{2.12}$$

where a plasma frequency $\omega_p^2 = Ne^2/\varepsilon_0 m$ has been defined. In this way, $\varepsilon_b(\omega)$ in Eq. 2.11 can be imagined as the result of many single-mode harmonic oscillators spectrally far-removed from electronic transition energies.[48,65] Some authors[66,67] write Eq. 2.12 in the form,

$$\varepsilon(\omega) = \varepsilon_b(\omega) + \sum_n \frac{f_n\, \omega_n^2}{\omega_n^2 - \omega^2 - i\omega\gamma_n}, \tag{2.13}$$

which necessitates redefinition of $f_i$. The form in Eq. 2.13 is suited to materials with a discrete number of resonances, termed Lorentz dielectrics.

Considering only a single resonance at $\omega_0$ and a constant background contribution, Eq. 2.13 reduces to,

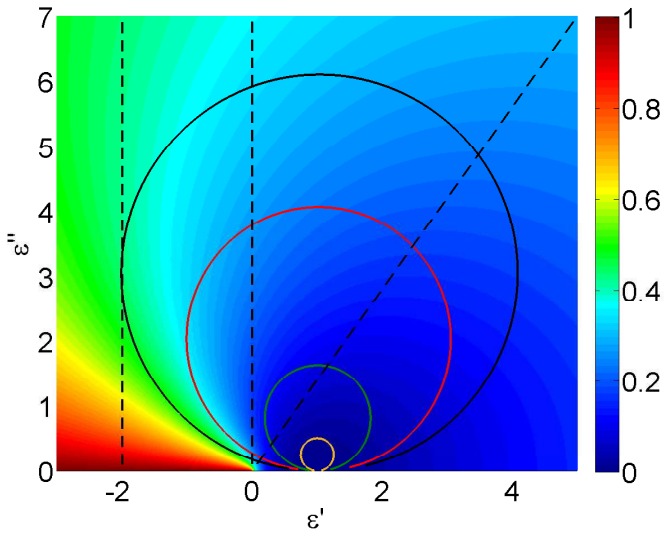


**Figure 2.1:** Colour plot: reflectance for a boundary constructed from $\varepsilon_1 = 1$ and $\varepsilon_2 = \varepsilon' + i\varepsilon''$. Solid lines: Cole-Cole plots for $\varepsilon$ arising from single-oscillator Lorentz models. Broken lines: the boundaries for differing behaviour ($\varepsilon' = 0$, $\varepsilon' = -2$ and $\varepsilon' = \varepsilon''$).

$$\varepsilon(\omega) = \varepsilon_b + \frac{f_0\,\omega_0^2}{\omega_0^2 - \omega^2 - i\omega\gamma}. \tag{2.14}$$

The properties of the single-oscillator Lorentz dielectric depend strongly upon the reduced oscillator strength, $f_0$: if $f_0$ is sufficiently large then the real part of the permittivity ($\varepsilon'$) will become negative in a small wavelength range below $\omega_0$[68] and the material will take on a metal-like appearance.[46] In practice, $\omega_0$ may correspond to an exciton excitation. Since any oscillator strength $f_i$ depends upon the emitter concentration, a threshold concentration necessary for a negative permittivity is produced, as illustrated in Fig. 2.1: in this figure, four Cole-Cole ($\varepsilon'$ *vs.* $\varepsilon''$) plots are shown for four differing values of $f_0$. In Fig. 2.1, the dielectric with the smallest value of $f_0$ is indicated by the orange line, and the largest in black. These plots are superimposed on a reflectance plot similar to Fig. 1.2. From Fig. 2.1, as $f_0$ increases, the reflectance of the macroscopic Lorentz dielectric increases in a small range of wavelengths as it becomes more metal-like in this range. As shown however, there is no escape from the inherent dielectric nature of such materials, as $\varepsilon$ in the Cole-Cole plot will always pass through the low loss tangent region. Therefore, Lorentz dielectrics behave optically like metals at some wavelengths, and like dielectrics at others.

This property is seen more readily in Fig. 2.2 (overleaf), where a best fit for the permittivity of the 70 *nm* 1.46 *wt%* TDBC:PVA film examined in Ch. 1 is shown using a single-oscillator Drude-Lorentz model (Eq. 2.14). This fit was obtained by determination of $\omega_0$, $f_0$ and $\gamma$ in turn by evaluation of $\varepsilon(\omega)$ using Eq. 2.14, with comparison to the experimentally-determined values of $\varepsilon(\omega)$.

The transient behaviour of $\varepsilon(\omega)$ is now examined semi-classically, by finding solutions for $A$ and $B$ in Eq. 2.6. This requires imposing initial conditions on $x$ and $\dot{x}$. Presuming the electrons in the material to be initially unperturbed and at rest within their orbitals, the conditions $x(0) = \dot{x}(0) = 0$ are chosen. These two conditions lead to the following expressions for $A$ and $B$,

$$A = \frac{x_0}{2b}\left(i\frac{\gamma}{2} - (b + \omega)\right) \tag{2.15}$$

$$B = \frac{x_0}{2b}\left(-i\frac{\gamma}{2} - (b - \omega)\right). \tag{2.16}$$

With the use of Eq. 2.10, the following full, time-dependent solution for $\varepsilon$ is obtained,

$$\varepsilon = \varepsilon_b + \left(\frac{Ne^2}{\varepsilon_0 m}\right)\frac{1 + e^{-\gamma t/2}\left[\left(\frac{\gamma}{2b} - i\frac{\omega}{b}\right)\sin(bt) + \cos(bt)\right]}{\omega_0^2 - \omega^2 - i\gamma\omega}, \tag{2.17}$$

which for $t \to \infty$ approaches Eq. 2.11.

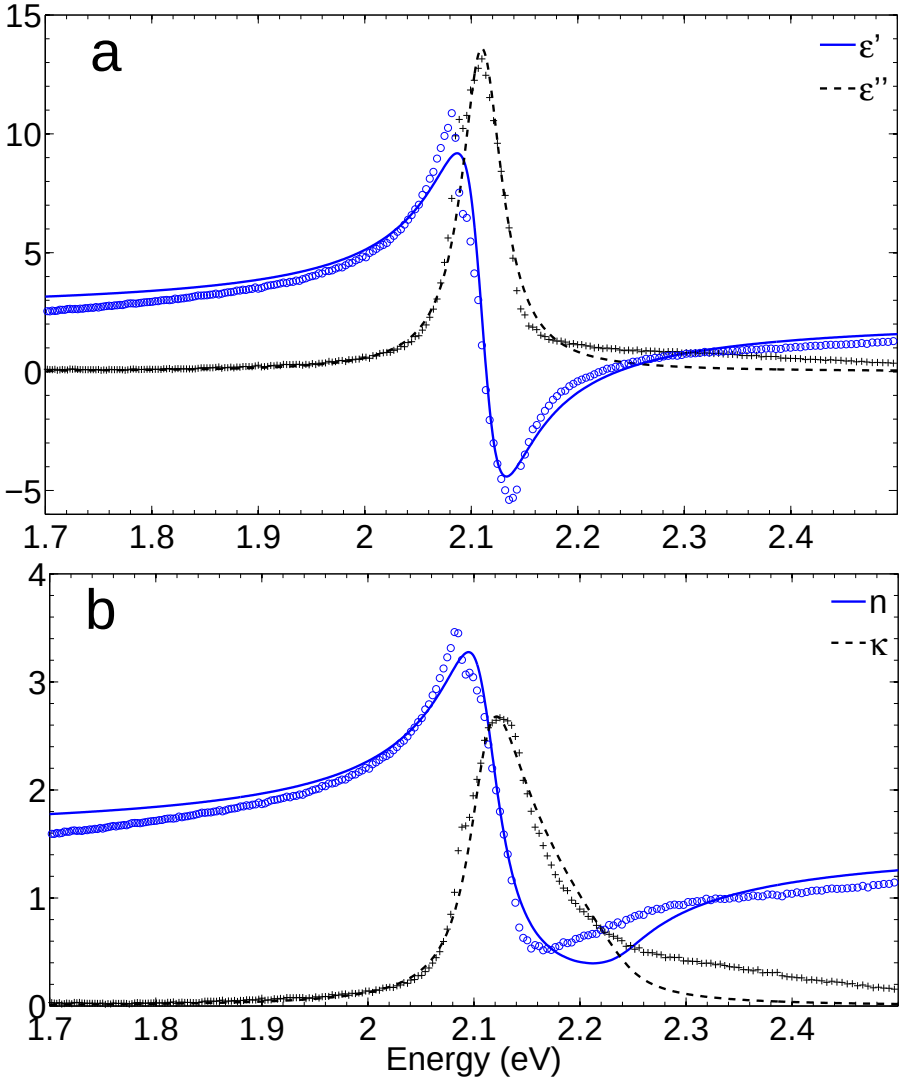


**Figure 2.2:** Experimentally-determined (a) $\varepsilon$ and (b) $\tilde{n}$ for a 70 *nm* thin film of 1.46 *wt%* TDBC:PVA (circles and crosses), with the same quantities from the best-fit single-oscillator Lorentz model (lines). The parameters used are $f_0 = 0.3$, $\gamma = 46.1$ *meV* and $\omega_0 = 2.11$ *eV*.

Using the same parameters used to plot $\varepsilon$ in Fig. 2.2, the time-dependent solution is plotted in Fig. 2.3. The oscillatory behaviour of $\varepsilon$ in Fig. 2.3 follows the angular frequency $b = \sqrt{\omega_0^2 - \gamma^2/4} - \omega$. When $\gamma \ll |\omega_0 - \omega|$, $b \approx \omega_0 - \omega$, which is approximately equal to the generalised Rabi frequency[69] $\tilde{\Omega} = \sqrt{\Omega^2 + (\omega - \omega_0)^2}$.

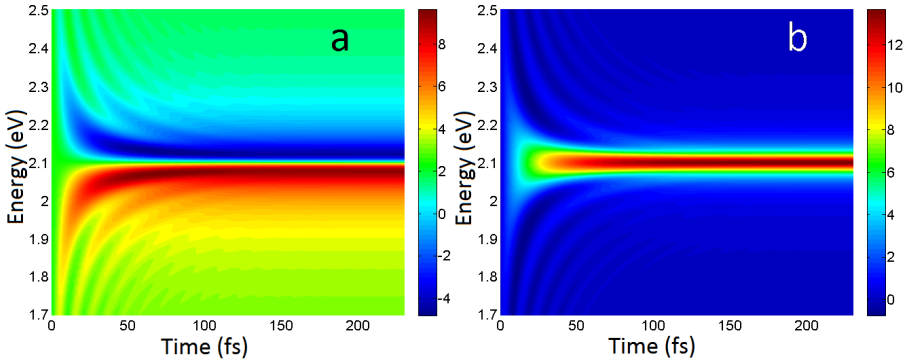


**Figure 2.3:** The real (a) and imaginary (b) parts of $\varepsilon$ in the time domain for 1.46 *wt%* TDBC:PVA using the best-fit Lorentz model, using the same parameters as Fig. 2.2.

## 2.2.2 The Drude model

In metals, the leading contribution to permittivity arises from free electrons.[70] The Lorentz model for dielectrics can be adapted to develop a semi-classical model which includes contributions from free (as opposed to bound) electrons. This is accomplished mathematically by removal of the resonant frequency in Eq. 2.4, *i.e.* $\omega_0 = 0$. This results in the electrons being unbound from their ions in the metal model. The phenomenological damping term $\gamma$ is retained, in order to account for all collisional processes. In doing this, the equation of motion for the Drude model is obtained,

$$m\ddot{x} - m\gamma\dot{x} = eE(t). \tag{2.18}$$

As before, a time-dependent solution can be found by solving Eq. 2.18 for $x$, with substitution of this solution into Eq. 2.10. The full, time-dependent solution for $\varepsilon$ takes the form,

$$\varepsilon(t) = \varepsilon_b + \left(\frac{Ne^2}{\varepsilon_0 m}\right)\frac{1}{\omega^2 + i\omega\gamma}\left(e^{-\gamma t}e^{-i\omega t} - 1\right), \tag{2.19}$$

for which as $t \to \infty$ gives the steady-state equation,

$$\varepsilon(\omega) = \varepsilon_b(\omega) - \frac{\omega_p^2}{\omega^2 + i\gamma\omega}, \tag{2.20}$$

where $\omega_p^2 = Ne^2/\varepsilon_0 m$. Besides the assumption that free electrons are the only contribution to $\varepsilon$, in the Drude model fixed ions are assumed, and it is also assumed that electron-electron interactions can be neglected.[70]

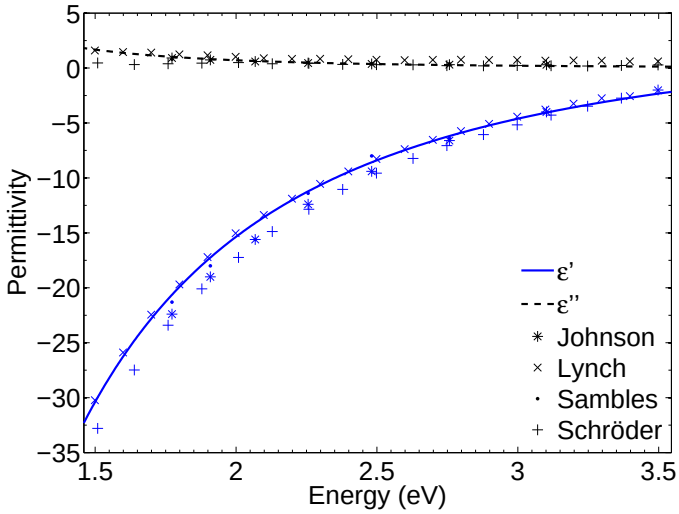


**Figure 2.4:** Permittivity for bulk silver over the optical range calculated with a Drude fit using the parameters as determined by Le Ru and Etchegoin[5] next to experimental data.[71–74]

The plasma frequency $\omega_p$ for metals such as silver and aluminium is in the ultraviolet (UV) region of the spectrum. Below this frequency, $\varepsilon' < 0$ and metals become highly reflective (*cf.* Fig. 2.1). This is the explanation for why silvered mirrors reflect visible frequencies particularly well. Permittivity calculations made using Eq. 2.20 for bulk silver are shown in Fig. 2.4, in comparison to four sets of experimentally-determined data.[71–74] The differences in experimental data can be attributed to variation in temperature for the various experiments: a higher temperature can give a slightly raised value[75] of $\varepsilon''$. Overall, the Drude model provides a close fit to the experimental values over the range shown. The Drude model can therefore be relied upon to calculate physically realistic values of the permittivity for bulk silver within this range.

In common with silver and aluminium, the plasma frequency for gold is in the UV, but there exists an extra contribution to the permittivity besides the contribution from free electrons: the interband contribution.[76] The Drude-Lorentz model can be adjusted phenomenologically to accommodate this additional contribution in the following way,[5,76]

$$\varepsilon(\omega) = \varepsilon_\infty \left(1 - \frac{\omega_p^2}{\omega^2 + i\omega\gamma}\right) + \sum_n A_n \omega_n \left[\frac{e^{i\phi_n}}{(\omega_n - \omega) - i\gamma_n} + \frac{e^{-i\phi_n}}{(\omega_n + \omega) + i\gamma_n}\right]. \quad (2.21)$$

Here, $\phi_n$ are phase shifts, $\omega_n$ are the frequencies of the interband transitions, and $\gamma_n$ are their associated damping terms. $A_n$ is a dimensionless constant. Using Eq. 2.21 with the parameters used by Le Ru and Etchegoin,[5,76] the permittivity for bulk gold is plotted in Fig. 2.5 against experimentally-determined values.[71–74] The fit is sufficiently

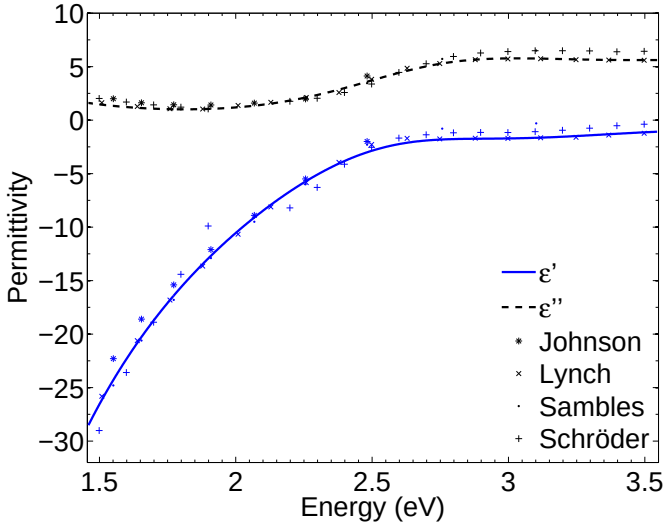


**Figure 2.5:** The calculated real (black) and imaginary (blue) parts of the permittivity for bulk gold using the Lorentz model with interband transitions (Eq. 2.21) plotted against experimental data.[71–74] The turning points of the interband transitions lie at 2.64 *eV* (470 *nm*) and 3.82 *eV* (325 *nm*).

close to the four datasets available for Eq. 2.21 to be used to make physically plausible calculations.

In order to model metal nanoparticles, one cannot simply take Eq. 2.21 at face value, because $\gamma$ is dependent upon the length scale of the system. Expressing $\gamma$ in terms of the Fermi velocity ($v_F$) of the metal and the radius ($r$) of the metal nanoparticle,[77]

$$\gamma = \gamma_b + A\frac{v_F}{r}, \tag{2.22}$$

where $A$ is a dimensionless constant of order unity. Eq. 2.22 implies that smaller nanoparticles (with diameters less than $d \approx 20$ *nm*) have correspondingly larger values of $\gamma$, leading to spectrally flatter permittivities.

## 2.3 Quantum Models for Permittivity

Throughout the whole discussion of the Lorentz and Drude models for permittivity, nothing was assumed about the specifics of the microscopic structure of the material modelled, except that the electrons in the material occupy orbitals and respond to light as classical damped harmonic oscillators. Equivalently, the Lorentz model assumes that each atom in the material can be modelled as a classical non-interacting harmonic

oscillator. Given that real atoms and molecules have energy eigenstates between which the electrons can transition, this simplicity does not capture all of the physics involved. To address this problem, physically more appealing quantum-mechanical models are now examined for molecular materials, based on the specifics of the microscopic structure of the material in question.

The start point is to examine the macroscopic polarisation, $\boldsymbol{P}$, induced in a general linear material by an applied electric field $\boldsymbol{E}$. Macroscopic polarisation is proportional to the average dipole moment of each molecule in the material, represented by $\langle \boldsymbol{d} \rangle$. Eq. 2.9 can be re-written for linear materials in the following way,[52]

$$\boldsymbol{P} = \frac{1}{2}\varepsilon_0 \boldsymbol{E}(\chi e^{-i\omega t} + \chi^* e^{i\omega t}) = N\langle \boldsymbol{d} \rangle, \tag{2.23}$$

where $N$ is now the number density of molecules. To find $\chi$ (and hence $\varepsilon$) an expression for $\langle \boldsymbol{d} \rangle$ is required. In quantum mechanics, $\langle \boldsymbol{d} \rangle$ is the expectation value of the dipole moment, computed from the trace of the matrix $\rho \boldsymbol{d}$, where $\rho$ is the density matrix for the system and $\boldsymbol{d}$ is the transition dipole matrix.

This general treatment can in principle be applied to any material. However, in this thesis it is excitonic dye molecules only which are treated quantum mechanically. The primary reason for this is that the Drude model suffices to model both gold and silver, whereas the Lorentz model for permittivity does not fully account for all of the features seen in the permittivity of a TDBC:PVA film. Indeed, the damping parameter used in the Lorentz model bears little correlation to the decay rate observed by others.[78] Therefore, in the following subsections, a quantum mechanical description for the permittivity of aggregated excitonic dyes is developed. The dual hope is to establish a more accurate model for permittivity than the Lorentz model, and to yield results which might help form an instructive microphysical picture of such dyes.

### 2.3.1 The density matrix

The dynamic evolution of a quantum system (or an ensemble of quantum systems) subject to a perturbing potential may be deduced by solving the Schrödinger equation[79] for the wave function $|\Psi\rangle$,

$$i\hbar \frac{\partial}{\partial t}|\Psi\rangle = \hat{H}|\Psi\rangle, \tag{2.24}$$

given the complete Hamiltonian $\hat{H}$. Performing this analysis for a two-level system illuminated by an electric field leads to unitary evolution between the two levels. However, when the system is brought into contact with a thermal environment, decay from the excited state - along with dephasing on the coherence of the two levels - becomes induced in the system; this causes the response to become damped. The

density matrix offers a neat way of representing this mathematically. The density operator is defined by,[80–82]

$$\hat{\rho} = \sum_{k} |\Psi\rangle\langle\Psi|, \tag{2.25}$$

where the wave function $|\Psi\rangle$ contains the set $\{|k\rangle\}$, *i.e.* the energy eigenstates of the system constituents, be these molecules, emitters, or atoms. The elements of the density matrix are computed using these eigenstates around the density operator,

$$\rho_{ij} = \langle i|\hat{\rho}|j\rangle. \tag{2.26}$$

The diagonal density matrix elements written in terms of the eigenstate coefficients are $\rho_{ii} = c_i^* c_i = |c_i|^2$. These diagonal elements are the populations[82] of the density matrix and correspond to the probability of any given emitter being in that particular state. This leads to two constraints on the density matrix such that,

$$\sum_{i} \rho_{ii} = Tr(\rho) = 1 \tag{2.27}$$

$$Tr(\rho^2) \leq 1. \tag{2.28}$$

The case where $Tr(\rho^2) = 1$ corresponds to a pure state,[80] and under this circumstance all the constituent systems occupy the same energy eigenstate. In theory, this only occurs for ensembles at $T = 0\ K$ (absolute zero). Boltzmann statistics[83] show that an undisturbed ensemble of two-level systems at room temperature may be regarded as occupying a pure state to an accuracy of 99% if the ground state of each system is separated from the first excited state by at least $0.112\ eV$.

In the case where $Tr(\rho^2) < 1$, the system is a thermal ensemble, equivalent to a mixed state ensemble, or a coherent superposition of states[81] used by other authors. The off-diagonal density matrix elements $\rho_{ij} = c_i^* c_j$ $(i \neq j)$ are the coherences of the density matrix. These are generally complex and relate the response of the system to the applied field;[82] they also give a measure of the superposition of any given element of the ensemble between the two levels.

The density matrix can be used to calculate the expectation value of an observable. This is seen by calculation of the expectation value of an observable $\hat{Q}$,

$$\begin{aligned}\langle\hat{Q}\rangle &= \langle\Psi|\hat{Q}|\Psi\rangle \\ &= \langle\Psi||\Psi\rangle\langle\Psi|\hat{Q}|\Psi\rangle \\ &= \langle\Psi|\hat{\rho}\hat{Q}|\Psi\rangle \\ &= \sum_i \rho_{ii}Q_{ii} \\ &= Tr(\rho Q). \end{aligned} \tag{2.29}$$

Therefore, the expectation value of an observable is the trace of the matrix product of the observable with the density matrix.

The time-dependency of $\rho$ can be determined by taking the time derivative of Eq. 2.25 with substitution of the Schrödinger equation (Eq. 2.24),

$$\begin{aligned}\frac{d\hat{\rho}}{dt} &= \frac{d}{dt}(|\Psi\rangle\langle\Psi|) \\ &= |\dot{\Psi}\rangle\langle\Psi| + |\Psi\rangle\langle\dot{\Psi}| \\ &= \frac{i}{\hbar}(-\hat{H}|\Psi\rangle\langle\Psi| + |\Psi\rangle\langle\Psi|\hat{H}) \\ &= -\frac{i}{\hbar}(\hat{H}\hat{\rho} - \hat{\rho}\hat{H}) \\ &= -\frac{i}{\hbar}[\hat{H},\hat{\rho}]. \end{aligned} \tag{2.30}$$

This result is the Liouville equation and governs the time evolution of an ensemble. For the case where the interactions with the environment are neglected, the expected unitary evolution is recovered.[84]

Given that the interaction of a system with its environment causes dephasing on the coherences of the density matrix, for a thermal bath with no memory of interaction (the Born-Markov regime[85]), an assumption can be made that this dephasing occurs exponentially. This leads to the following differential matrix equation for $\rho$,

$$\dot{\rho} = -\frac{i}{\hbar}[H,\rho] - L_D\rho, \tag{2.31}$$

which is the Liouville-von Neumann equation.[86] Here, $L_D$ is the dissipative Lindblad superoperator containing the constants corresponding to the population relaxation and dephasing rates between the levels.[84,87]

### 2.3.2 The Hamiltonian for an excitonic material

Excitons are quasi-particles comprising an electron and an electron hole, first described by Frenkel as, "excitation waves" .[88] Excitons in various guises can be hosted by insulators,[88] semiconductors[89] and organic dye molecules.[90] The excitons examined in this thesis are Frenkel excitons, where the electron holes are assumed to be localised. Excitons have a particular excitation energy.[88] Given these properties, an excitonic material comprising organic dye molecules can be treated as an ensemble of quantum systems with two energy eigenstates each. Each molecule in the ensemble is an open quantum system, and as such, the Hamiltonian for an open quantum system can be expressed as,[91,92]

$$\hat{H} = \hat{H}_0 + \hat{H}_B + \hat{H}_I, \tag{2.32}$$

where $\hat{H}_0$ is the Hamiltonian of the isolated system, $\hat{H}_B$ is the bath Hamiltonian which describes the interaction of $\hat{H}_0$ with the environment, and $\hat{H}_I$ is the interaction Hamiltonian to describe the interaction of $\hat{H}_0$ with an applied electric field.

For TDBC molecules in a PVA host medium, $\hat{H}_B$ should represent the $3\nu_m - 6 = 129$ intramolecular[93] vibrational modes (where $\nu_m$ is the number of atoms *per* molecule) and a multitude of intermolecular modes. These vibrational modes are responsible for induced decay and dephasing in the system,[94,95] along with a small shift in the excited state energy of the molecules.[96] Rather than determining $\hat{H}_B$ directly, two commonly-used simplifications can be made: first, the effects of the bath (vibrationally induced decay and dephasing) can be accounted for phenomenologically by application of the dissipative Lindblad superoperator (see above). Second, the small energy shift induced by the bath can be assumed to be small, and is ignored.[91,92,97]

#### 2.3.2.1 Single-exciton Hamiltonian

For an ensemble of $\mathcal{N}$ two-level excitonic molecules in a nanoparticle, $\hat{H}_0$ can be written as,[96,98,99]

$$\hat{H}_0 = \hbar\omega_0|0\rangle\langle 0| + \sum_{i=1}^{\mathcal{N}} \left( \hbar\omega_1^{(1)}|1_i\rangle\langle 1_i| + \sum_{\substack{j=1 \\ j\neq i}}^{\mathcal{N}} J_{ij}|1_i\rangle\langle 1_j| \right). \tag{2.33}$$

Here, $|0\rangle$ is the ground state of the nanoparticle, and $|1_i\rangle$ represents a single exciton excited in the nanoparticle, localized on molecule $i$, with all of the other molecules in their ground states, *i.e.* $|1_i\rangle = |0_1, ..., 1_i, ..., 0_{\mathcal{N}}\rangle$. In this way, only a single exciton is

permitted within the ensemble at any time. The first term in brackets in Eq. 2.33, $\hbar\omega_1^{(1)}$, represents the average energy eigenvalue of a non-interacting molecule in the excited state (an exciton). The second term corresponds to inter-molecular coupling, with coupling energy $J_{ij}$. The coupling is taken to be Förster (dipole-dipole) coupling[98,100] since the overlap between the wave functions of each site are assumed to be small. The corresponding interaction Hamiltonian $\hat{H}_I$ modelled in the Schrödinger picture[101] and written in the same basis is,

$$\hat{H}_I = \sum_{i=1}^{\mathcal{N}} \left( g_i^* |0\rangle\langle 1_i| + g_i |1_i\rangle\langle 0| \right). \tag{2.34}$$

The coupling strength of the dipole to the external optical driving field is defined as $g_i = -\boldsymbol{E}(\boldsymbol{r}_i) \cdot \boldsymbol{\mu}_i$, where $\boldsymbol{\mu}_i$ is the transition dipole moment of molecule $i$. The single-exciton Hamiltonian matrix written in site basis is therefore,

$$H_{\mathcal{N}} = \begin{pmatrix} \hbar\omega_0 & g_1^* & g_2^* & \cdots & g_{\mathcal{N}}^* \\ g_1 & \hbar\omega_1^{(1)} & J_{12} & \cdots & J_{1\mathcal{N}} \\ g_2 & J_{21} & \hbar\omega_1^{(1)} & \cdots & J_{2\mathcal{N}} \\ \vdots & \vdots & \vdots & \ddots & \vdots \\ g_{\mathcal{N}} & J_{\mathcal{N}1} & J_{\mathcal{N}2} & \cdots & \hbar\omega_1^{(1)} \end{pmatrix}. \tag{2.35}$$

Although thorough, the Hamiltonian in Eq. 2.35 has dimension $(\mathcal{N}+1)\times(\mathcal{N}+1)$, and a density matrix formed using Eq. 2.35 would also have these dimensions. Given that $\mathcal{N}$ can typically be several thousand (for even a moderately-doped 100 *nm* diameter nanosphere), solving for such a large matrix would be computationally very demanding, despite considering only a single exciton in the ensemble. Therefore, a simpler Hamiltonian for a TDBC-doped nanoparticle which approximates the formalism above is now sought, which can be used to model macroscopic excitonic materials.

#### 2.3.2.2 Nearest-neighbour Hamiltonian

As a first step of this simplification process, it is identified that for an ensemble of aggregates (where the monomers within each aggregate are aligned with each other), the *intra*-aggregate coupling terms dominate.[102] This enables neglection of the *inter*-aggregate coupling terms. By making this approximation, the approach taken to describe a material (film or nanoparticle) doped with randomly distributed aggregates is to first describe a Hamiltonian for a single aggregate, and then to take an orientational average. This approach significantly eases computation by reduction of the dimension of the Hamiltonian from the total number of molecules in the structure ($\mathcal{N} \approx 10^4$ or greater) to merely the number of monomers in each aggregate ($n \approx 10^1$).

The next step is to identify that for a single aggregate, nearest-neighbour couplings dominate the intra-aggregate interactions. The Hamiltonian matrix formed under

this approximation using Eq. 2.33 is termed the 'nearest-neighbour Hamiltonian', and denoted $\hat{H}_{NN}$. The nearest-neighbour Hamiltonian matrix for a single aggregate containing $n$ monomers takes the form,

$$H_{NN,n} = \begin{pmatrix} \hbar\omega_0 & 0 & 0 & 0 & \cdots & 0 \\ 0 & \hbar\omega_1^{(1)} & J & 0 & \cdots & 0 \\ 0 & J & \hbar\omega_1^{(1)} & J & \cdots & 0 \\ 0 & 0 & J & \hbar\omega_1^{(1)} & \cdots & 0 \\ \vdots & \vdots & \vdots & \vdots & \ddots & \vdots \\ 0 & 0 & 0 & 0 & \cdots & \hbar\omega_1^{(1)} \end{pmatrix}. \tag{2.36}$$

Here, $J$ represents the nearest-neighbour coupling (presumed equal for each site in the regular lattice). The eigenvalues and eigenstates for this Hamiltonian matrix are now derived. Eq. 2.36 can be written in the form,

$$H = \begin{pmatrix} \hbar\omega_0 & 0 \\ 0 & H_n + \lambda I \end{pmatrix}, \tag{2.37}$$

where $H_n + \lambda I$ is the sub-matrix of $H_{NN,n}$ written explicitly in Eq. 2.36, and represents an aggregate with $n$ molecular units. The eigenvalues of Eq. 2.36 can be determined by solving,

$$(\hbar\omega_0 - \lambda)|H_n| = 0. \tag{2.38}$$

The first of these is the ground state energy $\lambda_0 = \hbar\omega_0$, which readily yields the eigenvector $|0\rangle$. The other eigenvalues and eigenvectors require more consideration. The first step is to find an expression for $|H_n|$. Writing this determinant in terms of further sub-matrices gives the following recursive relationship,

$$|H_n| = (\hbar\omega_1^{(1)} - \lambda)|H_{n-1}| - J^2|H_{n-2}|. \tag{2.39}$$

The next step is to identify that this recursive relationship can be put into the same form as the recurrence relation for Chebyshev polynomials,[103] *i.e.*,

$$U_{n+1}(x) = 2xU_n(x) - U_{n-1}(x). \tag{2.40}$$

In order to do this, both sides of Eq. 2.39 are multiplied by $J^{-n}$,

$$J^{-n}|H_n| = \frac{\hbar\omega_1^{(1)} - \lambda}{J} J^{-(n-1)}|H_{n-1}| - J^{-(n-2)}|H_{n-2}|. \tag{2.41}$$

Redefining $|H_n'| = J^{-n}|H_n|$ gives,

$$|H'_n| = \frac{\hbar\omega_1^{(1)} - \lambda}{J}|H'_{n-1}| - |H'_{n-2}|. \tag{2.42}$$

In doing this, the matrix determinants $|H'_n|$ are identified as Chebyshev polynomials of the second kind (written as $U_n(x)$) with argument $x = (E - \lambda)/2J$. Therefore, the eigenvalues $\lambda$ are solutions of the equation,

$$|H_n| = J^n U_n\left(\frac{\hbar\omega_1^{(1)} - \lambda}{2J}\right) = 0. \tag{2.43}$$

Given that the explicit form of Chebyshev polynomials of the second kind is,

$$U_n(x) = \frac{\sin(n+1)\arccos(x)}{\sin(\arccos(x))}, \tag{2.44}$$

the set of eigenvalues $\lambda$ are found as,

$$\lambda = \hbar\omega_m = \hbar\omega_1^{(1)} - 2J\cos\left(\frac{m\pi}{n+1}\right). \tag{2.45}$$

The eigenvectors $|m\rangle$ are determined by analysis of $H_n|m\rangle$. The $j^{\text{th}}$ element of $H_n|m\rangle$ is,

$$Jm_{j-1} + \hbar\omega_1^{(1)}m_j + Jm_{j+1} = \lambda m_j, \tag{2.46}$$

which can be re-arranged into the form,

$$m_{j-1} + \left(\frac{\hbar\omega_1^{(1)} - \lambda}{J}\right)m_j + m_{j+1} = 0. \tag{2.47}$$

This expression is (again) identical to the recurrence relation for Chebyshev polynomials.[103] By identifying,

$$\begin{aligned} m_{j+1} &= U_j(-(\hbar\omega_1^{(1)} - \lambda)/2J) \\ &= C\sin\left((j+1)\arccos\left(\frac{\hbar\omega_1^{(1)} - \lambda}{2J}\right)\right) \\ &= C\sin\left(\frac{j+1}{n+1}m\pi\right), \end{aligned} \tag{2.48}$$

where $C = \sqrt{2/n+1}$ is a normalisation constant, the final expression for the excited states of the aggregate is,[97,104]

$$|m\rangle = \sqrt{\frac{2}{n+1}} \sum_{j=1}^{n} \sin\left(\frac{jm\pi}{n+1}\right)|1_j\rangle, \tag{2.49}$$

where $1 < m < n$. These states each describe a single exciton delocalised over the aggregate, with energy $\hbar\omega_m$.

The accuracy of the nearest-neighbour Hamiltonian is quantified by consideration of the next nearest-neighbour interactions using a similar process. Adopting the same approach as above inclusive of the next nearest-neighbour interactions generates a recurrence relation involving four terms. Such a recurrence relation might in principle be solved by comparison with four-term recurrence relations of the Hypergeometric function,[105] but it can be shown that such a correction is less than 5% different to the nearest-neighbour Hamiltonian. The nearest-neighbour Hamiltonian is therefore sufficiently accurate to describe the system as a whole.

#### 2.3.2.3 Reduction of the nearest-neighbour Hamiltonian

Thus far, the simplification process of the Hamiltonian for aggregates has reduced the number of excited eigenstates in the system from the number of molecules in the structure to merely the number of molecules in each aggregate. However, analysis of the relative strengths of the transition dipole moments of the aggregate shows that half of these eigenstates can be discarded with impunity. The starting point is the definition of the transition dipole moment for the aggregate,

$$\boldsymbol{d}_{0m} = \langle m| \sum_j \hat{\boldsymbol{\mu}}_{0j}|0\rangle \tag{2.50}$$

$$= \sqrt{\frac{2}{n+1}} \left( \sum_{j=1}^{n} \sin\left(\frac{jm\pi}{n+1}\right)\langle 1_j| \right) \left( \sum_j \hat{\boldsymbol{\mu}}_{0j} \right)|0\rangle, \tag{2.51}$$

where $\hat{\boldsymbol{\mu}}$ is the monomer dipole moment operator. Assuming that all sites are equal,

$$\boldsymbol{d}_{0m} = \sqrt{\frac{2}{n+1}} \sum_{j=1}^{n} \sin\left(\frac{jm\pi}{n+1}\right)\boldsymbol{\mu}. \tag{2.52}$$

The sum in Eq. 2.52 is a combination of two geometric series, which when evaluated gives $\cot(m\pi/2(n+1))$ for even $m$, and zero otherwise. The full formula for the transition dipole moment of the aggregate can therefore be written as,[106]

$$\boldsymbol{d}_{0m} = \boldsymbol{\mu}\sqrt{\frac{1-(-1)^m}{n+1}} \cot\left(\frac{m\pi}{2(n+1)}\right). \tag{2.53}$$

This proves that states with even $m$ cannot couple with the incident field, and can therefore be discarded. This reduces the number of states to be considered by a factor of two. By a similar process, it can be shown that $\boldsymbol{d}_{nn'} = 0$ where $n > 0$ and $n \neq n'$. The interaction Hamiltonian for the aggregate is now written as,

$$\hat{H}_I = \sum_{m}^{(n+1)/2} G_{0m} \left( |0\rangle\langle 2m-1| + |2m-1\rangle\langle 0| \right), \tag{2.54}$$

where $G_{0m} = \boldsymbol{E} \cdot \boldsymbol{d}_{0m}$ is the coupling strength of the electric field to the aggregate dipole moment $\boldsymbol{d}_{0m}$. In the case where the ensemble comprises randomly-distributed aggregates this dipole moment can be taken as the orientational average of the aggregate dipole moment, *i.e.*

$$\bar{\boldsymbol{d}}_{01} = \boldsymbol{d}_{01}/\mathcal{D}, \tag{2.55}$$

where $\mathcal{D}$ is the dimensionality of the space in which the dipoles are distributed. This orientational average is derived in App. B.1.

With the use of Eq. 2.45, 2.49 & 2.54, the reduced, diagonalised nearest-neighbour Hamiltonian for the aggregate is written in the form,

$$H = \begin{pmatrix} \hbar\omega_0 & G_{01} & G_{03} & \cdots & G_{0n'} \\ G_{01} & \hbar\omega_1 & 0 & \cdots & 0 \\ G_{03} & 0 & \hbar\omega_3 & \cdots & 0 \\ \vdots & \vdots & \vdots & \ddots & \vdots \\ G_{0n'} & 0 & 0 & \cdots & \hbar\omega_{n'} \end{pmatrix}, \tag{2.56}$$

where,

$$n' = \begin{cases} n & (n = \text{odd}) \\ n-1 & (n = \text{even}). \end{cases} \tag{2.57}$$

The matrix Hamiltonian in Eq. 2.56 can be further reduced while maintaining a relatively accurate - yet simpler - model. Eq. 2.53 implies that even for very modest aggregates with $n \approx 6$, the leading dipole moment ($\boldsymbol{d}_{01}$) is approximately a factor of three stronger than the next ($\boldsymbol{d}_{03}$). Given that the effective transition dipole moment of the aggregate is dominated by $\boldsymbol{d}_{01}$, one is able to approximate the system by taking this sole excited eigenstate, thereby retaining only the states $|0\rangle$ and $|1\rangle$. By Eq. 2.49, $|1\rangle$ is written explicitly as,

$$|1\rangle = \sqrt{\frac{2}{n+1}} \sum_{j=1}^{n} \sin\left(\frac{j\pi}{n+1}\right) |1_j\rangle, \tag{2.58}$$

which has the eigenvalue (by Eq. 2.45) of,

$$\hbar\omega_1 = \hbar\omega_1^{(1)} - 2J\cos\left(\frac{\pi}{n+1}\right), \tag{2.59}$$

which is of the form $\hbar\omega_1 = \hbar\omega_1^{(1)} + \Delta$. The excitation energy of the aggregate ($\hbar\omega_1$) is shifted from the monomer value by $\Delta$, and this shift arises from the interaction with other molecules in the aggregate. This energy shift has been observed elsewhere for aggregates,[96,107] and is loosely termed the 'effect of aggregation'.[100] For J-aggregates the shift is negative, and for H-aggregates the shift is positive.[107] The magnitude of $\Delta$ is typically hundreds of $meV$.[98]

By considering these two states only, the single-exciton Hamiltonian in Eq. 2.33 is written approximately as,

$$\begin{aligned}\hat{H}_0 &\approx \hbar\omega_0|0\rangle\langle 0| + (\hbar\omega_1^{(1)} + \Delta)|1\rangle\langle 1| \\ &= \hbar\omega_0|0\rangle\langle 0| + \hbar\omega_1|1\rangle\langle 1|,\end{aligned} \tag{2.60}$$

which enables the total Hamiltonian to be represented in the following matrix form,

$$H = \begin{pmatrix} \hbar\omega_0 & G_{01} \\ G_{01} & \hbar\omega_1 \end{pmatrix}, \tag{2.61}$$

using the same notation as above. Altogether, this is a major simplification of the Hamiltonian formed by Eq. 2.33 & 2.34, and enables fast computation of the optical response of a material comprising excitonic aggregates. The approximate nature of Eq. 2.61 can be quantified by comparison of results generated with the use of Eq. 2.56. A disadvantage of the use of Eq. 2.56 is that inclusion of extra levels necessitates evaluation of additional free parameters in the form of decay and dephasing rates.

### 2.3.3 The optical Bloch equations

Now that three alternative Hamiltonians for an excitonic material have been determined, the goal now is to find an effective medium value of $\varepsilon$ at time $t$ and at the frequency of illumination, $\omega$. The first step is to note that $H_I/|E(t)|$ defines the transition dipole matrix $\boldsymbol{d}$, the expectation value of which can be found using the trace of the density matrix acting upon it (see above). In order to find the density matrix itself, the Liouville-von Neumann equation (Eq. 2.31) is used. In general, when the Liouville-von Neumann equation is used in conjunction with a Hamiltonian of dimension $n$, $n^2$ coupled differential equations[108] are produced. These are the optical Bloch equations[109] (OBEs) which, when solved, yield the elements of the density matrix,

$\rho$. In this section, OBEs for the two-level Hamiltonian are derived explicitly, as an example.

In the case where the illuminating optical field is periodic, the rotating wave approximation[110] (RWA) can be applied. To do this, it is assumed that,

$$\begin{aligned}\hat{\boldsymbol{d}}_{0m} &= \cos(\omega t)(|0\rangle\langle m| + |m\rangle\langle 0|) \\ &= \frac{1}{2}(e^{i\omega t} + e^{-i\omega t})(|0\rangle\langle m| + |m\rangle\langle 0|) \qquad (2.62) \\ &\approx \frac{1}{2}(|0\rangle\langle m|e^{i\omega t} + |m\rangle\langle 0|e^{-i\omega t}). \qquad (2.63)\end{aligned}$$

The RWA makes the OBEs time-separable, and therefore solvable for any arbitrary time $t$ without additional computation. To help complete this objective, the substitution $\tilde{\rho}_{0m} = \rho_{0m}e^{-i\omega t}$ is made. For the approximated two-level Hamiltonian described in the previous section (Eq. 2.61), the OBEs under the RWA take the form,

$$\dot{\rho}_{00} = -\gamma_{10}\rho_{00} + \frac{i}{2}\Omega_{01}\tilde{\rho}_{01} - \frac{i}{2}\Omega_{01}\tilde{\rho}_{10} + \gamma_{01}\rho_{11} \qquad (2.64)$$

$$\dot{\tilde{\rho}}_{01} = \frac{i}{2}\Omega_{01}\rho_{00} - (\Gamma_{01} - i\delta_{01})\tilde{\rho}_{01} - \frac{i}{2}\Omega_{01}\rho_{11} \qquad (2.65)$$

$$\dot{\tilde{\rho}}_{10} = -\frac{i}{2}\Omega_{01}\rho_{00} - (\Gamma_{01} + i\delta_{01})\tilde{\rho}_{10} + \frac{i}{2}\Omega_{01}\rho_{11} \qquad (2.66)$$

$$\dot{\rho}_{11} = \gamma_{10}\rho_{00} - \frac{i}{2}\Omega_{01}\tilde{\rho}_{01} + \frac{i}{2}\Omega_{01}\tilde{\rho}_{10} - \gamma_{01}\rho_{11}, \qquad (2.67)$$

where $\Omega_{01} = 2\boldsymbol{E}\cdot\bar{\boldsymbol{d}}_{01}/\hbar$ is the Rabi frequency between states $|0\rangle$ and $|1\rangle$, and $\gamma_{ij}$ are the decay rates of the eigenstates from eigenstate $|j\rangle$ to eigenstate $|i\rangle$. $\delta_{01} = (\omega_1 - \omega_0) - \omega$ is the detuning from the transition. $\Gamma_{ij}$ is the dephasing rate of the $|i\rangle \leftrightarrow |j\rangle$ transition defined by,[84,111]

$$\begin{aligned}\Gamma_{ij} &= \Gamma_{ij}^{(d)} + \Gamma_{ij}^{(p)} \\ &= \Gamma_{ij}^{(d)} + \frac{1}{2}\sum_{k=1}^{n}(\gamma_{ki} + \gamma_{kj}). \qquad (2.68)\end{aligned}$$

Here, $\Gamma_{ij}^{(p)}$ arises from population decay (as shown), and $\Gamma_{ij}^{(d)}$ is responsible for inhomogeneous broadening from various sources: these include phase-changing collisions,[112] broadening of the transition due to static disorder[102] and other solid state dynamic processes.[113]

Whether or not the RWA is used, it is convenient to write the OBEs in the following compact matrix form,

$$\dot{\boldsymbol{\rho}}_V(t,\omega) = \overline{L}(t,\omega)\boldsymbol{\rho}_V(t,\omega), \tag{2.69}$$

where $\boldsymbol{\rho}_V$ is a vector composed of the elements of the density matrix[108] and $\overline{L}$ is a matrix of the OBEs. This is a general expression and one may solve these equations either by use of the RWA[110] as shown here, or by numerical methods such as one of the Runge-Kutta methods.[114] Both of these approaches are detailed and evaluated in App. B.2. To derive an expression for the permittivity, $\langle \boldsymbol{d} \rangle$ is determined using $\langle \boldsymbol{d} \rangle = Tr(\rho \boldsymbol{d})$. For the transition dipole matrix for the two-level system chosen above, this value is equal to $\rho_{01}\bar{\boldsymbol{d}}_{01} + c.c.$. By choosing the forward-propagating electric field, Eq. 2.23 is re-arranged to give $\varepsilon$ for an ensemble of two-level molecules as,

$$\begin{aligned} \varepsilon(t,\omega) &= \varepsilon_b + \frac{2N}{\varepsilon_0}\frac{|\bar{\boldsymbol{d}}_{01}|}{|\boldsymbol{E}|}\rho_{01}e^{-i\omega t} \\ &= \varepsilon_b + \frac{2N}{\varepsilon_0}\frac{|\bar{\boldsymbol{d}}_{01}|}{|\boldsymbol{E}|}\tilde{\rho}_{01}, \end{aligned} \tag{2.70}$$

where $\rho_{01}$ is a function of both $\omega$ and $t$. A similar and more general expression for $\varepsilon$ derived with multiple energy eigenstates is,

$$\varepsilon(t,\omega) = \varepsilon_b + \frac{2N}{\varepsilon_0|\boldsymbol{E}|}\sum_i |\bar{\boldsymbol{d}}_{0i}|\tilde{\rho}_{0i}. \tag{2.71}$$

At first glance, Eq. 2.70 & 2.70 may appear to diverge for the case where $|\boldsymbol{E}| \to 0$. The resolution to this becomes apparent when an explicit expression for the steady state permittivity is derived for the two-level system. As such, in the steady-state, $\dot{\rho}_{00} = \dot{\rho}_{11} = \dot{\tilde{\rho}}_{01} = \dot{\tilde{\rho}}_{10} = 0$ and Eq. 2.64-2.67 are re-written as,

$$-\gamma_{10}\rho_{00} + \frac{i}{2}\Omega_{01}\rho_{01} - \frac{i}{2}\Omega_{01}\rho_{10} + \gamma_{01}\rho_{11} = 0 \tag{2.72}$$

$$\frac{i}{2}\Omega_{01}\rho_{00} - (\Gamma_{01} - i\delta_{01})\rho_{01} - \frac{i}{2}\Omega_{01}\rho_{11} = 0 \tag{2.73}$$

$$-\frac{i}{2}\Omega_{01}\rho_{00} - (\Gamma_{01} + i\delta_{01})\rho_{10} + \frac{i}{2}\Omega_{01}\rho_{11} = 0 \tag{2.74}$$

$$\gamma_{10}\rho_{00} - \frac{i}{2}\Omega_{01}\rho_{01} + \frac{i}{2}\Omega_{01}\rho_{10} - \gamma_{01}\rho_{11} = 0. \tag{2.75}$$

Using the relation $\rho_{00} + \rho_{11} = 1$ and assuming that $\gamma_{10} = 0$, *i.e.* there is no decay out of the system, Eq. 2.72 & 2.73 lead to,

$$\rho_{11} = \frac{\Omega_{01}}{\gamma_{01}}\mathbb{I}\mathrm{m}(\rho_{01}) \tag{2.76}$$

$$\tilde{\rho}_{01} = \frac{i\Omega_{01}}{2}\frac{1 - 2\rho_{11}}{\Gamma_{01} - i\delta_{01}}. \tag{2.77}$$

Recognising that $\hbar\Omega_{01} = \boldsymbol{E} \cdot \bar{\boldsymbol{d}}_{01}$, these two equations can be used to find an expression for $\rho_{11}$, which can then in turn be used to find the following expression for $\tilde{\rho}_{01}$,

$$\tilde{\rho}_{01} = \frac{i\Omega_{01}}{2} \frac{\gamma_{01}(\Gamma_{01} + i\delta_{01})}{\gamma_{01}(\Gamma_{01}^2 + \delta_{01}^2) + \Gamma_{01}\Omega_{01}^2}. \tag{2.78}$$

This leads to the final expression for the permittivity of an ensemble of two-level quantum systems in the steady-state,

$$\varepsilon(\omega) = \varepsilon_b + \frac{iN|\bar{\boldsymbol{d}}_{01}|^2}{\varepsilon_0} \frac{\gamma_{01}(\Gamma_{01} + i\delta_{01})}{\gamma_{01}(\Gamma_{01}^2 + \delta_{01}^2) + \Gamma_{01}(\boldsymbol{E} \cdot \bar{\boldsymbol{d}}_{01})^2}. \tag{2.79}$$

Eq. 2.79 shows that in the limit where $|\boldsymbol{E}| \to 0$, $\varepsilon(\omega)$ becomes independent of the field as expected. Approximate expressions for multi-level systems can be derived by following a similar procedure.

### 2.3.4 Results for TDBC:PVA films

The single-exciton (Eq. 2.35), nearest-neighbour (Eq. 2.56) and approximated nearest-neighbour (Eq. 2.61) Hamiltonians are now employed to determine the permittivity and microscopic properties of the TDBC:PVA films measured in Ch. 1, with a more detailed focus on the 70 *nm* thick 1.46 *wt%* film.[46]

#### 2.3.4.1 Two level nearest-neighbour Hamiltonian

In order to calculate permittivity using Eq. 2.70 (based on the two-level nearest-neighbour Hamiltonian), four parameters are required: $\bar{\boldsymbol{d}}_{01}$, $\hbar\omega_1$, $\gamma_{01}$ and $\Gamma_{01}^{(d)}$. Using the permittivity determined from measured reflectance and transmittance spectra for the film in Ch. 1, it was determined that $\hbar\omega_1 = 2.11\ eV \equiv 588\ nm$. This value agrees with those obtained by van Burgel[115] and Valleau.[98]

From photoluminescence measurements,[78] the decay rate of $|1\rangle$ was found to be $\gamma_{01} = 1.15 \times 10^{12}\ s^{-1}$ for the aggregate in a PVA host medium. Using an online tool provided by Molinspiration ©, the molecular weight and the effective volume of the TDBC molecule were determined. For a concentration of 1.46 *wt%*, these quantities determined the molecular number density to be equal to $N = 1.47 \times 10^{25}\ m^{-3}$. Determination of $N$ enables estimation of the transition dipole moment for TDBC molecules in aggregate form ($|\bar{\boldsymbol{d}}_{01}|$) along with the dephasing rate ($\Gamma_{01}^{(d)}$) by fitting the steady-state solutions for Eq. 2.70 to the experimental data for the permittivity. Following this procedure, the dipole moment was determined to be $|\bar{\boldsymbol{d}}_{01}| = 48$ Debye (D). The TDBC-doped thin films from which the experimental data were obtained

were produced by spin-coating.[46] The orientation of dipole moments in thin polymer films produced by spin-coating lie predominantly in the plane.[116] Assuming that the TDBC aggregates also lie in the plane means that the determined value of 48 D is a two-dimensionally averaged value. This implies by Eq. 2.55 that the on-axis dipole moment of a TDBC aggregate is $d_{01} = 97$ D; and the value for a three-dimensionally averaged dipole moment is $|\bar{\boldsymbol{d}}_{01}| = 32$ D. This averaged dipole moment in three dimensions compares with the value of 24 D estimated by van Burgel *et al.*[115,117] from experiments in solution, for which the orientations and positions of the dipoles are distributed randomly in three dimensions. The same work has also shown that there are approximately 15 monomers *per* aggregate for TDBC aggregates. By working backwards using the well-known values of $\hbar\omega_0$ to run repeated calculations for $\varepsilon$, the monomer transition dipole moment was deduced as $\mu = 27$ D.

The dephasing rate was found to be equal to $\Gamma_{01}^{(d)} = 17$ *meV* for the 1.46 *wt%* film, which is approximately equal to $k_B T$, where $T$ is room temperature, as expected.[98] The results for permittivity against experimentally-determined data for the film are displayed in Fig. 2.6. In the figure, the result assuming a planar distribution of dipoles is shown alongside that of a volume distribution for the same concentration. In the case of the latter, the decrease in transition dipole moment causes the permittivity to be flattened with respect to the former. The consequence of this is that the negative value of the real part of the permittivity becomes lost for a volume distribution. In order to counteract the effect of the decrease in orientationally-averaged transition dipole moment brought about by raising the dimensionality of the space in which the dipoles are distributed, the concentration of the aggregates must be increased. In order

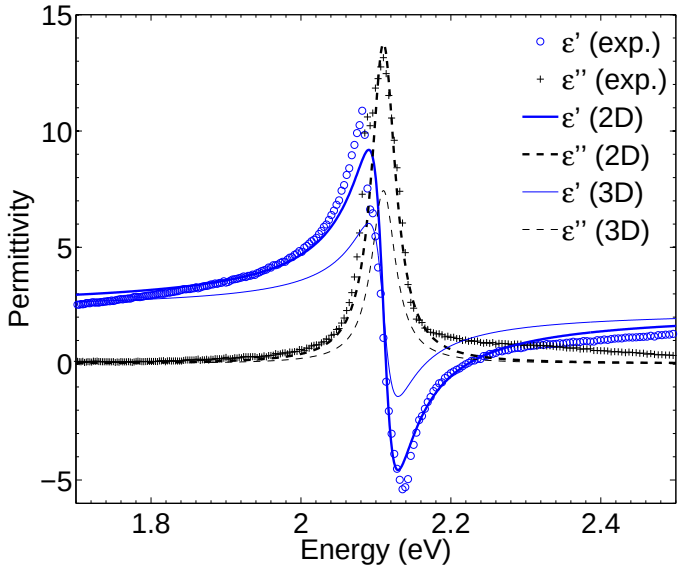


**Figure 2.6:** Real (blue) and imaginary (black) parts of the permittivity for 1.46 *wt%* TDBC:PVA, assuming a planar (thick lines) and volume (thin lines) distribution, alongside experimental data for the planar distribution.

to closely match the permittivity of the aggregates in the planar distribution shown in Fig. 2.6, this increase in concentration is from 1.46 *wt%* to 3.22 *wt%*, corresponding to an increase in number density from $N = 1.47 \times 10^{25}\ m^{-3}$ to $N = 3.29 \times 10^{25}\ m^{-3}$.

Comparing the two-level nearest-neighbour Hamiltonian (herein referred to as the the "two-level quantum model") with that of the single-oscillator Lorentz model (in Fig. 2.2), the lineshapes appear similar at first glance. Closer inspection proves otherwise, particularly in the $2.15\ eV < E < 2.25\ eV$ region, within which the two models differ most substantially for $\varepsilon'$. The curve produced by the two-level quantum model follows the experimental values more closely. This is expected in part because the two-level quantum model includes dephasing as well as decay within it, in comparison to the Lorentz model which only has the one (phenomenological) parameter to account for all damping and dephasing processes. This means that the two-level quantum model permits realistic values of the decay rate to be included, and is therefore based on more realistic physical phenomena. Point in fact, Lorentz himself expressed suspicion regarding the approximate nature of his own model[118 i]. It is therefore no surprise that the two-level quantum model produces a more realistic lineshape, in spite of the model's apparent simplicity.

The complex refractive index for the best fit to experimental data in this instance is displayed in Fig. 2.7. In this figure, the model closely follows the experimental data in the range $1.7\ eV < E < 2.2\ eV$. Above $2.2\ eV$, there exists a broad tail in the imaginary part of the complex refractive index, $\kappa$; this tail cannot be accounted for by a single Lorentzian lineshape. Therefore, additional energy levels must be considered in order to model it.

[i] „*Die übrigens den Mathematikern noch manche Frage darböte.*"

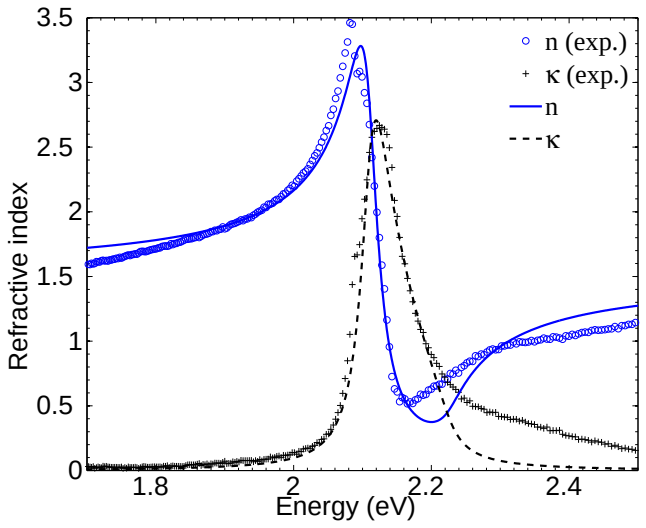


**Figure 2.7:** Real (blue) and imaginary (black) parts of the complex refractive index for 1.46 *wt%* TDBC:PVA (assuming a planar distribution) alongside experimental data.

### 2.3.4.2 n-Level nearest-neighbour Hamiltonian

In order to make use of a multi (more than two) level nearest-neighbour Hamiltonian, the nearest neighbour coupling $J$ must first be determined. By use of the parameters for the brickstone arrangement of TDBC molecules,[98,107] a value of $J = -667\ meV$ was found by calculation of extended dipole-dipole interactions. By substitution of this value of $J$ into Eq. 2.45, the first two odd excited energy eigenvalues above the known energy eigenvalue of $\hbar\omega_1 = 2.11\ eV$ were determined to lie at $\hbar\omega_3 = 2.31\ eV$ and $\hbar\omega_5 = 2.68\ eV$. Given that $2.68\ eV$ is just outside the range of photon energies considered and that $\boldsymbol{d}_{01} \approx 5\boldsymbol{d}_{05}$, these three excited states (together with the ground state) are sufficient to model the system within the range of photon energies of interest. This model is herein referred to as the "four-level quantum model".

By using the same procedure as above for the two-level Hamiltonian, the monomer transition dipole moment was deduced as $\mu = 20$ D. This decrease in the value from 27 D as reported in using the two-level model results from a compensation on the part of the two-level Hamiltonian for energy eigenstates left unmodelled.

The results for the use of the four-level quantum model are shown in Fig. 2.8 (overleaf), where $\Gamma_{ij}^{(d)}$ have been optimised within physical constraints: specifically, the critical rule used is,[84]

$$(\Gamma_{01}^{(d)} + \Gamma_{35}^{(d)} - \Gamma_{03}^{(d)} - \Gamma_{15}^{(d)})^2 \leq 4\Gamma_{05}^{(d)}\Gamma_{13}^{(d)}. \tag{2.80}$$

If the dephasing between the state pairs $|0\rangle \leftrightarrow |3\rangle$ and $|0\rangle \leftrightarrow |5\rangle$ are assumed to be equal, and the dephasing between the remaining pairs $|i\rangle \leftrightarrow |j\rangle$ are held equal to $\Gamma_{01}^{(d)}$, then the following inequality for $\Gamma_{03}^{(d)}$ (or equivalently $\Gamma_{05}^{(d)}$) is derived,

$$0 \leq \Gamma_{03}^{(d)} \leq (3 + 2\sqrt{2})\Gamma_{01}^{(d)}. \tag{2.81}$$

The value determined for $\Gamma_{03}^{(d)}$ by a fitting procedure was $4\Gamma_{01}^{(d)}$, which lies within the limits of this inequality, and is therefore physically plausible. As a result, the theoretical line in Fig. 2.8b for the imaginary part of the refractive index $\kappa$ is now closer to the experimental data points. In addition, a distinctive hump in the tail has now become more obvious, which corresponds precisely to the eigenvalue at $\hbar\omega_3 = 2.31\ eV$. The code used to generate these results is included in App. A.2.

So far in this chapter, the dye concentration 1.46 *wt%* has been studied exclusively. In order to apply the four-level quantum model to any dye concentration, care must be exercised: the parameters for the 1.46 *wt%* film, the energy eigenvalues, monomer transition dipole moment and photoluminescent decay rate are all independent of dye concentration, but the dephasing rates and the effective number of monomers within each aggregate ($n$) may not be. By making the assumption that environment in which the aggregates sit (the bath[119]) is constant across each sample, the dephasing rates can be assumed to be equal for each of the samples. Making this assumption leaves only

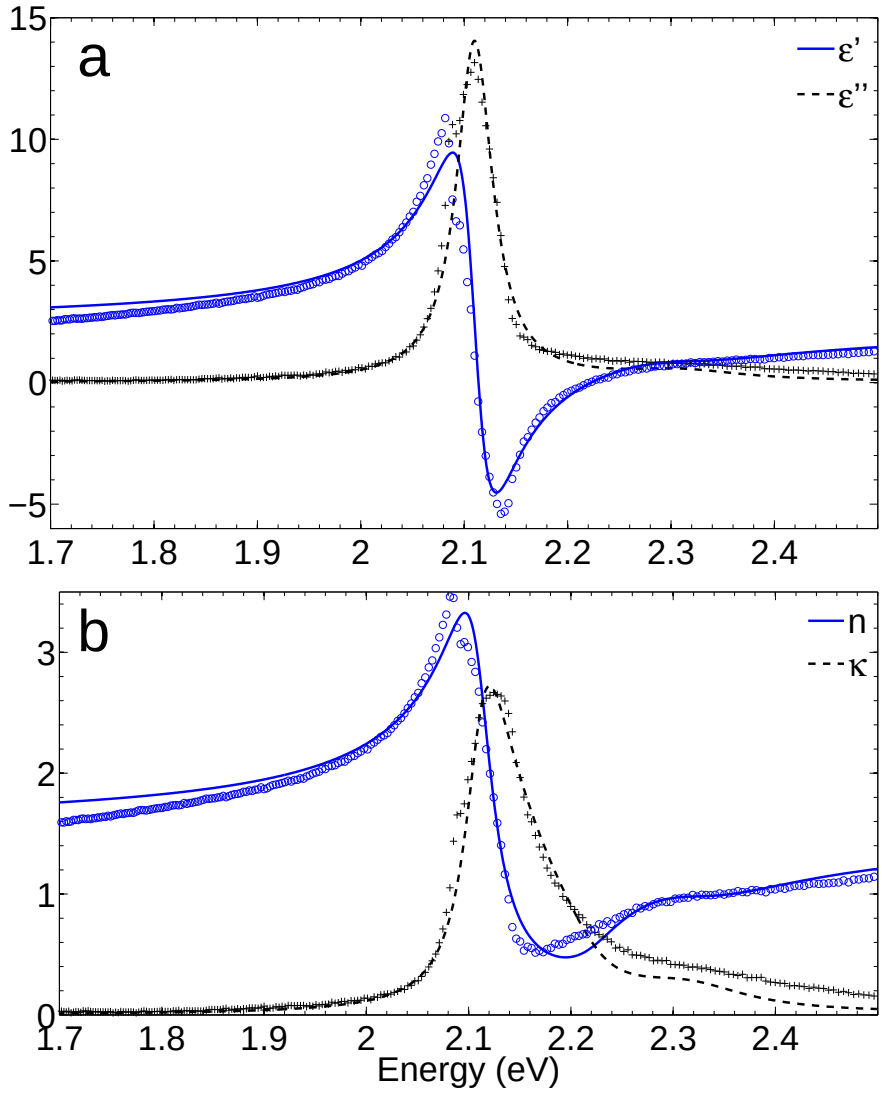


**Figure 2.8:** The complex permittivity (a) and refractive index (b) for a 70 *nm* film of 1.46 *wt%* TDBC:PVA as modelled using the four-level quantum model (lines), against experimental data (data points).

one remaining free parameter: $n$. The dependency of the transition dipole moments associated with the aggregate ($\boldsymbol{d}_{0m}$) on $n$ is represented in Eq. 2.53. Therefore, in theory, the best fit for the refractive index (and permittivity) can be found by adjustment of $n$ and comparison of the resulting curves with the experimentally-determined data.

In performing this procedure for the refractive index of the three other films studied in Ch. 1, the curves overlying the experimental data in Fig. 2.9 are obtained. By studying

the evolution of the lineshape of $\kappa$, it would appear that the broadening of the tail at higher energies occurs with an increase in concentration: in Fig. 2.9a, the tail is

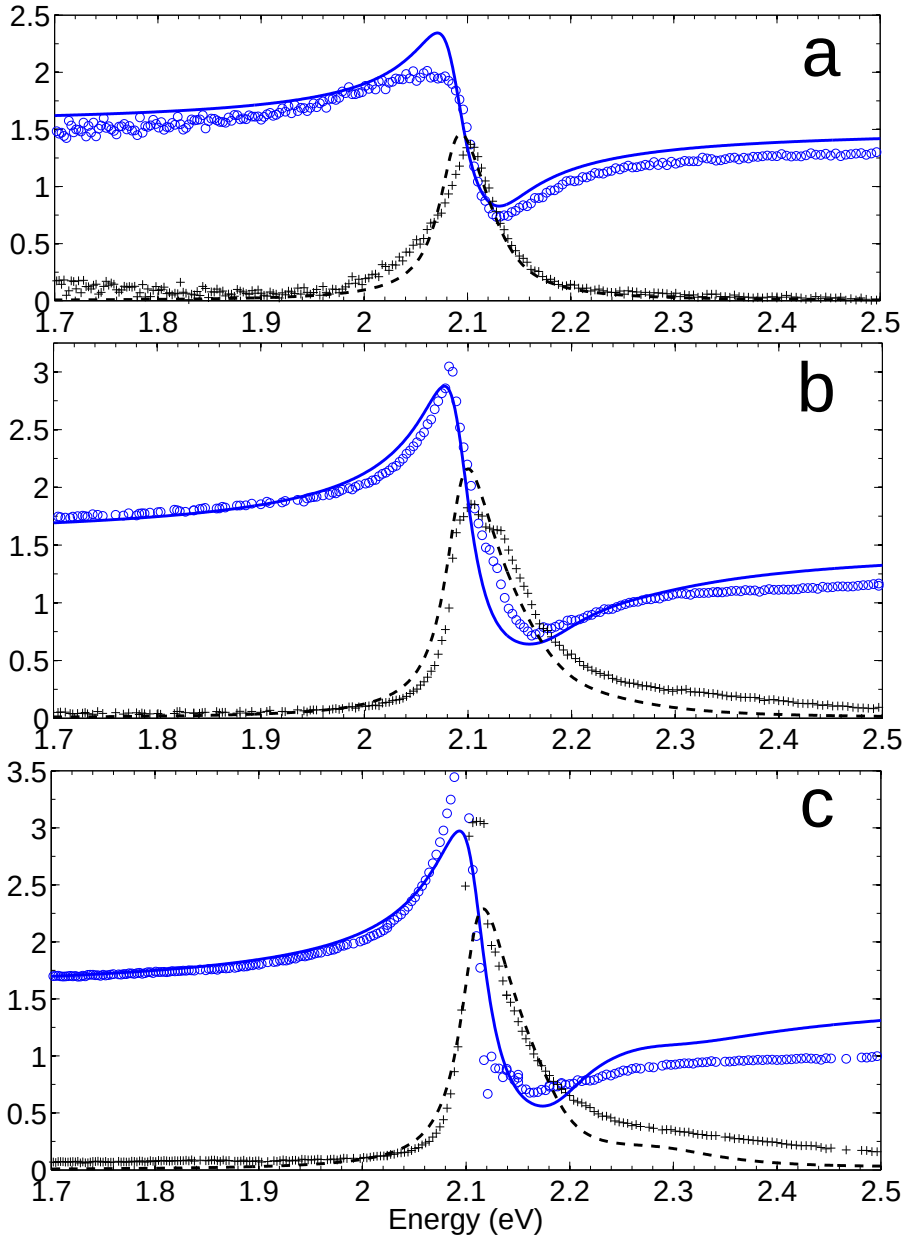


**Figure 2.9:** Experimentally-determined real ($n$, blue circles) and imaginary ($\kappa$, black crosses) parts of the complex refractive indices for (a) 0.12 *wt%* (b) 0.48 *wt%* and (c) 1.00 *wt%* TDBC:PVA films, with a four-level quantum model for each (lines).

well-modelled by the (near-Lorentzian) quantum model, and although a gap appears in Fig. 2.9b, the hump corresponding to the $|0\rangle - |2\rangle$ transition only becomes apparent in Fig. 2.9c, with a dye concentration of 1.00 *wt%*.

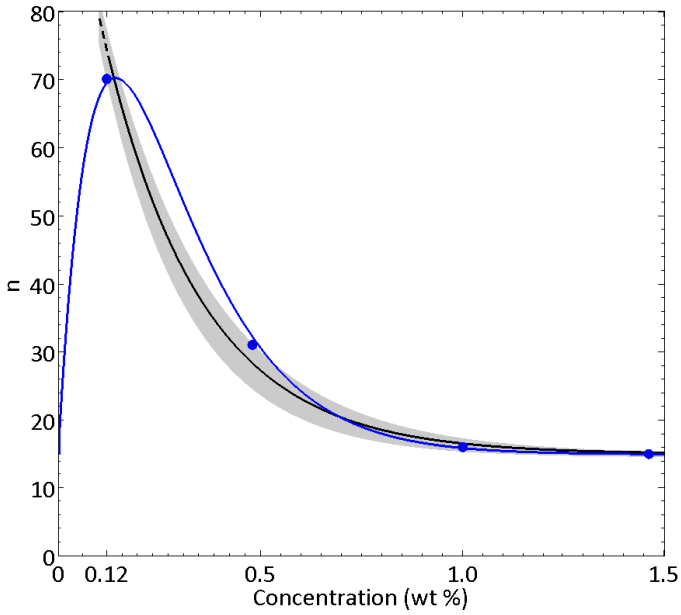


**Figure 2.10:** Effective number of monomers per aggregate for the four dye concentrations studied in TDBC:PVA films (blue circles). The exponential fit (black line, of form $\exp(-x)+n_\infty$) has its confidence intervals shown by the shaded area. The blue line is the result of a fit presuming a function of the form $n(x) = x\exp(-x) + n_\infty$.

The effective number of aggregates used in the quantum model for each of the three concentrations are $n = 70$, 31 and 16 for the 0.12 *wt%*, 0.48 *wt%* and 1.00 *wt%* films respectively. Combining these findings with the result that $n = 15$ for the 1.46 *wt%* film, it would appear that the number of monomers in the aggregate, and hence the effective length, decreases with an increase in dye concentration. This exponential decrease in $n$ is shown in Fig. 2.10, alongside two fittings obtained by least-squares fit procedures. This finding has two plausible physical interpretations for an increase in dye concentration:

1. The average number of monomers within the aggregates remains constant, and the disorder within the film acts to limit the *effective average number* of monomers within the aggregates. Hence, it is the effective length over which the excitons are delocalised which decreases with an increase in concentration.

2. The average number of monomers within the aggregate falls exponentially with an increase in dye concentration. As a consequence, the average length over which the excitons are delocalised follows an exponential decline with an increase in concentration.

Whichever of these interpretations is correct, the correct answer is only relevant for microscopic calculations for the optical response of monomers; it has no effect on the macroscopic optical calculations or the effective medium calculations for permittivity contained within this thesis.

The exponential fit to $n$ in Fig. 2.10 (black line) for concentrations less than 0.12 *wt%* is shown as a dotted line. The rationale for this is that the fit for values below the lowest experimental concentration is extrapolation only. Taking a thought experiment: with no monomers present, there can be no monomers in the aggregate. This restriction introduces a curve in Fig. 2.10 which rises quickly with an increase in concentration for low concentrations, and peaks somewhere in the concentration range 0 *wt%* – 0.48 *wt%*. An example of a plausible fit is indicated in Fig. 2.10 by the blue line. The concentration at which the peak occurs is yet to be determined, but future experimentation on films in the concentration range 0 *wt%* – 0.48 *wt%* should determine the answer to this question. In either of the two models shown, $n$ for large concentrations tends towards $14.87 \pm 0.25$; this indicates that the value of $n = 15$ used in the four-level quantum model for 1.46 *wt%* TDBC:PVA is reasonable.

So far, the quantum models for permittivity have been examined exclusively in the steady-state. As an aside, the response in the time domain is presented for 1.46 *wt%* TDBC:PVA using the four-level quantum model. It is assumed that at $t = 0$, the ensemble is in a pure state; furthermore, the optical field is turned on suddenly at $t = 0$. The resultant permittivity as a function of time is visualised in Fig. 2.11. The general features of the response are similar to that of the temporal response produced by the Lorentz model (*cf.* Fig. 2.3). This observation simultaneously verifies the Lorentz model as an approximate theory in the time domain, and demonstrates that the transient effects borne from a quantum mechanical model have a classical analogue associated with them.

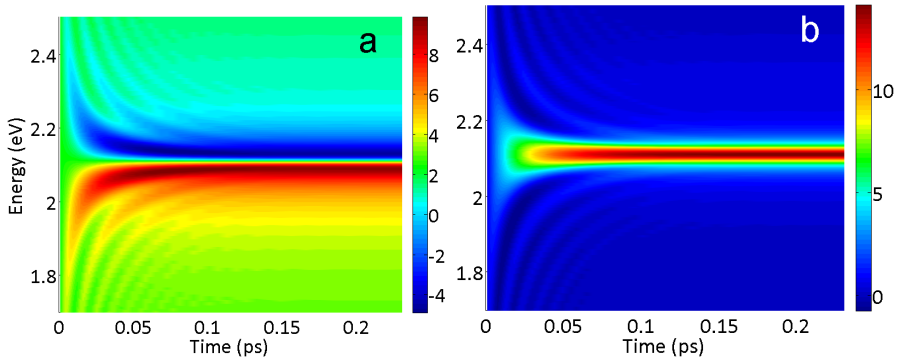


**Figure 2.11:** Real (a) and imaginary (b) parts of the permittivity for a 1.46 *wt%* TDBC:PVA 70 *nm* film in the time domain, assuming a planar distribution of dipoles and using the four-level quantum model.

### 2.3.4.3 General effects of J-aggregation

So far, the nearest-neighbour Hamiltonian has been used in order to model the permittivity of an aggregated system. In this section, the effects of J-aggregation are explored in general terms by analysis of the permittivity for a collection of randomly distributed monomers.

The exciton transition energy of the TDBC monomer is $\hbar\omega_1^{(1)}$. This energy can be deduced as $\hbar\omega_1^{(1)} = 3.42\ eV$ by use of Eq. 2.59 together with the value of the nearest neighbour coupling ($J = -667\ meV$), and the first excited energy eigenvalue of the aggregate ($\hbar\omega_1 = 2.11\ eV$). The value of $\hbar\omega_1^{(1)}$ illustrates that one important effect of J-aggregation is a dramatic redshift of the exciton transition.

Another effect of J-aggregation is an increase in the effective dipole moment, as seen above.

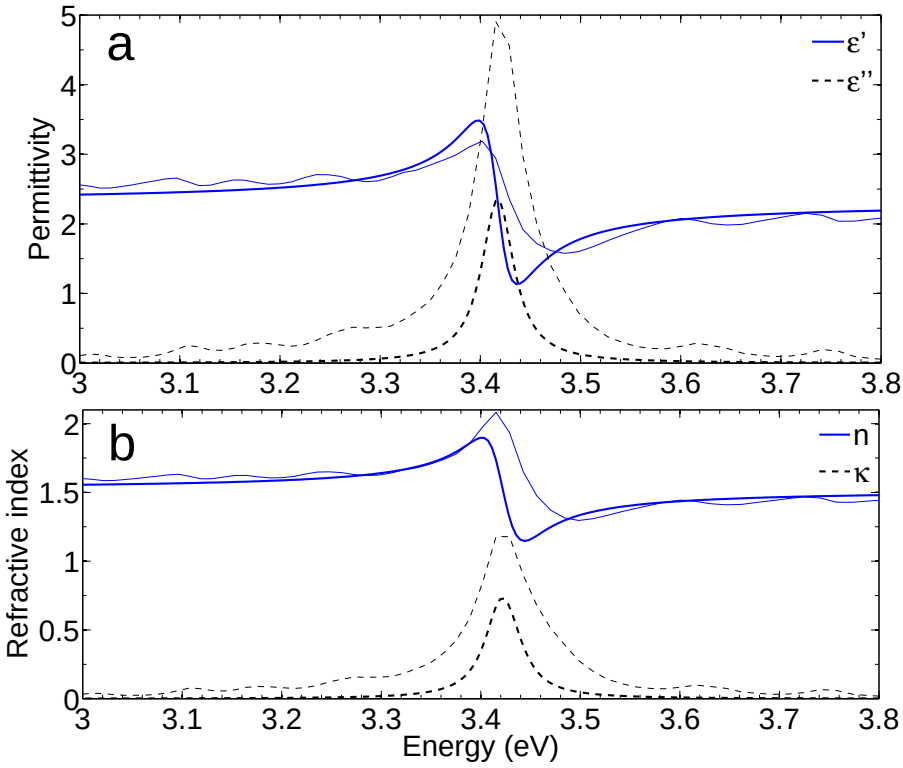


**Figure 2.12:** Estimate for the (a) permittivity and (b) refractive index of the non-aggregated form of 1.46 *wt%* TDBC:PVA. The thick lines correspond to a two-level model, and the thin lines indicate a three-dipole single-exciton Hamiltonian averaged over 100 arrangements.

These two general features are visualised in Fig. 2.12, where both a two-level quantum

model incorporating monomer values and a single-exciton Hamiltonian for a collection of randomly-distributed monomers have been used, each taking $\boldsymbol{\mu} = 20$ D and a concentration of 1.46 *wt%*. The axes of the plot are of the same length as Fig. 2.8 for easy comparison with the aggregate results. For the results corresponding to the single-exciton Hamiltonian, the effect of three dipoles has been calculated assuming the same dipole positions as in an aggregate, but with arbitrary rotations. The result shown is an average over one hundred different arrangements. It must be noted that the values for the permittivity in Fig. 2.12 are for illustrative purposes only, and do not necessarily represent physical values of the permittivity: this is primarily because TDBC has a tendency to aggregate in PVA for a concentration of 1.46 *wt%* (rendering a non-aggregated response at this concentration unlikely) and also because interactions with many dipoles have been neglected.

Despite these apparent shortcomings, both models in Fig. 2.12 in comparison with Fig 2.8 illustrate qualitatively the two well-known features of aggregation:[120] that the act of aggregation itself causes a shift in transition energy, accompanied by a dramatic increase in oscillator strength. The latter of these effects in particular is chiefly responsible for the transition of the appearance of TDBC:PVA from that of a translucent dielectric into that of a metal (within a narrow range of wavelengths). It is noted that the result arising from the two-level model is fairly close to the three-dipole single-exciton Hamiltonian. By approximating the lineshape from the single-exciton Hamiltonian in Fig. 2.12 with a single-oscillator Lorentz model (Eq. 2.14), the oscillator strength $f_0$ was determined as $f_0 = 0.075$; this value is four times weaker than the value of $f_0 = 0.3$ found to represent the response of the aggregate in Fig. 2.2.

## 2.4 Conclusions

The permittivity of a non-magnetic linear isotropic material illuminated with weak fields can be modelled by presuming that the electrons inside it sit inside harmonic potentials within their orbitals - this semi-classical approach is known as the Drude-Lorentz model. The major drawback of the Drude-Lorentz model is that harmonic potentials are often insufficient to describe the potentials in which the electrons sit, as has been illustrated with the addition of the interband contributions to the permittivity in the case of gold. For metals, the leading contribution to the permittivity arises from free electrons, and the Drude-Lorentz model can be adapted to yield the Drude model. The Drude model has been shown to model the permittivity of silver and gold to a sufficient level of accuracy without the necessity of more detailed quantum-mechanical treatment.

The single-oscillator Lorentz model can be applied to excitonic dye molecules, but such an approach does not necessarily incorporate physical damping rates. Development of more realistic models for the permittivity of excitonic dye molecules is eased by the binomial nature of the molecular energy levels associated with exciton excitation

(a ground state and an excited state); this enables the excitonic dye molecules to be modelled as discrete interacting quantum systems. Even in the single-exciton regime, such an approach can become computationally demanding, because each molecule requires individual consideration. This pushes up the number of energy eigenstates to be equal to the number of molecules in the ensemble, which can be prohibitively large.

Modelling the permittivity of excitonic dye molecules is simplified in the case where the molecules assume aggregate form: under this circumstance, the nearest-neighbour intra-aggregate interactions dominate, which enables diagonalisation of the Hamiltonian. This yields a discrete set of optically-active excited energy eigenstates, the number of which equates to half the number of molecules contained within the aggregate. Given that these energy eigenvalues are each spaced by a few hundred $meV$, the response in the optical range can be accounted for by consideration of only three or four of these energy eigenstates in the case of TDBC. It has been demonstrated that the two-level limit produces superior fit for the steady-state permittivity as determined from experiment in comparison to a Lorentz oscillator model for a 1.46 $wt\%$ TDBC:PVA film. A four-level model has been shown to provide an even better fit, and accounts for the next two (weaker) optical transitions of the aggregate which broaden the imaginary part of the complex refractive index.

A full nine-level nearest-neighbour Hamiltonian for aggregates does not significantly improve the fit produced by the four-level Hamiltonian. Therefore, a question yet to be answered is the extent to which the next-nearest neighbour interactions might improve the physicality of the model. Such an approach is beyond the scope of this thesis, but initial estimates indicate that a correction up to around 5% might be expected in the energy eigenvalues.

A finding drawn from analysis of the four-level quantum model is that the effective number of monomers within the aggregate falls with an increase in concentration, tending towards a value of around $n = 15$ for TDBC:PVA films of high concentration. Whether this dependency on concentration arises from an increase in disorder with concentration or is a real phenomenon is a potential area of future research. Certainly further experimentation will be able to provide a concentration for which the effective number of monomers in the aggregate is maximised.

Altogether, with the use of a four-level quantum model to describe TDBC aggregates, the permittivity of TDBC-doped plastics can be calculated to a level of accuracy exceeding that of using the Lorentz oscillator model. Hence, accurate optical calculations based upon this permittivity for nanostructures containing TDBC-doped plastics can be made. These nanostructures could be films, multilayer stacks or nanoparticles. The optical response of films and multilayer stacks is examined in Ch. 3, and the optical response of nanoparticles is examined in Ch. 4 & Ch. 5.

# 3

# Surface Exciton Polariton Modes in Planar Nanostructures

*In this chapter, surface exciton polariton (SEP) modes are introduced and explored in the geometry of thin excitonic films. The relative merits of hyperbolic modes in excitonic-metallic multilayer stacks are then investigated.*

## 3.1 Introduction

A plasmon is defined as a quantized plasma wave.[65] In the microscopic picture, plasmons on a material surface (surface plasmon polaritons, SPPs[121]) can be imagined to be induced by separation of charge (electrons from their nuclei); this separation of charge induces additional separations of charge in the neighbouring atoms, causing the charge oscillations to propagate out in space along the surface. This is illustrated in Fig. 3.1 for a generic surface, where the instantaneous electric field is plotted as a function of position in a top-down view across the surface of a material; here, the plasma waves propagate out along the surface and decay with length. The plasma waves also propagate and decay into the surface; this is visualised in Fig. 3.2 for a cross-section of the same system with the same scale. Surface modes (such as SPPs) can be excited by electrons[122] or by photons.[23] When excited by photons, photons are absorbed in the surface as a consequence of the conservation of energy. Therefore, absorption for thin films may be indicative of a surface mode.

Since Wood's observations of anomalously sharp features in the spectrum obtained through a speculum grating,[123] SPPs on metal surfaces have seen varied practical applications since their theoretical prediction[1] and experimental realisation.[2,3] The electric field enhancement close to the surface provided by SPPs has been used to induce non-linearity in nonlinear materials,[8] and to induce enhanced photoluminescence in molecules.[9] SPPs themselves have been shown to be of use in environmental sensing[13,14] and material characterisation.[20] More recently SPPs have been demonstrated within a waveguide context for microwave metamaterials[28,29] and for periodic

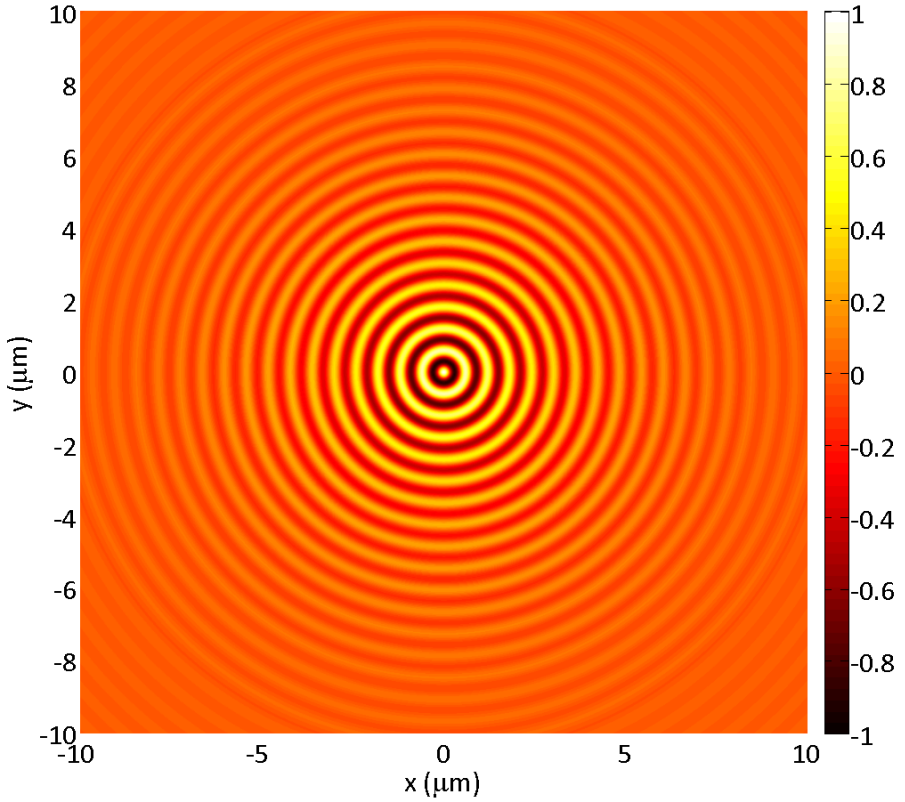


**Figure 3.1:** Normalised instantaneous electric field (colour scale) propagating across the top of a generic surface, assuming a point wave source at $x = y = z = 0$ and an in-plane wavevector of $k_{\|} = 10.4 + 0.323i\ \mu m^{-1}$.

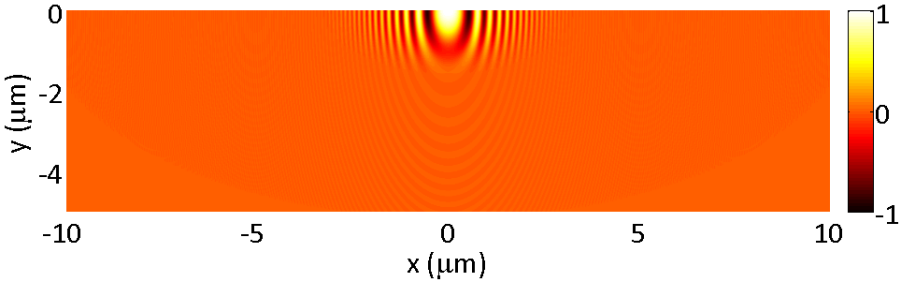


**Figure 3.2:** Normalised instantaneous electric field (colour scale) propagating into the $y = 0$ cross-section of the surface in Fig. 3.1. The in-surface wavevector is $k_z = 2.43 + 1.40i\ \mu m^{-1}$.

lattices of varying construction.[30–32] Altogether, this environmental dependency of SPPs coupled with their suitability to be guided in various geometries means that SPPs are potential candidates for applications within environmental sensing, optical computing[25] and the nanoscale control of light.[24] Plasma waves require the presence of free

electrons in the material. For this reason, surface modes, along with their properties of field enhancement and strong absorption, have been traditionally associated with metals. However, surface modes may be sustained using other materials, provided that a sufficiently high density of free (or effectively free) electrons is present. One way in which this is possible is by having excitons act as proxies for free electrons: excitons are quasi-particles consisting of an electron bound with an electron hole, and are able to jump from site-to-site,[124] as outlined in Ch. 2 when exciton sites exist in sufficiently high concentration. In this way, with sufficient site concentration, excitonic materials can support surface modes with similar properties to metals; the key difference being the origin of the charge carriers from which these properties arise. Consequently, given that excitons can only be excited within a narrow range of photon energies, excitonic materials can only host an exciton site density sufficient to exhibit these free-electron (metal-like) properties within this same narrow range of photon energies. On surfaces, these metal-like excitonic modes are termed surface exciton polariton[46,125,126] (SEP) modes.

In this chapter, the electromagnetic theory for SPPs (for metals) and SEPs in excitonic dye-doped polymers is outlined for planar nanostructures. These nanostructures include both thin films and multilayer stacks. By constructing and comparing dispersion diagrams for these systems with theoretical absorption plots, the existence of surface modes for these systems is evaluated. In each nanostructure geometry, the similarity between SEP and SPP modes in each is explored, and the merits of hybrid 'hyperbolic'[36] modes are considered.

## 3.2 Polarisation of Light (s and p)

As outlined in Ch. 1, light comprises both electric and magnetic fields, labelled $\boldsymbol{E}$ and $\boldsymbol{H}$ respectively. For linearly-polarised light incident upon a boundary, there are two orthogonal polarisations with respect to the boundary: first, where $\boldsymbol{E}$ only has components perpendicular to the interface, and second, where $\boldsymbol{E}$ only has components parallel to the interface. Equivalently, in the first case, $\boldsymbol{E}$ only has components parallel to the plane of incidence, whereas in the second case, $\boldsymbol{E}$ only has components perpendicular to the plane of incidence. These two polarisations are known as p and s polarisation respectively, "p" stemming from "parallel", and the "s" deriving from the German word "*senkrecht*" meaning "perpendicular".[127] Therefore, definition of these two polarisations with respect to the plane of incidence is more usual than with respect to the interface. Both polarisations are illustrated graphically in Fig. 3.3, and as will be seen, give rise to markedly different optical responses for both excitonic and plasmonic materials.

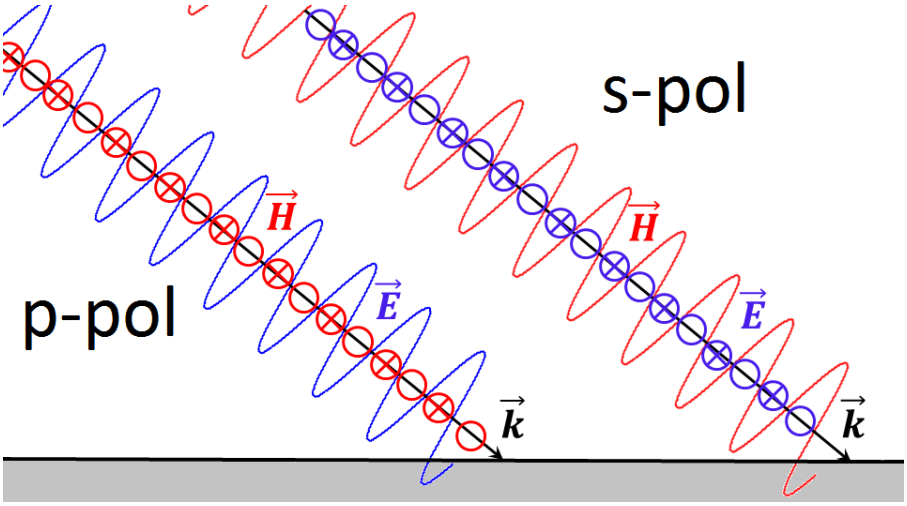


**Figure 3.3:** Light with p (left) and s (right) polarisation illustrated in two dimensions, with $\boldsymbol{E}$, $\boldsymbol{H}$ and $\boldsymbol{k}$ indicated. The horizontal black line represents the interface.

## 3.3 Isotropic Thin Films

Thin films isotropic in permittivity are the simplest planar nanostructures, and given their relative ease of fabrication,[128,129] are a natural start point for theoretical examination of nanostructures in general. In Ch. 1, isotropic excitonic thin films were examined experimentally and their permittivities extracted from reflectance and transmittance spectra measured at normal incidence. In this section, the dispersion relation for an isotropic thin film is determined, and compared with the corresponding theoretical absorption spectra for a range of incident angles, and ultimately, in-plane wavevectors.

### 3.3.1 Dispersion relation for a non-magnetic boundary

A thin film can be considered theoretically as a set of two boundaries, with each boundary separating the film from a semi-infinite medium. Therefore, two possible sites for surface mode propagation exist: either along one surface, or the other. In order to develop a dispersion relation for surface modes travelling along either surface, a single boundary is considered. The boundary is considered to lie in the $x - y$ plane, straddling two semi-infinite non-magnetic ($\mu_1 = \mu_2 = 1$) media with permittivities $\varepsilon_1$ (in positive $z$) and $\varepsilon_2$ (in negative $z$) respectively. The boundary is illuminated from

medium 1 (with permittivity $\varepsilon_1$) by a p-polarised plane wave. Expressions for the electric and magnetic fields of the light wave in medium $n$ are,

$$\boldsymbol{E}_n = e^{i(k_{x_n}x + k_{z_n}z - \omega t)}(E_{x_n}\hat{\boldsymbol{x}} + E_{z_n}\hat{\boldsymbol{z}}) \tag{3.1}$$

$$\boldsymbol{H}_n = e^{i(k_{x_n}x + k_{z_n}z - \omega t)}H_{y_n}\hat{\boldsymbol{y}}. \tag{3.2}$$

The relationship sought in this section is the induced wavevector along the boundary ($\boldsymbol{k}_{\|}$) as a function of illumination frequency ($\omega$): this relationship defines the dispersion relation[83] (p.92). In the following two-dimensional example, the choice made for the wavevector is $\boldsymbol{k}_{\|} = k_x\hat{\boldsymbol{x}}$. The starting point is to use Maxwell's equations (Eq. 1.1-1.4), to derive the following elementary boundary conditions for the electric and magnetic fields at the interface between the two media,

$$H_{y_1} = H_{y_2} = H_y \tag{3.3}$$

$$E_{x_1} = E_{x_2} = E_x \tag{3.4}$$

$$\varepsilon_1 E_{z_1} = \varepsilon_2 E_{z_2}. \tag{3.5}$$

Eq. 3.3 is now utilised within Maxwell's equation for the curl of the magnetic field,

$$\nabla \times \boldsymbol{H} = \epsilon\frac{\partial \boldsymbol{E}}{\partial t}. \tag{3.6}$$

Substitution of Eq. 3.1 & 3.2 into Eq. 3.6 gives,

$$\begin{aligned}(-k_{z_n}\hat{\boldsymbol{x}} + k_x\hat{\boldsymbol{z}})iH_y e^{i(k_{x_n}x + k_{z_n}z - \omega t)} &= -i\omega\epsilon_n(E_x\hat{\boldsymbol{x}} + E_{z_n}\hat{\boldsymbol{z}})e^{i(k_{x_n}x + k_{z_n}z - \omega t)} \\ (-k_{z_n}\hat{\boldsymbol{x}} + k_x\hat{\boldsymbol{z}})H_y &= -\omega\epsilon_n(E_x\hat{\boldsymbol{x}} + E_{z_n}\hat{\boldsymbol{z}}).\end{aligned} \tag{3.7}$$

The $\hat{\boldsymbol{x}}$ component of the above equation re-arranged for $H_y$ is,

$$H_y = \frac{\omega\epsilon_n E_x}{k_{z_n}}, \tag{3.8}$$

which yields the following relationship between the perpendicular wavevector components across the boundary for p-polarised light,

$$\frac{\varepsilon_1}{k_{z_1}} = \frac{\varepsilon_2}{k_{z_2}}. \tag{3.9}$$

As an aside, the same process repeated for s-polarised light gives $k_{z_1} = k_{z_2}$, where there is no dependence upon the material permittivity. Eq. 3.9 is used in conjunction with $k^2 = k_x^2 + k_{z_n}^2 = \varepsilon_n(\omega/c)^2$ to form the following matrix equation,

$$\begin{pmatrix} 1 & 1 \\ 1 & (\varepsilon_2/\varepsilon_1)^2 \end{pmatrix} \begin{pmatrix} k_x^2 \\ k_{z_1}^2 \end{pmatrix} = \left(\frac{\omega}{c}\right)^2 \begin{pmatrix} \varepsilon_1 \\ \varepsilon_2 \end{pmatrix}. \tag{3.10}$$

Inversion of Eq. 3.10 gives,

$$\begin{pmatrix} k_x^2 \\ k_{z_1}^2 \end{pmatrix} = \left(\frac{\omega}{c}\right)^2 \begin{pmatrix} (\varepsilon_2/\varepsilon_1)^2 & -1 \\ -1 & 1 \end{pmatrix} \begin{pmatrix} \varepsilon_1 \\ \varepsilon_2 \end{pmatrix} \frac{1}{(\varepsilon_2/\varepsilon_1)^2 - 1}, \tag{3.11}$$

from which the dispersion relation for p-polarised light at the interface is determined,

$$k_{\|} = \left(\frac{\omega}{c}\right) \sqrt{\frac{\varepsilon_1 \varepsilon_2}{\varepsilon_1 + \varepsilon_2}}. \tag{3.12}$$

This result is independent of the choice taken for $\hat{\boldsymbol{k}}_{\|}$ in the derivation. Attempting to form a dispersion relation for surface modes with s-polarised light does not yield a dispersion relation, indicating that s-polarised light cannot excite a surface mode. Therefore, only p-polarised light can excite surface modes. Eq. 3.12 is an entirely general expression and enables one to investigate SPPs and SEPs alike. To demonstrate the generality of Eq. 3.12, dispersion diagrams obtained using Eq. 3.12 for gold, silver

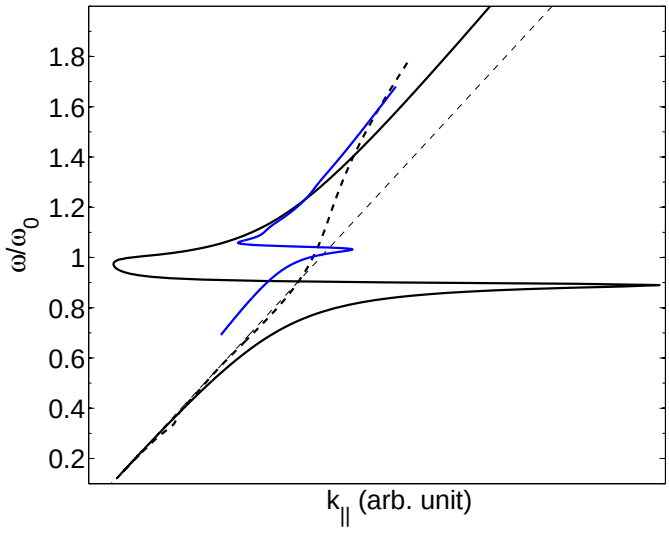


**Figure 3.4:** Normalised dispersion diagrams for 1.46 *wt*% TDBC:PVA (blue), gold (dashed) and silver (black), with the free space light line (thin dashed line).

and 1.46 *wt%* TDBC:PVA against an air boundary are plotted in Fig. 3.4. The $\omega$ axis in Fig. 3.4 is normalised to the plasma frequency $\omega_p$ for gold and silver, and to the exciton excitation energy $\omega_0$ for TDBC:PVA.

### 3.3.2 Surface mode classifications

The curves in Fig. 3.4 can be analysed with the help of the equivalent dispersion relation for the perpendicular axis. Performing the derivation in a similar manner to the derivation above for Eq. 3.12, the dispersion relation for the perpendicular axis is obtained,

$$k_{z_2} = \left(\frac{\omega}{c}\right) \frac{\varepsilon_2}{\sqrt{\varepsilon_1 + \varepsilon_2}}. \tag{3.13}$$

There are three possible sets of conditions on $k_{||}$ and $k_z$ for which surface modes can be supported by a film. All three are illustrated in Fig. 3.5, where an annotated dispersion diagram for 1.46 *wt%* TDBC:PVA is plotted.

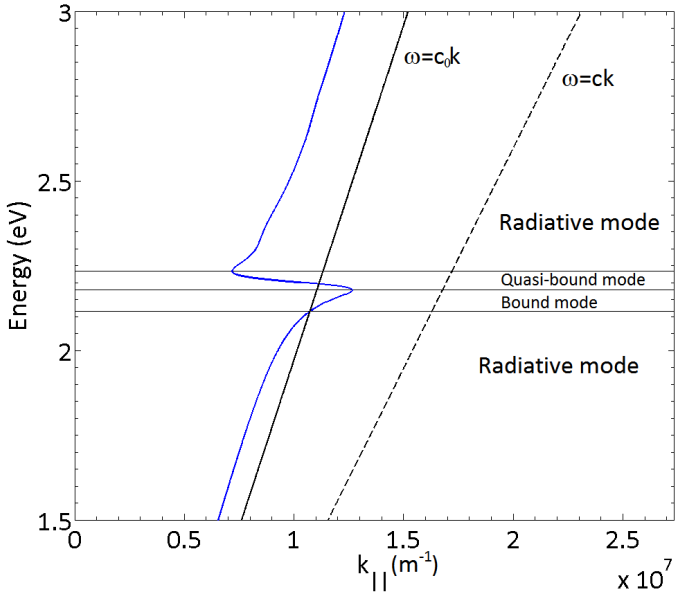


**Figure 3.5:** Dispersion diagram (blue line) for a 1.46 *wt%* TDBC:PVA film, using the four-level quantum model as outlined in Ch. 2. The black line represents the free space light line, and the dashed line represents the light line in a prism with refractive index $n = 1.5$.

The case of primary interest within this chapter is where (within the film) $k_{||}$ is real and $k_z$ is imaginary. Under this circumstance, a surface mode along the interface is

permitted and propagation into the material is impeded - this is known as a 'bound mode'.[130,131] By use of Eq. 3.12 & 3.13 with the assumption that $\varepsilon_1$ is real and positive, the following constraint on the permittivity of the material ($\varepsilon_2$) is established,

$$\varepsilon_2' \leq -\varepsilon_1. \tag{3.14}$$

Therefore, the condition for a material to host a bound mode is such that $\varepsilon$ must change by at least a sign across the boundary. Substitution of the upper and lower bounds on $\varepsilon_2'$ for a bound mode ($-\infty$ and $-\varepsilon_1$) into Eq. 3.12 leads to two constraints on $k_{\|}$ such that,

$$k_0 < k_{\|} < \infty. \tag{3.15}$$

Put into physical terms, Eq. 3.15 indicates that bound modes are indicated by a dispersion diagram when $k_{\|}$ lies beyond (to the right of) the free-space light line. As a consequence, the phase velocity ($v_p = \omega/k$) of such modes is less than the speed of light, but the in-plane momentum is greater than free-space light can supply. Therefore, in order to excite a bound mode, a prism is needed on the incident side to reduce the phase velocity of the light, and increase the in-plane momentum. The maximum momentum available by performing this procedure is indicated by the prism light line in Fig. 3.5, where the incident angle must be equal to 90°. An example of an experimental set up is the Kretschmann configuration[2], as shown in Fig. 3.6.

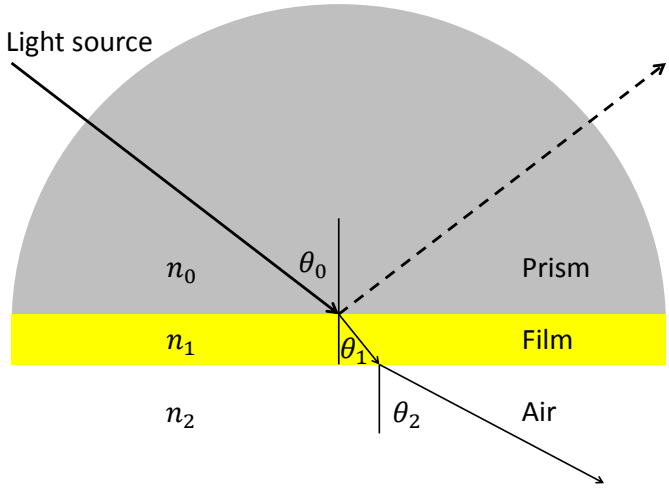


**Figure 3.6:** An illustration of the Kretschmann configuration in the ray optics picture. Depending on its properties, the film under investigation may host a surface mode along either interface.

Bound modes for silver occur over a broad energy range as shown in Fig. 3.4, from low energies, up to a value below the plasma frequency. For the TDBC film shown,

bound modes can only occur over a relatively narrow range of frequencies: a range corresponding to the window where $\varepsilon' < -1$ (*cf.* Fig. 2.8).

The conjugate of a bound surface mode can also be excited, where the mode propagates along the $z$-axis and decays along the x-axis. This is known as a 'quasi-bound' mode.[131] In this case, $k_z$ is real, and $k_\parallel$ is imaginary. Performing the same analysis as above for the bound mode leads to the following condition on $\varepsilon$ for such a mode,

$$-\varepsilon_m < \varepsilon' < 0. \tag{3.16}$$

By substitution of the upper and lower bounds on $\varepsilon'$ into Eq. 3.12, the following range for $k_\parallel$ can be established for quasi-bound modes,

$$0 < k_\parallel < \infty. \tag{3.17}$$

Therefore, quasi-bound modes can be found at all in-plane wavevectors, or equivalently, at all phase velocities (including infinity). Quasi-bound modes are evidenced in Fig. 3.4 by the relatively flat regions of $\omega(k_\parallel)$ for silver and TDBC, where the dispersion lines cross the light lines with a small increase in $\omega$. In this region, the group velocity $v_g = d\omega/dk$ is both minimised and (uniquely) negative. This region for the 1.46 *wt%* TDBC:PVA film is indicated explicitly in Fig. 3.5.

A third class of surface mode exists under the circumstance that both $k_\parallel$ and $k_z$ are real. In such a case, a mode can propagate freely along both the surface and perpendicular to it, causing the mode not to be confined to the surface. This type of mode is known as a 'radiative' mode,[131] since light can couple to and excite such modes readily. Use of Eq. 3.12 & 3.13 together leads to the condition for radiative modes such that,

$$\varepsilon' > 0. \tag{3.18}$$

This condition leads to the constraint on the in-plane wavevector such that,

$$0 < k_\parallel < k_0. \tag{3.19}$$

Therefore, $k_\parallel$ for a radiative mode lies below (to the left of) the light line on a dispersion diagram, implying that the phase velocity for such a mode exceeds the speed of light in free space. Such a case can be seen in Fig. 3.4 for silver (TDBC) in the region where $\omega$ exceeds the plasma (exciton) frequency and the material becomes transparent.[132] This is also indicated explicitly in Fig. 3.5 for the 1.46 *wt%* TDBC:PVA film.

### 3.3.3 Surface modes on thin films

For real materials, permittivity is generally complex. This leads to two consequences: firstly, spatial decay is incurred in any surface mode, so the three classes of surface modes as outlined in the previous section are not procured perfectly; secondly, $k_{\parallel}$ also becomes complex. Therefore, in order to analyse how a wave propagates along a material interface, the real part of $k_{\parallel}$ is taken to produce a dispersion diagram.

The spatial decay of the surface mode can be seen with examination of the parallel electric field component (the electric field of the surface mode),

$$E_{\parallel} = E_0 e^{ik'_{\parallel} x} e^{-k''_{\parallel} x}, \tag{3.20}$$

where $k_{\parallel} = k'_{\parallel} + ik''_{\parallel}$. The length for which the electric field intensity ($E_{\parallel}^2$) falls to $1/e$ of its peak value is defined as the propagation length, an expression for which is easily derived as,

$$L_{\parallel} = \frac{1}{2k''_{\parallel}}. \tag{3.21}$$

The electric field perpendicular to the boundary is written as,

$$E_{\perp} = E_0 e^{ik'_{\perp} x} e^{-k''_{\perp} x}, \tag{3.22}$$

which by performing a similar analysis leads to the following expression for skin depth,

$$L_z = \frac{1}{k''_z}. \tag{3.23}$$

Both $L_{\parallel}$ and $L_z$ calculated for 1.46 *wt%* TDBC:PVA, silver, gold and aluminium across the optical range are plotted in Fig. 3.7. In the figure, the four-level quantum model for the permittivity of TDBC aggregates has been used, and Drude models for the three metals have been used. As shown, the propagation length of a metal is in the approximate range $1\ \mu m < L_{\parallel} < 10\ \mu m$, and the skin depth of a metal spans (approximately) $0.1\ \mu m < L_z < 1\ \mu m$. These values are comparable with those found elsewhere.[133]

In Fig. 3.7, the regions for which TDBC:PVA exhibits bound and quasi-bound SEP modes are shown by the dashed and dotted lines respectively, in both $L_{\parallel}$ and $L_z$. As expected for TDBC:PVA, $L_{\parallel}$ for the bound SEP mode exceeds that of the quasi-bound SEP mode, and *vice versa* for $L_z$. From Fig. 3.7a, $L_{\parallel}$ for either of these SEP modes is shorter than the same quantity for the three metals indicated in the plot; this implies that SEP modes on a 1.46 *wt%* TDBC:PVA film exhibit relatively high localisation

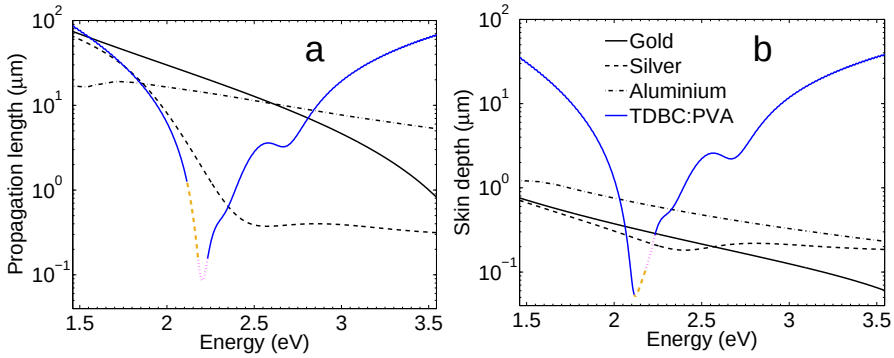


**Figure 3.7:** Propagation lengths (a) and skin depths (b) for 1.46 *wt%* TDBC:PVA (blue), silver (black line), gold (black dashed) and aluminium (black dash-dot). The solid, dashed and dotted parts of the blue line correspond to the radiative, bound and quasi-bound modes respectively.

with respect to SPP modes for the three metals shown. From Fig. 3.7b, $L_z$ for both the bound and quasi-bound SEP modes is shorter than for the gold SPP mode, although $L_z$ on the higher-energy side of the quasi-bound SEP mode exceeds that of the silver SPP mode. Therefore, in spite of the relatively short propagation length, SEP modes for a 1.46 *wt%* TDBC:PVA film show a higher degree of confinement to the surface than SPP modes for the three metals shown.

### 3.3.4 Reflectance and transmittance for thin films

As outlined in the introduction of this chapter, surface modes manifest themselves by a peak in absorption. If this peak can be matched to features on the dispersion diagram, surface modes for thin films can be detected from reflectance and transmittance spectra, measured across a range of angles. In order to explore this theoretically, a method for calculation of these quantities is required. In this section therefore, expressions for reflectance and transmittance are derived for thin films.

First, the reason for a peak in absorption within the film for a surface mode is explored. Starting with Snell's law[134] of refraction for waves across a boundary,

$$n_1 \sin(\theta_1) = n_2 \sin(\theta_2), \tag{3.24}$$

where the incident angle $\theta_1$ is related to the refracted angle $\theta_2$ for an incident medium of index $n_1$ and a refracted medium of index $n_2$. From Snell's law, a limiting incident angle can be derived for which the refracted light propagates along the interface, akin to a surface mode,

$$\theta_c = \arcsin\left(\frac{n_2}{n_1}\right). \tag{3.25}$$

This incident angle is the 'critical angle'. For $\theta_1 > \theta_c$ when $n_1$ and $n_2$ are both real, incident light is totally reflected. This changes if an imaginary part is introduced into $n_2$: in this circumstance, the critical angle cannot be strictly defined, since light is no longer completely refracted along the interface for *any* incident angle, and the refracted angle itself decreases with an increase in the imaginary part of $n_2$. Beyond the critical angle, light is still transmitted, but decays exponentially in space due to absorption within the material. Therefore, a dip in reflectance beyond the original critical angle is indicative of the complex refractive index of a material; this is true of both s-polarised and p-polarised light.

Bound surface modes can only be excited with p-polarised light, by the arguments put forward in Sec. 3.3.1. This excitation of surface modes occurs beyond the light line, *i.e.* beyond the critical angle. By conservation of energy arguments, this process correlates with an increase in absorption. The implication is that a peak in absorption for p-polarised beyond the critical angle in contrast to no such evident peak using s-polarised light for the same set of angles is indicative of the presence of a bound surface mode. Given that absorption for thin films can be found from both reflectance and transmittance, these two quantities are now sought.

Reflectance and transmittance are defined as the fraction of reflected and transmitted light across the boundary, and given the symbols $R$ and $T$ respectively. The most efficient way to calculate $R$ and $T$ for a film is to adopt a transfer matrix approach to find the reflected and transmitted electric fields in terms of the incident field, as outlined by Pedrotti and Pedrotti.[135] Here, expressions for the electric and magnetic fields in media $a$ and $b$ are represented as follows,

$$\begin{pmatrix} E_a \\ B_a \end{pmatrix} = \begin{pmatrix} \cos\delta & i/\gamma_1 \sin\delta \\ i\gamma_1 \sin\delta & \cos\delta \end{pmatrix} \begin{pmatrix} E_b \\ B_b \end{pmatrix}, \tag{3.26}$$

where $\gamma_1 = (\tilde{n}_1/c)/\cos\theta_{t_1}$ ($\gamma_1 = (\tilde{n}_1/c)\cos\theta_{t_1}$) for p-polarised (s-polarised) light and,

$$\begin{aligned} \delta &= k_0\Delta \\ &= (2\pi/\lambda_0)\tilde{n}_1 t\cos(\theta_0). \end{aligned} \tag{3.27}$$

$\tilde{n}_1$ is the complex refractive index of the film of thickness $t$. $\theta_0$ is the incident angle, $\theta_{t_1}$ is the refracted angle within the film and $\lambda_0$ is the wavelength of the incident light. The electric field on the left hand side of Eq. 3.26 is $E_a = E_0 + E_{r_1}$, where $E_0$ and $E_{r_1}$ are the incident and reflected fields respectively; the electric field on the right

hand side is the transmitted field, $E_b = E_{t_2}$. Using $B = (nE/c)\cos(\theta)$, $B_b = \gamma_2 E_{t_2}$ and $B_a = \gamma_0(E_0 - E_{r_1})$, Eq. 3.26 can be re-written as,

$$\begin{pmatrix} E_0 + E_{r_1} \\ \gamma_0(E_0 - E_{r_1}) \end{pmatrix} = \begin{pmatrix} m_{11} & m_{12} \\ m_{21} & m_{22} \end{pmatrix} \begin{pmatrix} E_{t_2} \\ \gamma_2 E_{t_2} \end{pmatrix}$$

$$= \mathcal{M} \begin{pmatrix} E_{t_2} \\ \gamma_2 E_{t_2} \end{pmatrix}. \tag{3.28}$$

The matrix $\mathcal{M}$ on the right hand side of Eq. 3.28 is the transfer matrix.[135] Using Eq. 3.28 with the definition of the (amplitude) reflection and transmission coefficients $r_{10} = E_{r_1}/E_0$ and $t_{02} = E_{t_2}/E_0$, the following two expressions for $r_{10}$ and $t_{02}$ in terms of the matrix elements of $\mathcal{M}$ are obtained,

$$t_{02} = \frac{2\gamma_0}{\gamma_0 m_{11} + \gamma_0\gamma_2 m_{12} + m_{21} + \gamma_2 m_{22}} \tag{3.29}$$

$$r_{10} = \frac{\gamma_0 m_{11} + \gamma_0\gamma_2 m_{12} - m_{21} - \gamma_2 m_{22}}{\gamma_0 m_{11} + \gamma_0\gamma_2 m_{12} + m_{21} + \gamma_2 m_{22}}. \tag{3.30}$$

The (intensity) reflectance and transmittance coefficients $R$ and $T$ are written in terms of $r_{10}$ and $t_{02}$ as,

$$R = |r_{10}|^2 \tag{3.31}$$

$$T = \frac{n_2 \cos\theta_{t_2}}{n_0 \cos\theta_0} |t_{02}|^2. \tag{3.32}$$

As a test of these formulae, one thousand reflectance spectra calculated for a $t = 70$ *nm* silver film in the Kretschmann configuration (see Fig. 3.6) with a prism of index $n = 1.52$ as a function of incident angle are plotted in Fig. 3.8 as a colour plot (overleaf). Here, the Drude model for silver has been used, and positive and negative angles correspond to p and s polarised light respectively. For p-polarised light, a dip in reflectance is evident; a feature which betrays the plasmonic nature of silver.[136] The colour calculated from the reflectance spectra which would be observed by the human eye is shown beneath the plot (as calculated using the code in App. A.1). Here, the colour reflects the expected whitish colour of bulk silver metal, with a blue-yellow feature at around 45° for p-polarised light, corresponding to the SPP mode.

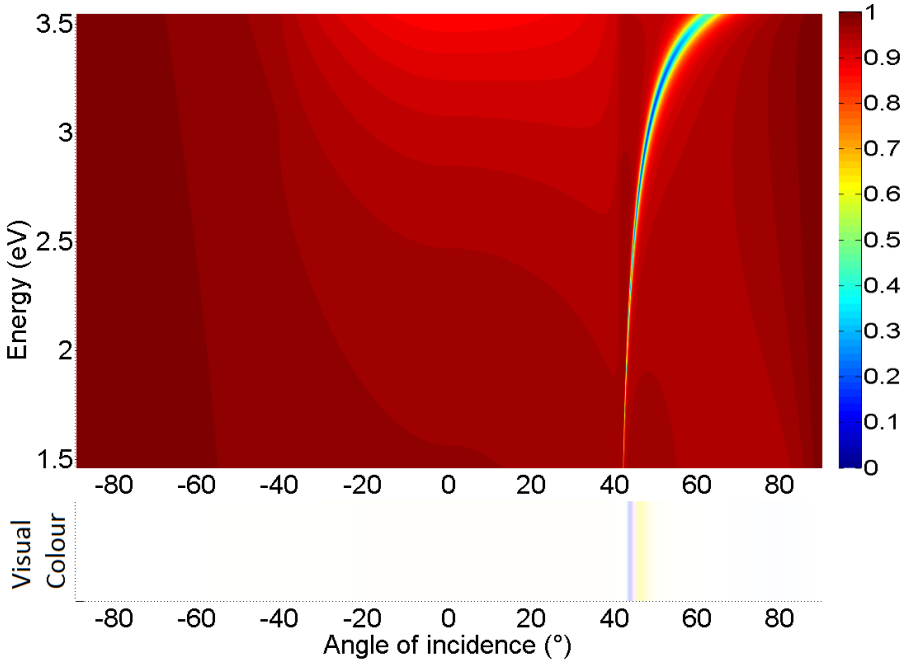


**Figure 3.8:** Reflectance spectra (top) for a 70 *nm* silver film in Kretschmann configuration as a function of angle, together with calculated visual colour (bottom). Negative and positive angles correspond to s and p polarised light respectively. The index of the prism is $n = 1.52$.

Similar reflectance spectra calculated for a $t = 70$ *nm* 1.46 *wt%* TDBC:PVA film in the same Kretschmann configuration are plotted in Fig. 3.9. Here, positive and negative angles indicate p and s polarised light, as in Fig. 3.8. The permittivity used for the film is taken from the four-level quantum model for TDBC:PVA as outlined in Ch. 2. From Fig. 3.9, there is a dip in reflectance for p-polarised light beyond the critical angle for the prism-air interface (41°) at 2.16 *eV*, as circled in the figure; this dip is absent from the calculations based upon s-polarised light. Therefore, it is p-polarised light which minimises the reflectance spectrum beyond the critical angle, and hints at a plasmon-like SEP mode at this photon energy.

Plotted underneath Fig. 3.9 are the calculated colours, again calculated using the code in App. A.1. As a consequence of the presence of the dips in $R$ towards the red end of the spectrum for p-polarised light, the chief difference between the calculated colour for s and p polarised light at around 60° is that the colour appears more blue for p-polarised light. However, if this is a signature of a plasmon-like mode in the film, it is by no means as sharp a distinction as that of the feature exhibited by the silver film in Fig. 3.8 at around 45°.

The accuracy of the reflectance calculations and the calculated colours can be assessed by visual comparison with physical samples, using the prepared films outlined in Ch. 1.

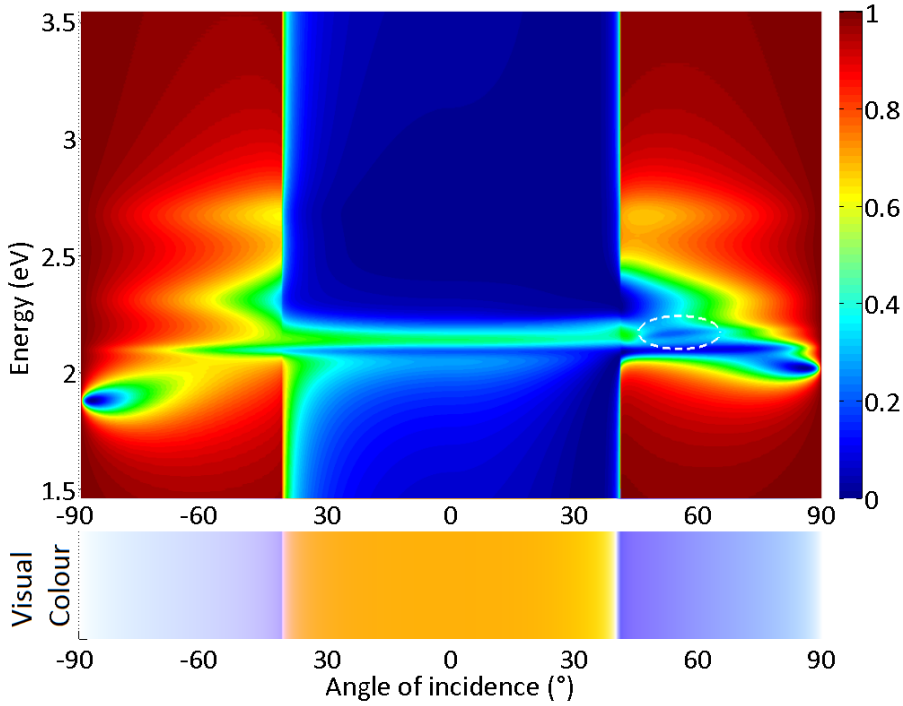


**Figure 3.9:** Reflectance spectra (top) in Kretschmann configuration for a 1.46 *wt%* TDBC:PVA film of thickness 70 *nm* as a function of angle, where positive (negative) angles indicate p (s) polarised light. The calculated visual colour as a function of angle is shown below the plot. The broken circle in the figure indicates a feature of interest.

In order to obtain theoretical reflectance spectra for these samples as a function of incident angle, the 1 *mm* glass substrate upon which each film was prepared was taken to be a semi-infinite medium (this approximation can be shown to hold by comparison of the result with more precise multilayer calculations). The resulting reflectance spectra were then used to calculate the corresponding visual colours as a function of angle, the results for which are shown in Fig. 3.10 (overleaf). This figure leads to the following predictions for TDBC:PVA films of differing concentration:

1. For either s or p polarised light for any dye concentration, the films for incident angles tending towards 90° become highly reflective for all wavelengths.

2. For p-polarised light, a yellow colour is observed for any of the dye concentrations exceeding 0.12 *wt%* for incident angles around 60° – 70°; for the 0.12 *wt%* film, the colour is off-white.

3. For s-polarised light with an incident angle of 60° – 70°, the calculated colour changes from off-pink through salmon to orange with an increase in concentration.

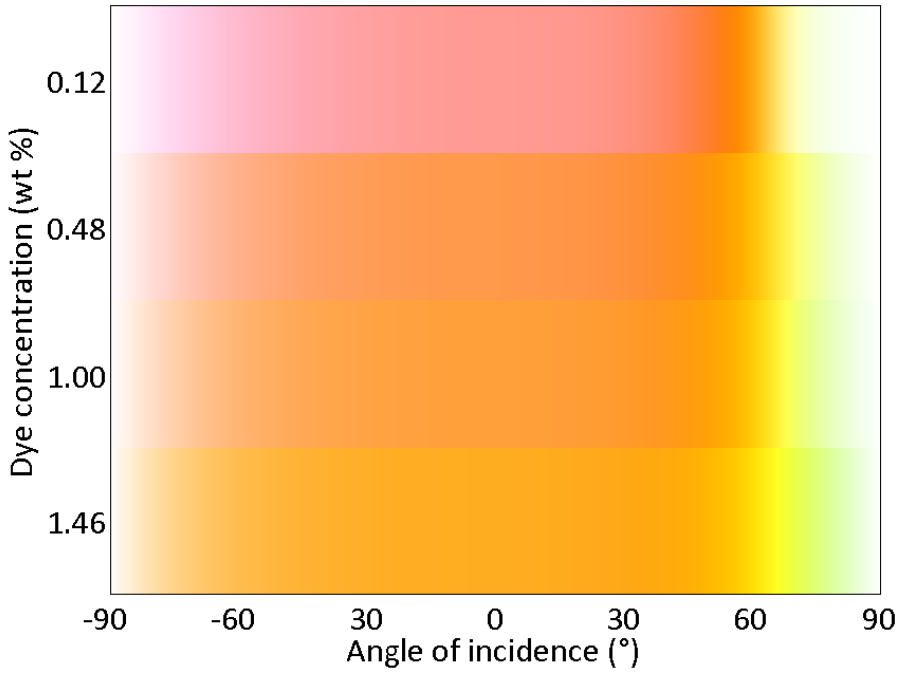


**Figure 3.10:** The calculated visual colours as a function of angle for four TDBC:PVA films with concentrations (top to bottom) 0.12, 0.48, 1.00, 1.46 *wt%*. The theoretical thicknesses of these films are 64.9, 76.6, 69.7 and 69.6 *nm* respectively. Negative and positive angles correspond to s and p polarised light respectively.

The first of these predictions is a simple consequence of the limit of the Fresnel equations.

The second and third predictions are evaluated with the help of Fig. 3.11, where photographs of the four films are displayed for both normal incidence and for an incident angle of 65°, for both s and p polarised light. Fig. 3.11b shows that for angles near normal incidence, an orange colour is observed with unpolarised light for each of the four films with different concentrations. The apparent difference in colour between the 0.48 *wt%* and 1.00 *wt%* films is subtle, but the colour is a more golden orange for the film of higher concentration. The prediction of a pinkish colour at normal incidence for the 0.12 *wt%* film (*cf.* Fig. 3.10) is at first sight incorrect, but close examination proves otherwise: firstly, the film is not coated uniformly, and the edges of the film appear orange. However, the interior of the film has a saturated RGB value of $(r, g, b) = (255, 162, 145)$, which is a salmon pink colour as predicted in Fig. 3.10. From this, it can be concluded that the local dye concentration of this film varies across the surface, and in some places may exceed 0.12 *wt%*.

The colours predicted in Fig. 3.10 using p-polarised light for an incident angle in the vicinity of 65° are proved in Fig. 3.11c to be correct: for the 0.12 *wt%* film, the colour is white, as expected, and a yellow colour is observed for the other three films. For

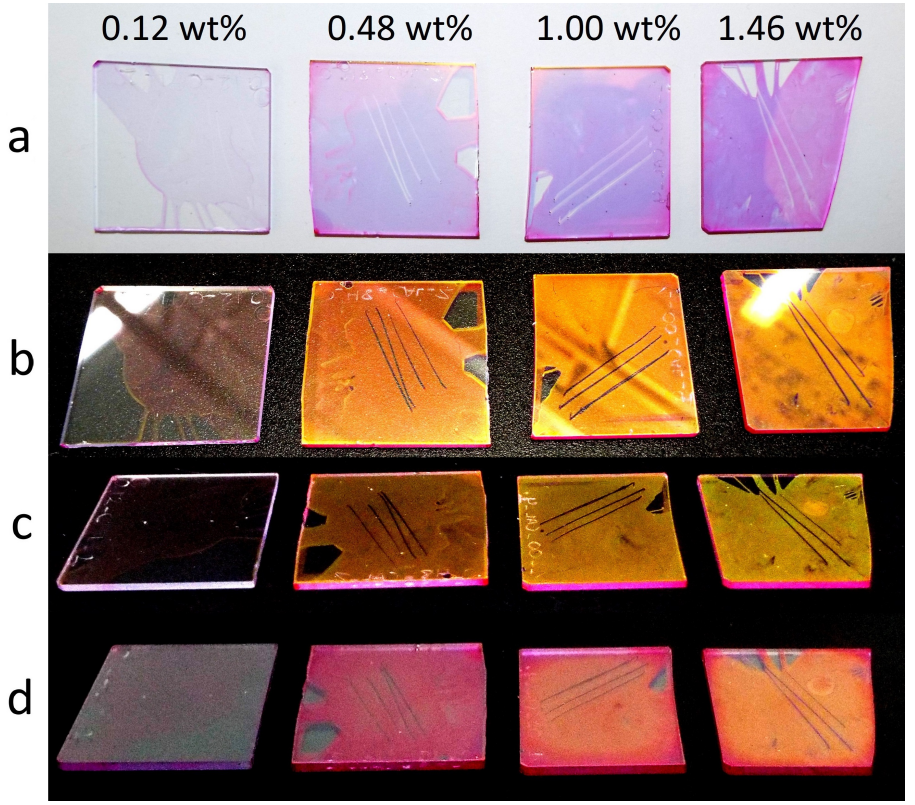


**Figure 3.11:** Photographs of four TDBC:PVA films with concentrations (left to right) 0.12, 0.48, 1.00 and 1.46 *wt%* with thicknesses 64.9, 76.6, 69.7 and 69.6 *nm* respectively. Panels a & b show the colours in transmission and reflection respectively for the four films at normal incidence. Panels c & d show the colours in reflection for p and s polarised light respectively, at an incident angle of 65°.

s-polarised light, the expected colours at 65° are observed in Fig. 3.11d for each of the four films: the 0.12 *wt%* and 0.48 *wt%* films show a pinkish colour as expected, which changes to a more orange-pink colour with an increase in concentration. The fact that the colours calculated from the colour code for reflectance yield colours of similar hue to those observed in experiment demonstrates the validity of the four-level quantum model for the permittivity and of the transfer matrix formalism used.

Fig. 3.11a shows that for transmission at normal incidence, the metallic appearance of the TDBC:PVA films is not apparent, as it was in the case of reflection: instead, a bluish-purple colour is observed - a colour which increases in saturation with a increase in concentration. By calculation of the transmittance through the same film as in Fig. 3.9 with extraction of the RGB values for $T$ at normal incidence, a bluish colour is produced. This is not entirely equivalent to the observed colour, as illustrated in Fig. 3.12, where the 1.46 *wt%* film is held in front of a scene (in the shadow of the camera), and contrasted with the calculated colour of the same film. This discrepancy

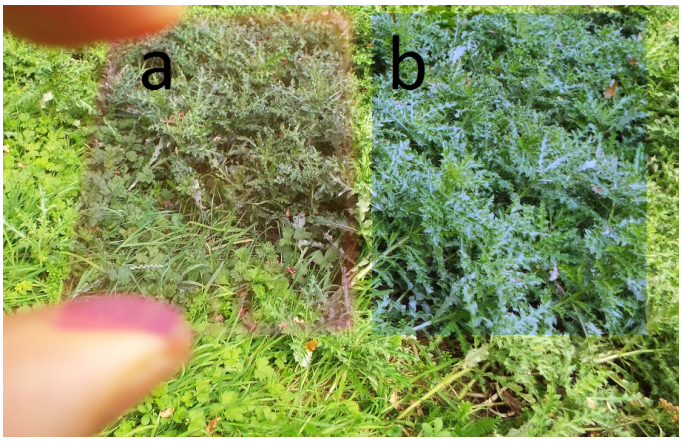


**Figure 3.12:** The observed (a) and calculated (b) effect of using a 70 *nm* 1.46 *wt%* TDBC:PVA film as an optical filter.

may arise from two sources, the first of which is the absorption curve taken for the l cone in the colour perception program: the l cone is chiefly responsible for the perception of the colour red. Conceivably, the l cone may be more sensitive to light at the blue end of the spectrum than assumed;[51] this would account for the lack of red in the calculated colour of the film shown in Fig. 3.12b. The second possible source of error is that no measurements for the permittivity were taken experimentally at the blue end of the visible range, from 380 $nm < \lambda < 450$ *nm*. This could potentially lead to the permittivity assumed in the model at this range to be incorrect. Therefore, an improvement on the experiment would be to take measurements in this range. Despite the discrepancy, the calculated blue colour is much closer to the observed colour of the film than the pale green calculated in Ch. 1 (*cf.* Fig. 1.11), since the calculated green colour was produced using (experimentally measured) transmittance values in the truncated visible range 450 $nm < \lambda < 850$ *nm*. As such, transmittance at the blue end of the visible range (380 $nm < \lambda < 450$ *nm*) was presumed to be zero, causing the calculated colour based on the experimentally-determined transmittance values to be much less blue than it should be.

For practical applications, the colours arising from reflectance and transmittance may be harnessed simultaneously, as visualised in Fig. 3.13. In this figure, the same scene is visualised in both panels, with and without the film, assuming the film is positioned outside of the shadow of the camera (an ambient light source is assumed). Without the film, the scene shows a white sheep suckling a black lamb. With the film, the black sheep's fleece becomes golden, in a nod to the Greek hero Jason's mythological quest. This apparent triviality serves an important role however: the visualisation in Fig. 3.13 recovers the observed metal-like appearance of the film, as displayed in Fig. 1.4. This result, together with the experimental results above, demonstrates that the transfer matrix method for making reflectance and transmittance calculations can reproduce physically observable phenomena, and that the model used for the permittivity produces values sufficiently close to those of the real film from which

**Figure 3.13:** The simulated effect of holding a 70 *nm* 1.46 *wt%* TDBC:PVA film in front of a scene, with an ambient light source: The same scene is visualised without (left) and with (right) the film placed at normal incidence in front of the camera. The rendering was produced using GIMP 2.8.

to base physical calculations. The next step is to use both $R$ and $T$ in order to probe surface modes of thin films.

### 3.3.5 Absorption for thin films

Absorption (denoted $A$) is defined as $A = 1 - T - R$. This quantity calculated for the same film as in Fig. 3.9 using the transfer matrix is plotted against incident angle and energy for p-polarised light in Fig. 3.14 (overleaf). In this plot, the critical angle associated with the prism/air interface at 41.1° is evidenced by a rise in absorption with angle, followed by a sharp drop off. This transition corresponds to a sudden change in reflectance (*cf.* Fig. 3.9) and transmittance.

The peak in absorption at 2.11 $eV$ in Fig. 3.14 corresponds to exciton excitation. This is very much stronger than the absorption at the next exciton absorption at 2.31 $eV$, as expected, due to the relative strengths between these two transition dipole moments (see Ch. 2).

The peak in absorption at 2.22 $eV$ in Fig. 3.14 corresponds to the part of the spectrum where the permittivity of the film is closest to zero: it is at this energy that the film is closest to behaving as an epsilon near zero (ENZ) material (*cf.* Fig. 2.8). In this circumstance, $T \to 0$, and $A \to 1 - R$, leading to a peak value for absorption in the range $A = \{0.6, 0.7\}$.

The feature for high angles at 2.01 $eV$ in Fig. 3.14 occurs due to a rise in the real part of the permittivity, leading to a dip in $R$ and no change in $T$, hence a rise in $A$.

Although incident angle is a variable which is easy to relate to conceptually, for investigation of surface modes it is more useful to plot absorption spectra against $k_{\|}$, as shown in Fig. 3.15. Here, negative and positive $k_{\|}$ represent s and p polarised light

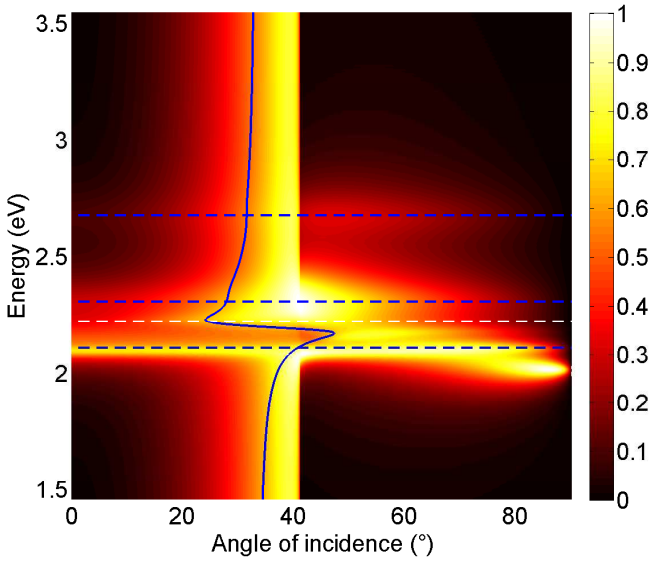


**Figure 3.14:** Calculated absorption for a 70 *nm* 1.46% TDBC:PVA film in Kretschmann configuration with a $n = 1.52$ prism using p-polarised light. The ENZ and exciton absorptions are indicated by the white and blue dashed lines respectively.

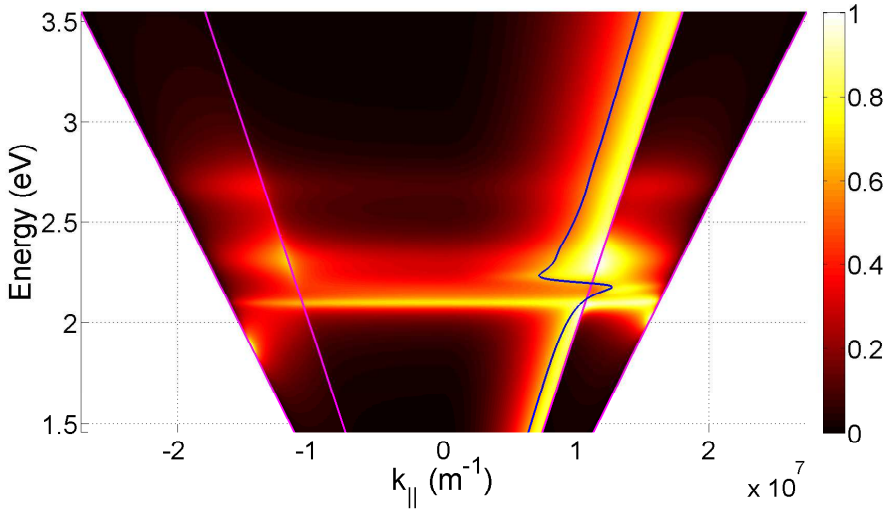


**Figure 3.15:** Dispersion relation (blue line) for 1.46 *wt%* TDBC:PVA with *A* for the film in Fig. 3.14, and with the light lines in free space and the prism (magenta lines). Positive (negative) $k_{\|}$ represents the p-polarised (s-polarised) light.

respectively. The dispersion relation for p-polarised light calculated using Eq. 3.12 for the film-air interface is plotted as a blue solid line in Fig. 3.15. For the region beyond the free space light line in the p-polarised calculations there exists a peak in

absorption at 2.18 $eV$ where the dispersion diagram indicates a bound mode, thereby indicating the existence of a bound SEP mode. For further confirmation of this mode, a difference plot is shown in Fig. 3.16, where the difference $A_p - A_s$ is plotted on a colour scale, where $A_p$ and $A_s$ represent $A$ for p and s polarised light respectively. Since

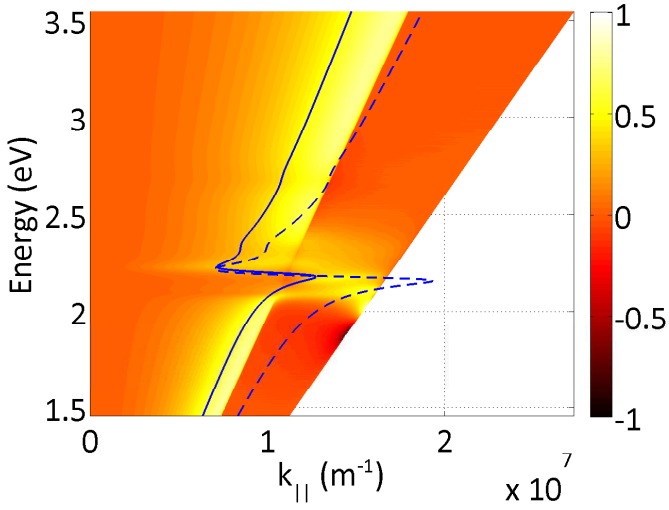


**Figure 3.16:** $A_p - A_s$ for a 70 $nm$ 1.46 $wt\%$ TDBC:PVA film, with dispersion diagrams for the air-TDBC and prism-TDBC interfaces indicated as solid and dashed lines respectively.

s-polarised light may excite excitons in the film just as effectively as p-polarised light, this difference highlights the features unique to that of illumination by p-polarised light, and removes the features corresponding to exciton absorption. Alongside the calculated absorption difference, dispersion diagrams for the air-film and the prism-film interfaces are plotted in Fig. 3.16. The peak in absorption in Fig. 3.16 follows the air-film dispersion diagram, giving further indication that the peak in absorption at 2.18 $eV$ corresponds to a bound SEP mode along the air-film interface. A possible quasi-bound mode is also evidenced in the energy range 2.18 $eV < E < 2.22$ $eV$ with an absorption of $A \approx 0.33$.

The definition for the quality factor of a peak used from this point onwards in this thesis is,

$$Q = \frac{\max(A)}{\text{FWHM}}, \tag{3.33}$$

where FWHM is the full-width half-maximum of the peak. Using this equation, the quality factor for the peak corresponding to the bound SEP mode in Fig. 3.16 was determined as $Q \approx 4.7$. The peak in absorption was found to be equal to $A = 0.71$. These values will be used to quantify how other surface modes considered in this chapter compare to (thin film) SEP modes.

Given that the minimum in $\varepsilon'$ lies below minus one for both the 0.48 *wt%* and 1.00 *wt%* films (*cf.* Fig. 1.9), it is possible for these films to host bound SEP modes. Performing the same procedure to obtain the difference plot in $A$ for these two concentrations, similar results to those shown in Fig. 3.16 are obtained (not shown), albeit with an increased minimum in the phase velocity of the SEP mode, together with a decrease in the range over which the SEP mode can be established, as expected.

For the 0.12 *wt%* film, the minimum in $\varepsilon'$ does not lie below minus one, and therefore the film cannot host a bound SEP mode. The absorption difference plot obtained using the procedure above is shown in Fig. 3.17. From this figure, the air-TDBC:PVA dispersion relation does not cross the free-space light line, and no bound SEP mode is possible along this interface, as expected. However, there is a feature corresponding to a possible quasi-bound mode in the range $2.13\ eV < E < 2.14\ eV$, with a relatively nominal amount of absorption ($A \approx 0.25$).

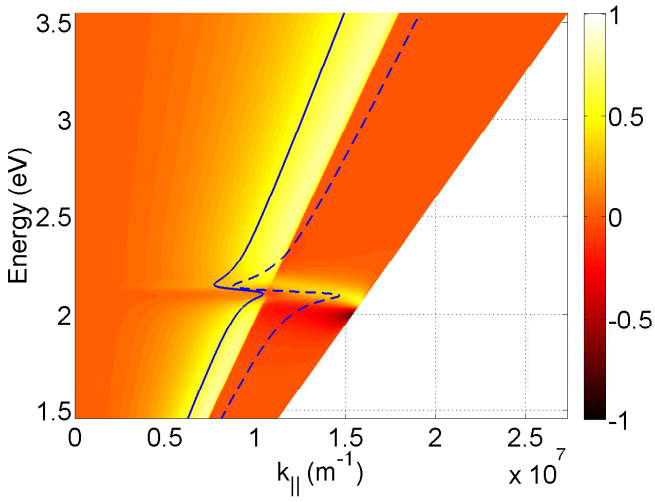


**Figure 3.17:** $A_p - A_s$ for a 65 *nm* 0.12 *wt%* TDBC:PVA film, with dispersion diagrams for the air-TDBC and prism-TDBC interfaces indicated as solid and dashed lines respectively.

Altogether, these findings demonstrate that bound SEP modes can be hosted by TDBC:PVA thin films. By increasing the dye concentration in the film, the phase velocity of these modes can be reduced, and the range of photon energies over which these modes can be supported increased. In addition, evidence for quasi-bound SEP modes in TDBC:PVA thin films is presented.

## 3.4 Anisotropic Materials

Anisotropic materials are defined by having directionally-dependent properties;[137] one of these properties can be permittivity. Anisotropy in permittivity can be either an intrinsic property of the material arising from its crystal structure (*e.g.* Barium Titanate[138]), or induced by an arrangement of two or more materials with isotropic permittivity[139] (referred to here as 'isotropic materials').

So far, surface modes have only been considered for isotropic materials in thin films. Given that the spectral location, group velocity and quality factor of a surface mode all depend fundamentally on the permittivity of the material in question, the capacity for fabrication of thin films designed to host a surface mode of a specific frequency is limited by the range of materials available. However, anisotropic materials provide the possibility of surface mode design by tailoring the geometry of the planar nanostructure: by layering two different materials together to form a stack, the effective permittivity of the multilayer can be controlled, along with the multilayer dispersion relation, and hence the frequencies of the surface modes.

Under the right circumstances, the dispersion relation of a multilayer stack can yield 'hyperbolic' surface modes,[36] in addition to possible SPP and SEP modes, which may provide unique optical properties. Therefore, in the following subsections, an effective medium dispersion relation for multilayer stacks is derived, with a view to investigate whether hyperbolic modes can be tuned and designed by fabrication of multilayers in the correct geometry.

### 3.4.1 Anisotropic permittivity

For anisotropic materials, the permittivity becomes a tensor, denoted $\bar{\varepsilon}$. Determination of the tensor elements is central to the prediction of the optical properties of such materials. The starting point is examination of the electric displacement vector $\boldsymbol{D}$: this quantity is related to the permittivity tensor and the electric field vector $\boldsymbol{E}$ by $\boldsymbol{D} = \varepsilon_0 \bar{\varepsilon} \boldsymbol{E}$. The permittivity tensor for a general non-magnetic ($\mu = \mu_0$) material is diagonal, and may be written in the following form,[140]

$$\bar{\varepsilon} = \begin{pmatrix} \varepsilon_{xx} & 0 & 0 \\ 0 & \varepsilon_{yy} & 0 \\ 0 & 0 & \varepsilon_{zz} \end{pmatrix}. \tag{3.34}$$

Materials with isotropic permittivity are materials for which $\bar{\varepsilon} = \varepsilon \boldsymbol{I}$, *i.e.* $\varepsilon_{xx} = \varepsilon_{yy} = \varepsilon_{zz}$. So far in this thesis, these are the only materials which have been considered. In this section, the simplest anisotropic materials are explored: these are uniaxial materials,

materials for which $\varepsilon_{xx} = \varepsilon_{yy} \neq \varepsilon_{zz}$. Multilayer stacks composed from isotropic materials fall under this category. For uniaxial materials, it is convenient to define a permittivity for electric fields parallel to the surface, $\varepsilon_{\parallel} = \varepsilon_{zz}$ and a permittivity for electric fields perpendicular to the surface, $\varepsilon_{\perp} = \varepsilon_{xx} = \varepsilon_{yy}$.

The goal now is to investigate how changes in $\varepsilon_{\perp}$ and $\varepsilon_{\parallel}$ govern the response of the in-plane wavevector $\boldsymbol{k}_{\parallel}$ for uniaxial materials. As such, a relationship between the electric field $\boldsymbol{E}$ and the wavevector $\boldsymbol{k}$ is sought. Maxwell's equations for the curl of the electric and magnetic fields for non-magnetic, charge-free and current free materials are written as,

$$\nabla \times \boldsymbol{E} = -\mu_0 \frac{\partial \boldsymbol{H}}{\partial t} \qquad (3.35) \qquad\qquad \nabla \times \boldsymbol{H} = \varepsilon_0 \bar{\varepsilon} \frac{\partial \boldsymbol{E}}{\partial t}. \qquad (3.36)$$

If the material is illuminated with plane waves, $\boldsymbol{E}$ and $\boldsymbol{H}$ for the incident field are written in the following form,

$$\boldsymbol{E} = \boldsymbol{E}_0 \exp[i\omega t - i\boldsymbol{k} \cdot \boldsymbol{r}] \qquad (3.37)$$

$$\boldsymbol{H} = \boldsymbol{H}_0 \exp[i\omega t - i\boldsymbol{k} \cdot \boldsymbol{r}]. \qquad (3.38)$$

Substituting these two expressions into Eq. 3.35 & 3.36 and recognising in this case that $\nabla \times \boldsymbol{E} = i\boldsymbol{k} \times \boldsymbol{E}$ and that $\nabla \times \boldsymbol{H} = -i\boldsymbol{k} \times \boldsymbol{H}$ gives,

$$\boldsymbol{k} \times \boldsymbol{E} = \mu_0 \omega \boldsymbol{H} \qquad (3.39)$$

$$\boldsymbol{k} \times \boldsymbol{H} = -\varepsilon_0 \bar{\varepsilon} \omega \boldsymbol{E}. \qquad (3.40)$$

The cross product of Eq. 3.39 with $\boldsymbol{k}$ is,

$$\boldsymbol{k} \times \boldsymbol{k} \times \boldsymbol{E} = \omega \mu_0 (\boldsymbol{k} \times \boldsymbol{H}). \qquad (3.41)$$

Substitution of Eq. 3.40 into this expression gives a relationship between $\boldsymbol{k}$ and $\boldsymbol{E}$ as required,

$$\boldsymbol{k} \times \boldsymbol{k} \times \boldsymbol{E} + k_0^2 \bar{\varepsilon} \boldsymbol{E} = 0, \qquad (3.42)$$

where the relationship $k_0^2 = \varepsilon_0 \mu_0 \omega^2$ has been used, and $k_0$ is the wavenumber of the applied field. Eq. 3.42 can be written in the following matrix form,[140]

$$\begin{pmatrix} k_0^2\varepsilon_\perp - k_y^2 - k_z^2 & k_x k_y & k_x k_z \\ k_x k_y & k_0^2\varepsilon_\perp - k_x^2 - k_z^2 & k_y k_z \\ k_x k_z & k_y k_z & k_0^2\varepsilon_\parallel - k_x^2 - k_y^2 \end{pmatrix} \begin{pmatrix} E_x \\ E_y \\ E_z \end{pmatrix} = 0. \tag{3.43}$$

The next step is to solve Eq. 3.43 for $k_0$ by taking the determinant of the matrix. The problem can be simplified considerably by reduction to two dimensions, with subsequent generalisation. By setting $k_y = 0$, $k_x = k_\perp$ and $k_z = k_\parallel$, the following expression for the determinant is obtained,

$$(k_0^2\varepsilon_\perp - k_\parallel^2)(\varepsilon_\parallel\varepsilon_\perp k_0^2 - \varepsilon_\perp k_\perp^2 - \varepsilon_\parallel k_\parallel^2)k_0^2 = 0. \tag{3.44}$$

This expression is valid for any set of Cartesian axes on the material interface, subject to the condition that the z-axis is orientated normal to the interface. Therefore, in general, $k_\perp^2 = k_x^2 + k_y^2$. Eq. 3.44 implies three families of solutions for $k_0$: the first of these is trivial, where $k_0 = 0$. The second family of solutions is of the form,

$$k_0^2 = \frac{k_\parallel^2}{\varepsilon_\perp}, \tag{3.45}$$

implying that the solutions lie on a sphere in k-space, equivalent to the isotropic solutions. The third family of solutions is of the form,

$$k_0^2 = \left(\frac{k_\perp^2}{\varepsilon_\parallel} + \frac{k_\parallel^2}{\varepsilon_\perp}\right), \tag{3.46}$$

implying that the solutions lie on a hyperbolic region of k-space when $\varepsilon_\parallel\varepsilon_\perp < 0$. There are two possibilities to satisfy this condition: the first occurs where $\varepsilon_\parallel < 0$ and $\varepsilon_\perp > 0$, and the second occurs where $\varepsilon_\parallel > 0$ and $\varepsilon_\perp < 0$. The first of these cases corresponds to Type I hyperbolic metamaterials, and the second corresponds to Type II hyperbolic metamaterials. For the purposes of determination of the class in question, only the real part of $\varepsilon$ is taken while ohmic losses are ignored[140] *i.e.* only the polarisation response is examined.

### 3.4.2 Dispersion relation for a uniaxial material

One can derive a dispersion relation for a non-magnetic uniaxial material by adopting a similar approach to that used for the isotropic film. The boundary condition in Eq. 3.9 becomes,

$$\frac{k_{z_1}}{\varepsilon_m} = \frac{k_{z_2}}{\varepsilon_\parallel}. \tag{3.47}$$

Putting this into the hyperbolic solution for $k_0$ (Eq. 3.46) gives,

$$k_0^2 = \frac{k_x^2}{\varepsilon_\parallel} + \left(\frac{\varepsilon_\parallel}{\varepsilon_m}\right)^2 \frac{k_{z_1}^2}{\varepsilon_\perp} = \left(\frac{\omega}{c}\right)^2. \tag{3.48}$$

The corresponding equation for $k_0$ in the surrounding medium is,

$$k_0^2 = k_x^2 + k_{z_1}^2 = \varepsilon_m \left(\frac{\omega}{c}\right)^2. \tag{3.49}$$

Eq. 3.48 & 3.49 can be cast into the following matrix equation,

$$\begin{pmatrix} 1/\varepsilon_\parallel & (\varepsilon_\parallel/\varepsilon_m)^2/\varepsilon_\perp \\ 1 & 1 \end{pmatrix} \begin{pmatrix} k_x^2 \\ k_{z_1}^2 \end{pmatrix} = \begin{pmatrix} 1 \\ \varepsilon_m \end{pmatrix} \left(\frac{\omega}{c}\right)^2. \tag{3.50}$$

From this, the dispersion relation can be found by once again setting $k_\parallel = k_x$, and operating the inverse of the matrix on the equation above,

$$\boxed{k_\parallel = \left(\frac{\omega}{c}\right) \sqrt{\frac{\varepsilon_\parallel \varepsilon_m (\varepsilon_\perp \varepsilon_m - \varepsilon_\parallel^2)}{\varepsilon_\perp \varepsilon_m^2 - \varepsilon_\parallel^3}}}. \tag{3.51}$$

As expected, in the limiting case where $\varepsilon_\perp = \varepsilon_\parallel$, the dispersion relation for a simple interface (Eq. 3.12) is recovered, specifically,

$$k_\parallel = \left(\frac{\omega}{c}\right) \sqrt{\frac{\varepsilon_m \varepsilon_\perp}{\varepsilon_m + \varepsilon_\perp}}. \tag{3.52}$$

Several conditions can be found for modes with zero group velocity in uniaxial materials by examination of Eq. 3.51. Given that group velocity along the surface is given by $v_g^\parallel = d\omega/dk_\parallel$, in seeking $v_g^\parallel = 0$ one can (equivalently) solve for $dk_\parallel/d\omega = \infty$. Taking this derivative,

$$\begin{aligned} \frac{dk_\parallel}{d\omega} = & \sqrt{\frac{\varepsilon_\parallel \varepsilon_m (\varepsilon_\perp \varepsilon_m - \varepsilon_\parallel^2)}{\varepsilon_\perp \varepsilon_m^2 - \varepsilon_\parallel^3}} + \\ & \frac{1}{2}\left(\frac{\omega}{c}\right) \sqrt{\frac{\varepsilon_\perp \varepsilon_m^2 - \varepsilon_\parallel^3}{\varepsilon_\parallel \varepsilon_m (\varepsilon_\perp \varepsilon_m - \varepsilon_\parallel^2)}} \frac{d}{d\omega} \left( \sqrt{\frac{\varepsilon_\parallel \varepsilon_m (\varepsilon_\perp \varepsilon_m - \varepsilon_\parallel^2)}{\varepsilon_\perp \varepsilon_m^2 - \varepsilon_\parallel^3}} \right). \end{aligned} \tag{3.53}$$

From Eq. 3.53, the following two solutions can be drawn,

$$\varepsilon_{\perp}\varepsilon_m^2 - \varepsilon_{\parallel}^3 = 0 \tag{3.54}$$

$$\varepsilon_{\parallel}\varepsilon_m(\varepsilon_{\perp}\varepsilon_m - \varepsilon_{\parallel}^2) = 0. \tag{3.55}$$

Eq. 3.54 gives solutions which cause $k_{\parallel} \to \infty$, and Eq. 3.55 gives solutions which cause $k_{\parallel} \to 0$; these expressions can also be arrived at by direct examination of Eq. 3.51. The solutions for which $k_{\parallel} \to \infty$ and $k_{\parallel} \to 0$ correspond to bound and quasi-bound surface modes respectively.

## 3.5 Multilayer Stacks

As stated in Sec. 3.4, a uniaxial material can be created by layering two isotropic materials in a multilayer stack.[139] In this section, the effective permittivity of such structures is determined, and surface modes for multilayer stacks investigated. In particular, the relative strengths and quality factors of hyperbolic modes in comparison to the SPP and SEP modes of their constituent materials are evaluated, with a focus on silver, gold and TDBC:PVA.

### 3.5.1 Multilayer stack classifications

Provided that the overall thickness of a multilayer stack is subwavelength, the stack itself can be approximated as an effective medium. This enables one to express $\varepsilon_{\parallel}$ and $\varepsilon_{\perp}$ in terms of the filling fraction $f = t_1/(t_1 + t_2)$, where $t_1$ and $t_2$ are the thicknesses of the two constituent materials with permittivities $\varepsilon_1$ and $\varepsilon_2$ respectively. One set of possible expressions for $\varepsilon_{\perp}$ and $\varepsilon_{\parallel}$ are,[36]

$$\varepsilon_{\perp} = f\varepsilon_1 + (1-f)\varepsilon_2 \tag{3.56}$$

$$\varepsilon_{\parallel} = (f/\varepsilon_1 + (1-f)/\varepsilon_2)^{-1}. \tag{3.57}$$

These expressions can be used to determine the classifications of multilayer stacks as both a function of wavelength and a function of $f$. To do so, the definitions outlined in Tab. 3.1 (overleaf) are used.

| Material Type | Conditions | |
|---|---|---|
| Dielectric | $\varepsilon_\perp > 0$ | $\varepsilon_\parallel > 0$ |
| Type I hyperbolic metamaterial | $\varepsilon_\perp > 0$ | $\varepsilon_\parallel < 0$ |
| Type II hyperbolic metamaterial | $\varepsilon_\perp < 0$ | $\varepsilon_\parallel > 0$ |
| Metal | $\varepsilon_\perp < 0$ | $\varepsilon_\parallel < 0$ |

**Table 3.1:** Definitions for the four classes of multi-layered materials.

Denoting gold as material 1 and PVA as material 2, the material classes obtainable in the optical range for a multi-layered stack comprising these two materials is plotted in Fig. 3.18. PVA is assumed to have a refractive index of $n = 1.52$ across the optical range, and the modified Drude model for gold is used to model its permittivity, as outlined in Ch. 2. From the figure, the multilayer stack is classed as a metal (dielectric) when comprising mostly gold (PVA) as intuitively expected. A Type II hyperbolic metamaterial is produced for intermediate filling fractions.

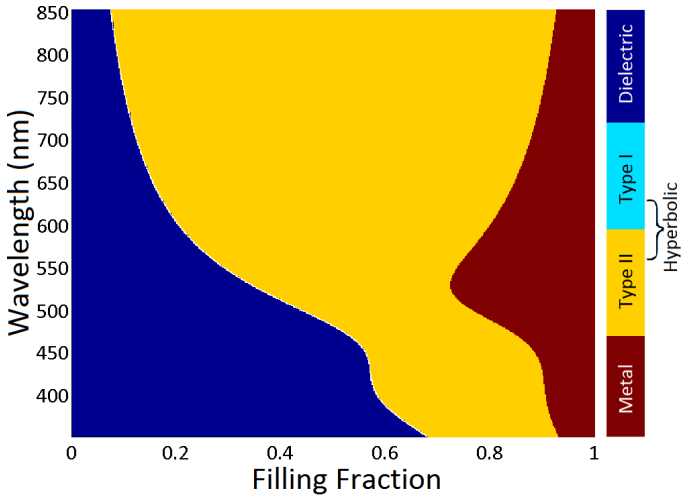


**Figure 3.18:** Material class as a function of filling fraction of gold ($f$) and wavelength ($\lambda$) for a PVA and gold multilayer stack.

A similar class plot using PVA doped with TDBC molecules to a concentration of 1.46 *wt%* is shown in Fig. 3.19. In Ch. 1, it was shown that 1.46 *wt%* TDBC:PVA has a spectral region where $\varepsilon' < 0$; this is evidenced in Fig. 3.19, where the material class becomes metal-like for wavelengths in the range $558\ nm < \lambda < 587\ nm$ for a zero filling fraction (entirely TDBC:PVA). A similar picture arises when the gold in Fig. 3.19 is substituted for silver, as shown in Fig. 3.20. In either example, the Type I hyperbolic metamaterial only exists in a narrow range of frequencies.

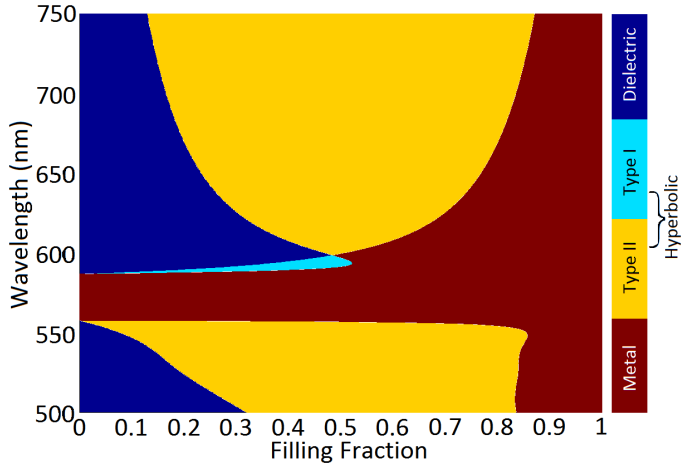


**Figure 3.19:** Material class as a function of filling fraction of gold $f$ and $\lambda$ for a 1.46 *wt%* TDBC:PVA and gold multilayer stack.

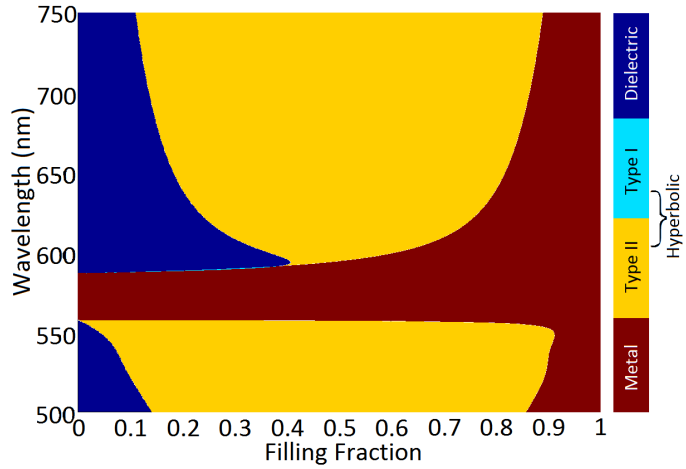


**Figure 3.20:** Material class as a function of filling fraction of silver $f$ and $\lambda$ for a 1.46 *wt%* TDBC:PVA and silver multilayer stack.

## 3.5.2 Modes for stacks

In designing multilayer stacks to host bound surface modes for two given materials, an optimal value for $f$ can be determined. By using the condition on $\varepsilon_\perp$ and $\varepsilon_\parallel$ for a surface mode given by Eq. 3.54 with substitution of the definitions for $\varepsilon_\perp$ and $\varepsilon_\parallel$ given in Eq. 3.56 & 3.57, the following quartic equation in $f$ is obtained,

$$(f\varepsilon_1 + (1-f)\varepsilon_2)(f\varepsilon_2 + (1-f)\varepsilon_1)^3\varepsilon_m^2 = \varepsilon_1^3\varepsilon_2^3. \tag{3.58}$$

When Eq. 3.58 is solved for $f$, the filling fraction required to give a bound surface mode is obtained; specifically, a value for $f$ which maximises $k_{\|}$. Solving this quartic depends critically on the values of $\varepsilon_1$ and $\varepsilon_2$. It must be noted that solutions of Eq. 3.58 for $f$ are generally complex, whereas $f$ can only be a real number in practice. One trivial solution (for which $k_{\|}$ diverges) is $\varepsilon_1 = \varepsilon_2 = 0$.

In order to find quasi-bound surface modes, solutions for $f$ which minimise $k_{\|}$ must be found. One approach is to take Eq. 3.51 (excluding $\omega = 0$, and taking $\varepsilon_m$ to be a positive real constant) and solve for $k_{\|} = 0$ directly. This gives the following two conditions,

$$\varepsilon_{\|}\varepsilon_m = 0 \tag{3.59}$$

$$\varepsilon_{\perp}\varepsilon_m - \varepsilon_{\|}^2 = 0. \tag{3.60}$$

The first of these is equivalent to,

$$\frac{\varepsilon_1\varepsilon_2}{f\varepsilon_2 + (1-f)\varepsilon_1} = 0, \tag{3.61}$$

which leads to two rather trivial independent conditions: $\varepsilon_1 = 0$, or $\varepsilon_2 = 0$. Quasi-bound modes are therefore manifested when the permittivity of one of the materials in the multilayer is equal to zero; if both are equal to zero, the mode becomes bound (see above).

The second condition for quasi-bound modes (Eq. 3.60) leads to the following cubic equation for $f$,

$$(f\varepsilon_1 + (1-f)\varepsilon_2)(f\varepsilon_2 + (1-f)\varepsilon_1)^2\varepsilon_m = \varepsilon_1^2\varepsilon_2^2. \tag{3.62}$$

By using Eq. 3.62 with the specific values of $\varepsilon_1$ and $\varepsilon_2$, an optimal value of $f$ can be determined for quasi-bound modes.

The full range of possible dispersion relations for multilayers of 1.46 *wt%* TDBC:PVA and silver is displayed in Fig. 3.21, where fifty dispersion diagrams have been plotted in the range $0 < f < 1$; the equivalent set of dispersion relations for TDBC:PVA and gold is shown in Fig. 3.22.

In both Fig. 3.21 & 3.22, the dispersion diagrams have been colour-coded to show the material type at each photon energy. Beyond the light line, multilayers comprising TDBC:PVA-silver or TDBC:PVA-gold behave either as metals or as Type II hyperbolic

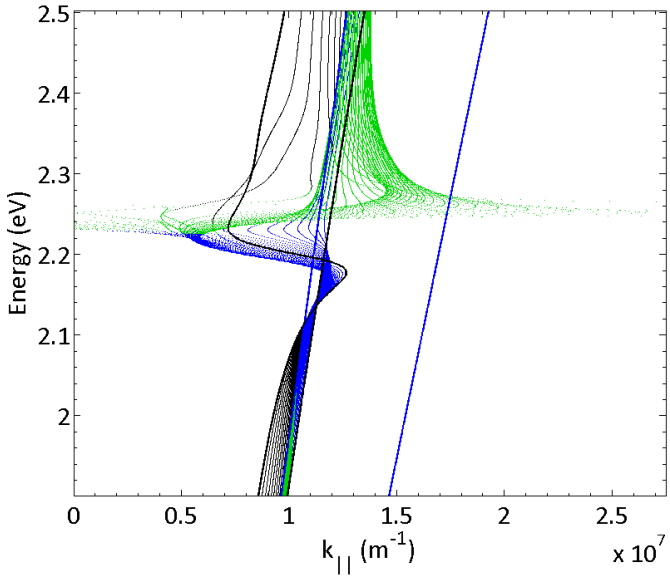


**Figure 3.21:** Full range of dispersion diagrams for multilayer stacks comprising silver and 1.46 *wt%* TDBC:PVA. Black, blue and green represent dielectric, metal and a Type II hyperbolic metamaterial respectively. The thick blue lines are the light lines for air and PVA. The thick black lines are the dispersion diagrams for 1.46 *wt%* TDBC:PVA and silver.

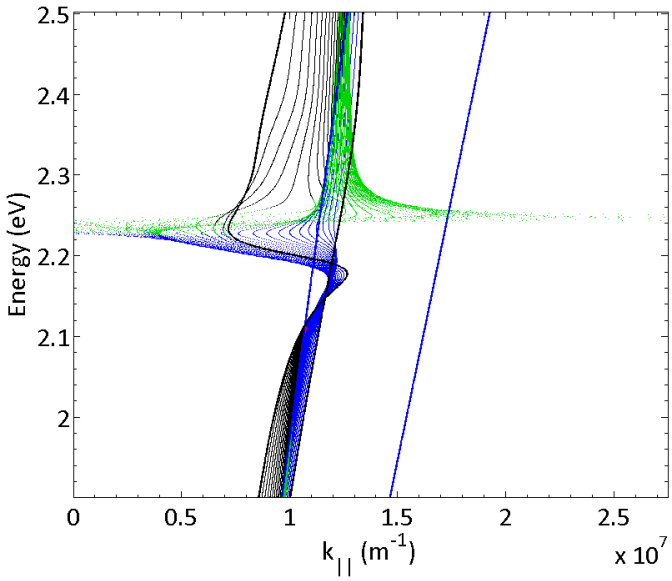


**Figure 3.22:** Full range of dispersion diagrams for multilayer stacks comprising gold and 1.46 *wt%* TDBC:PVA, using the same colour scheme as Fig. 3.21. The thick black lines are the dispersion diagrams for 1.46 *wt%* TDBC:PVA and gold.

metamaterials, as indicated by the blue and green lines respectively. The dispersion diagram for the nanostructure made entirely from TDBC:PVA follows that of Fig. 3.16 as expected. The bound surface modes below 2.2 *eV* arise from the metallic nature of the multilayer stack, and occur for any filling fraction of TDBC:PVA and metal, given the metallic nature of both these materials at these frequencies.

For photon energies above 2.22 *eV* in Fig. 3.21 & 3.22, the set of dispersion curves turn and go beyond the light line once more, implying the existence of further bound modes not found for isotropic films alone. These bound modes at higher energies occur exclusively for when the material is a Type II hyperbolic metamaterial. The minimum group and phase velocities of these bound hyperbolic modes are significantly lower than that of the bound SPP and SEP modes hosted by silver and TDBC:PVA films alike. The implication is that bound hyperbolic modes are even more tightly confined than SEP modes, and may be excited over a wider range of incident angles. For the TDBC:PVA-silver multilayer, the propagation length of the hyperbolic mode is minimised at a value of $L_{\|} = 29.0\ nm$, with a group velocity of $v_g^{\|} = 0.052c_0$, where $c_0$ is the speed of light in free space. This is in contrast to the minimised propagation length of the SEP mode in the 1.46 *wt%* TDBC:PVA film at $L_{\|} = 39.5\ nm$, with a group velocity of $v_g^{\|} = 0.169c_0$.

It is interesting to note that the change in metal between Fig. 3.21 and Fig. 3.22 does not significantly shift the photon energy at which the group velocity of the hyperbolic mode is minimised. Therefore, this particular mode is seen to be dominated by the ENZ contribution of the TDBC dye, which occurs at 2.23 *eV* (*cf.* Fig. 2.8) for this particular concentration.

Altogether, these findings demonstrate that tightly-bound hyperbolic modes with relatively low group velocity may be realised with a careful choice of the filling fraction for a two-material multilayered metamaterial. One of the materials in the multilayer must have a permittivity close to zero at some particular wavelength, and the other must behave as a metal around this wavelength in order for hyperbolic behaviour to be realised.

### 3.5.3 Reflectance and transmittance for stacks

In order to investigate the dispersion relations theorised in the previous sections, absorption for multilayer stacks must be computed. The most efficient way to accomplish this is to compute reflectance and transmittance for multilayer stacks *via* a generalised transfer matrix method (as outlined above for thin films, Eq. 3.26). To perform this generalisation, the transfer matrix for the entire stack is denoted $\mathcal{M}_r$. This quantity is related to the transfer matrix for each layer *via*,[135]

$$\mathcal{M}_r = \prod_{i=1}^{N} \mathcal{M}_i. \tag{3.63}$$

The transfer matrix equation is therefore re-written as,

$$\begin{pmatrix} E_a \\ B_a \end{pmatrix} = \mathcal{M}_r \begin{pmatrix} E_N \\ B_N \end{pmatrix} = \left( \prod_{i=1}^{N} \mathcal{M}_i \right) \begin{pmatrix} E_N \\ B_N \end{pmatrix}. \tag{3.64}$$

Once $\mathcal{M}_r$ is calculated, Eq. 3.29-3.32 can be used to calculate $R$ and $T$ for the multilayer, in the same way as for thin films.

From Fig. 3.21, the filling fraction of 1.46 *wt%* TDBC:PVA (in relation to that of silver) for which the group velocity is minimised is $f = 0.388$. For a multilayer stack with overall thickness 70 *nm* and twenty constituent layers, this filling fraction is achieved for film thicknesses of 2.71 *nm* and 4.29 *nm* for the TDBC:PVA and silver respectively. Undoubtedly, practical fabrication of such thin layers would be challenging, and great care would need to be taken in order to fabricate each layer with minimal surface roughness. However, presuming that these fabrication challenges can be overcome, the calculated reflectance spectra for this system in Kretschmann

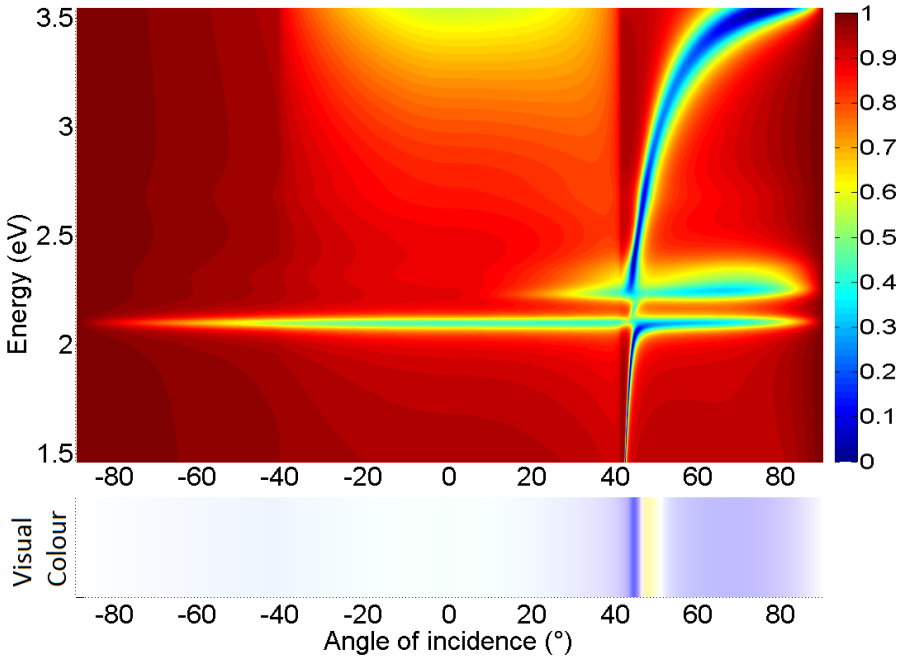


**Figure 3.23:** Reflectance for a twenty layer stack 70 *nm* thick, with alternate layers of 2.71 *nm* 1.46 *wt%* TDBC:PVA and 4.29 *nm* silver. The calculated visual colour as a function of angle is indicated beneath the plot, where positive (negative) angles correspond to p (s) polarised light.

configuration (with a $n = 1.52$ prism) as a function of angle is plotted in Fig. 3.23, where negative and positive angles correspond to s-polarised and p-polarised light respectively. The colour of the stack which would be observed by the human eye for the range of angles shown is indicated below the plot.

The calculated visual colours shown in Fig. 3.23 demonstrate that for both s-polarised light and for angles close to normal incidence, an off-white colour would be observed; this is a very similar colour to a 70 *nm* silver film (*cf.* Fig. 3.8). Given that the theoretical multilayer stack in Fig. 3.23 is 61% silver, this finding is unsurprising. For p-polarised light, the colour is bluish, with the exception of a feature around 45° for which there is a switch from blue to yellow and back again with increasing angle. This feature is also observed for a 70 *nm* silver film, as shown in Fig. 3.8. In the case of the silver thin film, this feature corresponded to an SPP in the silver film; here, it may indicate a surface mode in the multilayer stack. The chief difference between the observed colour of the silver film and the silver-TDBC:PVA multilayer is that the overall colour for the multilayer (over all angles) is more blue than that of the silver. This betrays the metamaterial nature of the multilayer stack: if the material were not a metamaterial, interference colours would be produced as (for example) seen in an oil-water multilayer. The absence of these interference colours demonstrates the validity of treating the multilayer stack as an effective medium over optical frequencies.

The colour plot for $R$ in Fig. 3.23 shows that there exists a dip in $R$ for p-polarised light beyond the critical angle (light line) which may indicate a dispersive, bound, surface mode similar to that of the SPP for a silver film (*cf.* Fig. 3.8 and Fig. 3.21). This dip appears to be due mainly to the presence of the silver, but analysis of the absorption for the multilayer may prove otherwise.

### 3.5.4 Absorption for stacks

If a multilayer stack were fabricated from alternate layers of a metallic material and a dielectric material, bound SPP modes along each interface would be able to be hosted.[139] As a consequence, the electric field would vary significantly over the stack, and the effective medium treatment for permittivity (Eq. 3.56 & 3.57) would become invalid. Therefore, it is expected that for shorter wavelengths (higher frequencies), the dispersion relation in Eq. 3.51 will break down. In this section, absorption for stacks is calculated *via* the transfer matrix method in order to evaluate the accuracy of the effective medium approximation.

Absorption for the same multilayer stack as considered in Fig. 3.23 is plotted in Fig. 3.24a, assuming p-polarised light. The dispersion diagram for the multilayer calculated using Eq. 3.51 is overlaid on the colour plot.

From Fig. 3.24a, the uniaxial dispersion curve is accompanied by peaks in absorption for energies below 2.5 $eV$. Specifically, in the spectral regions for which the dispersion curve lies beyond the free-space light line ($2.15\ eV < E < 2.19\ eV$ and $2.22\ eV$), peaks in absorption occur, indicating bound surface modes. Quasi-bound modes are

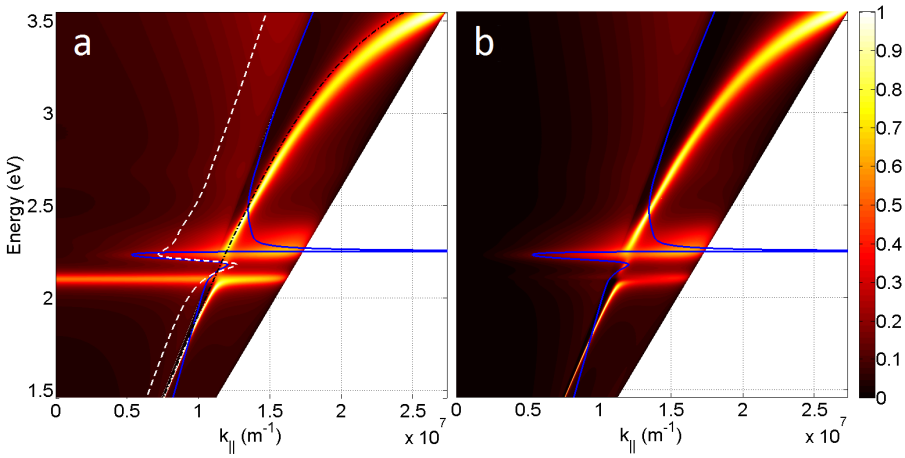


**Figure 3.24:** (a) Absorption ($A_p$) spectra with the dispersion relation (thick blue line) for a 20-layer stack of 1.46 *wt%* TDBC:PVA and silver, with film thicknesses 2.71 *nm* and 4.29 *nm* respectively ($f = 0.388$). The dispersion relations for the TDBC:PVA and silver are indicated by the dashed white and black lines respectively. (b) $A_p - A_s$ for the same system.

also indicated by the dispersion curve in the region of 2.19 $eV < E < 2.22$ $eV$, for which there is a corresponding peak in absorption.

For energies greater than 2.5 $eV$ in Fig. 3.24, the uniaxial dispersion relation does not follow any peak in absorption. The dispersion relation for silver shown in Fig. 3.24a demonstrates that the absorption peak at the high-energy end of the spectrum corresponds to a modified SPP arising primarily from the silver. This demonstrates a breakdown of the effective medium approximation assumed for the permittivity, as expected for shorter wavelengths. Specifically, 2.5 $eV$ is approximately equal to a wavelength of $\lambda = 508$ *nm*: a value just over seven times that of the overall thickness of the multilayer ($t = 70$ *nm*). This implies that the multilayer can be both considered subwavelength and suitably approximated as an effective medium for $t \leq \lambda/7$.

At 2.11 $eV$ in Fig. 3.24a, there exists a feature corresponding to exciton absorption. The uniformity of this absorption (*cf.* Fig. 3.15) has been modified by the bound SPP mode of the silver, and there is a dip in the absorption just before the free-space light line.

Fig. 3.24b can be used to discern the features of Fig. 3.24a more clearly, where the difference in absorption between p and s polarised light ($A_p - A_s$) has been plotted. This removes the feature corresponding to exciton absorption at 2.11 $eV$, and demonstrates that the peak in absorption beyond the free-space light line between 2.15 $eV < E < 2.19$ $eV$ is a veritable bound surface mode. By comparison with Fig. 3.21, this mode is seen to be metallic in nature. This mode has a peak of $A = 0.51$ and quality factor of $Q \approx 9.6$: an increase from that of the SEP mode exhibited by the single film in Fig. 3.15. The other mode present beyond the free-space light line (at 2.22 $eV$) is a mode with a hyperbolic Type II nature. This mode has a greater peak in

absorption ($A = 0.63$) in comparison to the metallic mode, but a quality factor of only $Q = 4.2$, slightly lower than that of the thin film SEP mode in Fig. 3.15. Making a further comparison of the hyperbolic mode with this SEP mode, the hyperbolic mode exhibits a lower group velocity, and is evident over a greater range of $k_{\|}$, hence, a greater range of incident angles. These findings imply that an optical filter constructed from a multilayer can be designed to absorb with greater uniformity beyond the critical angle than a single film would be able to, due to absorption from a bound hyperbolic surface mode.

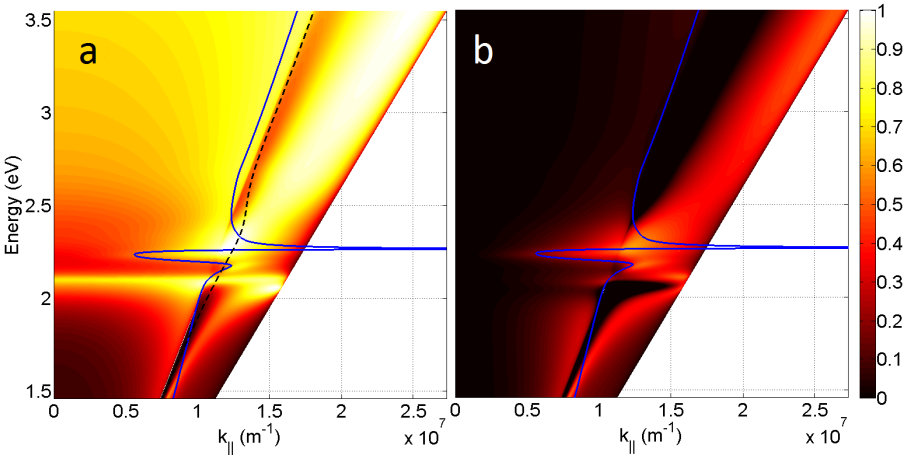


**Figure 3.25:** (a) Absorption ($A_p$) and dispersion relation (blue line) for a 20-layer stack of 1.46 *wt%* TDBC:PVA and gold, with film thicknesses 5 *nm* and 2 *nm* respectively ($f = 5/7$). The dispersion relation for gold is indicated by a dashed line. (b) $A_p - A_s$ for the same system.

Repeating the calculations above using gold in the place of silver for a value of $f$ which maximises $k_{\|}$ yields the plots in Fig. 3.25. Again, for energies less than 2.5 $eV$, the uniaxial dispersion relation is accompanied by a peak in absorption. As in the case of silver, the bound hyperbolic surface mode gives a greater peak in absorption (1.00) than that of the bound metallic surface mode (0.71).

Analysis of Fig. 3.25 is muddled by the absorption arising from the intraband transitions for gold. This can be seen in the dispersion relation for gold, shown as a dashed line in Fig. 3.25a: although it correctly predicts an SPP mode between $2.2\ eV < E < 2.4\ eV$, the gold dispersion relation diverges from any peak in absorption for energies exceeding 2.5 $eV$. In broad terms however, the bound hyperbolic mode has a broader range of absorption beyond the light line than the bound metallic surface mode; this is the same result obtained through theoretical calculations with silver, albeit with less uniformity in absorption.

## 3.6 Conclusions

By application of the dispersion relation for p-polarised light across a boundary to the permittivity of thin films of TDBC:PVA, it has been shown in principle that excitonic films may host bound surface modes, termed surface exciton polariton (SEP) modes. Such modes may be excited in the Kretschmann configuration. The group velocity of SEP modes for 1.46 *wt%* TDBC:PVA is relatively high in comparison to the group velocity of surface plasmon polariton (SPP) modes for silver in the region of the plasma frequency, but the propagation lengths of the two modes are comparable, being in the region of one micron. The skin depth for SEP modes in 1.46 *wt%* TDBC:PVA is below that of silver, indicating that such modes are more strongly confined to the surface, thereby exhibiting a higher degree of localisation.

In using the four-level quantum model for the permittivity of TDBC:PVA in conjunction with the transfer matrix and colour perception code, it was predicted that such films appear yellowish in reflection at incident angles in the region of 65° when illuminated by p-polarised light. This prediction was confirmed by experimentation. In transmission, the films appear purplish, although the colour perception code used predicts blue. This indicates one of two possibilities: first, that the absorption curves of the l, m and s cones in the human eye do not strictly correspond to the perception of R, G and B respectively. Further revision on the colour code may be necessary in order to accurately investigate the blue end of the visible spectrum. In the second possibility, the values for the permittivity of TDBC:PVA are not what they were assumed to be in the wavelength range $380\ nm < \lambda < 450\ nm$; further experimentation is required in order to shed light on this.

Absorption calculations for thin films of TDBC:PVA in the Kretschmann configuration with p-polarised light have demonstrated that peaks in absorption follow the dispersion relation. By calculation of the difference in absorption between p and s polarised light for such films, existence of SEP modes along the surface of TDBC:PVA films is inferred. SEP modes require at least a sign change across the boundary provided by the film, and the minimum dye concentration for which SEP modes can be excited at the interface of a TDBC:PVA film is yet to be determined. However, this value has been shown to lie in the range $0.12\ wt\% - 0.48\ wt\%$. Absorption corresponding to exciton excitation in these films occurs with equal efficiency for s or p polarised light. Another peak in absorption for TDBC:PVA films occurs at the photon energy for which the permittivity is close to zero, leading to a possible epsilon-near-zero (ENZ) mode.

Planar multilayer nanostructures may be considered as uniaxial materials. A dispersion relation using an effective medium approximation for $\varepsilon_\perp$ and $\varepsilon_\parallel$ has been developed and used to investigate bound surface modes in such nanostructures. For a twenty-layer 70 *nm* stack of gold (or silver) with TDBC:PVA, it has been shown that the dispersion relation based upon the effective medium approximation breaks down for wavelengths of light less than around seven times that of the total multilayer thickness. This implies

an upper limit of approximately $\lambda/7$ on the length for which a planar nanostructure may be considered to be subwavelength for a wavelength $\lambda$.

Bound or quasi-bound surface modes in two-material uniaxial multilayers can either be metallic or hyperbolic in nature, and their properties arise from a combination of the composite materials. In order to obtain a dispersion relation for which the group velocity of the hyperbolic modes is minimised, a metallic material and a material for which the permittivity is close to zero at some photon energy is required. Under this circumstance, bound hyperbolic surface modes lead to a greater amount of absorption in the multilayer than the bound metallic surface modes in the multilayer, and exhibit a greater degree of uniformity in absorption over a wider range of angles. The quality factor in absorption for the hyperbolic modes is approximately half that of the (metallic) multilayer SEP modes for the combinations of materials considered. It has been shown that the presence of hyperbolic modes can sharpen the absorption peak of an SEP mode. Therefore, multilayers can be used for this purpose, or to introduce a surface mode which has the capacity to absorb uniformly across a wide range of incident angles. These hyperbolic modes of TDBC:PVA-silver (or TDBC:PVA-gold) can exhibit an even greater degree of confinement along the surface than the SEP counterparts of thin-film TDBC:PVA. With correct determination of the filling fraction $f$ for two materials, these optical properties can be exploited.

In this chapter, planar excitonic nanostructures in the form of thin films have been shown to host SEP modes, the properties of which are similar to SPP modes. Multilayer metamaterials comprising excitonic and plasmonic materials have been shown to host hyperbolic modes which offer the prospect of surface modes by design. In all, planar excitonic nanostructures offer the potential for field enhancement and enhanced absorption in a similar way to that of planar plasmonic nanostructures, paving the way to the nanoscale control of light using excitonic nanostructures. However, planar nanostructures are cumbersome in fields such as biosensing within cells - and in this particular field, nanoparticles are more suited to the environment. Therefore, in the following chapter, the polariton modes of excitonic nanoparticles are explored.

# 4

# Particle Exciton Polariton Modes in Nanoparticles

*In this chapter, particle exciton polariton (PEP) modes are introduced as analogues to particle plasmon polariton (PPP) modes. Tunability offered by PEP modes is explored for both nanospherical and nanospheroidal nanoparticle geometries.*

## 4.1 Introduction

As seen in Ch. 3, quantised charge oscillations in the form of surface modes can be excited at the interface between two materials. For metals, these are surface plasmon polariton (SPP) modes and for excitonic materials, these are surface exciton polariton (SEP) modes. In this chapter, quantised charge oscillations confined to nanoparticles - henceforth termed 'particle modes' - are explored. For metallic and excitonic nanoparticles, these modes are termed particle plasmon polariton (PPP) modes and particle exciton polariton (PEP) modes respectively.

Particle modes are accompanied by electric field enhancement in the vicinity of the nanoparticle[5–7] along with an increase in absorption cross-section[141]. The strength of the electric field enhancement depends sensitively upon the environment and geometry[15] of the nanoparticle. This property can be utilised within the area of chemical detection in biosensing[16], specifically within surface-enhanced Raman scattering (SERS)[142] where excitation of a PPP mode underpins the principle involved. Already, the monitoring of cell membranes using SERS has been demonstrated.[21] PPP modes have also been shown to modify molecular fluorescences,[10,11] and a proof of principle chemical detection system utilising PPP modes for industrial applications has also been relayed.[17]

Despite these achievements, current mainstream fabrication techniques for plasmonic nanoparticles depend principally upon expensive, small-scale, top-down techniques such as electron-beam lithography. Recently, an alternative bottom-up approach has been demonstrated,[22] but this field is relatively unexplored. Metals have been used traditionally as plasmonic materials due to their negative permittivity: PPP modes (like SPP modes) depend upon a negative permittivity in order to be excited. As

shown in Ch. 2, the negative permittivity of metals arises from the contribution of free electrons. However, as outlined in Ch. 1, excitonic materials can also exhibit a negative permittivity over a narrow range of frequencies[143] arising from a strengthening in the transition dipole moment of the excitonic molecules under aggregation, as shown in Ch. 2. Therefore, nanoparticles of these resultant excitonic materials present an alternative to the use of metals as plasmonic materials, as explored in the context of planar nanostructures in Ch. 3. Excitonic materials are also of interest for control of light at the nanoscale in the context of nanoparticles,[144] and as means to support PEP modes.[46, 145, 146] In addition, excitonic materials offer a fabrication alternative based on supramolecular chemistry and self-assembly. Therefore, in this chapter the properties and merits of PEP modes for nanoparticles are investigated and weighed against those of PPP modes.

Nanoparticles as defined in this chapter are particles for which the smallest dimension is of the order of 100 *nm* or less. Therefore, 100 *nm* diameter nanospheres are treated as a limiting case, and are given particular attention throughout this chapter. For optical wavelengths, this length scale is in the subwavelength regime by a factor of four. The shape of the nanoparticles considered in this chapter are nanospheres and nanospheroids, both for their relative simplicity and relative ease of fabrication with modern techniques.[16]

In Ch. 3, the evidence for surface modes was presented using absorption calculations for planar nanostructures with the aid of dispersion diagrams overlaid upon these calculations. The comparison between the two helped to provide evidence that surface modes could be supported by films and multilayer stacks. In addition, the reflectance and transmittance spectra were used to calculate the visual appearance of such systems. For nanoparticles on resonance (whose diameter is less than that of the skin depth of the surface mode) the mode is distributed throughout the volume of the particle - the definition of a particle mode. Therefore, there is no direct equivalent of an induced wavevector parallel to the surface, as there is for surfaces: hence a dispersion relation for nanoparticles cannot be constructed in the same way. Accordingly, surface modes and particle modes are seen to be distinct from each other, and a different approach is needed in order to analyse particle modes.

The approach taken in this chapter is to first calculate the approximate resonant energies for the nanoparticle modes. This is accomplished by incorporation of the findings from Ch. 2 for the permittivity of the materials involved. By finding the resonant energies as functions of experimentally adjustable parameters (such as the nanoparticle dimensions, or dopant concentration), the tunability of these modes can be determined. Scattering and absorption cross-sections are then calculated, along with the electric field enhancement in the vicinity of the nanoparticle.

## 4.2 Dipole Particle Modes

The theoretical starting point for nanoparticles under illumination by an optical field is to consider the lowest order mode which can be induced in the nanoparticle: a dipole mode. By making the assumption that a dipole mode possesses a dipole electric potential, a general expression for the electric potential of a dipole mode at position $\boldsymbol{r}$ in a medium with relative permittivity $\varepsilon_m$ is,

$$\Phi(\boldsymbol{r}) = \frac{e}{4\pi\varepsilon_0\varepsilon_m}\left(\frac{1}{|\boldsymbol{r}-\boldsymbol{d}/2|} - \frac{1}{|\boldsymbol{r}+\boldsymbol{d}/2|}\right), \tag{4.1}$$

where $\boldsymbol{d}$ is the length and orientation of the dipole. In the point dipole approximation, the electric potential for a dipole orientated along the z-axis reduces to,

$$\Phi(r,\theta) \approx \frac{|\boldsymbol{p}|\cos\theta}{4\pi\varepsilon_0\varepsilon_m r^2}, \tag{4.2}$$

where $\theta$ is the angle which subtends the z-axis and the position vector $\boldsymbol{r}$. This electric dipole can in principle be excited by any incident light source with an electric field component in the z-direction, but exciting this mode in isolation requires a z-polarised light source incident in the x-y plane; this is the situation under consideration. The induced dipole moment $\boldsymbol{p}$ of the dipole mode depends linearly on the incident electric field $\boldsymbol{E}_i$. These two quantities are linked by,[61]

$$\boldsymbol{p} = \varepsilon_m\bar{\alpha}\boldsymbol{E}_i, \tag{4.3}$$

where $\bar{\alpha}$ is the polarizability tensor of the nanoparticle. For nanospheres, or for illumination of a non-spherical nanoparticle with a fixed orientation, $\bar{\alpha}$ reduces to a scalar, here denoted $\alpha = \alpha' + i\alpha''$. This complex quantity is key to determination of resonance conditions for the nanoparticle, and it governs the optical response of subwavelength nanoparticles themselves. This is seen by using the elementary relation $\boldsymbol{E} = -\nabla\Phi$ with Eq. 4.2 to give the following expression for the dipole electric field induced by the incident field in nanospheres,

$$\begin{aligned}\boldsymbol{E}_d &\approx \frac{|\boldsymbol{p}|}{4\pi\varepsilon_0\varepsilon_m r^3}\left(2\cos\theta\,\hat{\boldsymbol{r}} + \sin\theta\,\hat{\boldsymbol{\theta}}\right)\\ &= \frac{|\alpha||\boldsymbol{E}_i|}{4\pi\varepsilon_0 r^3}\left(2\cos\theta\,\hat{\boldsymbol{r}} + \sin\theta\,\hat{\boldsymbol{\theta}}\right).\end{aligned} \tag{4.4}$$

Here it is seen that the relative strength of the dipole electric field to the incident field at all points in space is linearly dependent upon $|\alpha|$.

The superposition of the incident field with the induced dipole electric field is now considered. As previously stated, the dipole mode considered above is orientated along the z-axis and the simplest incident electric field which can induce this mode is a z-polarised field, *i.e.*

$$\begin{aligned} \boldsymbol{E}_i &= E_i\,\hat{\boldsymbol{z}} \\ &\equiv E_i\left(\cos\theta\,\hat{\boldsymbol{r}} - \sin\theta\,\hat{\boldsymbol{\theta}}\right). \end{aligned} \tag{4.5}$$

Denoting the total field as $\boldsymbol{E} = \boldsymbol{E}_d + \boldsymbol{E}_i$, the following expression for the ratio of the magnitude of the total electric field strength to the incident electric field strength can be derived,

$$\zeta = \frac{|\boldsymbol{E}|}{E_i} = \sqrt{\frac{|\alpha|^2\beta^2}{r^6}(3\cos^2\theta + 1) + \frac{4\beta\alpha'}{r^3}\cos 2\theta + 1}, \tag{4.6}$$

where $\beta = 1/4\pi\varepsilon_0$. Two observations of Eq. 4.6 are made: firstly, the field distribution is independent of axial rotation. Secondly, given that the first term in the square root is dominant and positive, the relative strength of the total electric field can exceed that of the incident field within a region of space surrounding the nanosphere given a sufficiently strong value of $|\alpha|$. The specific shape of this region of space can be determined by construction of the following polar equation for isosurfaces for which the parameter $\zeta$ as defined above is constant,

$$r^3 = \frac{-2\beta\alpha'\cos 2\theta}{(\zeta^2 - 1)} \pm \beta\sqrt{\frac{4\alpha'^2\cos^2 2\theta}{(\zeta^2-1)^2} + \frac{|\alpha|^2(3\cos^2\theta + 1)}{(1-\zeta^2)}}. \tag{4.7}$$

The sign taken in Eq. 4.7 is the one which gives a real solution for $r$, given the specific value of $\alpha$. Given that the strength of a dipole electric field falls off with observation distance, the region of space within the isosurface defined by Eq. 4.7 is generally a region for which $\zeta$ exceeds its value upon the isosurface. This means that the region of space for which the electric field is enhanced can be determined by calculation of the $\zeta = 1$ isosurface. One *caveat* of Eq. 4.7 is that the $\zeta = 1$ isosurface is not directly calculable by Eq. 4.7, owing to a pole at $\zeta = 1$. This pole arises from the quasistatic theory used in order to derive Eq. 4.7. In order to avoid this pole, the isosurfaces plotted using Eq. 4.7 in this chapter are of the $\zeta = 1.01$ isosurface. These isosurfaces are used in this chapter to inform the nature of the results obtained using more exact (and hence less analytically tractable) scattering theories. The specific nature of the isosurfaces for nanospheres are examined in the following section.

## 4.3 Nanospheres

In this section, the resonant modes of bare nanospheres are considered. The resonance condition for nanosphere modes (the Clausius-Mossotti relation) is introduced, followed by consideration of the electric field strength in the vicinity of the nanosphere in the quasistatic regime. Quasistatic scattering and its relationship with the nanoparticle polarizability is then outlined, followed by the introduction of Mie theory: an exact scattering theory for spheres. Lastly, calculations made using Mie theory are presented, and the results are evaluated against the more approximate predictions from quasistatic theory.

### 4.3.1 The Clausius-Mossotti relation

The aim within this section is to find a value for the relative permittivity $\varepsilon$ of a nanosphere for which the dipole moment $\boldsymbol{p}$ induced by the incident field is maximised. By Eq. 4.3, this quantity is maximised where the polarizability $\alpha$ is also maximised. For nanospheres, an expression for the polarizability is given by,[61]

$$\begin{aligned}\alpha &= 3\varepsilon_0 V \frac{\varepsilon - \varepsilon_m}{\varepsilon + 2\varepsilon_m} \\ &= 4\varepsilon_0 \pi R^3 \frac{\varepsilon - \varepsilon_m}{\varepsilon + 2\varepsilon_m},\end{aligned} \tag{4.8}$$

where $V$ ($R$) is the nanosphere volume (radius). A condition can be drawn immediately from Eq. 4.8 for the maximisation of $\alpha$ as[6] $\min(\varepsilon + 2\varepsilon_m)$: this is known as the Clausius-Mossotti (CM) condition.[61] Re-writing this expression in the limit where $\varepsilon'' \to 0$ (and $\varepsilon_m$ is real-valued) gives the more familiar form of the CM condition,

$$\varepsilon' = -2\varepsilon_m. \tag{4.9}$$

| Material | CM resonance | $n_m$ |
|---|---|---|
| 1.46 *wt%* TDBC:PVA | 2.17 $eV \equiv 572\ nm$ | 1 |
| Gold | 2.66 $eV \equiv 466\ nm$ | 1 |
| Silver | 3.02 $eV \equiv 411\ nm$ | 1.5 |
| Aluminium | 7.76 $eV \equiv 160\ nm$ | 1.5 |

**Table 4.1:** Resonant energies for nanospheres of four materials as determined using the CM condition.

Using this condition with the permittivity results from Ch. 2, the resonant energies for nanospheres of four different materials in media of refractive index $n_m$ are tabulated in Tab. 4.1.

The approximate dependence of the resonant energy on the material properties of excitonic materials can be examined by substitution of the single-oscillator Lorentz model (Eq. 2.14) into the CM condition, and solving for the resonant frequency $\omega$ of the PEP mode (also known as the Fröhlich frequency[65]). This yields the equation,

$$\omega = \omega_0 \sqrt{1 + \frac{f}{\varepsilon_b + 2\varepsilon_m}}. \tag{4.10}$$

This equation demonstrates that the PEP mode will redshift for an increase in medium index. In addition, since the oscillator strength $f$ is directly proportional to concentration, the mode will blueshift for an increase in concentration. It is worth noting that the resonant frequency is always on the high-energy side of the exciton transition at $\omega_0$ for positive media ($\varepsilon_m > 0$).

Performing the same analysis for a metal nanosphere using the Drude model (Eq. 2.20) yields the following expression for the resonant frequency of a particle plasmon mode,

$$\omega = \frac{\omega_p}{\sqrt{\varepsilon_\infty + 2\varepsilon_m}}. \tag{4.11}$$

Like the formula for the PEP mode energy, Eq. 4.11 demonstrates that an increase in the medium index leads to a redshift in the PPP resonant energy.

Substitution of the best-fit Lorentz oscillator values for the TDBC:PVA in Tab. 4.1 ($f = 0.3$ and $\varepsilon_b = 1.52^2$) into Eq. 4.10 yields a value of 2.18 $eV$ for the resonant energy when the nanosphere is in vacuum ($\varepsilon_m = 1$); this value is within 0.5 % of the tabulated value from the quantum mechanical model, proving the validity of the Lorentz oscillator model to make approximate predictions for the PEP mode energy.

### 4.3.2 Field confinement in nanosphere dipole modes

The electric field strength around nanospheres hosting a dipole particle mode is now outlined in general terms using quasistatic theory, and then examined for three specific materials. These calculations are made with a view to help inform calculations made using Mie theory.

Firstly, the point dipole approximation upon which Eq. 4.7 relies needs to be justified for nanospheres of TDBC:PVA. The dipole lengths quantified in Ch. 2 are of the order of ångströms. Given that the radii of the nanospheres considered in this chapter are $R = 50$ $nm$ (a value around one hundred times that of the dipole length) the point

dipole approximation is justified and Eq. 4.7 can be used as a suitable approximation for the system.

Using Eq. 4.8 for $\alpha$ in Eq. 4.7 with the family of values of $\varepsilon$ for which the CM condition is satisfied ($\varepsilon = -2\varepsilon_m + i\varepsilon''$), the following polar equation for electric field isosurfaces on resonance is obtained,

$$\frac{r}{R} = \left( -\frac{2\cos 2\theta}{\zeta^2 - 1} \pm \sqrt{\left(\frac{2\cos^2\theta}{\zeta^2 - 1}\right)^2 + \frac{(1 + (3\varepsilon_m/\varepsilon'')^2)}{\zeta^2 - 1}(3\cos^2\theta + 1)} \right)^{1/3}. \tag{4.12}$$

At the nanosphere equator ($\theta = \pi/2$) this equation becomes,

$$\frac{r}{R} = \left( \frac{2}{\zeta^2 - 1} + \sqrt{\frac{4}{(\zeta^2 - 1)^2} + \frac{(1 + (3\varepsilon_m/\varepsilon'')^2)}{\zeta^2 - 1}} \right)^{1/3}. \tag{4.13}$$

Eq. 4.13 defines a circle around the nanosphere equator which increases in size with medium index.

In Eq. 4.12 & 4.13, there is a pole at $\varepsilon'' = 0$. This implies in the case where $\varepsilon = -2\varepsilon_m$, the electric field enhancement would be felt over all space. Such a material is unrealistic however, because in reality, $\varepsilon''$ is non-zero where the CM condition is fulfilled, and the speed of light is finite. Furthermore, the maximum extent of the

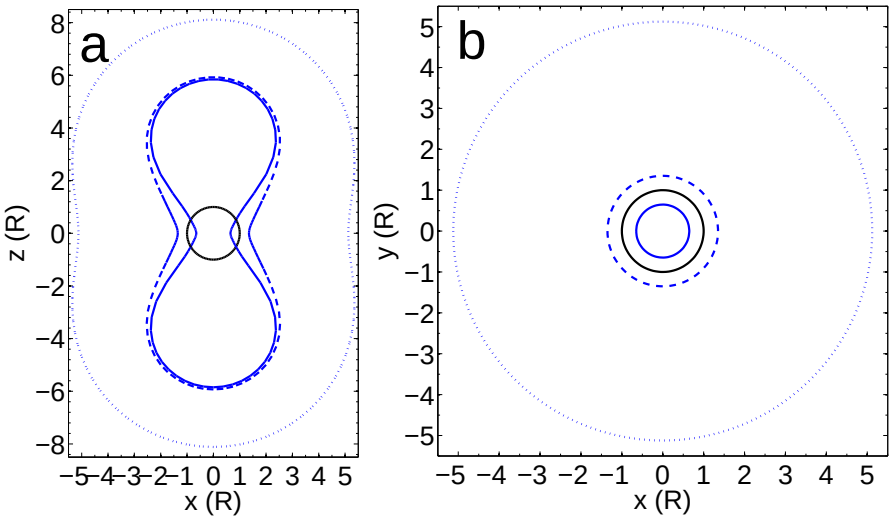


**Figure 4.1:** Cross-sections of $\zeta = 1.01$ isosurfaces (blue lines) for a nanosphere in vacuum with $\varepsilon' = -2$ and $\varepsilon'' = 0.1i$ (dotted), $1i$ (dashed) and $10i$ (solid). The nanosphere surface is indicated by the black line. The axes are in units of the nanosphere radius $R$.

enhanced field is tightly confined to the nanoparticle with even a modest value of $\varepsilon''$: taking an example of $\varepsilon = -2 + 0.1i$, the maximum extent of $r$ within which electric field enhancement ($\zeta > 1$) occurs in vacuum ($\varepsilon_m = 1$) is less than seven times the radius of the nanoparticle, as illustrated in Fig. 4.1. An increase in the loss ($\varepsilon''$) of the nanoparticle material causes the profile of this isosurface to shrink and narrow at the neck, as illustrated for the example permittivity of $\varepsilon = -2 + i$ in Fig. 4.1. A sufficiently large value of $\varepsilon''$ results in an isosurface which does not fully contain the nanoparticle, as again demonstrated in Fig. 4.1, with $\varepsilon = -2 + 10i$. These elementary calculations therefore demonstrate that electric field enhancement is only observed over all solid angles of the nanoparticle if $\varepsilon''$ is sufficiently low and the CM condition is fulfilled: similar plots to the innermost curve in Fig. 4.1 are produced for arbitrary values of $\varepsilon$ (not shown). This demonstrates that this property of electric field enhancement over all solid angles is a special case, which if demonstrated for a nanoparticle, is strong evidence for a particle polariton mode.

Isosurfaces for nanospheres of real materials are now considered. On-resonance calculations made using Eq. 4.7 for $\zeta = 1.01$ isosurfaces for silver nanospheres in a $n_m = 1.5$ medium along with gold and 1.46 *wt%* TDBC:PVA nanospheres in vacuum are visualised in Fig. 4.2. The resonant energies used for this figure are taken from the tabulated values in Tab. 4.1 and the incident light is z-polarised, following the formalism adopted above.

One finding from Fig. 4.2 is that the $\zeta = 1.01$ isosurface for the three nanospheres considered is not more that $5.5R$ from the surface of the nanosphere. This distance

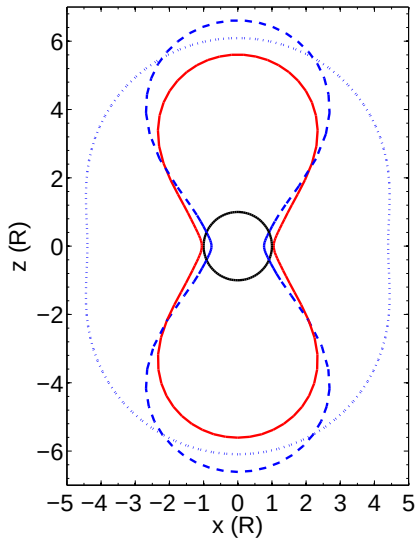


**Figure 4.2:** Cross-sections of $\zeta = 1.01$ isosurfaces in the x-z plane on resonance for nanospheres of silver in a $n_m = 1.5$ medium (blue dotted line), along with those in vacuum for nanospheres of 1.46 *wt%* TDBC:PVA (red solid line), and gold (blue dashed line). The nanosphere cross-section is indicated by the black solid line, and the axes are in units of the nanosphere radius $R$.

is maximised at the poles of the nanosphere ($x = y = 0$). At the nanosphere equator ($z = 0$), the isosurface lies outside the nanosphere for both the silver and TDBC:PVA nanospheres, but not for the gold nanosphere. Therefore, on resonance, the TDBC:PVA nanosphere exhibits electric field enhancement over all solid angles, whereas the gold nanosphere does not. However, the total volume of space enclosed by the isosurface for the gold nanosphere exceeds that of the TDBC:PVA nanosphere. The calculations for the silver nanosphere in vacuum resemble those of the gold nanosphere, but by raising the index of the medium to $\varepsilon_m = 1.5^2$, the volume of the $\zeta = 1.01$ isosurface around the nanosphere is increased (see Eq. 4.12 & 4.13). These calculations demonstrate that if a particle mode can be excited in a nanosphere in a higher index medium, it is likely to be accompanied by a greater volume over which electric field enhancement will occur.

There is another value of the permittivity for which electric field enhancement can be demonstrated over all solid angles: the case where $\varepsilon' \to 0$, *i.e.* for epsilon near zero (ENZ) materials. By using Eq. 4.7 & 4.8, the following polar equation can be derived for isosurfaces with $\varepsilon = 0 + i\varepsilon''$,

$$\left(\frac{r}{R}\right)^3 = 2\left(\frac{2\varepsilon_m^2 - \varepsilon''^2}{4\varepsilon_m^2 + \varepsilon''^2}\right)\frac{\cos 2\theta}{1-\zeta^2} \pm \sqrt{4\left(\frac{\varepsilon''^2 - 2\varepsilon_m^2}{4\varepsilon_m^2 + \varepsilon''^2}\right)^2 \frac{\cos^2 2\theta}{(\zeta^2-1)^2} + \left(\frac{\varepsilon_m^2 + \varepsilon''^2}{4\varepsilon_m^2 + \varepsilon''^2}\right)\frac{(3\cos^2\theta + 1)}{\zeta^2 - 1}}, \tag{4.14}$$

where light with a z-polarised electric field has been assumed. For $\varepsilon'' = 0$, Eq. 4.14 becomes,

$$\left(\frac{r}{R}\right)^3 = \frac{\cos 2\theta}{1-\zeta^2} \pm \sqrt{\frac{\cos^2 2\theta}{(1-\zeta^2)^2} + \frac{(3\cos^2\theta + 1)}{4(\zeta^2 - 1)}}. \tag{4.15}$$

The shape of the surface described by Eq. 4.15 is that of a doughnut, and bulges at the equator. By substitution of $\theta = \{0, \pi\}$ into Eq. 4.15, it can be shown that no isosurface breaks the surface of the nanosphere ($r = R$) at the poles when $\varepsilon'' = 0$. Therefore, electric field enhancement is not present over all solid angles for $\varepsilon = 0$. However, by performing the same calculation for $\varepsilon = 0 + i\varepsilon''$ with Eq. 4.14, it can be demonstrated that for small values of $\varepsilon''$, electric field enhancement *can* be present over all solid angles in a similar way to that of a PEP or PPP mode. To illustrate this point graphically, five x-z plane cross-sections of $\zeta = 1.01$ isosurfaces are plotted in Fig. 4.3 (overleaf) for differing values of $\varepsilon''$. It can be seen that for $\varepsilon'' < \varepsilon_m$, the shape of the isosurface described is markedly different from that of the dipole isosurfaces (as seen above) in that electric field enhancement occurs predominantly in the same plane in which the light is incident (the x-y plane in this case). For the curve calculated with $\varepsilon'' = 2$, the isosurface resembles that of the isosurfaces calculated with arbitrary $\varepsilon$, as seen above. In all, Fig. 4.3 demonstrates that there is a range of $\varepsilon''$ for which the

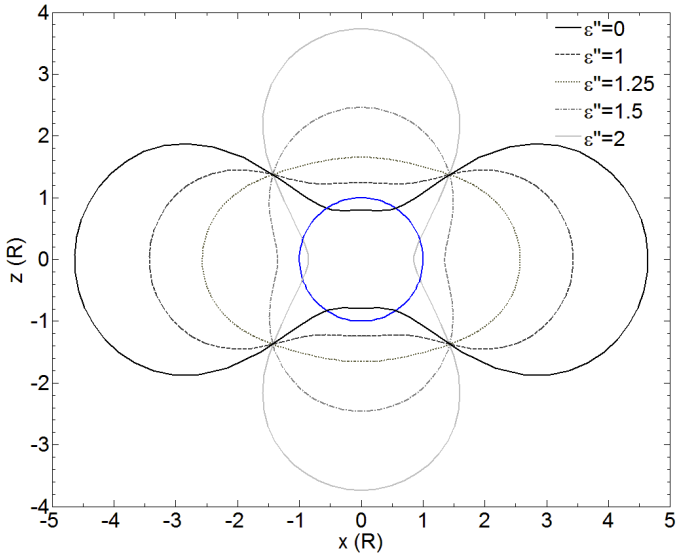


**Figure 4.3:** Five $\zeta = 1.01$ isosurfaces for a nanoparticle with $\varepsilon = 0 + i\varepsilon''$. Axes are in units of the nanoparticle radius, and the nanoparticle is indicated by the blue circle.

$\zeta = 1.01$ isosurface wholly contains the nanoparticle, giving electric field enhancement over all solid angles. In this way, an ENZ mode may be expected to act in a similar way to that of a PEP (or PPP) mode.

### 4.3.3 Quasistatic scattering

The effect of the particle polarizability on scattering, absorption and extinction cross-sections for nanospheres is now investigated. In the quasistatic regime (where the size of the particle is negligible in comparison to the wavelength) the scattering and absorption cross-sections $\sigma_{\text{sca}}$ and $\sigma_{\text{abs}}$ are related to the nanoparticle polarizability by,[65]

$$\sigma_{\text{sca}} = \left(\frac{\omega}{c}\right)^4 \frac{|\alpha|^2}{6\pi} \tag{4.16}$$

$$\sigma_{\text{abs}} = -\frac{\omega}{c}\alpha''. \tag{4.17}$$

As an aside, these two equations can be applied to quasistatic non-spherical nanoparticles. The negative sign taken in Eq. 4.17 is chosen due to the $\varepsilon = \varepsilon' + i\varepsilon''$ convention used in this thesis. It can be seen from these equations that the larger the imaginary

part of the polarizability of a nanoparticle, the larger the absorption cross-section will be. By the use of Eq. 4.8, an explicit expression for $\alpha''$ for nanospheres is,

$$\alpha'' = \frac{-\varepsilon''\varepsilon_m}{\varepsilon'^2 + \varepsilon''^2 + 4\varepsilon_m(\varepsilon' + \varepsilon_m)}. \tag{4.18}$$

This quantity is maximised for $\varepsilon' \to -2$, and $\varepsilon'' \to 0$, as illustrated in Fig. 4.4 where $\ln|\alpha''|$ has been plotted.

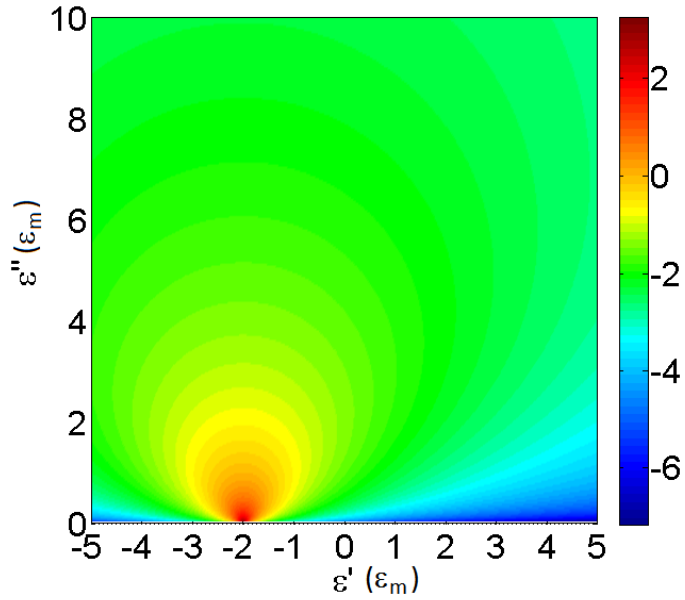


**Figure 4.4:** The natural logarithm of $\alpha''$ as a function of $\varepsilon'$ and $\varepsilon''$ in units of $\varepsilon_m$.

A more useful quantity in the measurement of absorption in preference to absorption cross-section is the absorption efficiency of a nanoparticle, defined by $Q_{abs} = \sigma_{\text{abs}}/\pi R^2$, where $R$ is the radius of the nanoparticle presented to the incident field. By Eq. 4.17, it is feasible that this quantity may exceed unity for a sufficiently large value of $\alpha''$. Under this circumstance, the particle will absorb more flux than strikes it geometrically, implying that the nanoparticle acts as a 'magnet for light', providing a facility for near-field enhancement around the nanoparticle: a prime indicator of a particle mode.[147]

### 4.3.4 Mie theory

Whereas quasistatic scattering theory helps provide physical insight for how one might expect a particle mode to manifest itself on an absorption efficiency spectrum, an exact scattering theory is needed in order to evaluate the accuracy of the Clausius-Mossotti

condition; Mie theory[148] provides the solution to this problem. Mie theory is an exact, steady-state scattering theory for spheres. By solving Maxwell's equations across the boundary of an isotropic nanoparticle in spherical co-ordinates with application of the vector spherical harmonics $\boldsymbol{M}$ and $\boldsymbol{N}$ for an x-polarised plane wave (with electric field amplitude $E_0$) incident on the sphere along the z-axis, the following vector equations for the scattered electric and magnetic fields are obtained,[65,148]

$$\boldsymbol{E}_s = E_0 \sum_{n=1}^{\infty} \frac{i^n(2n+1)}{n(n+1)} \left( i a_n \boldsymbol{N}_{e1n}^{(3)} - b_n \boldsymbol{M}_{o1n}^{(3)} \right) \tag{4.19}$$

$$\boldsymbol{H}_s = \frac{k}{\omega\mu} E_0 \sum_{n=1}^{\infty} \frac{i^n(2n+1)}{n(n+1)} \left( i b_n \boldsymbol{N}_{o1n}^{(3)} + a_n \boldsymbol{M}_{e1n}^{(3)} \right), \tag{4.20}$$

where $a_n$ and $b_n$ are the Mie a and b coefficients respectively, for mode $n$. Expressions for these coefficients are well known, and can be written as,

$$a_n = \frac{m\psi_n(mx)\psi_n'(x) - \psi_n(x)\psi_n'(mx)}{m\psi_n(mx)\xi_n'(x) - \xi_n(x)\psi_n'(mx)} \tag{4.21}$$

$$b_n = \frac{\psi_n(mx)\psi_n'(x) - m\psi_n(x)\psi_n'(mx)}{\psi_n(mx)\xi_n'(x) - m\xi_n(x)\psi_n'(mx)}. \tag{4.22}$$

where $\psi_n$ and $\xi_n$ are the Riccati-Bessel functions, $m$ is the ratio of the refractive index of the sphere to the medium, and $x = kR$ is the size parameter, where $k = 2\pi/\lambda$ is the wavenumber of the incident field. The expressions above for the scattered fields are used to calculate the scattered Poynting vector, $\boldsymbol{S}_s = 1/2\mathbb{R}\mathrm{e}(\boldsymbol{E}_s \times \boldsymbol{H}_s^*)$, which when integrated over all solid angles gives the averaged scattered power. This quantity (when normalised) is equivalent to the scattering efficiency of the nanosphere,

$$Q_{sca} = \frac{2}{x^2} \sum_{n=1}^{\infty} (2n+1) \left( |a_n|^2 + |b_n|^2 \right). \tag{4.23}$$

Adopting a similar procedure for the extinction Poynting vector (defined as $\boldsymbol{S}_{ext} = 1/2\mathbb{R}\mathrm{e}\{\boldsymbol{E}_i \times \boldsymbol{H}_s + \boldsymbol{E}_s \times \boldsymbol{H}_i^*\}$), the following expression for the extinction efficiency of the nanosphere is obtained,

$$Q_{ext} = \frac{2}{x^2} \sum_{n=1}^{\infty} (2n+1) \mathbb{R}\mathrm{e}(a_n + b_n). \tag{4.24}$$

These expressions for scattering and extinction efficiency are used to find the nanoparticle absorption efficiency *via*, $Q_{abs} = Q_{ext} - Q_{sca}$.

### 4.3.5 Nanosphere PEPs vs. PPPs

Now that a theoretical framework has been established to determine the resonant energies and scattering efficiencies of nanospheres, accurate absorption spectra can be calculated and analysed for nanospheres. The excitonic material of particular interest in this chapter is TDBC:PVA, and in this section, the optical properties of TDBC:PVA nanospheres are compared against nanospheres of gold, silver and aluminium, each of which can exhibit PPP modes. The TDBC:PVA films considered in Ch. 3 were fabricated by a spin-coat procedure; as a direct consequence of this process, the aggregate dipole moments are constrained to lie in the plane of the film (herein referred to as the 'planar distribution'). Therefore, if a nanoparticle were to be constructed directly from this material, the nanoparticle would not be isotropic, as illustrated in Fig. 4.5a. While the Mie absorption efficiency for this nanosphere in the forward

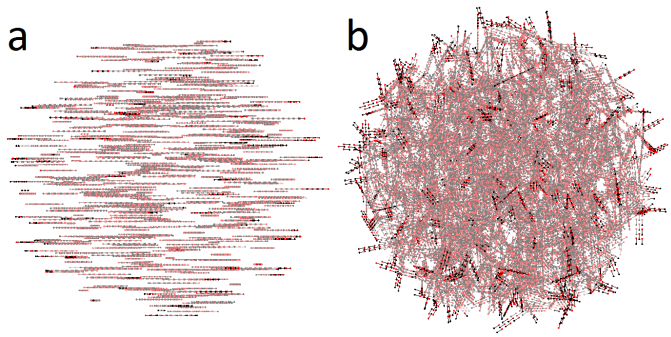


**Figure 4.5:** Graphical representations of PVA nanospheres doped with TDBC aggregates to a concentration of (a) 1.46 *wt%* in the planar distribution and (b) 3.22 *wt%* in the volume distribution.

direction (with the incident field in the plane in which the aggregates are distributed) is equivalent to the (orientationally-averaged) Mie absorption efficiency given by Eq. 4.23 & 4.24 for the isotropic nanosphere, the electric field distributions around these two nanospheres differ from each other. Given that electric field plots around excitonic nanospheres are needed in order to analyse the existence of PEP modes, to simplify the theoretical treatment, isotropic excitonic nanospheres are sought. In this section therefore, a volume distribution of randomly-orientated aggregates within the nanoparticle is considered, as illustrated in Fig. 4.5b (herein referred to as the 'volume distribution').

The volume distribution of aggregates weakens the magnitude of the effective aggregate dipole moment (as derived in App. B.1); this causes significant spectral changes in the permittivity (as shown in Ch. 2) and hence changes in the optical properties of the nanoparticle. Therefore, for the sake of consistency, the same lineshape of $\varepsilon$ for an isotropic nanoparticle is sought as for the 1.46 *wt%* TDBC:PVA film studied in Ch. 1-3. This lineshape can be achieved to a good approximation by increasing

the concentration of the dye to 3.22 *wt%* (see discussion around Fig. 2.6 for further details). By this treatment, the absorption efficiency spectrum calculated for a 3.22 *wt%* TDBC:PVA nanoparticle with a volume distribution of aggregates is very similar to that of the forward absorption efficiency spectrum for a 1.46 *wt%* TDBC:PVA nanoparticle with a planar distribution of aggregates, provided that the illumination of the latter is such that the incident electric field lies parallel to the plane in which the aggregates are distributed. Therefore, PEP modes can be inferred for nanoparticles with a planar distribution of aggregates from evidence for PEP modes in nanoparticles with a volume distribution of aggregates.

From this point on in this thesis, TDBC aggregates are assumed to be in the volume distribution inside the host nanoparticle and modelled using the four-level quantum model, unless otherwise stated.

Absorption efficiency spectra calculated using Mie theory for nanospheres of gold, silver, aluminium and 3.22 *wt%* TDBC:PVA each with diameter $d = 100$ *nm* are displayed in Fig. 4.6. From this figure, the accuracy of the values for the resonant energies predicted in Tab. 4.1 can be evaluated: in Fig. 4.6, the absorption peaks (corresponding to the dipole resonance) for gold, silver and 3.22 *wt%* TDBC:PVA occur at 2.42 *eV*, 2.94 *eV* and 2.17 *eV* respectively, giving percentage errors of 9.9%, 2.7% and $< 0.10\%$ in relation to the values predicted by the CM condition; these values are indicated by crosses in the figure. The 100 *nm* diameter aluminium nanosphere exhibits its Mie resonance at 6.53 *eV* in a medium of $n_m = 1.5$, giving an error of 19 %. This resonance corresponds to a wavelength of $\lambda = 190$ *nm*, in the far ultraviolet, and

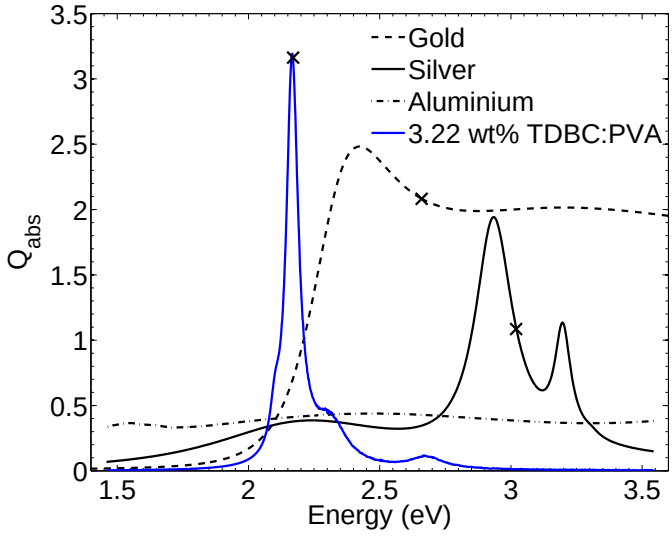


**Figure 4.6:** Mie absorption efficiency spectra for 100 *nm* diameter nanospheres of silver (black), gold (dashed), 3.22 *wt%* TDBC:PVA (blue), and aluminium (dash-dot). The medium index for silver and aluminium is $n_m = 1.5$; the others vacuum. The resonant energies determined from the CM condition are indicated by black crosses on each curve.

this spectral region is not examined in this thesis.

Of the four nanospheres in Fig. 4.6, it is the TDBC:PVA nanosphere which exhibits the largest peak value of $Q_{abs}$ (3.19), exceeding the peak value for both the gold (2.48) and the silver (1.94) nanospheres. The TDBC:PVA nanosphere is also the nanosphere for which the CM condition is the most accurate. Altogether, these Mie calculations demonstrate that the CM condition is only approximately true, especially when $\varepsilon''$ is large, as in the case of gold. For gold in particular, both $\varepsilon'$ and $\varepsilon''$ increase with photon energy in the range $2.0\ eV < E < 2.6\ eV$, and this shifts the value of the peak absorption to longer wavelengths than predicted. Another factor pushing the resonance off the quasistatic value is that the incident electric field strength varies over the nanoparticle due to retardation: this gives rise to dynamic depolarization and radiative damping[149], both of which are accounted for within Mie theory, but are not included in the quasistatic theory. These effects can be included in the quasistatic theory by a first-order correction to the polarizability,[149] giving what is known as the 'modified long-wavelength approximation'. However, for small nanosphere diameters, the resonant energies from Mie theory tend towards those given from the quasistatic theory. With this constraint in mind, Eq. 4.8 is used to determine the spectral locations of the resonances as an ancillary to Mie theory.

In spite of the peak in the Mie absorption efficiency curve for the TDBC:PVA nanosphere being the narrowest of the curves shown, the peak is sufficiently broad to obscure the ENZ mode at $E = 2.223\ eV$, where $\varepsilon = 0.64i$. The absorption efficiency at this energy does not exceed unity ($Q_{abs} = 0.78$). Therefore, the prediction in Sec. 4.3.2 stating that particle ENZ modes might show similarity to PEP modes is proved to be false in terms of strong absorption in this case.

The Mie absorption efficiency peak corresponding to the PPP mode for the gold nanosphere in Fig. 4.6 is relatively broad in comparison to both the peak for the PEP mode for the 3.22 *wt%* TDBC:PVA nanosphere and the peak for the PPP mode for the silver nanosphere. The quality (Q) factor for the gold (dipole) PPP mode in air is 6.75, in comparison to 67.7 for the TDBC PEP mode in air and 9.96 for the silver (dipole) PPP mode at 2.95 $eV$ in $n_m = 1.5$ (the other peak at 3.20 $eV$ in the silver absorption efficiency spectrum is the quadrupole PPP mode). These differences in Q-factor arise from the behaviour of the derivative $d\varepsilon'/d\omega$ in the region where $\varepsilon'$ crosses the resonance condition: the smaller the value of the derivative, the broader the resonance will be, leading to a lower Q-factor. For gold and silver, this derivative is approximately constant in comparison to the derivative for the TDBC. A high Q-factor is of interest in applications such as biosensing[150], due to the tunability with the host medium this offers (by Eq. 4.8); this is seen best for silver. From inspection of the lineshape of $\varepsilon'$ for TDBC:PVA in Fig. 2.8, this implies that the quality factor associated with the TDBC:PVA PEP mode would depend on the refractive index of the surrounding medium, provided that $\min(\varepsilon') < -2\varepsilon_m$. This condition places a restriction on the range of wavelengths for which the resonance can be tuned with a change in the host medium, and demands a high concentration of dye for this tunability to be accessible. This range is determined from Fig. 2.8 as $2.11\ eV < E < 2.24\ eV$ ($558\ nm < \lambda < 587\ nm$) for a concentration of 3.22 *wt%* (volume distribution).

As previously stated, an absorption efficiency above unity implies that the nanosphere absorbs more light than strikes it. This apparent paradox is resolved by plotting lines of power flow in the vicinity of the nanosphere. In Fig. 4.7, streamlines of power flow around a 3.22 *wt%* TDBC:PVA nanosphere are plotted on (a & c) and off (b & d) resonance for x-polarised light incident along the positive z-axis. The streamlines are calculated from the total Poynting vector $\boldsymbol{S} = \boldsymbol{S}_s + \boldsymbol{S}_{ext} + \boldsymbol{S}_i$. On resonance at 2.16 $eV$ (where $Q_{abs} = 3.39$), the nanoparticle acts akin to a magnet for light in the y-z plane, as seen in Fig. 4.7a: here, the streamlines for power flow bend towards the nanoparticle for up to approximately 1.5 times the particle radius. This is in contrast to the off-resonance case in Fig. 4.7b at 2.12 $eV$, where $Q_{abs} = 0.8$. Here, the field lines do not bend nearly as much towards the nanoparticle and instead the lines which are absorbed are largely those which strike it geometrically. Examining the power

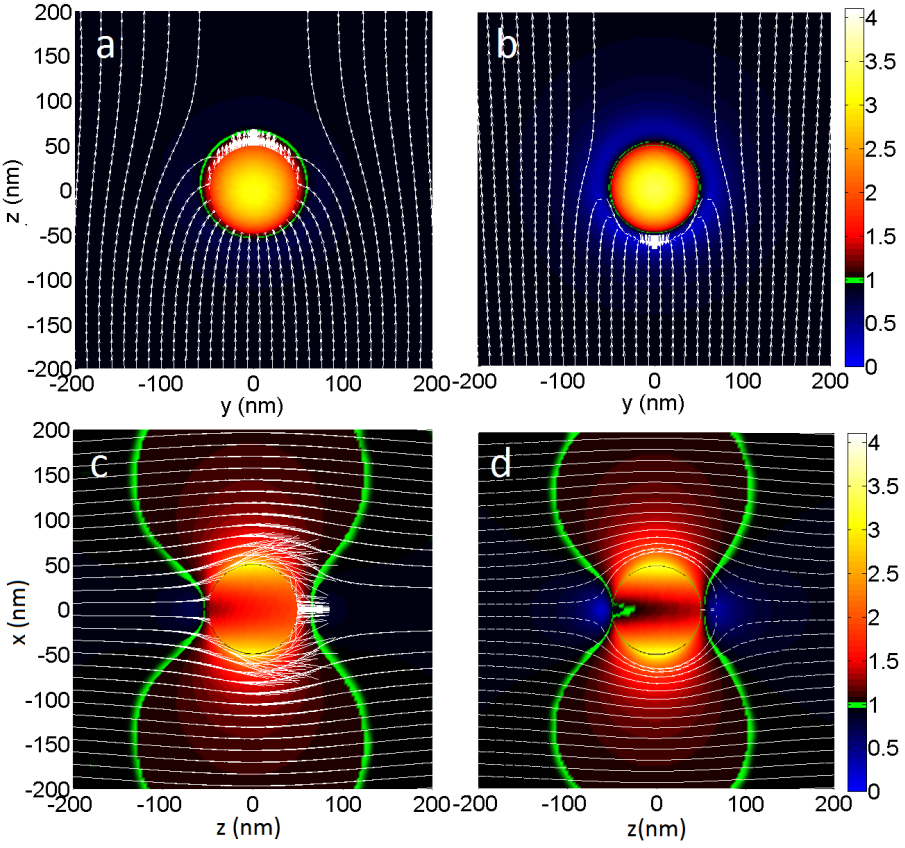


**Figure 4.7:** Colour plot: time-averaged $|\boldsymbol{E}|/E_0$ in the vicinity and on the surface of the 100 *nm* 3.22 *wt%* TDBC:PVA nanosphere on resonance (left hand plots) and off resonance (right hand plots). Streamlines: power flow, with incident light along the positive z-axis. The incident photon energies are (a & c) 2.16 $eV \equiv 574$ *nm* and (b & d) 2.12 $eV \equiv 586$ *nm*. The region within which $|\boldsymbol{E}|/E_0 > 1$ is bounded by a green line.

flow for these two cases in the x-z plane in Fig. 4.7c & 4.7d, it can be seen that less incident light flows past the nanoparticle on-resonance (Fig. 4.7c), leading to a higher absorption efficiency, and *vice versa* off-resonance (Fig. 4.7d).

The colour plots in Fig. 4.7 indicate the time-averaged electric field strength on the nanoparticle surface and in the surrounding space of the nanoparticle, normalised to the incident field strength. At both photon energies shown, there is a region of space within which the field is enhanced, the shape of which follows the two-lobed shape, as expected from the theory based on the point dipole approximation outlined in Sec. 4.3.2. The plots in Fig. 4.7 from Mie theory demonstrate that the dipole mode is the dominant mode of the nanoparticle, as assumed within the quasistatic theory. The plots at the two different energies appear to be only subtly different from each other however, and electric field enhancement is not observed over all solid angles off resonance as is the case on resonance. Therein lies the important difference: Fig. 4.7a shows that this region is circular and outside the nanoparticle equator on resonance as predicted. The regions of electric field enhancement around the nanoparticle off resonance arise from scattering of the electric field at this energy.

Altogether, the two crucial properties of (1) electric field enhancement over all solid angles and (2) strong absorption are only present for the nanoparticle on-resonance. Therefore, a PEP mode is demonstrated at a photon energy of 2.16 *eV* (574 *nm*) for a $d = 100$ *nm* nanosphere of 3.22 *wt%* TDBC:PVA in vacuum, with a stronger peak absorption and higher quality factor than either that of gold, or (in a $n_m = 1.5$ medium) silver or aluminium.

The reliability of these results is now discussed. To help evaluate the accuracy

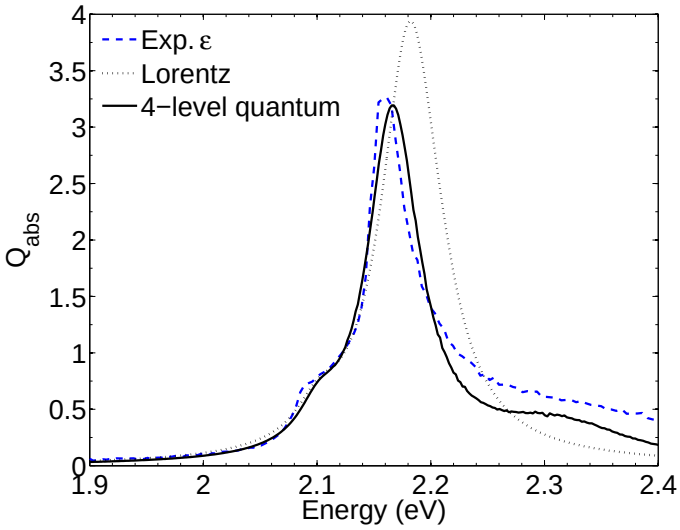


**Figure 4.8:** Mie absorption efficiency spectra for a 100 *nm* diameter 1.46 *wt%* (planar distribution) TDBC:PVA nanosphere in vacuum using $\varepsilon$ from: experiment (dashed line); a best-fit Lorentz oscillator model (dotted line); the four-level quantum model (black line).

of the Mie theory results, Mie absorption efficiency spectra are calculated using the experimentally-determined values of the permittivity for the 70 *nm* 1.46 *wt%* TDBC:PVA film produced *via* spin-coating, as outlined in Ch. 1, and contrasted against the same calculations made using two different theoretical models for the permittivity of TDBC aggregates in the planar distribution. The theoretical models for the permittivity are the four-level quantum model and the single oscillator Lorentz model. The Mie absorption efficiency spectra are plotted in Fig. 4.8, and these spectra are interpreted such that they represent absorption efficiency in the forward direction, as would be obtained in an experiment for a 100 *nm* diameter PVA nanosphere doped with a planar distribution of TDBC aggregates to a concentration of 1.46 *wt%*. In Fig. 4.8, it can be seen that the four-level quantum model for permittivity provides a much closer fit to $Q_{abs}$ calculated using the experimentally-determined values of the permittivity than the Lorentz oscillator model does. This demonstrates that (despite apparent similarities) small differences in the lineshape of $\varepsilon$ between the Lorentz model and the quantum model lead to substantial differences in $Q_{abs}$ in the photon energy range $2.15\ eV < E < 2.25\ eV$. More importantly, the absorption efficiency for each of the three spectra exceeds unity by a factor of three: given that the permittivity of 1.46 *wt%* TDBC:PVA in the planar distribution is very similar to that of 3.22 *wt%* TDBC:PVA in the volume distribution, these calculations provide evidence of PEP modes for both 1.46 *wt%* TDBC:PVA nanospheres with a planar distribution of aggregates (with illumination in the appropriate direction), and for 3.22 *wt%* TDBC:PVA nanospheres with a volume distribution of aggregates.

Given that in Fig. 4.8 the four-level quantum model for permittivity yields a closer fit to the absorption efficiency spectrum predicted by experimental values, and that the parameters used in the Lorentz model are the best fit parameters to $\varepsilon$, evidence is presented such that the quantum model is both a more realistic and more accurate model. This suggests that the assertions made within this section regarding evidence for PEP modes in TDBC:PVA nanospheres can be relied upon. In addition, this indicates that the use of a forced damped harmonic oscillator to model the permittivity of a quantum ensemble is indeed an approximation only, and Lorentz's doubts about his model[118] are justified. By no means is the quantum model as used here perfect: the high-energy tail in the curve using experimental values is not replicated in its entirety by the quantum model, in spite of the contribution from the $|0\rangle \rightarrow |3\rangle$ aggregate transition at 2.31 $eV$. In addition, given that the tail borne from the experimental data appears to be non-Lorentzian, this could demonstrate that the held assumption that aggregates are non-interacting is not entirely accurate: further research could help to shed light on this question, either by further experimentation on films, or by re-evaluation of the Hamiltonian used.

### 4.3.6 PEP tunability with dye concentration

The PEP mode in TDBC:PVA nanospheres can be tuned by adjustment not only of the host medium index, but also by the molecular concentration, as indicated through the

dependency on oscillator strength ($f$) in Eq. 4.10. As stated in the discussion around Eq. 4.10, the resonant frequency is always on the high-energy side of the transition $\omega_0$ ($\omega_{01}$ in the quantum model). This translates as $E > 2.11\ eV$ ($\lambda < 588\ nm$) for the resonant energy of the PEP mode for TDBC:PVA nanospheres with arbitrary molecular concentration. In reality, the range of resonant energies might be restricted by the presence of the next exciton transition, at $\hbar\omega_3 = 2.31\ eV$ in TDBC aggregates (see Sec. 2.3.4.2).

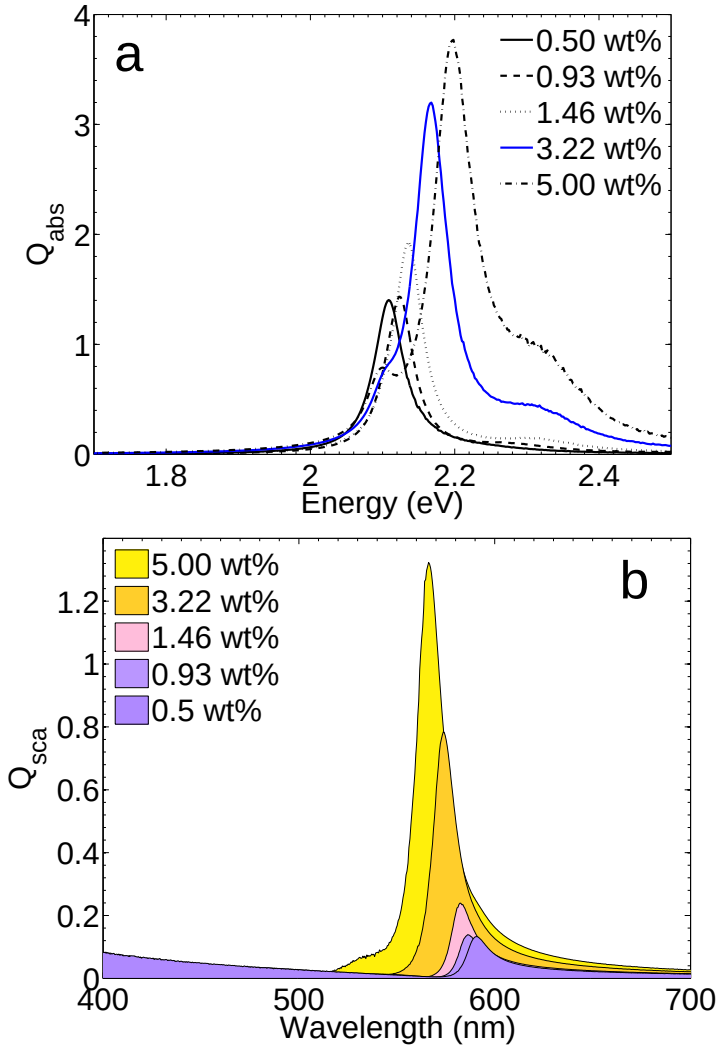


**Figure 4.9:** (a) Mie absorption efficiency spectra against photon energy, and (b) Mie scattering efficiency spectra wavelength for 100 *nm* diameter TDBC:PVA nanospheres in vacuum, for five dye concentrations. The calculated colours are shown underneath the curves in (b).

To test these predictions, Mie absorption efficiency spectra calculated for a set of five 100 *nm* diameter TDBC:PVA nanospheres with dye concentrations in the range 0.5 *wt%* − 5.0 *wt%* (volume distribution) are plotted in Fig. 4.9a, where the four-level quantum model has been used for the permittivity of each, and the assumption has been made that the damping and dephasing processes considered in Ch. 2 are concentration independent. The corresponding scattering efficiencies ($Q_{sca}$) for the same nanoparticles are plotted in Fig. 4.9b as functions of wavelength, together with their respective apparent colours for these nanoparticles assuming that $Q_{sca}$ spectra can be used as proxy for reflectance spectra. From these figures, the resonant energy is seen to blueshift from 2.12 $eV \rightarrow$ 2.20 $eV$ (585 $nm \rightarrow$ 564 $nm$) as the concentration is increased through the range considered. In addition, the apparent colour changes from a purple for low concentrations (0.5 *wt%* − 0.93 *wt%*) through pinkish (1.46 *wt%*), orange (3.22 *wt%*), and finally to yellow (5.00 *wt%*). The Q-factor in absorption efficiency visibly increases with concentration due to an increase in the value of the derivative $d\varepsilon'/d\omega$ with concentration. At first glance, the orange colour observed from thin films with a planar distribution of aggregates with 1.46 *wt%* concentration (*cf.* Fig. 3.11) is recovered for nanospheres with a volume distribution of aggregates for 3.22 *wt%* concentration; but this is simply a matter of coincidence. In fact, the colour calculated for the 3.22 *wt%* nanosphere is more yellow than the 70 *nm* 1.46 *wt%* film, owing to the strength of the PEP mode at 2.17 $eV$ (572 $nm$).

| **Concentration** ($wt\%$) | **Res. Energy** ($eV$) | **max**($Q_{abs}$) | **Q-factor** |
|---|---|---|---|
| 0.50 | 2.11 | 1.40 | 28.1 |
| 0.93 | 2.12 | 1.43 | 29.9 |
| 1.46 | 2.14 | 1.94 | 38.7 |
| 3.22 | 2.17 | 3.20 | 56.1 |
| 5.00 | 2.20 | 3.77 | 53.9 |

**Table 4.2:** Resonant energies, absorption efficiency maxima and associated Q-factors for 100 *nm* diameter TDBC:PVA nanospheres in vacuum for a range of dye concentrations (volume distribution).

The Q-factors and peak values of absorption efficiency shown in Fig. 4.9 are tabulated in Tab. 4.2. From this table are drawn two immediate observations:

1. The highest quality factor in $Q_{abs}$ (56.1) occurs for a concentration of 3.22 *wt%*, for which the permittivity is equal to $\varepsilon = -2.02 + 1.68i$ (*cf.* Fig. 2.8), fulfilling the CM condition to within 1%.

2. The highest peak in $Q_{abs}$ occurs for a concentration of 5.00 *wt%*. Here, the permittivity is equal to $\varepsilon = -2.59 + 1.52i$, a value 30% away from the CM condition.

The first of these two observations is explained by a difference in the value of the derivative $d\varepsilon'/d\omega$ in the region of each resonance: these derivative values are 65.5 and 56.7 for the 3.22 *wt%* and 5.00 *wt%* nanospheres respectively. In the case of the 5.00 *wt%* nanosphere, the derivative around the resonance is modified by the presence of the exciton transition $\hbar\omega_3 = 2.31\ eV$; this leads to a broader peak for the 5.00 *wt%*

nanosphere, and a smaller Q-factor. The second of these observations is explained by the relatively weaker value of $\varepsilon''$ at the resonant energy for the 5.00 *wt%* nanosphere. Given that $\varepsilon''$ controls the loss within the material, a smaller value of $\varepsilon''$ leads to a larger peak value in absorption.

The evidence for PEP modes hosted by each of the five nanospheres in Fig. 4.9 is now investigated in turn. For each of the nanospheres, the scattering efficiency in Fig. 4.9b appears to follow Rayleigh scattering[151] for wavelengths shorter than about 500 *nm*, as indicated by the rising tails for short wavelengths. Given the relatively small amount of scattering and absorption present around the exciton transition energies for the 0.5 *wt%* TDBC:PVA nanosphere, the scattering is dominated by Rayleigh scattering, leading to a purple colour from scattering in this case. The absorption efficiency for the 0.5 *wt%* TDBC:PVA nanosphere does exceed unity, a prime indicator of a PEP mode; but the real part of the permittivity for this material is not negative for any visible frequency. Given that a negative real permittivity is a requirement for a PEP mode (*via* the CM condition), this particular nanosphere cannot host a PEP mode at visible frequencies. The resolution to this apparent paradox is that at a photon energy of 2.11 *eV*, the permittivity of the material in the nanosphere is close to zero ($\varepsilon = 0.21 + 2.54i$), leading to an ENZ particle mode in this region of the spectrum. The electric field enhancement and power flow around the nanoparticle on this mode is illustrated in Fig. 4.10. Here it is shown that the $\zeta = 1$ isosurface is that of a doughnut

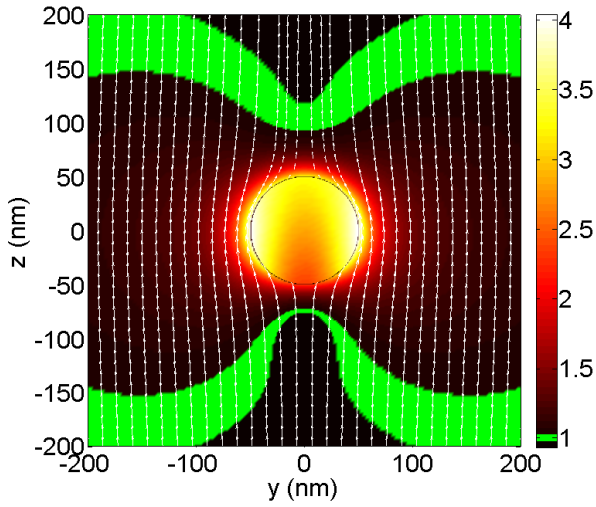


**Figure 4.10:** Power flow (streamlines) and electric field strength (colour plot) around a $d = 100$ *nm* 0.5 *wt%* (volume distribution) TDBC:PVA nanosphere in vacuum at 2.11 *eV*. The $\zeta = 1$ isosurface is demarcated in green.

as predicted (*cf.* Fig. 4.3), and that electric field enhancement occurs over all solid angles - in this case to a greater extent than for the PEP mode (*cf.* Fig. 4.7a). Therefore, the prediction in Sec. 4.3.2 that ENZ modes might show similarity to PEP modes by way of strong absorption and electric field enhancement over the nanoparticle is demonstrated in this case. However, in contrast to Fig. 4.3, this ENZ mode occurs

in spite of a relatively high value of $\varepsilon''$. It is possible that the small positive value of $\varepsilon'$ at this energy has modified the ENZ resonant condition to enable the ENZ mode properties to be manifested. Performing Fresnel calculations for $R$ and $T$ across a plane boundary for $\varepsilon = 0.21 + 2.54i$ reveals that $R \approx 0.2$ and $T \approx 0.8$ (*cf.* Fig. 1.1). This value of $T$ ($R$) is significantly higher (lower) than the same coefficients for a material with $\varepsilon = -2 + \varepsilon'' i$, for any value of $\varepsilon''$ (again, *cf.* Fig. 1.1). These elementary calculations demonstrate that a nanoparticle of ENZ material permits greater transmittance of the field through the nanoparticle, which in turn results in a lower absorption efficiency than for a PEP mode on resonance. This greater transparency to the incident field is confirmed through the relative prevalence of the streamlines of power flow passing through the nanoparticle in Fig. 4.10 in comparison to the equivalent plots for which the PEP mode is excited (Fig. 4.7a), or the loss is much greater (Fig. 4.7b).

A similar ENZ mode is encountered for the 0.93 *wt%* TDBC:PVA nanosphere at 2.12 *eV* in Fig. 4.9, where $\varepsilon = 0.17 + 2.59i$: this results in a similar purple colour in scattering.

For the 1.46 *wt%* TDBC:PVA nanosphere in Fig. 4.9, the minimum in $\varepsilon'$ is equal to $-0.85$, a value insufficiently negative to satisfy the CM condition in vacuum. However, this negative value of $\varepsilon'$ leads to some metal-like optical properties which begin to dominate the response. In this case, the observed colour from the scattering spectrum is pink, rather than purple as in the previous two examples, as Rayleigh scattering begins to be overcome by the increasing oscillator strength borne from the increase in the transition dipole moments due to a rise in dye concentration. This fairly modest peak in scattering is however dwarfed next to the scattering curve for the 3.22 *wt%* TDBC:PVA nanosphere in Fig. 4.9b, for which an orange colour is apparent. This dramatic colour change results from the large absorption peak arising from a value of $\varepsilon = -2.02 + 1.68i$ for the permittivity at 2.168 *eV* (572 *nm*). This value of the permittivity satisfies the CM condition: therefore, a PEP mode can be hosted by a nanosphere with this concentration of dye. Similarly, evidence is presented for a PEP mode in the 5.00 *wt%* TDBC:PVA nanosphere, where the permittivity is equal to $\varepsilon = -2.39 + 1.37i$ at 2.20 *eV* (564 *nm*).

## 4.4 Nanospheroids

Now that evidence for PEP modes has been presented for excitonic nanospheres in a theoretical framework, the next step is to perform an experiment to observe such modes directly. However, the fabrication of perfect nanospheres is difficult; nanospheroids are easier to produce. Nanospheroids exhibit different physics to that of nanospheres and therefore, scattering and absorption calculations for nanospheroids must be made in order to evaluate experimental results from nanospheroids. Therefore, this section begins by defining nanospheroids mathematically, and by considering two scattering theories for nanospheroids. Scattering and absorption calculations are then made from which the evidence for PEP modes in TDBC:PVA nanospheroids is evaluated

when compared against experimental data. Lastly, the polarisation dependency of the transmission of light through nanospheroids is studied, the findings of which may be utilised in a future investigation.

### 4.4.1 Definition of a spheroid

Mathematically, nanospheroids are related to nanospheres by a distortion along one axis: this distortion leads to two classes of nanospheroid - oblate and prolate - for which a cross-section across the axis of distortion gives a circle larger and smaller than the average radius respectively. In layman's terms, oblate spheroids are 'squashed' spheres, and range from spheres to 'pancakes' or (in the extreme case) 'discs'. Prolate spheroids are 'stretched' sphere, and range from spheres to 'rugby balls' (or 'cigars'), to (in the extreme case) 'needles'. Many planetary bodies are roughly oblate spheroids, including the Earth, and most notably Jupiter. These general shapes are illustrated in Fig. 4.11.

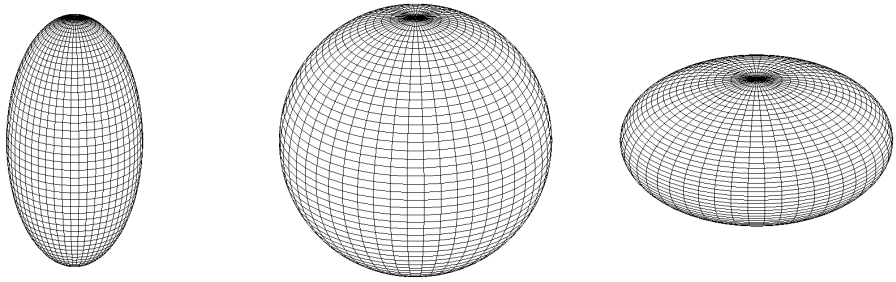

**Figure 4.11:** Illustrations of (from left to right), a prolate spheroid, a sphere, and an oblate spheroid.

In general mathematical terms, a spheroid is a special case of an ellipsoid, where an ellipsoid has three distinct semi-axes $a$, $b$ and $c$. The Cartesian equation for an ellipsoid is[152] (p.17),

$$\left(\frac{x}{a}\right)^2 + \left(\frac{y}{b}\right)^2 + \left(\frac{z}{c}\right)^2 = 1. \tag{4.25}$$

For the two spheroids in Fig. 4.11, the distortion axis was chosen to be the z-axis, leading to $a = b$ in the expression above. This general treatment allows one to choose the axis of distortion freely.

### 4.4.2 Nanospheroid resonance conditions

The polarizability of a nanospheroid is now examined. Given that nanospheroids are not triaxially symmetric, the polarizability tensor[153] is used *i.e.*,

$$\bar{\alpha} = \begin{pmatrix} \alpha_{xx} & \alpha_{xy} & \alpha_{xz} \\ \alpha_{yx} & \alpha_{yy} & \alpha_{yz} \\ \alpha_{zx} & \alpha_{zy} & \alpha_{zz} \end{pmatrix}. \tag{4.26}$$

This tensor is diagonal for a non-magnetic nanospheroid. It is convenient to prescribe that the orientation of the nanospheroid is such that the principle axes of the nanospheroid coincide with the co-ordinate axes. In this theoretical framework, expressions for the polarizability tensor elements along each axis (the diagonal elements) are[65,153] (p.145),

$$\alpha_{ii} = 3V \frac{\varepsilon - \varepsilon_m}{3\varepsilon_m + 3L_i(\varepsilon - \varepsilon_m)}, \tag{4.27}$$

where $L_i$ is the shape factor for axis $i$, where $i = \{x, y, z\}$. These expressions for $\alpha_{ii}$ can be used within the quasistatic formalism (Eq. 4.16 & 4.17) to obtain scattering and absorption cross-sections and efficiencies for illumination of the nanospheroid with an electric field parallel to the $i$ direction. An integral expression for $L_i$ is[65] (p.146),

$$L_i = \frac{abc}{2} \int_0^\infty \frac{dq}{(q + x_i^2)\sqrt{(q + a^2)(q + b^2)(q + c^2)}}, \tag{4.28}$$

where $x_i$ is the semi-axis in question. A constraint upon $L_i$ is such that $\sum L_i = 1$. For a sphere, symmetry arguments lead to $L_i = 1/3$, and Eq. 4.27 reduces to Eq. 4.8. In the extreme case where the spheroid becomes a needle, $L_z \to 0$ and $L_x = L_y \to 1/2$. In the other extreme, the spheroid becomes a disc and $L_z \to 1$ and $L_x = L_y \to 0$.

The full range of $L_x$, $L_y$ and $L_z$ for spheroids with a distortion along the z-axis is shown in Fig. 4.12. In this case, spheroids are prolate (oblate) for aspect ratios greater (less than) than unity. Included in the plot are three example nanoparticles with aspect ratios 1/3, 1 and 3, modelled as silver, in a medium of refractive index $n_m = 1.5$. The colours of the nanoparticles are calculated from the scattering spectra using Eq. 4.16 and the colour code in App. A.1, where illumination is such that the electric field is parallel to the long axes of each nanoparticle *i.e.* towards the side of the prolate nanospheroid and 'top down' towards the face of the oblate nanospheroid. The range of colour produced for a distortion in the silver nanoparticle demonstrates that the scattering properties of a silver nanoparticle are intimately linked with its shape. Indeed, the range of colours produced extends across the visible spectrum. This dependency of scattering properties on shape can be seen best by study of the resonance condition for each axis $i$ of nanospheroids; this can be found from the denominator of Eq. 4.27,

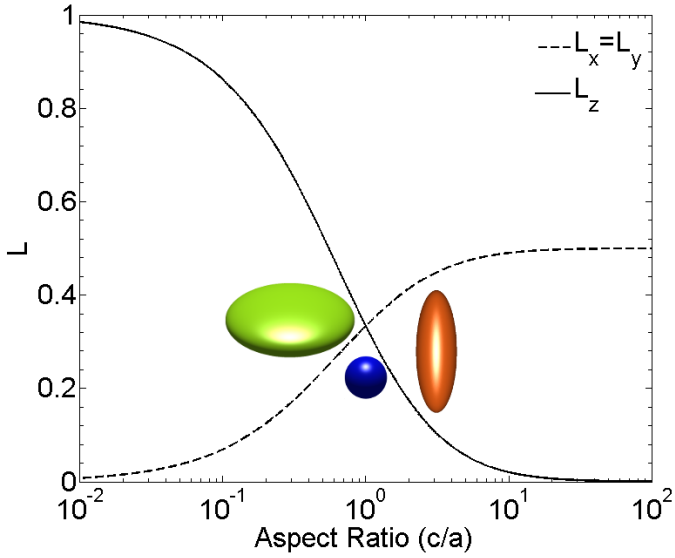


**Figure 4.12:** Spheroid shape factors as functions of aspect ratio, with distortion along the z-axis, with renderings of silver nanospheroids with aspect ratio (left to right) 1/3, 1 and 3.

$$\varepsilon + \left(\frac{1 - L_i}{L_i}\right)\varepsilon_m = 0. \tag{4.29}$$

This expression for nanospheroids is equivalent to that of the CM condition (Eq. 4.8) for nanospheres, and reduces to the CM condition for the spherical case ($L_x = L_y = L_z = 1/3$). By definition, two of the three shape factors are equal for spheroids. This leads to two distinct modes: a 'longitudinal' mode for which the incident electric field is parallel to the nanospheroid long axis, and a 'transverse' mode for which the incident light is perpendicular to the nanospheroid deformed axis. In Fig. 4.12, it is the longitudinal PPP modes which have been excited in the silver nanospheroids.

For oblate nanospheroids, the nanospheroid long axis is not uniquely defined. The longitudinal mode can be envisaged as an excitation distributed across the flatter faces of an oblate nanospheroid, or between the two ends of a prolate nanospheroid. In the extreme case of a needle, the ends of the prolate nanospheroid become infinitely small in comparison to the curved area of the nanoparticle, and the nanoparticle becomes like that of an infinitely long cylinder,[154] or equivalently, a flat surface. It is therefore expected that the resonance condition for the transverse mode of a prolate nanospheroid will approach that of a surface as the eccentricity is increased.

This hypothesis is now examined: the resonance conditions for both the transverse and longitudinal modes of nanospheroids are plotted in Fig. 4.13 as a function of aspect ratio. In the limiting case of a needle, the resonance conditions tend towards $\varepsilon_L = -\infty\ \varepsilon_m$ and $\varepsilon_T = -\varepsilon_m$ for the longitudinal and transverse modes respectively. The transverse mode therefore tends towards the same condition as for a bound surface

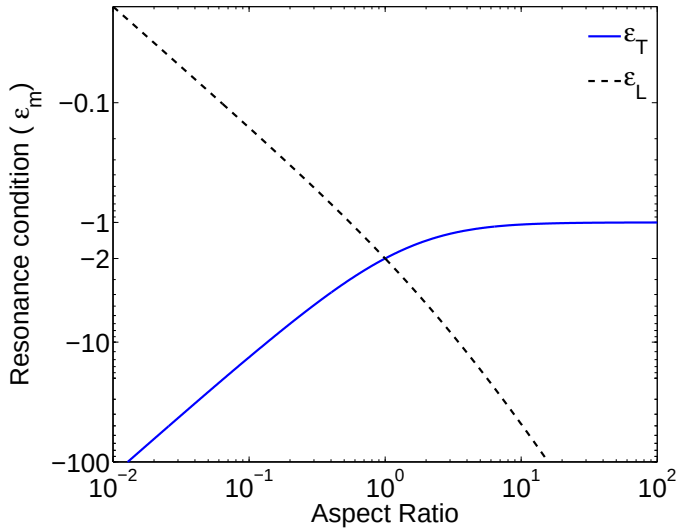


**Figure 4.13:** The longitudinal (black dashed line) and transverse (blue line) resonance conditions on the real part of the permittivity ($\varepsilon'$) for nanospheroids as a function of aspect ratio $c/a$, *i.e.* the ratio of the distorted to non-distorted axes.

mode (see Eq. 3.14) and is expected to dominate the prolate nanospheroid response for extreme distortion.

By a similar argument, the longitudinal mode is expected to dominate the oblate nanospheroid response, and the limiting condition on transverse modes for discs is equal to $\varepsilon_T = -\infty\ \varepsilon_m$ as expected, implying the mode becomes unreachable with a significant distortion of the nanospheroid. In contrast to the resonance condition for a planar surface, the longitudinal resonance condition tends towards $\varepsilon_L = 0$ for increasing eccentricity. This suggests that the ENZ and longitudinal modes can coincide as the nanoparticle approaches the geometry of a disc.

### 4.4.3 Nanospheroid forward scattering

In this section, theory is identified which allows one to probe the extinction efficiency of nanospheroids through experiment. It is assumed that identical nanospheroids have been fabricated in a square array with a pitch sufficiently large to ensure the interactions between adjacent nanospheroids are small. The transmittance through the array of nanospheroids is linked to the extinction efficiency of the individual nanospheroids. By quantifying this relationship, the extinction efficiency of nanospheroids can be determined experimentally from transmittance measurements.

Beginning with the transmitted electric field ($\boldsymbol{E}_t$) through a slab of thickness $d$ embedded with (identical) particles with volume number density $N$ gives the following

expression[65] (p.77 & p.112),

$$\boldsymbol{E}_t = E_i e^{ikx}\left(\exp\left[-\frac{2\pi N d}{k^2}S_2\right]\hat{\boldsymbol{x}} - \frac{2\pi N}{k^2}S_4\hat{\boldsymbol{y}}\right), \tag{4.30}$$

where the incident electric field $\boldsymbol{E}_i$ is x-polarised. $S_2$ and $S_4$ in Eq. 4.30 are elements of the amplitude scattering matrix[155] for any of the individual nanoparticles. The scattering matrix relates the angular components of the incident and scattered fields by the following (written in spherical polar co-ordinates),

$$\begin{pmatrix} E_{s\theta} \\ E_{s\phi} \end{pmatrix} = \frac{e^{ikr}}{r}\begin{pmatrix} S_1 & S_3 \\ S_4 & S_2 \end{pmatrix}\begin{pmatrix} E_{i\theta} \\ E_{i\phi} \end{pmatrix}, \tag{4.31}$$

where $\boldsymbol{E}_s = E_{s\theta}\hat{\boldsymbol{\theta}} + E_{s\phi}\hat{\boldsymbol{\phi}}$ is the scattered field. For non-scattering, non-absorbing nanoparticles, $S_i = 0$ and the transmitted field in Eq. 4.30 is given by $\boldsymbol{E}_t = \boldsymbol{E}_i$. In general, the electric field transmitted through the slab of nanoparticles is rotated if $S_4 \neq 0$: this leads to the following polarisation-dependency upon transmittance,

$$\begin{aligned}\boldsymbol{T} &= \left(\frac{|\boldsymbol{E}_t|}{E_i}\right)^2 \\ &= \left(\exp\left[-\frac{4\pi N d}{k^2}\mathbb{R}\mathrm{e}(S_2)\right]\hat{\boldsymbol{x}} + \left(\frac{2\pi N}{k^2}\right)^2 |S_4|^2\hat{\boldsymbol{y}}\right),\end{aligned} \tag{4.32}$$

where $\boldsymbol{T} = T_x\hat{\boldsymbol{x}} + T_y\hat{\boldsymbol{y}}$. For nanospheres, the amplitude scattering matrix is a multiple of the identity matrix,[156] and no rotation occurs. In this circumstance, the transmittance reduces (for unpolarised light) to,

$$T \approx \exp\left[-\frac{4\pi}{(\mu k)^2}\mathbb{R}\mathrm{e}(S_2)\right], \tag{4.33}$$

where the number density $N = 1/(\mu^2 d)$ has been used, with $\mu$ equal to the pitch of the nanoparticle array. The approximation symbol in Eq. 4.33 indicates the approximate nature of applying this expression to nanospheroids, where $S_4$ is non-zero. However, for nanospheres, this expression can be taken as exact. Eq. 4.33 can be re-arranged into the form,

$$\begin{aligned}T &= \exp[-NC_{ext}d] \\ &= \exp\left[-\frac{Q_{ext}\pi r^2}{\mu^2}\right],\end{aligned} \tag{4.34}$$

where $r$ is the geometrically-presented nanoparticle radius. This can be derived using either Mie theory or quasistatic theory. The same result can be derived by making the assumption that the Beer-Lambert law[157] applies, as shown in App. B.3. From Eq. 4.34, the extinction efficiency of a nanoparticle can be obtained through the formula,

$$Q_{ext} = -\frac{\mu}{\pi r^2} \ln |T|, \tag{4.35}$$

which can (for nanospheres) be compared against the value of $Q_{ext}$ obtainable through Mie theory, keeping in mind that the orientationally-averaged efficiency is identical to the forward efficiency for nanospheres. For nanospheroids, a modified version of Mie theory in spheroidal co-ordinates[158] can be used. However, a more convenient approach is to use a T-matrix method,[156, 159, 160] the details of which are beyond the scope of this thesis.

Unfortunately, a similar expression to Eq. 4.35 involving $Q_{sca}$ and reflectance ($R$) cannot be constructed. Therefore, in designing an experiment to investigate PEP modes, it is recommended that $Q_{sca}$ be minimised by manufacture of the smallest nanoparticles possible. In this way, $Q_{ext}$ approaches $Q_{abs}$ and PEP modes can be more easily investigated. Another advantage of small nanoparticles is that the quasistatic regime becomes approximately correct, leaving the system more open to elementary theoretical probing.

A theoretical expression for $\boldsymbol{T}$ can also be found for single nanospheroids in the quasistatic regime. The easiest theoretical framework is to assume that the nanospheroid lies at the origin and is illuminated with unpolarised light incident along the positive y-axis. This enables electric dipole modes to be established in the nanoparticle along the x and z axes. The potentials of these dipoles (in the point dipole approximation) written in spherical polar co-ordinates take the form,

$$\Phi_x = \frac{|\boldsymbol{p}_x| \cos\phi}{4\pi\varepsilon_0 r^2} \tag{4.36}$$

$$\Phi_z = \frac{|\boldsymbol{p}_z| \cos\theta}{4\pi\varepsilon_0 r^2}, \tag{4.37}$$

where $p_i = \alpha_{ii}\varepsilon_m E_i$. Using these potentials to compute the dipole electric field $\boldsymbol{E}_d = -\nabla\Phi$ (where the total electric potential is considered to be $\Phi = \Phi_x + \Phi_z$), the following expression can be derived for the normalised electric field intensity (transmittance) on the opposite side of the nanoparticle for a distance $y$ along the y-axis,

$$\boxed{\boldsymbol{T} = \left(\frac{|\alpha_{xx}|^2\beta^2}{y^6} - \frac{2\alpha'_{xx}\beta}{y^3} + 1\right)\hat{\boldsymbol{x}} + \left(\frac{|\alpha_{zz}|^2\beta^2}{y^6} - \frac{2\alpha'_{zz}\beta}{y^3} + 1\right)\hat{\boldsymbol{z}}}, \tag{4.38}$$

where $\beta = 1/4\pi\varepsilon_0$. A full derivation of this expression is outlined in App. B.4.

### 4.4.4 Nanospheroid results

In order to investigate the existence of these nanospheroidal modes, a set of nanospheroids were fabricated[161] composed of the same 1.46 *wt%* TDBC:PVA (planar distribution) as examined in Ch. 1-3. This set of nanospheroids were of constant height $h = 90$ *nm*, as illustrated in the schematic in Fig. 4.14. These nanospheroids were fabricated in square arrays of pitch $\mu = 750$ *nm*.

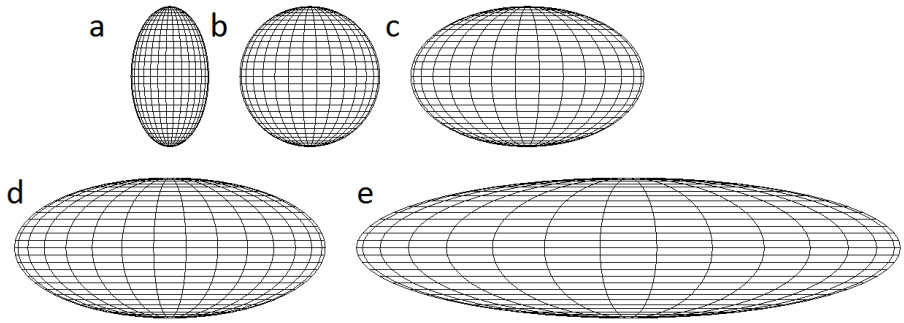


**Figure 4.14:** Illustrations of the four nanospheroid aspect ratios fabricated alongside a nanosphere (b). All nanoparticles shown have height 90 *nm*, and are arranged in ascending order of width, with widths (a-e) 50, 90, 150, 200 and 350 *nm* respectively.

As a consequence of the fabrication process, the nanospheroids were located on supporting cylinders, as illustrated by the SEM image in Fig. 4.15 (overleaf), resulting in a mushroom-like shape for each of the nanoparticles. The extent to which these supporting cylinders affect the resonances of the nanospheroids is a question for further research.

In the experimental setup, transmittance ($T$) measurements were taken through these arrays at normal incidence. The arrays were sat in a medium with refractive index $n_m = 1.46$. The expected longitudinal and transverse mode energies for these nanospheroids in this medium calculated with reference to Fig. 4.13 are tabulated in Tab. 4.3.

| $d$ (*nm*) | $\varepsilon_L$ | $\varepsilon_T$ | $E_L$ (*eV*) | $E_T$ (*eV*) |
|---|---|---|---|---|
| 50 | −8.82 | −3.16 | – | 2.12, 2.15 |
| 90 | −4.26 | −4.26 | 2.12, 2.14 | 2.12, 2.14 |
| 150 | −2.35 | −6.00 | 2.12, 2.16 | – |
| 200 | −1.70 | −7.47 | 2.12, 2.17 | – |
| 350 | −0.92 | −11.97 | 2.12, 2.19 | – |

**Table 4.3:** Tabulated resonance conditions and resonant energies for the longitudinal (subscript $L$) and transverse (subscript $T$) modes for 1.46 *wt%* (planar distribution) TDBC:PVA nanospheroids of diameter $d$, with height $h = 90$ *nm* in a $n_m = 1.46$ medium.

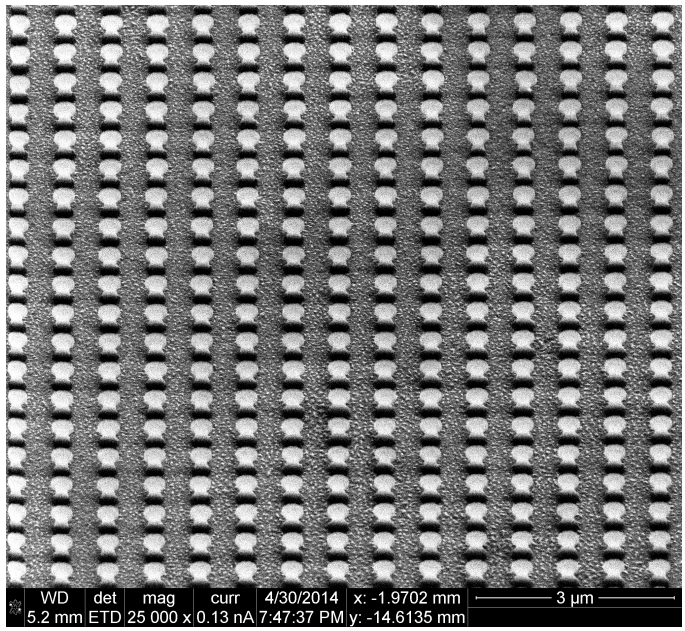


**Figure 4.15:** An SEM image of a square array of 1.46 *wt%* TDBC:PVA nanospheroids, with pitch $\mu = 750$ *nm*, height $h = 90$ *nm* and diameter $d = 350$ *nm*. The image is taken at an angle to the sample; measurements through the sample were taken at normal incidence. Image and sample fabrication credit: Sara Núñez-Sánchez.

Tab. 4.3 indicates that for this material, the longitudinal mode for the prolate nanospheroid and the transverse modes for the oblate nanospheroids are unreachable in this medium; this can be seen by the minimum value in the real part of the permittivity in Fig. 2.6, at $\varepsilon' = -4.81 (\equiv -2.26\varepsilon_m$, where $\varepsilon_m = 1.46^2$ in this case). This suggests that for nanospheroids of 1.46 *wt%* (planar distribution) TDBC:PVA in this medium, the range of aspect ratios for which both longitudinal and transverse modes can be excited is severely restricted, since the CM condition is only just satisfied for (undistorted) nanospheres. Another striking feature from Tab. 4.3 is that the range over which the resonant energies in the table can be shifted with a change in geometry is 0.05 *eV i.e.* $2.14\ eV < E < 2.19\ eV$ ($566\ nm < \lambda < 580\ nm$). This finding implies that although the spectral position of a PEP mode in a nanospheroid can be tuned with a change in aspect ratio, in this medium the tuning is not as substantial as the change achievable by a change in medium ($558\ nm < \lambda < 587\ nm$: see above). This shift is however comparable to the shift achievable for the PEP mode with a change in dye concentration ($572\ nm < \lambda < 564\ nm$). The other modes at $E = 2.12\ eV$ do not shift significantly with a change in geometry, and are not expected to be evident owing to the relatively high loss present at this photon energy.

Using an adapted version of the scattering code freely available from NASA[162] based on Waterman's T-matrix method,[159] the absorption efficiencies of 3.22 *wt%* (volume distribution) TDBC:PVA nanospheroids calculated using the same aspect ratios as

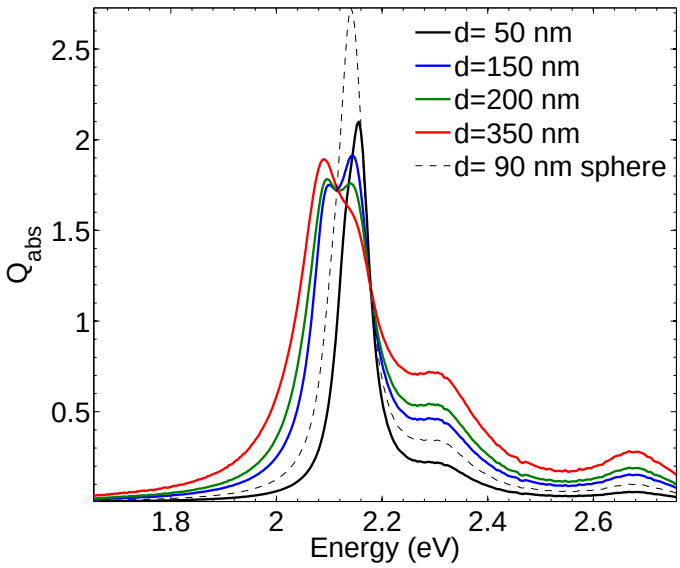


**Figure 4.16:** Mie absorption efficiency for four 3.22 *wt%* (volume distribution) TDBC:PVA nanospheroids (solid lines) of differing diameters ($d$), with height 90 *nm* in a $n_m = 1.46$ medium. $Q_{abs}$ for a 90 *nm* diameter nanosphere is shown for comparison.

tabulated in Tab. 4.3 are plotted in Fig. 4.16. The absorption efficiency for a $d = 90$ *nm* nanosphere is plotted alongside for comparison. Fig. 4.16 shows that in the region $2.14\ eV < E < 2.19\ eV$, the absorption efficiency exceeds unity, indicating transverse and longitudinal PEP modes for the prolate and oblate nanospheroids respectively. The other mode evidenced around 2.10 *eV* in Fig. 4.16 corresponds to a higher-order Mie mode arising from the large value of $\varepsilon'$ at this energy.

Experimental transmittance spectra (as measured by Sara Núñez-Sánchez) through square arrays of nanospheroids with pitch $\mu = 750$ *nm* are shown in Fig. 4.17 (overleaf), alongside forward scattering calculations for $T$ based on the T-matrix formalism (Eq. 4.33), normalised to the experimental data. The equivalent (non-normalised) results using the quasistatic approximation are plotted in Fig. 4.18: here, the calculations have been performed using the elements of $\bar{\alpha}$ in Eq. 4.17 for which the distortion axis of the nanoparticle is along the axis of observation.

From Fig. 4.17 & 4.18, the lineshapes obtained using the T-matrix formalism provide a closer fit to the experimental data than the lineshapes obtained using the quasistatic approach. This indicates that the quasistatic approach is insufficient to accurately describe scattering by nanospheres of these sizes at these wavelengths; particularly the broadening in the lineshape of the 350 *nm* diameter nanospheroid. Given that the quasistatic formalism relies upon the diameter of the nanoparticle being subwavelength, it is unsurprising that this theory begins to break down for nanoparticle sizes comparable with the wavelength of the light used. A question pertaining to the reliability of the experimental data might be raised, owing to the observation that the transmittance curve for the 200 *nm* oblate nanospheroid does not seem to cause as much of a dip in

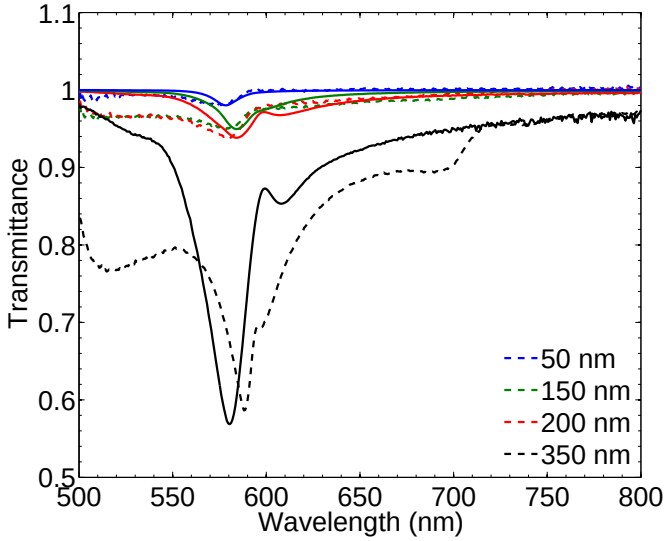


**Figure 4.17:** Theoretical (solid) and experimental (dashed, data credit: Sara Núñez-Sánchez) transmittance spectra for a square array of 1.46 *wt%* (planar distribution) TDBC:PVA nanospheroids with $h = 90$ *nm* and $\mu = 750$ *nm* in a $n_m = 1.46$ medium, using Waterman's T-matrix.

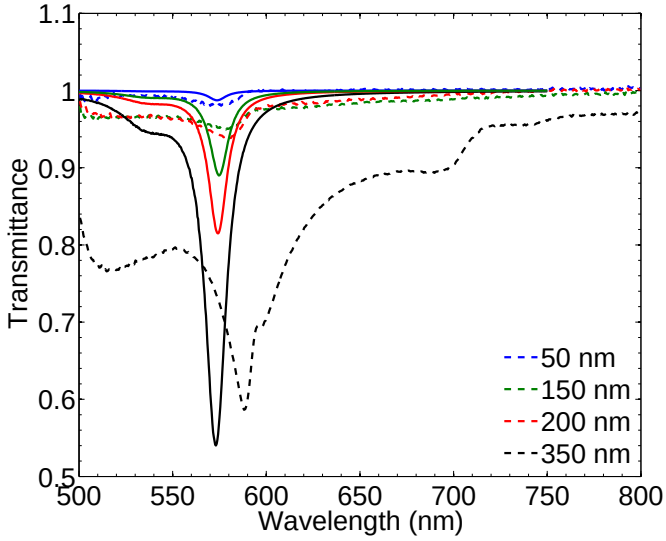


**Figure 4.18:** Theoretical (solid) and experimental (dashed, data credit: Sara Núñez-Sánchez) transmittance spectra for the same nanospheroids as in Fig. 4.17, using a quasistatic approach.

transmittance as might be expected: the curve is not much different from the curve for the 150 *nm* nanospheroid, in stark contrast to the results from the quasistatic treatment. Therefore, repeat measurements are called for, either on this or a similar system in order to shed light on this question.

Forward extinction ($Q_{ext}(\theta = 0°)$) spectra from experiment and T-matrix calculations are now considered. Assuming that Eq. 4.33 can be used to transform $T$ into forward extinction for nanospheroids, plotted in Fig. 4.19 are the forward extinction spectra for each of the nanospheroids, using the experimental data for $T$. Alongside these curves are the (normalised) forward-extinction efficiency spectra as calculated using the T-matrix.

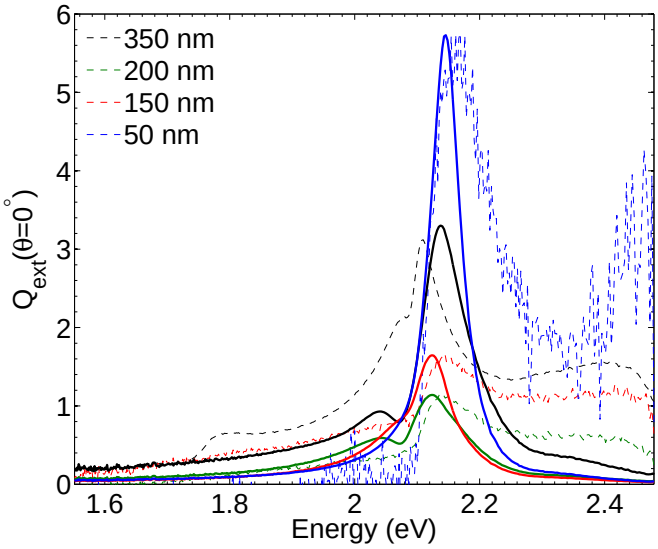


**Figure 4.19:** Forward extinction spectra for the same TDBC:PVA nanospheroids considered in Fig. 4.17. Dashed lines: derived values from experimental data in Fig. 4.17 & 4.18, solid lines: normalised theory.

One immediate finding from Fig. 4.19 is that the experimental data for the $d = 50$ *nm* nanospheroid is very noisy. However, this does not detract from the fact that the peak efficiency is in excess of five, hinting at a transverse PEP mode. The peak efficiency of three for the $d = 350$ *nm* nanospheroid is indicative of a longitudinal PEP mode, with far less experimental noise than for the smaller nanospheroid. The other two curves peak above unity, though not as strongly as for the largest nanospheroid; this was initially thought to be attributed to the fact that the resonance condition for the larger nanospheroid requires a less negative value of $\varepsilon'$ (*cf.* Fig. 4.13), leading to a smaller $\varepsilon''$ at the resonant energy, resulting in a stronger extinction efficiency. However, forward absorption efficiency calculations made with the use of the freely-available nanospheroid code SMARTIES[163] shown in Fig. 4.20 (overleaf) demonstrate that the strong peak in absorption for the largest nanospheroid is an aberration: the strength of the absorption peak of a nanospheroid is revealed to be inversely proportional to its diameter and as such, the peak value of absorption for the largest nanospheroid should

be the smallest. Another finding of Fig. 4.20 is that the peaks corresponding to the

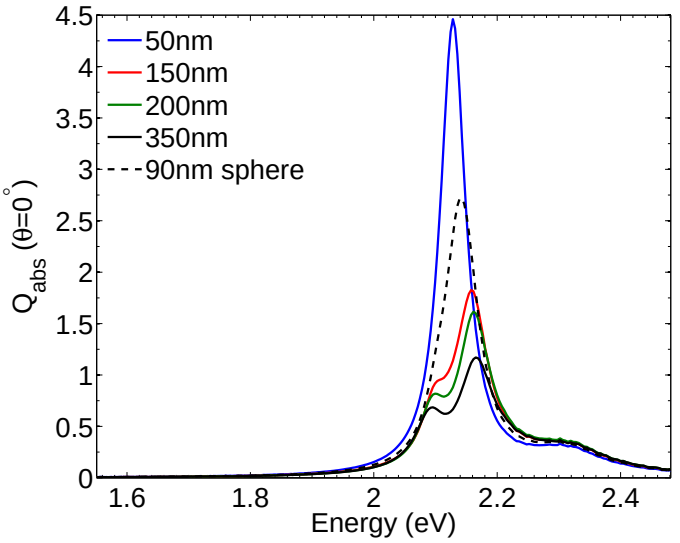


**Figure 4.20:** Calculated forward absorption efficiency for the same TDBC:PVA nanospheroids considered in Fig. 4.17, alongside that of a $d = 90\ nm$ nanosphere in a $n_m = 1.46$ medium.

modes which had been masked in the extinction spectra of Fig. 4.19 are visible. The spectral locations of these modes are slightly redshifted from the values predicted in Tab. 4.3, but only within the range $1.00\% - 1.15\%$.

All of the forward-absorption efficiency curves shown in Fig. 4.20 peak above unity, providing further proof that both longitudinal and transverse PEP modes for 1.46 *wt%* (planar distribution) TDBC:PVA nanospheroids are feasible. The strongest peak corresponds to the transverse mode for the $d = 50\ nm$ (prolate) nanospheroid, which exceeds that of the nanosphere in both its peak value (4.46 compared to 2.71) and quality factor (93 compared to 26). The peak values of the curves for the oblate nanospheroids (corresponding to the longitudinal mode) blueshift and diminish with increasing distortion.

None of the theoretical lineshapes in Fig. 4.19 appear to follow the experimental results particularly well outside the extinction peak. Comparison of Fig. 4.20 with Fig. 4.19 enables one to determine the contribution of the supporting cylinders to the experimentally-deduced forward extinction spectra: this comparison reveals that much of the broadening - particularly on the high energy side of each curve - probably originates from the supporting cylinders. This finding may help to explain the anomalously large peak value of the experimental forward-extinction efficiency for the $d = 350\ nm$ nanospheroid presented in Fig. 4.19, suggesting that the supporting cylinders scatter strongly.

### 4.4.5 Polarisation dependency of transmission

The polarisation dependency of transmittance spectra across single nanospheroids is now investigated. The rationale for this is that the $|\alpha_{il}|^2/y^6$ term in the expression for transmittance obtained through quasistatic theory (Eq. 4.38) suggests that for distances close to nanospheroids, a polarisation-dependent peak in transmission might be observed, rather than a dip as seen from the experimental results in the previous section. It is hypothesised that this peak might be harnessed in future experiments in order to detect the orientation of quasistatic nanospheroids in a sample.

In what follows, a quasistatic theoretical framework is assumed so as to reveal more clearly the features sought after. It must be noted however that calculations borne from this framework are size independent, and that these results may only present themselves in experiment with nanospheroids far smaller than considered in this chapter in general.

In the theoretical framework, unpolarised light is assumed incident upon a single nanospheroid along the positive y-axis. Two sets of distortions are considered: along the x-axis and along the y-axis, so that the nanospheroid in each case is either 'face on' or 'edge on' respectively to the observer. These two orientations of the nanospheroid permit unique combinations of the longitudinal and transverse dipole modes in the nanospheroid, resulting in two distinct transmittance spectra for the x and z polarisations. In an experiment, these spectra could be observed either by the use of polarised light to illuminate the nanoparticle, or by the use of a polarising filter on the objective. In order to estimate the range of spectra obtainable across the four nanospheroids fabricated of TDBC:PVA, and to probe the relative optical strength of the possible

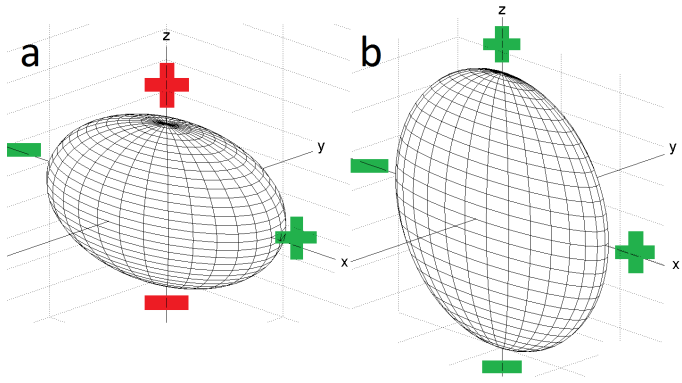


**Figure 4.21:** The $d = 50$ *nm* prolate nanospheroid in the edge-on orientation (a) and the $d = 350$ *nm* oblate nanospheroid in the face-on orientation (b). The orientation of the dipole modes excitable along the x and z axes with unpolarised light incident along the positive y-axis are colour-coded red and green corresponding to the transverse and longitudinal modes respectively.

nanospheroidal modes, the two most extreme geometries (as fabricated) are considered: the (prolate) $d = 50$ *nm* and the (oblate) 350 *nm* nanospheroids, each composed of 1.46 *wt%* (planar distribution) TDBC:PVA. The $d = 50$ *nm* nanospheroid in the edge-on orientation and the $d = 350$ *nm* nanospheroid in the face-on orientation are illustrated in Fig. 4.21a & 4.21b respectively.

From Tab. 4.3, and as shown above, the longitudinal mode is easier to reach than the transverse mode for oblate nanospheroids irrespective of the medium index. In the face-on orientation for oblate nanospheroids, the longitudinal mode is the only mode which can be excited, as shown in Fig. 4.21b. For the 1.46 *wt%* TDBC:PVA $d = 350$ *nm* nanospheroid in vacuum, this mode lies at $\lambda = 563$ *nm* (2.20 *eV*), a value which can be calculated from Eq. 4.29, or by examination of Fig. 2.8a. The transverse PEP mode cannot be excited for this particular nanospheroid (even in the edge-on orientation), but comes closest to being on-resonance at $\lambda = 580$ *nm* (2.14 *eV*).

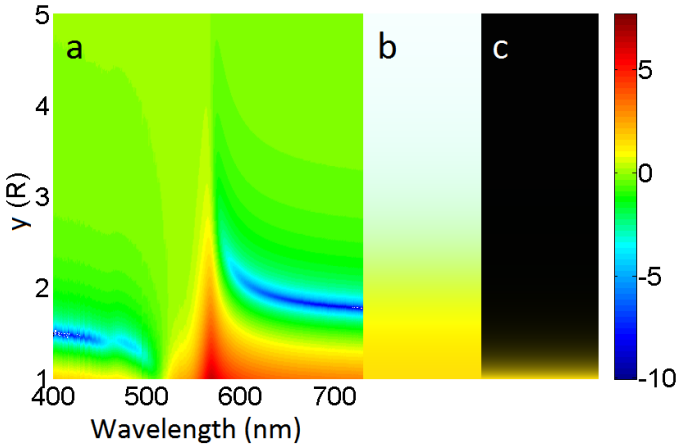


**Figure 4.22:** (a) Transmittance with arbitrary polarisation for the $350 \times 350 \times 90$ *nm* 1.46 *wt%* (planar distribution) TDBC:PVA nanospheroid, in the face-on orientation ($R = 45$ *nm*). (b) Calculated colour as a function of observational distance. (c) Calculated colour with relative intensity normalised to the point $y = R$.

The natural logarithm of the transmittance spectra ($\ln|T|$) calculated using Eq. 4.38 as a function of observation distance along the y-axis (normalised to nanospheroid semi-axis along the y-axis, $R$) for this nanospheroid is plotted in Fig. 4.22a. $\ln|T|$ was chosen in order to show the main features of the spectra. The regions for which $\ln|T| > 0$ indicate electric field enhancement. Fig. 4.22a shows that the longitudinal PEP mode is evidenced at $\lambda = 563$ *nm* as expected. The calculated colour associated with the spectra as a function of distance are plotted in Fig. 4.22b, where an orange colour is observed close to the nanospheroid which fades to white with an increase in distance as the effect of the nanospheroid is felt less strongly, and the spectrum flattens. There is a strong electric field enhancement near the surface of the nanospheroid, and this causes the nanospheroid to glow for short distances along the y-axis; this is represented in Fig. 4.22c, where the calculated colours are again plotted, but normalised to the intensity observed at the nanoparticle surface ($y = R$). Fig. 4.22c demonstrates the

strength of the longitudinal mode for the $d = 350\ nm$ TDBC:PVA nanospheroid, since the relative intensity appears black within $y < 5R$ of the nanospheroid. Similar calculations in the edge-on orientation assuming a simple rotation would reveal the nanoparticle to be invisible, since excitons in the aggregates cannot be excited, leading to a spectrally flat permittivity. However, edge-on calculations made assuming the aggregates to be arranged such that the incident electric field lies in the plane in which the aggregates are distributed reveal a pale blue colour in transmission (not shown) for the same range of distances, implying that the transverse PEP mode would be very much weaker by comparison. This finding implies that the relative strength of the longitudinal mode of the oblate TDBC:PVA nanospheroid may be used to easily identify the orientation of the nanospheroid with a volume distribution of aggregates in an experiment.

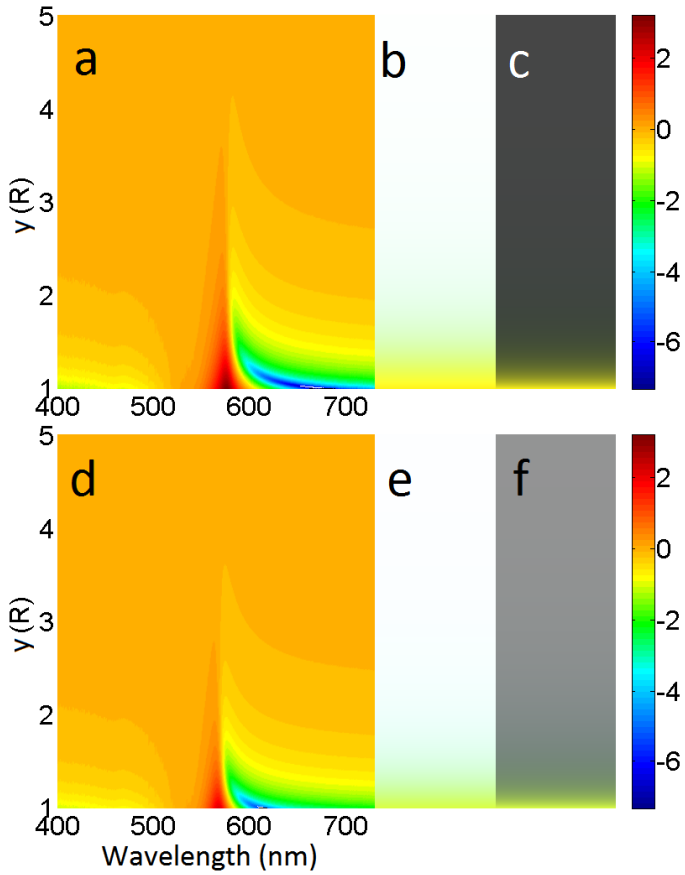


**Figure 4.23:** Transmittance for the x (a) and z (d) polarisations for the $50\times50\times90\ nm$ 1.46 *wt%* (planar distribution) TDBC:PVA nanospheroid in the edge-on orientation ($R = 25\ nm$), with the calculated colour (b & e) and the calculated colour with relative intensity normalised to the point $y = R$ (c & f), as functions of the observational distance.

The transverse mode of a prolate nanospheroid can be excited in the face-on orientation. However, the edge-on orientation has two advantages: firstly, both the longitudinal and transverse modes can be excited, which permits one to compare the relative strength of the transverse and longitudinal modes together. Secondly, the edge-on orientation for the prolate nanospheroid presents the semi-minor axis to the observer, thereby permitting one to observe the nanospheroid from a closer range, leading potentially to stronger electric field enhancement.

In vacuum for the $d = 50$ *nm* TDBC:PVA nanospheroid, both the longitudinal and transverse modes can be excited. By performing the same calculations as before (*via* Eq. 4.29), the longitudinal and transverse PEP modes are found to lie at $\lambda = 580$ *nm* (2.14 *eV*) and $\lambda = 570$ *nm* (2.18 *eV*) respectively. The natural logarithm of the transmittance spectra in the x and z polarisations borne from these two modes are visualised in Fig. 4.23a & 4.23d respectively. The spectra in the x and z polarisations have contributions arising from the longitudinal and transverse PEP modes respectively. The colours calculated for the spectra from the longitudinal mode shown in Fig. 4.23b appear yellow/orange, whereas the colours from the spectra for the transverse mode shown in Fig. 4.23e appear green. This difference is sufficiently strong as to make the colour difference between the two polarisations visually discernible. This finding therefore demonstrates the theoretical plausibility of an experiment with the aim to determine the orientation of such nanospheroids. This shift or the actual colours may differ slightly in reality, given the redshift in the modes whenever Mie theory has been employed above.

As seen for the $d = 350$ *nm* nanospheroid in the face-on orientation, the strength of the modes in the $d = 50$ *nm* nanospheroid fade with distance, and the spectra become flat. However, analysis of the colours normalised to the intensity seen on the nanoparticle surface in Fig. 4.23c & 4.23f reveals that the longitudinal mode is optically stronger than the transverse mode. This finding is counter to what might be expected, since for prolate nanospheroids with extreme distortion, the transverse mode is shown to dominate (see above). The answer to this apparent problem may lie in the relatively lower level of loss within the TDBC:PVA material at $\lambda = 570$ *nm* in comparison to $\lambda = 580$ *nm* (*cf.* Fig. 2.8a).

Now that the PEP modes of 1.46 *wt%* TDBC:PVA nanospheroids have been identified in calculated spectra for a range of observational distances, normalised spectra taken at the nanoparticle surfaces ($y = R$) are now considered for the four nanospheroid aspect ratios outlined in the previous section. By this process, the range of tunability in the transmission peaks may be more easily quantified. Plotted in Fig. 4.24 are the spectra for the four nanospheroids in the face-on orientation in a $n_m = 1.46$ medium, together with the same calculations for a $d = 90$ *nm* nanosphere. The medium index was chosen to closely represent the conditions of the experiment outlined above. In the orientation shown, the peak originates from the longitudinal (transverse) PEP mode for $d > 90$ *nm* ($d < 90$ *nm*). The increase in medium index has narrowed the range for which the peak can be tuned with a change in aspect ratio to $567\ nm < \lambda < 573\ nm$, as shown. In addition, it is the longitudinal PEP mode which most closely resembles the PEP mode of the nanosphere. The opposite of this is true for the edge-on orientation, as shown in Fig. 4.25. Here, Fig. 4.25a and Fig. 4.25b correspond to x and z-polarised light

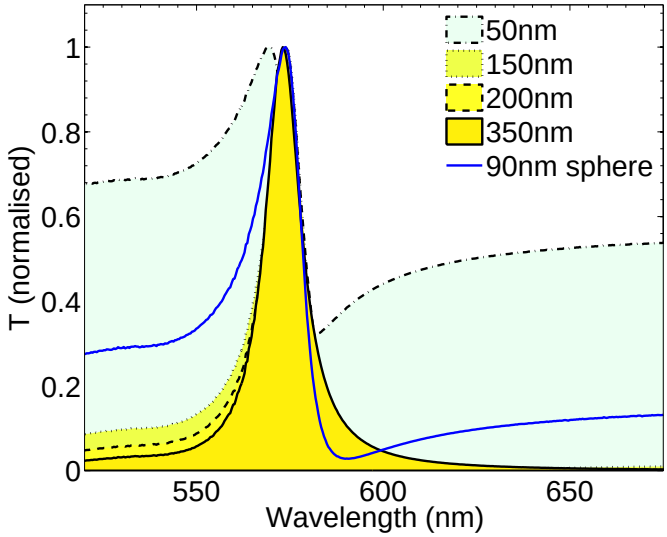


**Figure 4.24:** $T$ spectra for the four 1.46 *wt%* (planar distribution) TDBC:PVA nanospheroids in the face-on orientation, together with $T$ for a 90 *nm* nanosphere.

respectively. The transmittance curve for the $d = 50$ *nm* nanospheroid in Fig. 4.25b arises from the transverse PEP mode, and is closest to the response of the nanosphere, as shown, in contrast to the other three curves in Fig. 4.25b which arise from the longitudinal PEP mode.

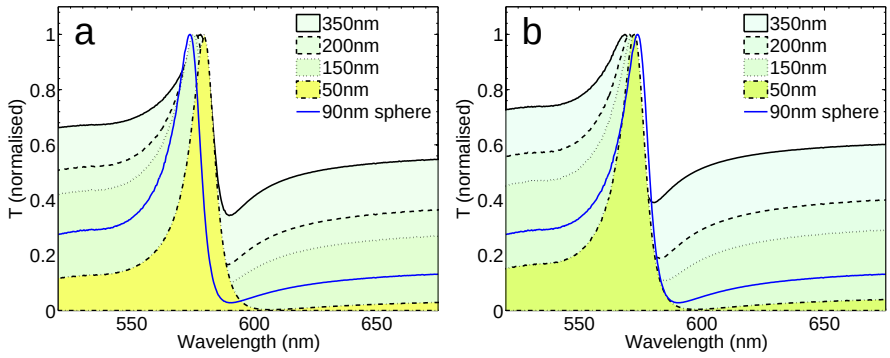


**Figure 4.25:** (a) $T_x$ and (b) $T_z$ spectra for the four 1.46 *wt%* (planar distribution) TDBC:PVA nanospheroids in the edge-on orientation, together with $T$ for a $d = 90$ *nm* nanosphere.

Taking Fig. 4.24 & 4.25 together, a peak in the near-field $T$ spectrum is obtained as a result of an excitation of a PEP mode. The quality factor of this peak is maximised for longitudinal PEP modes using a highly distorted oblate nanospheroid in the face-on orientation. Given the relatively high strength of this particular mode (as evidenced in Fig. 4.22c), it is this mode which should be sought for strong electric field enhancement

and a high quality factor of the resonance, provided that the nanoparticle is sufficiently subwavelength for the quasistatic theory assumed here to hold. This strong peak is highly directional, and if the nanospheroid were rotated, the peak would vanish. This provides a mechanism by which orientation of an excitonic nanospheroid can be detected using optical frequencies.

## 4.5 Conclusions

For silver or gold nanospheres, particle plasmon polariton (PPP) modes can be excited at optical frequencies given the correct medium index. The PPP mode of aluminium lies in the ultraviolet, even when embedded in glass. TDBC-doped PVA nanospheres can exhibit particle modes which bear much similarity to PPP modes in terms of strong absorption cross-section, electric field enhancement and electric field confinement. However, these modes originate from the exciton transitions in the molecular aggregates, and are therefore termed particle exciton polariton (PEP) modes. These modes are excitable over a narrower set of wavelengths than PPP modes.

PEP modes in 100 *nm* diameter TDBC:PVA nanospheres can exhibit higher quality factors and absorption efficiencies than PPP modes in either gold or silver nanospheres of the same size. It has been shown through the use of Mie theory that the spectral positions of these PEP modes are more accurately predicted by the CM condition than the PPP modes of either the gold or silver nanospheres are. These findings originate from a low value of the imaginary part of the permittivity ($\varepsilon''$) for TDBC when the CM condition is satisfied, along with a sharper change in the real part of the permittivity ($\varepsilon'$) around this energy than either that of gold or silver.

Both PEP and PPP modes cause the absorption efficiency of the host nanospheres to exceed unity on resonance. It has been shown that on resonance the nanosphere acts as a 'magnet for light', wherein the nanoparticle draws power in from outside its geometrical radius. Another property of particle modes is that on resonance, the electric field strength is enhanced over all solid angles close to the surface of the nanosphere; this property has been shown through quasistatic calculations for both PEP and PPP modes, and for epsilon-near-zero (ENZ) modes. In addition, it has been demonstrated that electric field isosurfaces can be increased in volume by raising the medium index.

Through Mie absorption efficiency calculations for nanospheres, the four-level quantum model for permittivity has been shown to produce much closer results to the same calculations using experimental data for permittivity than in assuming a best-fit Lorentz oscillator model. This demonstrates both the approximate nature of the Lorentz model and the relative accuracy of the four-level quantum model.

It has been demonstrated through Mie calculations over a range of dye concentrations that a TDBC dye concentration of approximately 3 *wt%* with the volume distribution is required in order to permit the excitation of PEP modes in TDBC:PVA nanospheres

(this concentration decreases to around 1.5 *wt%* for the planar distribution). Tunability of this PEP mode with concentration has been demonstrated for the wavelength range 564 $nm < \lambda < 572$ *nm*, by increasing the dye concentration up to 5.00 *wt%*. This range may in principle extended further for higher dye concentrations. The nanosphere PEP mode can also be tuned with a change in medium index, and this range of tunability for a 3.22 *wt%* (volume distribution) TDBC:PVA nanosphere has been shown to be 558 $nm < \lambda < 587$ *nm*. This sensitivity to the environment combined with a high quality factor of the resonance may find application in biosensing.

For TDBC:PVA nanospheres with a volume distribution of aggregates and dye concentrations in the range 0.5 *wt%* $\rightarrow$ 3 *wt%*, ENZ modes can be excited. The ENZ resonances can be tuned over the wavelength range 572 $nm < \lambda < 585$ *nm* for a change in dye concentration. Although these ENZ modes have both a lower quality factor and strength than their PEP counterparts, ENZ modes have been shown through Mie calculations to exhibit the two main properties of PEP modes: that of an absorption efficiency exceeding unity, and electric field enhancement over all solid angles.

Two distinct classes of PEP modes have been demonstrated for nanospheroids: longitudinal and transverse modes. For prolate (oblate) nanospheroids, transverse (longitudinal) modes dominate the optical response as the aspect ratio is increased. The resonance conditions on these modes are in the range $\varepsilon' = \{0, -\infty\varepsilon_m\}$. Consequently, if a material has a widely varying real permittivity across optical wavelengths, the apparent colour of a nanospheroid of that material can be engineered with a change in aspect ratio. For silver in a $n_m = 1.5$ medium, this range is the entire optical range (blue to red). For TDBC:PVA nanospheroids in a $n_m = 1.46$ medium, this range of wavelengths is restricted to 566 $nm < \lambda < 580$ *nm* (green to orange).

Calculations have shown that nanospheroidal PEP modes are evidenced by peaks in absorption spectra made using the T-matrix method. In order to confirm these modes experimentally, transmittance spectra have been taken through arrays of 1.46 *wt%* (planar distribution) TDBC:PVA nanospheroids in a $n_m = 1.46$ medium; these transmittance spectra have been shown to be in fair agreement with those calculated by the T-matrix. The transmittance spectra obtained using the quasistatic model recover the main features in the spectra well, but do not account for the broadening in the response due to retardation effects (as the T-matrix model does), and become increasingly inaccurate as the size of the nanospheroid is increased. Therefore, the use of quasistatic scattering for nanospheroids is restricted to the prediction of the spectral locations of nanospheroidal PEP modes, and to the response of small nanospheroids only, for which more accurate predictions of the scattering and absorption spectra can be computed with greater ease.

By reverse-engineering the experimental transmittance spectra, approximate forward extinction spectra have been obtained for the nanospheroids, which are (again) in fair agreement with those calculated using the T-matrix. The extinction efficiency spectra for all the nanospheroids considered peak in excess of unity, hinting at possible nanospheroidal PEP modes: transverse and longitudinal modes for the prolate and oblate nanospheroids respectively. By performing forward-absorption efficiency

spectra calculations, these modes have been shown to be concealed within the forward-extinction spectra. Much of the broadening observed in the experimental forward-extinction spectra was found to be the response of the supporting cylinders, but the main peaks were found to correspond to the response of the nanospheroids. Further experimentation is encouraged in order to provide further confirmation for these modes, provided that a fabrication technique for nanospheroids can be developed without the supporting cylinders being present. In addition, since it is the prolate nanospheroid which provides the strongest response (both theoretically and experimentally) from the set of four nanospheroid arrays tested, experimentation upon prolate nanospheroids within the quasistatic limit is encouraged, since it is expected that these will yield the strongest optical response.

Quasistatic transmittance calculations have been made for single excitonic nanospheroids in vacuum in order to determine the theoretical plausibility for optical measurement of the orientation of excitonic nanospheroids. These calculations have shown that strong electric field enhancement can be obtained on resonance, provided the observational distance is sufficiently close to the surface of the nanospheroid. In the face-on orientation, the optical response is independent of polarisation. In this orientation, the electric field enhancement arising from longitudinal PEP modes associated with oblate nanospheroids is particularly strong. In addition, the quality factor of these modes both exceeds that of the nanospherical PEP mode, and increases with the nanospheroid eccentricity. In the edge-on orientation, either the longitudinal or the transverse modes can be excited. The exact nature of the transmittance spectra for these modes is the subject of a future investigation, but these qualitative results suggest that the peak in transmittance for 1.46 *wt%* (planar distribution) TDBC:PVA nanospheroids can be tuned with a change in the polarisation of the incident light in the wavelength range $572\ nm < \lambda < 580\ nm$. Colour calculations based upon the quasistatic results suggest that this shift in wavelength should be noticeable to the human eye. In all, the transmittance spectra are highly directional for excitonic nanospheroids, and the plausibility of a detection system to probe the orientation of excitonic nanospheroids has been demonstrated.

The main objective stated at the beginning of this chapter is to investigate the use of excitonic materials as alternatives within nanoparticle plasmonics. Given that the analogues of PPP modes (PEP modes) have been demonstrated for both excitonic nanospheres and excitonic nanospheroids, and that greater field enhancement and absorption efficiency may be achieved with the use of excitonic nanoparticles, excitonic nanoparticles have been demonstrated as viable alternatives to plasmonic nanoparticles. These PEP modes have a degree of tunability, either through a change in medium index, dopant concentration, or through a change in the aspect ratio of the nanoparticle. All-in-all for TDBC:PVA nanoparticles, the most effective technique for PEP tuning has been determined to be a change in the medium index, provided that the dye concentration is sufficiently high. This is also by far the most practical technique, since it does not require re-fabrication of the nanoparticles themselves, unlike changing the nanospheroid aspect ratio, or the dye concentration within the nanoparticles. One other possibility for shifting the resonant wavelength of a nanoparticle is by coating the nanoparticle with a shell: this can be done in a number of different ways, and

relative merits of some of these possibilities are explored in the following chapter.

# 5

# Particle Polariton Modes in Coated Nanospheres

*In this chapter, particle polariton modes are studied in the context of coated nanospheres. It is shown that particle exciton and particle plasmon modes can hybridise to form modes with both plasmonic and excitonic origin: so-called 'plexciton' modes, which may be tuned by changes in nanoparticle geometry, dye species, or dye concentration.*

## 5.1 Introduction

In Ch. 4 it was shown that excitonic nanospheres can exhibit particle exciton polariton (PEP) modes, which can under the right conditions not only exhibit two properties which are usually associated with plasmon polariton modes (field enhancement and strong absorption), but can also exhibit even stronger absorption than that associated with either silver or gold nanospheres and with a higher quality factor. However, since for excitonic materials the negative real permittivity necessary for these effects arises from excitons rather than free electrons, the range of tunability for these PEP modes is greatly restricted in relation to that of noble metals.

The advent of nanoparticle fabrication techniques[164,165] has enabled the production of a number of distinct coated nanosphere configurations. Nanospheres with metal cores and inert shells have been demonstrated for their application as chemical sensors,[17] and nanospheres with inert cores and plasmonic shells have been shown to exhibit two plasmon modes[166–168] arising from the hybridisation of the particle plasmon mode with the cavity plasmon mode. The spectral locations of these two hybridised modes can be tuned with a change in core and medium index, along with the relative shell thickness of the nanoparticle; altogether, the resonances for these coated nanospheres provide greater potential for tunability than bare nanospheres can offer. This potential for extended particle mode tunability with changes in the coated nanoparticle configuration or the medium index is the *raison d'être* for this chapter. Here, the tunability of PEP modes across several different coated nanosphere geometries is studied with the aim to find the geometry which will yield the greatest tunability.

The approach taken in this chapter is as follows: first, PEP modes for nanospheres with excitonic cores and inert shells are studied, following on from the findings of Ch. 4. Next, excitonic nanoshells are examined for their potential hybrid PEP modes, as analogues to plasmonic nanoshells. Going further, nanospheres with both excitonic cores and shells are studied. Lastly, particle modes for nanospheres with metallic cores and excitonic shells are investigated. It is hoped that by consideration of these different systems, a greater understanding for the engineering of PEP tunability may be obtained, and the conditions necessary for polariton mode hybridisation and maximisation of mode splitting established.

The theoretical framework taken in this chapter is to begin with a quasistatic approach, which can then be used in order to inform the findings from Mie theory calculations, extended to coated nanospheres. In the case of a coated nanosphere, the polarizability of the nanosphere becomes a function of both the permittivity of the core and the coating. In addition, the polarizability becomes dependent upon the relative volume of both materials present. This chapter is restricted to the investigation of nanospheres with rotational symmetry - the additional complexity introduced by consideration of coated nanospheroids is a possible topic of investigation borne from the findings of this chapter.

Several symbol definitions and conventions are now outlined for use within this chapter: a coated nanosphere is defined as having a core of diameter $d$ with radius $r_1$, and a coating of thickness $t$. The overall radius of the nanosphere is denoted $r_2$. The core and shell have permittivities denoted by $\varepsilon_1$ and $\varepsilon_2$ respectively. Such a nanoparticle can be expressed using the notation $\varepsilon_2@\varepsilon_1$. The permittivity of the medium is denoted $\varepsilon_m$. These seven quantities are all illustrated in Fig. 5.1. In this chapter, the excitonic dye considered is the same TDBC dye as studied in previous chapters. The aggregates of the dye are assumed to be in the volume distribution (*cf.* Fig. 4.5b) unless otherwise stated.

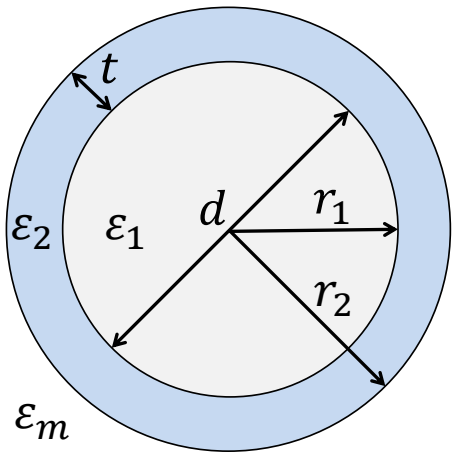


**Figure 5.1:** Schematic of the coated nanosphere with overall radius $r_2$: the core has permittivity $\varepsilon_1$ and diameter $d = 2r_1$; the shell has permittivity $\varepsilon_2$ and thickness $t$; and the medium has permittivity $\varepsilon_m$.

## 5.2 Resonance Conditions

In order to determine the resonant frequencies of a coated nanosphere, the polarizability tensor $\bar{\alpha}$ is considered. For rotationally-symmetric coated nanospheres, this tensor reduces to a zero-order tensor, $\alpha$, in the same way as for an uncoated nanosphere. Calculation of $\alpha$ for a coated nanosphere can be performed in the same way as for an uncoated nanosphere, using the Clausius-Mossotti (CM) relation,

$$\alpha = 3V\frac{\varepsilon_{\text{eff}} - \varepsilon_m}{\varepsilon_{\text{eff}} + 2\varepsilon_m}, \tag{5.1}$$

except here the *effective* permittivity of the nanosphere ($\varepsilon_{\text{eff}}$) is used. This effective permittivity can be expressed as,[166]

$$\varepsilon_{\text{eff}} = \varepsilon_2\frac{2\varepsilon_2 + \varepsilon_1 - 2x^3(\varepsilon_2 - \varepsilon_1)}{2\varepsilon_2 + \varepsilon_1 + x^3(\varepsilon_2 - \varepsilon_1)}, \tag{5.2}$$

where the aspect ratio $x = r_1/r_2 = d/(d + 2t)$. In the limit of thin shells ($x \to 1$) the effective permittivity tends to that of the core ($\varepsilon_{\text{eff}} \to \varepsilon_1$). Conversely, in the limit of thick shells, ($x \to 0$) the effective permittivity tends to that of the shell ($\varepsilon_{\text{eff}} \to \varepsilon_2$). Substitution of the expression for $\varepsilon_{\text{eff}}$ into the denominator of Eq. 5.1 gives (after a little algebra) the following master equation for a coated nanosphere,

$$\boxed{2(1 - x^3)\varepsilon_2^2 + [(1 + 2x^3)\varepsilon_1 + 2\varepsilon_m(2 + x^3)]\varepsilon_2 + 2\varepsilon_m\varepsilon_1(1 - x^3) = 0}, \tag{5.3}$$

which when solved for $\omega$ yields the resonant frequencies of the coated nanosphere. It can be seen readily that Eq. 5.3 reduces to the CM condition for bare nanospheres (Eq. 4.9) in the thin-shell limit ($x \to 1$).

In general, $\varepsilon_1$ and $\varepsilon_2$ in Eq. 5.3 are both non-constant functions of $\omega$ and determination of the resonant frequencies in terms of the other variables depends on the models used for $\varepsilon_1$ and $\varepsilon_2$.

## 5.3 Mie Theory For Coated Nanospheres

Mie theory as outlined in Ch. 4 can be adapted to make scattering calculations for coated nanospheres. By solving the relevant boundary conditions, the following expressions for the Mie a and b coefficients in a coated nanosphere geometry are obtained,[65,169]

$$a_n = \frac{\psi_n(x_2)[\psi_n'(m_2x_2) - A_n\chi_n'(m_2x_2)] - m_2\psi_n'(x_2)[\psi_n(m_2x_2) - A_n\chi_n(m_2x_2)]}{\xi_n(x_2)[\psi_n'(m_2x_2) - A_n\chi_n'(m_2x_2)] - m_2\xi_n'(x_2)[\psi_n(m_2x_2) - A_n\chi_n(m_2x_2)]} \quad (5.4)$$

$$b_n = \frac{m_2\psi_n(x_2)[\psi_n'(m_2x_2) - B_n\chi_n'(m_2x_2)] - \psi_n'(x_2)[\psi_n(m_2x_2) - B_n\chi_n(m_2x_2)]}{m_2\xi_n(x_2)[\psi_n'(m_2x_2) - B_n\chi_n'(m_2x_2)] - \xi_n'(x_2)[\psi_n(m_2x_2) - B_n\chi_n(m_2x_2)]}, \quad (5.5)$$

where the quantities $A_n$ and $B_n$ are defined as,

$$A_n = \frac{m_2\psi_n(m_2x_1)\psi_n'(m_1x_1) - m_1\psi_n'(m_2x_1)\psi_n(m_1x_1)}{m_2\chi_n(m_2x_1)\psi_n'(m_1x_1) - m_1\chi_n'(m_2x_1)\psi_n(m_1x_1)} \quad (5.6)$$

$$B_n = \frac{m_2\psi_n'(m_2x_1)\psi_n(m_1x_1) - m_1\psi_n(m_2x_1)\psi_n'(m_1x_1)}{m_2\chi_n'(m_2x_1)\psi_n(m_1x_1) - m_1\chi_n(m_2x_1)\psi_n'(m_1x_1)}, \quad (5.7)$$

where $m_i = \varepsilon_i/\varepsilon_m$, $x_i = kr_i = 2\pi r_i/\lambda$ are the size parameters, and $\chi$ is the Riccati-Bessel function of the second kind.[170] With these expressions for the Mie a and b coefficients, Eq. 4.23 & 4.24 can be used to make scattering and absorption calculations for coated nanospheres.

## 5.4 Active Core, Inert Shell

As stated in Ch. 4, nanoparticles have the potential to be used as transducers within biosensing[150], and their worth as chemical sensors has already been proven.[17] A number of absorption microscopy techniques are available for measuring absorption cross section spectra of single nanoparticles through experiment,[171,172] and a technique for the detection of gold nanoparticles inside cells has been demonstrated.[173] If the experimental absorption spectra of the nanoparticles can be related to the properties of the environment in which they reside, these applications can be realised. In biosensing applications, it is feasible that a layer of biomaterial might accumulate around a nanoparticle to form a shell. This provides a motivation to quantify the effect that such a shell has on the absorption spectra of excitonic nanospheres.

In this section, absorption spectra for coated TDBC:PVA and silver nanospheres are calculated using the extension to Mie theory for coated nanoparticles as outlined above. In order to analyse these spectra, an analytical quasistatic approach is taken based on solutions of the master equation (Eq. 5.3). In order to extract analytical solutions for the resonant energies of a coated nanosphere with an active core and an inert shell from the master equation, a suitable model must be used for the core material, $\varepsilon_1$. For a nanosphere with an excitonic core, the permittivity of the core material can be approximated by the single-oscillator Lorentz model (see Eq. 2.14). By substitution of

the Lorentz model for $\varepsilon_1$ into the master equation (Eq. 5.3) and by assuming that the shell material possesses a spectrally constant permittivity $\varepsilon_2$, the following expression for the resonant frequency of this system is obtained,

$$\omega = \omega_0 \sqrt{\frac{2(1-x^3)\left(\varepsilon_2^2 + \varepsilon_m(\varepsilon_\infty + f)\right) + \left[(2x^3+1)(\varepsilon_\infty + f) + 2(x^3+2)\varepsilon_m\right]\varepsilon_2}{2(1-x^3)(\varepsilon_2^2 + \varepsilon_m\varepsilon_\infty) + \left[(2x^3+1)\varepsilon_\infty + 2(x^3+2)\varepsilon_m\right]\varepsilon_2}}. \tag{5.8}$$

This expression reduces to the bare nanosphere solution (Eq. 4.10) for thin shells ($x \to 1$). As *per* the bare nanosphere solution, the resonant frequency in Eq. 5.8 blueshifts with an increase in oscillator strength $f$, which can be increased by raising the concentration of the dye in the core. However, the presence of the shell weakens this effect, and given that it is the effect of the shell which is of interest in this chapter rather than the core, the focus is confined to the following three variables and their effect on the resonant frequency: shell thickness, shell index and medium index.

### 5.4.1 Shell thickness

From Eq. 5.8, an increase in shell thickness ($t$) redshifts the resonant frequency, provided that $\varepsilon_m < \varepsilon_2$; in the case where $\varepsilon_m > \varepsilon_2$, the resonant frequency is blueshifted. For biosensing applications, nanoparticles are likely to be in an aqueous environment, and may bond with (for example) proteins[174] to form shells around the nanoparticles. In this section, it is assumed that the nanoparticles considered bond with fatty acids[175] with effective refractive index $n_2 = 1.5$, and that the aqueous medium is non-dispersive with an index of $n_m = 1.33$.

The resonant wavelength of a $d = 100$ *nm* nanosphere with a 3.22 *wt%* TDBC:PVA core is now examined using the best-fit single oscillator Lorentz model (with parameters $f = 0.3$, $\varepsilon_\infty = 1.52^2$, $\omega_0 = 2.11$ *eV* and $\gamma = 46.1$ *meV*) in Eq. 5.8. Without a shell, the resonant wavelength lies at $\lambda_0 = 573.9$ *nm*. This mode redshifts with the addition of an $n_2 = 1.5$ coating, up to a wavelength of 575.8 *nm* for a $t = 100$ *nm* coating. This modest redshift of $\Delta\lambda = 1.9$ *nm* is visualised in Fig. 5.2 (overleaf), along with the calculated redshift for the equivalent system with a silver core (using the Drude model); it can be seen that the substitution of the excitonic core with the silver core leads to a much larger redshift, up $\Delta\lambda = 25.7$ *nm* from the bare nanosphere value at 387 *nm* for the same $t = 100$ *nm* coating. Detailed analysis of the two curves reveals that the wavelength shift for the TDBC nanosphere becomes saturated more rapidly with an increase in shell thickness than for the silver nanosphere, with 50% saturation for shell thicknesses thinner than 20 *nm* in either case. This is indicative of electric field confinement for both the PEP and particle plasmon polariton (PPP) modes, given that most of the redshift occurs over a length scale which is a fraction of both the nanoparticle diameter and the resonant wavelength itself.

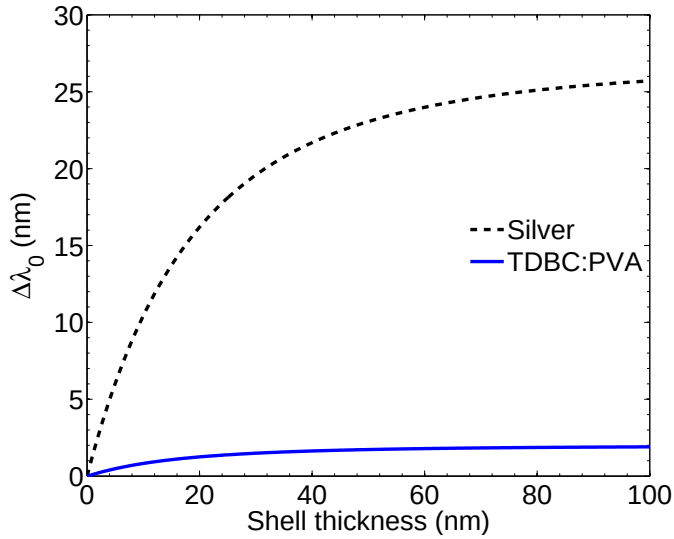


**Figure 5.2:** Redshift in particle mode wavelength as a function of shell thickness for $d$ = 100 *nm* nanospheres of silver and 3.22 *wt%* (volume distribution) TDBC:PVA, modelled with the Drude model and the Lorentz oscillator model respectively, with a shell index of $n_2 = 1.5$ in a $n_m = 1.33$ medium.

The accuracy of these predictions are evaluated in Fig. 5.3, where $\sigma_{\text{abs}}$ (in units of $\mu m^2$) from Mie calculations for these two systems have been plotted both with and without the $t = 100$ *nm* coating, in order to visualise what might reasonably be expected from an experiment. The four-level quantum model has been used for the excitonic core. For this system, a redshift of $\Delta\lambda = 2.0$ *nm* is observed, demonstrating that the value of the redshift predicted by the quasistatic treatment (Eq. 5.8) shown in Fig. 5.2 compared to the Mie theory calculations is correct to within 5%. The Mie theory values of the resonant wavelengths (578.2 *nm* and 580.2 *nm*) are further redshifted from the values predicted by Eq. 5.8 due to retardation effects (see Sec. 4.3.5). However, the predicted resonance wavelengths are correct to within 1% of the Mie calculations, demonstrating the applicability of the use of this approximate treatment.

The spectra for the nanospheres with silver cores in Fig. 5.3 reveal that the redshift in resonant wavelength is slightly larger than the value indicated in Fig. 5.2, at $\Delta\lambda$ = 30.1 *nm*. The predicted value of the shift is however correct to within 15%, and the absolute values of the resonant wavelengths calculated from Mie theory (392.5 *nm* and 422.6 *nm*) are correct to within 2.5% of the predicted values from Eq. 5.8.

Altogether, these core-shell Mie and quasistatic calculations demonstrate that the resonant wavelength of silver nanospheres is approximately fifteen times more sensitive to a shell of material in a biosensing context than nanospheres of 3.22 *wt%* TDBC:PVA. The relative strength in absorption and the rigidity of the resonant wavelength for the TDBC:PVA nanospheres might suggest that such nanospheres could be candidates in applications for which a consistent absorption or scattering profile is necessary regardless of the addition of a coating. For example, such nanoparticles may find potential

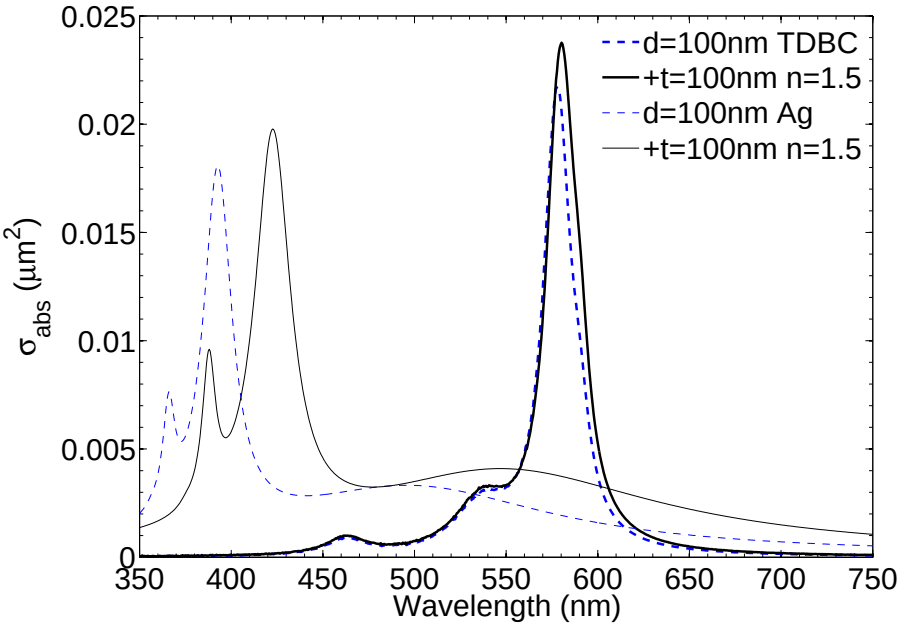


**Figure 5.3:** Absorption cross section (in units of $\mu m^2$) from Mie theory for silver (thin lines) and 3.22 *wt%* (volume distribution) TDBC:PVA nanospheres (thick lines) with (solid) and without (dashed) $t = 100$ *nm* coatings of index $n_2 = 1.5$ in water ($n_m = 1.33$).

for use as tracking devices within the body of a patient, providing non-radioactive signals the peak of which would be consistent regardless of the amount of biomatter adsorbed upon their surfaces.

Another observation of the spectra in Fig. 5.3 is that the peak values of the absorption spectra are increased subtly with the addition of the shell; in broad terms the peak values are similar for a nanosphere with and without the coating, despite an increase in overall diameter from 100 *nm* to 300 *nm*, and hence a nine-fold increase in cross-sectional area. Therefore, despite the peak absorption efficiencies of the bare TDBC:PVA and silver nanospheres in Fig. 5.3 being equal to 2.8 and 2.3 respectively, the absorption efficiency of the same nanospheres with the addition of a coating do not exceed 0.33 for either. At first sight, this seems to indicate that particle polariton modes can only be excited with the bare nanospheres, and not with the coated nanospheres. This is however, not strictly true: by calculation of the effective absorption radius of the nanosphere by,

$$r_{\text{eff}} = \sqrt{\frac{\sigma_{\text{abs}}}{\pi}}, \tag{5.9}$$

using the values of the peaks in Fig. 5.3, $r_{\text{eff}}$ is shown to be equal to 83 *nm* and 86 *nm* for the uncoated and coated TDBC:PVA nanospheres respectively; both of these values are larger than the active core radius, and the effective radius is in fact increased with

the addition of the coating. This is evidence that a PEP mode can be established within the core in either case, but not for the coated nanosphere as a whole: in this case, the PEP mode is not distributed over the whole volume of the coated nanosphere, and any electric field enhancement is expected to occur within the shell of the nanoparticle only, and not outside it.

### 5.4.2 Medium index

As shown above, the PEP mode of a nanosphere with an excitonic core and an inert coating will redshift with an increase in shell thickness provided that the medium index is below that of that shell index, and *vice versa*. The extent to which this shift occurs as a function of medium index is now explored for the TDBC:PVA nanospheres outlined in the previous section. In Fig. 5.4, the resonant wavelengths for nanospheres with shells of thickness $t = 0$ *nm* and $t = 100$ *nm* are plotted as a function of medium index in the range $1 < n_m < 2.5$, whilst the index of the shell is held at $n_2 = 1.5$.

As expected, the resonant wavelength redshifts (blueshifts) with the addition of the coating for medium indices below (above) that of $n_m = 1.5$. This shift is maximised for large differences between the medium index and the shell index. For the example system plotted, the maximum redshift and blueshift obtainable over the range of medium indices considered are $\Delta\lambda = 6.6$ *nm* and $\Delta\lambda = 6.5$ *nm* respectively.

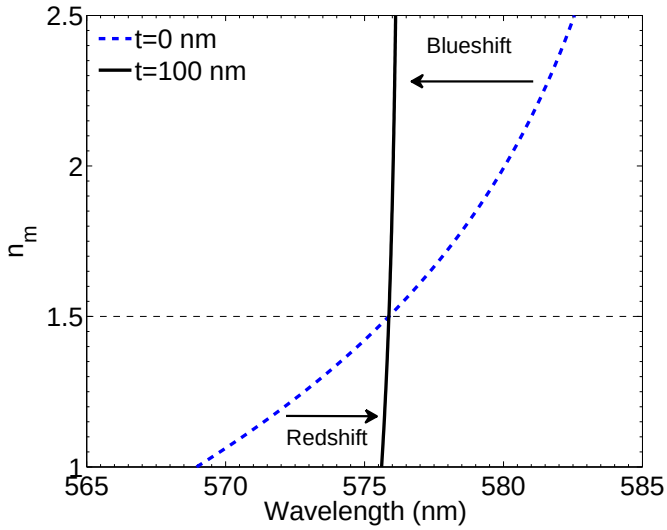


**Figure 5.4:** Resonant wavelengths for $d = 100$ *nm* 3.22 *wt%* TDBC:PVA nanospheres with (solild) and without (dashed) a $t = 100$ *nm* coating of index $n_2 = 1.5$ as a function of medium index.

Another way of examining this system is as follows: with the addition of the $t = 100\,nm$ coating to the TDBC:PVA nanosphere, the resonant wavelength is confined to the range $575.6\,nm < \lambda < 576.2\,nm$ for the medium indices considered. Without the coating, the resonant wavelength is more sensitive to a change in its environment, with the possible range of resonance wavelengths increased to $569\,nm < \lambda < 582\,nm$ for the medium indices considered. This demonstrates that an increase in coating thickness around the nanosphere causes the shell to dominate the optical response; this leads to a decreased degree of tunability with a change in medium index. Therefore, in broad terms, a coating around a nanosphere could be used as a stabilising agent in nanoparticle design, if a consistent resonance wavelength is required.

## 5.5 Inert Core, Excitonic Shell

The inverse of the nanoparticle considered in the previous section is now studied *i.e.* a nanosphere with an excitonic shell and an inert core, herein referred to as an excitonic nanoshell. As stated in the introduction, the plasmonic (metal) nanoshell system is already well-understood,[167] and it is for this reason that excitonic nanoshells are explored in order to determine whether or not they have equivalent optical properties.

For a nanosphere with an inert core, $\varepsilon_1$ is assumed to be a real constant across optical frequencies. The master equation (Eq. 5.3) can be re-arranged in terms of the shell permittivity $\varepsilon_2$ to give,

$$\begin{aligned}\varepsilon_2 =& \frac{-[(1+2x^3)\varepsilon_1 + 2\varepsilon_m(2+x^3)]}{4(1-x^3)} \\ &\pm \frac{\sqrt{[(1+2x^3)\varepsilon_1 + 2\varepsilon_m(2+x^3)]^2 - 16\varepsilon_m\varepsilon_1(1-x^6)}}{4(1-x^3)}.\end{aligned} \tag{5.10}$$

By the use of Eq. 5.10 with the best-fit single oscillator Lorentz model (see above) in the limit where $\gamma \ll \omega$, the following approximate analytic expression for the two resonant frequencies of the coated nanosphere can be derived,[176]

$$\omega_\pm^2 = \omega_0^2 + \frac{4f\omega_0^2(1-x^3)}{4\varepsilon_\infty(1-x^3) + B_0 \mp A_0}, \tag{5.11}$$

where,

$$A_0 = \sqrt{[(1+2x^3)\varepsilon_1 + 2\varepsilon_m(2+x^3)]^2 - 16\varepsilon_m\varepsilon_1(1-x^3)^2} \tag{5.12}$$

$$B_0 = (1+2x^3)\varepsilon_1 + 2\varepsilon_m(2+x^3). \tag{5.13}$$

The two modes in Eq. 5.11 are hybrid exciton polariton modes, deriving from hybridisation of the cavity and particle modes of the excitonic nanoshell. The $\omega_-$ and $\omega_+$ modes are labelled the 'symmetric' and 'antisymmetric' modes respectively.[166] It can be shown through a jellium model that the electric dipole moments arising from charge distributions on the inner and outer surfaces of the nanoshell are aligned (anti-aligned) for the symmetric (antisymmetric) mode.[167]

From Eq. 5.11, the splitting of the PEP is maximised for thin shells ($x \to 1$). This can be shown by definition of a "splitting parameter" $g(x) = \omega_+^2 - \omega_-^2$,

$$g(x) = \frac{8f\omega_0^2(1-x^3)A_0}{(4\varepsilon_\infty(1-x^3)+B_0)^2 - A_0^2}. \tag{5.14}$$

This expression together with the definitions for $A_0$ and $B_0$ and Eq. 5.11 can be used to derive two general results for the system: firstly, for infinitesimally thin shells ($x \to 1$), there exists a single resonant mode at $\omega_0$ as expected; the other mode diverges, leading to $g(x) = \infty$, providing continuity with the bare nanosphere case. The strength of this single mode is expected to be weak, owing to the relatively low concentration of excitonic material on the outside of the nanoparticle for thin shells. Secondly, for thick shells (where $x \to 0$) the following two limiting values of $\omega_\pm$ are arrived at,

$$\omega_-^2 = \left(1 + \frac{4f}{4\varepsilon_\infty + \varepsilon_1 + 4\varepsilon_m + \sqrt{\varepsilon_1^2 + 16\varepsilon_m^2}}\right)\omega_0^2 \tag{5.15}$$

$$\omega_+^2 = \left(1 + \frac{4f}{4\varepsilon_\infty + \varepsilon_1 + 4\varepsilon_m - \sqrt{\varepsilon_1^2 + 16\varepsilon_m^2}}\right)\omega_0^2. \tag{5.16}$$

Again, these two modes blueshift with an increase in dye concentration.

A less approximate equation than Eq. 5.11 can be derived by expanding the expression in Eq. 5.10 without assuming $\gamma \ll \omega$; doing so yields a quadratic in $\omega^2$, *i.e.*

$$c_4\omega^4 + c_2\omega^2 + c_0 = 0. \tag{5.17}$$

The solutions to this equation are too long to be written out here, but the coefficients are written out in full in App. C.1.

The effects of shell thickness, core index and medium index on the resonant frequencies and relative strengths of the modes in this coated nanosphere system are now each considered in turn.

### 5.5.1 Shell thickness

The effect of a change in shell thickness on the nanosphere with an excitonic shell and inert core is now examined. The system chosen in this section is a $d = 100\ nm$ silica ($SiO_2$) core (approximated by $n_1 = 1.46$) with a 3.22 $wt\%$ TDBC:PVA shell in vacuum.

Absorption efficiency spectra for this system as a function of shell thickness are plotted in Fig. 5.5. The spectra are calculated using coated Mie theory, incorporating the permittivity for the shell from the four-level quantum model for TDBC:PVA. The dashed lines on the plot indicate the resonant frequencies obtained using Eq. 5.11 for the system. The solutions arising from the use of the more accurate Eq. 5.17 are plotted in Fig. 5.5 as black lines. The more accurate calculations are in general closer to the Mie theory peaks - the higher energy solution in particular, which is substantially closer, especially for thin shells. This demonstrates that although the approximate solution illustrates the general behaviour of the system fairly well, a more physical model produces more accurate results.

The splitting in Fig. 5.5 is maximised for thin shells as expected from the analysis of Eq. 5.11 above. As predicted, the two modes appear to converge to limiting values for thick shells. The values observed at $t = 40\ nm$ are $\omega_- = 2.157\ eV$ and $\omega_+ = 2.196\ eV$.

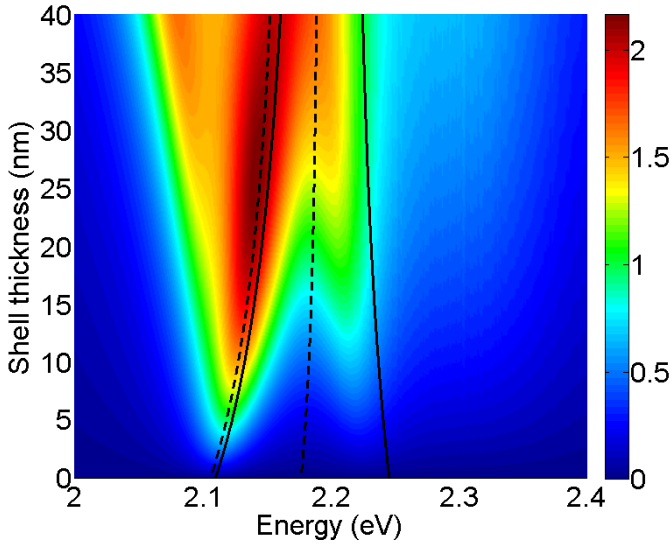


**Figure 5.5:** Mie absorption efficiency spectra (colour plot) as a function of shell thickness for a $d = 100\ nm\ SiO_2$ nanosphere coated with 3.22 $wt\%$ TDBC:PVA in vacuum. Also shown are the calculated resonant energies in the $\gamma \ll \omega$ approximation (dashed lines) and the full quasistatic approximation (black lines). The Lorentz parameters for the shell are $f = 0.3$, $\varepsilon_\infty = (1.52)^2$, $\gamma = 46.1\ meV$, $\omega_0 = 2.11\ eV$.

These Mie theory values are redshifted from the predicted values of $\omega_- = 2.173\ eV$ and $\omega_+ = 2.224\ eV$ by Eq. 5.15 & 5.16, but have percentage errors of only 0.74 % and 1.26 % respectively. This redshift is attributed to retardation effects accounted for within Mie theory.

In Fig. 5.5 there is a lower limit on the shell thickness of $t = 6\ nm$ in order to achieve absorption efficiency in excess of unity. At this point, there is a sufficient amount of dye present in the shell in order for electric field enhancement to be exhibited, without shielding the core completely and losing the distinction between the hybrid modes, as is the case for thicknesses in excess of approximately $t > 25\ nm$, where only one peak is discernible. However, there is a degree of asymmetry between the two hybrid modes: in the range $6\ nm < t < 16\ nm$, only the lower energy mode has an absorption efficiency in excess of unity. This asymmetry is visualised in Fig. 5.6, where the normalised electric field strength and power flow has been plotted for a shell thickness

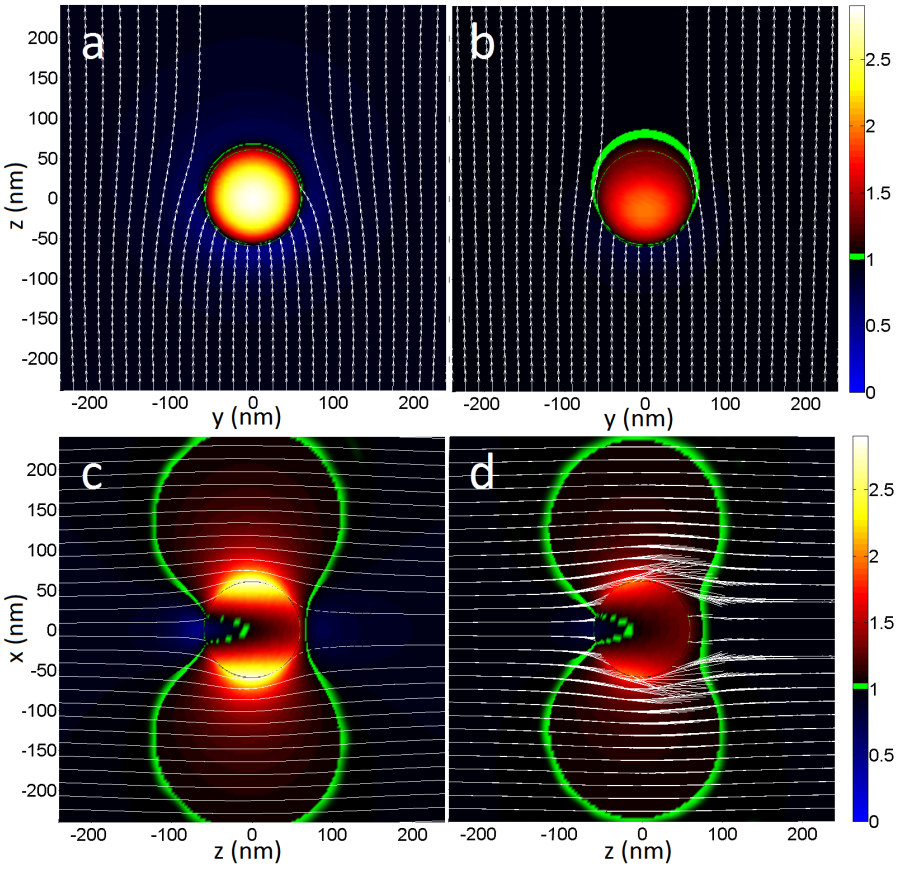


**Figure 5.6:** Normalised electric field strength and power flow around a nanoparticle with a $SiO_2$ core and 3.22 *wt*% TDBC:PVA shell, with $d = 100\ nm$ and $t = 10\ nm$ at (a & c) 2.13 *eV* (582 *nm*) and (b & d) 2.20 *eV* (563 *nm*). Green line: $\zeta = 1$ isosurface.

of $t = 10\ nm$ for each of the two modes. The general shapes of the $\zeta = 1$ isosurfaces are the same as predicted from the quasistatic dipole calculations in Ch. 4. The colour scale in the figure is slightly too course to show it, but field enhancement is evidenced over all solid angles for both modes. However, the streamlines of power flow from the total Poynting vector indicate that the absorption is much less for the $\omega_+$ mode, as the Mie absorption calculations confirm. These calculations therefore demonstrate that electric field enhancement over all solid angles can be brought about in spite of an absorption efficiency below unity.

As the shell thickness is increased in Fig. 5.5, the $\omega_+$ mode exhibits stronger absorption. However it is only between $16\ nm < t < 20\ nm$ where there is a clear splitting between the two modes. This narrow range of shell thicknesses is somewhat limiting from a fabrication perspective if two distinct PEP modes are desired in a spectrum, and therefore the next step is to explore whether the asymmetry illustrated above can be addressed by adjustment of the core index.

### 5.5.2 Core index

For the TDBC@$SiO_2$ nanosphere considered in Fig. 5.5, the $\omega_-$ mode dominates the response of the nanoparticle. However, the relative strength of the two hybridised modes can be seen to be dependent upon the index of the core material, since an increase in core index will tend to increase strength of the electric field within the nanoparticle, leading to a greater degree of depolarisation. In addition, this depolarisation is proportional to frequency to the fourth power through Rayleigh scattering.[151] Therefore, an increase in the core index for a coated nanosphere will lead to an increase in the strength of the $\omega_+$ mode. One material which could provide this behaviour in practice for a TDBC:PVA nanoshell is $TiO_2$, since it possesses a relatively high refractive index[177] of $n = 2.19 \rightarrow 3.08$ across optical frequencies. It is also suitable for nanosphere fabrication.[178]

By modelling $TiO_2$ using the Conrady dispersion formula,[179] Mie absorption efficiency calculations made for a $d = 100\ nm$ nanosphere of $TiO_2$ with a TDBC:PVA coating as a function of coating thickness are plotted in Fig. 5.7 (overleaf). The analytical solutions for the two modes from Eq. 5.17 (where the approximation has been taken such that $TiO_2$ has a constant refractive index of $n_1 = 2.37$ across optical wavelengths) are overlaid on the Mie calculations. In Fig. 5.7, the two Mie theory peaks correspond to the two hybridised modes of the system predicted by the quasistatic theory, albeit with a slight redshift as seen previously for other similar systems due to retardation effects.

In Fig. 5.7, the $\omega_+$ mode now dominates the optical response of the system, due to an increase in the core index. For shell thicknesses in the range $7\ nm < t < 14\ nm$, it is the $\omega_+$ mode only which exhibits absorption efficiency in excess of unity, almost opposite to the system with the $SiO_2$ core considered above. This indicates that the index of the core has been increased too much to balance the two modes equally, and

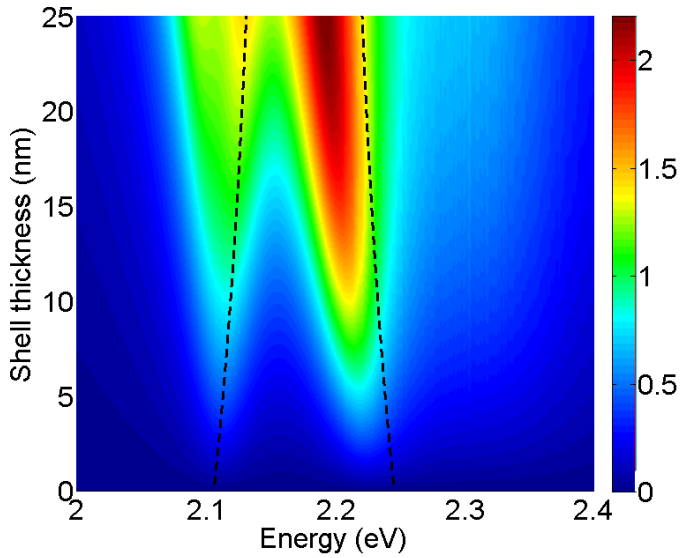


**Figure 5.7:** Mie absorption efficiency spectra for a $d = 100\ nm$ nanosphere of $TiO_2$ with a coating of 3.22 $wt\%$ TDBC:PVA in vacuum. The dashed lines indicate the quasistatic solutions to the resonant energies.

a material with an intermediate index is required to achieve this goal. To perform this redress, an increase in medium index can be utilised, as shown in the following section.

The asymmetry of the two modes in Fig. 5.7 is now examined: the absorption efficiencies of the $\omega_-$ and $\omega_+$ modes peak at 0.8 and 1.4 respectively. The effect of these two modes on the surrounding environment is visualised in Fig. 5.8, where the electric field strength (normalised to the incident field) and the power flow around the nanoparticle (calculated from the total Poynting vector) are plotted for two orthogonal viewpoints for each mode on resonance. In each plot, the light is x-polarised and incident along the positive z-axis. Values on the colour plot in excess of unity indicate electric field enhancement.

The shape of the region of electric field enhancement brought about by these two modes shown in Fig. 5.8 mirrors the shape expected from the elementary dipole calculations outlined in Ch. 4. The plots for both modes show electric field enhancement over all solid angles, evidenced by a circle of field enhancement around the nanoparticle equator in each case, implying a PEP mode. The streamlines of power flow in the y-z plane in Fig. 5.8b indicate that for the $\omega_+$ mode, the nanoparticle bends the incident light around it more significantly than the $\omega_-$ mode does in Fig. 5.8a (this is the opposite to the findings of Fig. 5.6). In addition, there is a greater extinction of power from the $\omega_+$ mode which leads to a higher absorption efficiency for the $\omega_+$ mode. In the case of the $\omega_+$ mode, the light is drawn into the nanoparticle from outside its geometrical reach, a property indicative of a particle polariton mode (see Ch. 4). However, the absorption efficiency for the $\omega_-$ mode is at first glance insufficient to

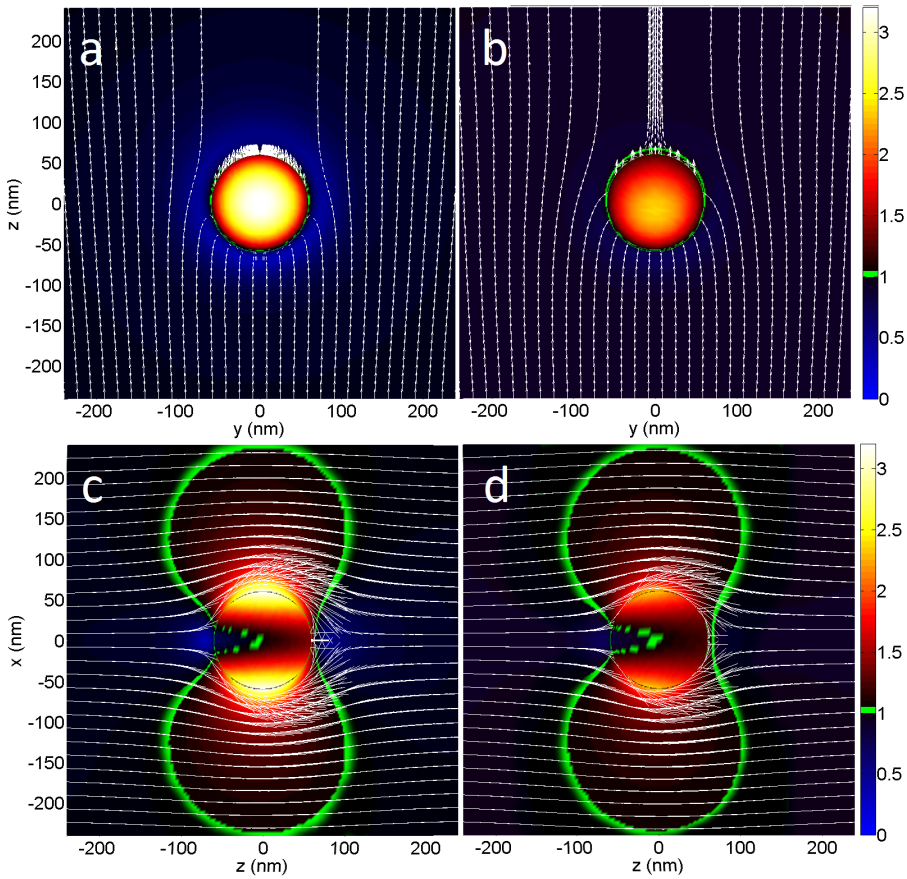


**Figure 5.8:** Relative time-averaged electric field strength and power flow in the vicinity and on the surface of a $d = 100\ nm\ TiO_2$ nanosphere with a $t = 10\ nm$ coating of 3.22 $wt\%$ TDBC:PVA in vacuum, on the (a & c) $\omega_-$ resonance at 2.11 $eV$ (586.7 $nm$) and the (b & d) $\omega_+$ resonance at 2.21 $eV$ (560.7 $nm$) in the (a & b) y-z and (c & d) x-z planes. Light is incident along the positive z-axis. Green line: $\zeta = 1$ isosurface.

demonstrate a PEP mode. Computing the mean effective radii of these two modes using Eq. 5.9 gives $r_{\text{eff}} = 53.7\ nm$ and $r_{\text{eff}} = 71.0\ nm$ for the $\omega_-$ and $\omega_+$ modes respectively. This shows that the effective radius of the $\omega_-$ mode lies outside the core of the nanoparticle, but within the shell, suggesting that if this PEP mode is excited, its electric field enhancement is contained within the nanoparticle - this is a possible manifestation of the cavity exciton polariton mode. The effective radius of the $\omega_+$ mode suggests that field enhancement should be felt (on average) for distances up to 11.0 $nm$ away from the nanoparticle surface, giving strong evidence for the existence of the $\omega_+$ PEP mode for this nanoparticle system.

### 5.5.3 Medium index

An increase in medium index around a coated nanosphere acts to effectively decrease the core index, and *vice versa*. Given that an isolated non-absorbing nanosphere will tend to scatter more strongly towards the blue end of the spectrum (Rayleigh scattering[151]) and that a nanosphere with a higher refractive index will scatter more strongly, an increase in medium index will act to decrease the strength of the $\omega_+$ mode relative to the $\omega_-$ mode, the former of which lies towards the bluer end of the spectrum. This dependency is illustrated in Fig. 5.9, in which absorption efficiency spectra are plotted for four different embedding media. The system in question is a nanosphere with a $TiO_2$ core and a $t = 10$ *nm* coating of 3.22 *wt%* TDBC:PVA. The models used for the permittivity of $TiO_2$ and TDBC are the Conrady dispersion formula[179] and the four-level quantum model respectively. The four spectra in Fig. 5.9 have been offset for clarity. For $n_m < 2$, the $\omega_+$ mode dominates the response; for $n_m = 2$ the strength

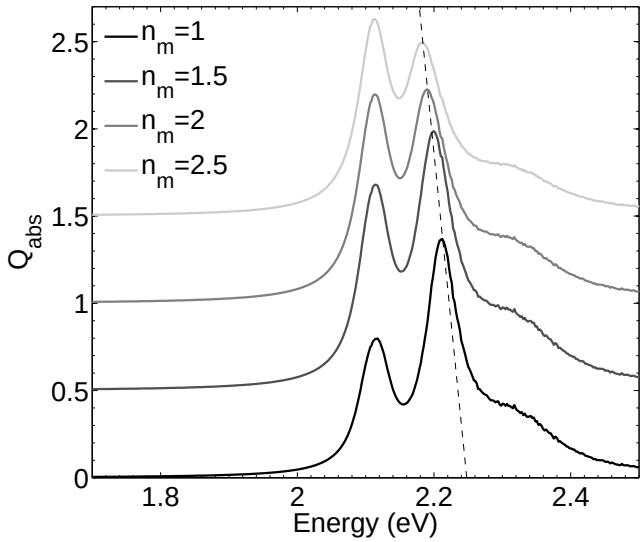


**Figure 5.9:** Offset Mie absorption efficiency spectra for a $d = 100$ *nm* nanosphere of $TiO_2$ with a $t = 10$ *nm* coating of 3.22 *wt%* TDBC:PVA for four different medium indices.

of the two resonance peaks are approximately in balance; and for $n_m = 2.5$, the $\omega_-$ mode dominates. Another finding from Fig. 5.9 is that the $\omega_+$ mode redshifts subtly with an increase in medium index: this dependency can be seen from examination of Eq. 5.16.

The electric field strength and power flow around the nanoparticle for the $\omega_-$ and $\omega_+$ modes when brought into balance by a $n_m = 2$ medium is examined in Fig. 5.10 from two orthogonal viewpoints. In the y-z plane shown in Fig. 5.10a & 5.10b, the lines of power flow reveal that the nanoparticle acts as a 'magnet for light' for both modes, in

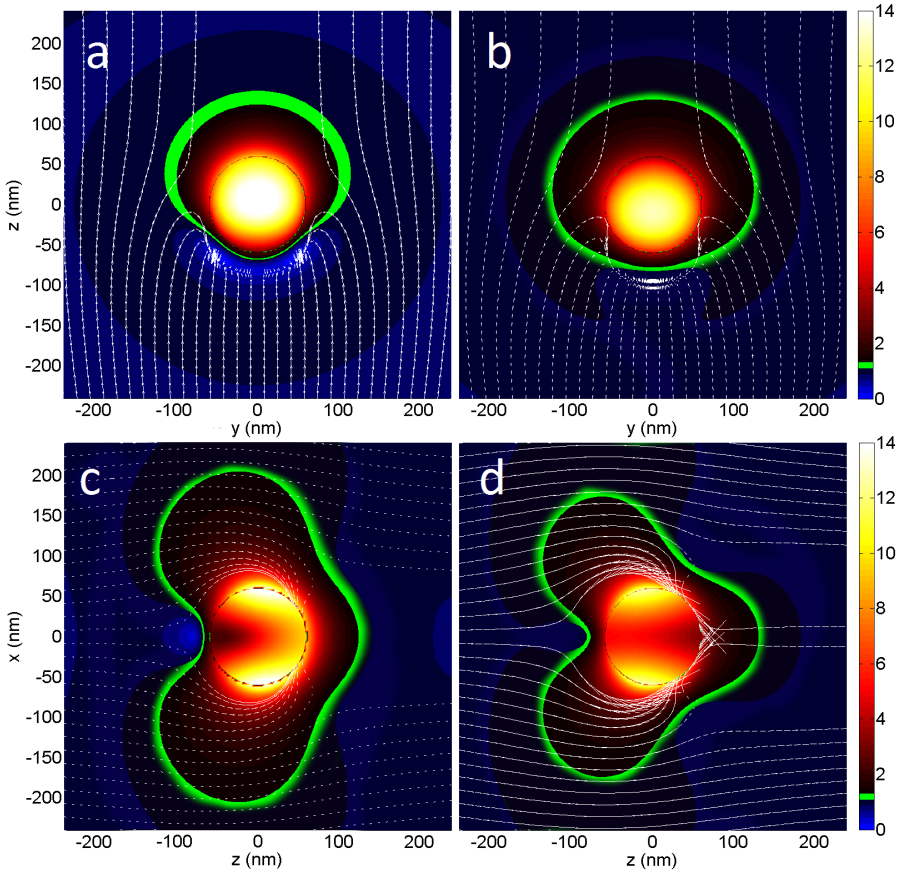


**Figure 5.10:** Electric field strength and power flow for the same system as Fig. 5.8 but in an $n_m = 2$ medium. The $\omega_-$ mode is visualised at 2.11 $eV$ (587.7 $nm$) (a & c) and the $\omega_+$ mode is visualised at 2.21 $eV$ (566.7 $nm$) (b & d).

that light incident from outside the geometrical radius of the nanoparticle ends up on the surface of the nanoparticle; this effect is stronger than the same effect observed for the $\omega_+$ mode in Fig. 5.8, for which the only difference is a change in medium index. This strengthening of the effect in Fig. 5.10 is aided by the fact that a nanoparticle with an index lower than the medium index will act as a nanoparticle void, which can act as an attractor to light,[180] which in turn boosts the electric field enhancement around the nanoparticle.

Fig. 5.10a & 5.10b seem to indicate that incident light never reaches the nanoparticle, but Fig. 5.10c & 5.10d reveal that the incident light is transported up and around the nanoparticle before being tightly confined at two points on the nanoparticle surface, elevating the electric field enhancement around these two points. This mechanism is also responsible for depression of the electric field on the nearside of the nanoparticle, seen most clearly by the blue region in Fig. 5.10a & 5.10c for the $\omega_-$ resonance.

The similarity in the absorption efficiencies of the two nanoparticle modes (*cf.* Fig. 5.9) implies that the electric field isosurfaces of the two modes should be similar in volume to each other. Fig. 5.10a-d reveal that this is so, where the region of electric field enhancement in each is marked by a green line. These isosurfaces are larger than observed for the same system in the $n_m = 1$ medium (Fig. 5.8). This is an expected result, since it was shown in Ch. 4 through consideration of the quasistatic dipole that an increase in medium index would result in an increase in the size of the electric field isosurface on a nanosphere resonance (*cf.* Eq. 4.12). From Fig. 5.10, the same would appear to be true for dipole modes in coated nanospheres. The electric field distributions on the nanoparticle surface for these two modes also appear different to each other as expected.

Overall, Fig. 5.10 indicates field enhancement over all solid angles around the TDBC@$TiO_2$ coated nanosphere, together with the nanoparticle acting as a 'magnet for light' on these two resonances. These two properties combined are evidence that these two modes are indeed (hybrid) PEP modes.

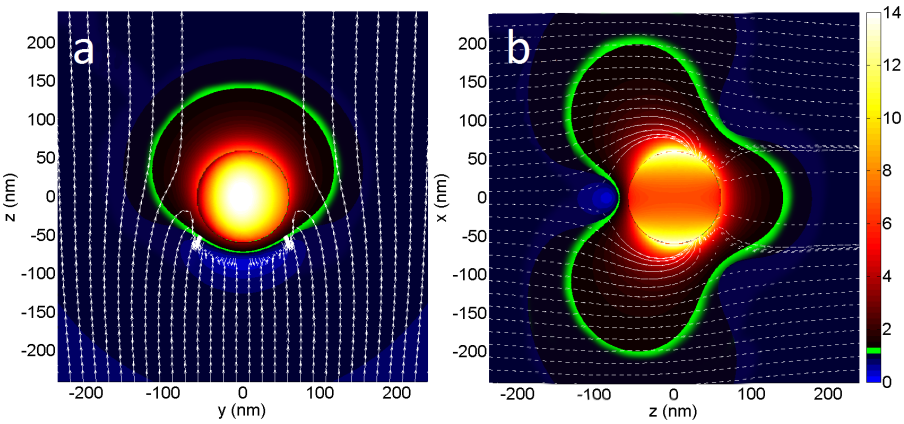


**Figure 5.11:** Relative time-averaged electric field strength and power flow in the vicinity of the same system shown in Fig. 5.10, but off-resonance at 2.15 *eV* (577 *nm*).

In Fig. 5.11, power flow and field enhancement is shown for the same system as in Fig. 5.10 but off-resonance, between the two modes at 2.15 *eV* (577 *nm*), again for a medium index of $n_m = 2$. In this figure, electric field enhancement is evidenced as before, but crucially, the nanoparticle permits a greater flux of light past it or through it, resulting in a lower absorption efficiency. The electric field distribution over the surface of the nanoparticle is an intermediate distribution between the distribution exhibited by the $\omega_-$ and $\omega_+$ modes, indicating that at this frequency, both modes may contribute equally to the optical response.

In all, both hybrid PEP modes can be excited in a nanoshell of excitonic material. These modes exhibit field enhancement and strong absorption provided that the shell thickness and dye concentration in the shell are sufficient. In addition, the relative strength of the two modes can be balanced through adjustment of both the core and medium indices.

## 5.6 Excitonic Core and Shell

Now that hybrid PEP modes have been demonstrated for an excitonic nanoshell, the inert core is substituted for an excitonic core in order to explore hybrid modes in a new context. So far, the excitonic dye chosen has been the dye TDBC. In this section, the excitonic dye is not necessarily representational of TDBC. In addition, the planar distribution (rather than the volume distribution) for the dye aggregates is assumed. These choices are made so as to examine general qualitative results, and to enable a straightforward comparison with the results which would be obtained using the experimentally-determined permittivities for the TDBC:PVA films of differing dye concentration.

In this section, in order to obtain values of the resonances from quasistatic theory through the master equation (Eq. 5.3), both the core and shell are modelled as single-oscillator Lorentz dielectrics, *i.e.*

$$\varepsilon_n = \varepsilon_{\infty_n} + \frac{f_n \omega_{0_n}^2}{\omega_{0_n}^2 - \omega^2 - i\gamma_n \omega}. \tag{5.18}$$

The approach taken in this section is similar to that of the previous section, *i.e.* by expansion of Eq. 5.3 to obtain a polynomial, which when solved, yields the resonance frequencies.

First, an aside to determine the expected number of hybrid modes in such a nanoparticle: as seen above, an excitonic nanoshell can exhibit two hybrid PEP modes, whereas a bare nanosphere will exhibit one PEP mode only. The system considered in this section can be imagined as a superposition of these two sub-systems, leading to a maximum of three modes for the system.

Using Eq. 5.18 in Eq. 5.3 and expanding in terms of $\omega$ gives a polynomial of the following form,

$$\begin{aligned} &c_6\omega^6 + c_4\omega^4 + c_2\omega^2 + c_0 + \\ &i\omega(c_5\omega^4 + c_3\omega^2 + c_1) = 0, \end{aligned} \tag{5.19}$$

where the coefficients $c_i$ are real-valued. For $\gamma \gg 1$, the real part of Eq. 5.19 has only one real solution, whereas the imaginary part gives two real solutions. Therefore, three roots arise from this equation: the number expected as postulated above. The coefficients of the cubic imaginary part are written out in full in App. C.2. In order to simplify the system a little, it is assumed throughout this section that the embedding material for the dye is the same for both the core and the shell *i.e.* $\varepsilon_{\infty_1} = \varepsilon_{\infty_2} = \varepsilon_\infty$.

## 5.6.1 Shell exciton energy

In this section, the energy of the exciton transition in the core material ($\omega_{0_1}$) is held constant, and the energy of the exciton transition in the shell material ($\omega_{0_2}$) is varied. The question to be addressed in this section is to what extent the three modes of the nanoparticle interact with each other, and if they do, whether they avoid each other or not. The materials referred to in this section do not necessarily represent physical materials, but the calculations made here help to inform the reader from where the modes in such nanoparticles arise.

Re-writing the imaginary part of Eq. 5.19 in terms of $\omega_{0_2}$ gives the following,

$$c_5\omega^4 + (A_2\omega_{0_2}^2 - A_5)\omega^2 + (A_1\omega_{0_2}^2 + A_3)\omega_{0_2}^2 = 0, \tag{5.20}$$

where $A_i$ are constants in $\omega_{0_2}$. Solving for $\omega^2$ gives the following two solutions,

$$\omega^2 = -\frac{(A_2\omega_{0_2}^2 - A_5)}{2c_5} \pm \sqrt{\frac{(A_2\omega_{0_2}^2 - A_5)^2}{c_5^2} - \frac{(A_1\omega_{0_2}^2 + A_3)\omega_{0_2}^2}{c_5}}. \tag{5.21}$$

In the limit where $\omega_{0_2} \to 0$, the limiting solution $\omega = A_5/c_5$ is obtained where,

$$\begin{aligned} A_5 =& (2[\varepsilon_\infty(1+2x^3) + 2\varepsilon_m(1-x^3)]f_1\omega_{0_1}^2 \\ &+ 3\varepsilon_\infty[(\varepsilon_\infty + 2\varepsilon_m)\gamma_1\gamma_2 + 2(\varepsilon_\infty + 2\varepsilon_m)\omega_{0_1}^2])\gamma_2, \end{aligned} \tag{5.22}$$

and $c_5$ in this case is equal to $c_5 = 3\varepsilon_\infty(\varepsilon_\infty + 2\varepsilon_m)(\gamma_1 + 2\gamma_2)$. In the limit where $\gamma_1 \ll 1$, the solution reduces to,

$$\omega = \omega_{0_1}\sqrt{\left(\frac{1}{3\varepsilon_\infty} + \frac{2(\varepsilon_\infty - \varepsilon_m)x^3}{3\varepsilon_\infty(\varepsilon_\infty + 2\varepsilon_m)}\right)f_1 + 1}. \tag{5.23}$$

This solution implies a particle mode in the core which scales with $\sqrt{f_1}$, similar to that of the particle mode of an excitonic nanosphere with an inert shell (Eq. 5.8). Therefore, for values of $\omega_{0_2}$ far detuned from $\omega_{0_1}$, there is only one mode which will be evident: the particle mode arising from the excitonic core. Symmetry arguments can be used to find a similar result for $\omega_{0_2} \to \infty$. Therefore, the range of values for $\omega_{0_2}$ to be examined for splitting behaviour should be values for which $\omega_{0_1}$ and $\omega_{0_2}$ are similar.

These predictions are now tested. The specific core material studied in this section is assumed to be 1.46 *wt%* TDBC:PVA (planar distribution, *cf.* Fig. 4.5a). The two-level quantum model is used for clarity. The material of the shell is taken as the same material but for a dye concentration of 0.4 *wt%* so that the field may penetrate

the shell more easily. The range of exciton transition energies in the shell material is 2.0 $eV < \omega_{0_2} < 2.3\ eV$, and the orientation of the nanoparticle is held fixed such that the incident electric field lies in the plane within which the aggregates are orientationally distributed.

Mie absorption spectra calculated for a nanosphere of these two materials in vacuum with a $d = 100\ nm$ core and a $t = 15\ nm$ shell are illustrated in Fig. 5.12. The resonant energies determined using Eq. 5.19 are indicated by the lines overlaid on the plot.

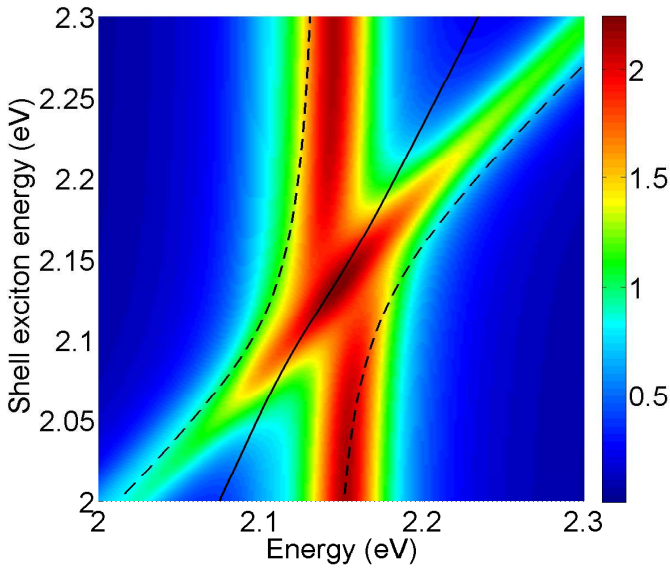


**Figure 5.12:** Mie absorption efficiency spectra (colour plot) as a function of shell exciton transition energy for a $d = 100\ nm$, $t = 15\ nm$ nanosphere, together with resonant frequencies calculated from the real (solid line) and imaginary (dashed lines) parts of Eq. 5.19 respectively. The core and shell materials are 1.46 *wt%* TDBC:PVA ($\omega_0 = 2.11\ eV$) and a 0.4 *wt%* TDBC:PVA-like material respectively.

For regions on Fig. 5.12 for which the energy difference between the shell and core exciton transitions is large, two absorption peaks are evident; these peaks are mirrored by the analytical solutions for the hybrid modes. The absence of a third absorption peak indicates that in this case, two hybrid modes are 'bright', and the other mode is 'dark'. It can be seen that one of the modes remains close to 2.15 $eV$, close to the PEP mode of the core at 2.16 $eV$, as predicted by Eq. 5.23.

The two bright modes in Fig. 5.12 do not cross, and seem to avoid each other in avoided crossing behaviour for $\omega_{0_2} \approx \omega_{0_1}$ (2.11 $eV$). For this value of $\omega_{0_2}$, the two nanoparticle materials are most alike and the splitting between the two hybrid modes is minimised. At this point, the nanosphere behaves almost like a homogeneous nanosphere, and only one peak is evident, accounted for by the third analytical (central) solution indicated in the figure, which becomes bright in the range $2.07\ eV < \omega_{0_2} < 2.17\ eV$. The position of the peak at 2.15 $eV$ indicates that this mode may either be the result of hybridisation, or simply the limiting case for which the mode approaches that of a homogeneous

nanoparticle; this is a question which is yet to be resolved, since the two energies are very close - within 0.01 $eV$ of each other.

### 5.6.2 Shell dye concentration

Absorption spectra for the same nanoparticle system are now examined as a function of dye concentration in the shell material. In order to determine the expected behaviour of the resonant modes of the nanoparticle, a similar procedure to the one outlined in the previous section is followed: first, the imaginary part of Eq. 5.19 is written in terms of the oscillator strength $f_2$,

$$c_5\omega^4 - (A_5 + A_2 f_2)\omega^2 + (A_1 f_2^2 + A_3 f_2 + A_6) = 0, \tag{5.24}$$

where $A_i$ are real positive constants and $c_5$ has the same value as outlined in the previous section. Solving for $\omega^2$,

$$\omega^2 = \frac{1}{2c_5}\left[(A_5 + A_2 f_2) \pm \sqrt{(A_5 + A_2 f_2)^2 - 4c_5(A_1 f_2^2 + A_3 f_2 + A_6)}\,\right]. \tag{5.25}$$

Given that $f_2$ is related linearly to dye concentration by $f_2\omega_{0_2}^2 = N_2 e^2/\varepsilon_0 m$ (see Ch. 2), for an increase in shell dye concentration, the first term in Eq. 5.25 demonstrates that the mean of the two modes will blueshift; the term in the square root shows that the splitting between the two modes will increase.

In order to test these predictions, Mie absorption spectra are plotted in Fig. 5.13 for a 1.46 *wt%* TDBC:PVA core and a TDBC:PVA shell, both with aggregates in the planar distribution. The permittivity of the TDBC is calculated using the four-level quantum model, so that the spectra produced can represent best what might be accomplished in an experiment. The nanoparticle geometry is fixed with a diameter $d = 100$ *nm* and a shell thickness $t = 10$ *nm*. The quasistatic solutions from Eq. 5.19 are overlaid as thick lines in Fig. 5.13, along with the quasistatic solutions for the shell only (as thin lines). The higher-energy mode is best accounted for by the result from Eq. 5.19, as might be expected, and the results from either model for the lower-energy mode are fairly similar. It must be emphasised that the quasistatic calculations are based upon a single-oscillator Lorentz model, and therefore only one transition: these quasistatic models cannot account for the higher-order effects associated with multiple energy levels, as circled in Fig. 5.13.

One immediate observation from Fig. 5.13 is that out of the three modes theorised from the quasistatic calculations, only two are bright: the (central) dark mode is only bright for very low dye concentrations in the shell ($< 0.75\%$). This suggests that the central mode may correspond to the particle mode of the core, or to the mode of the homogeneous nanosphere (as hypothesised above). The two predictions regarding the blueshifting and splitting of the two outer modes are seen to be correct.

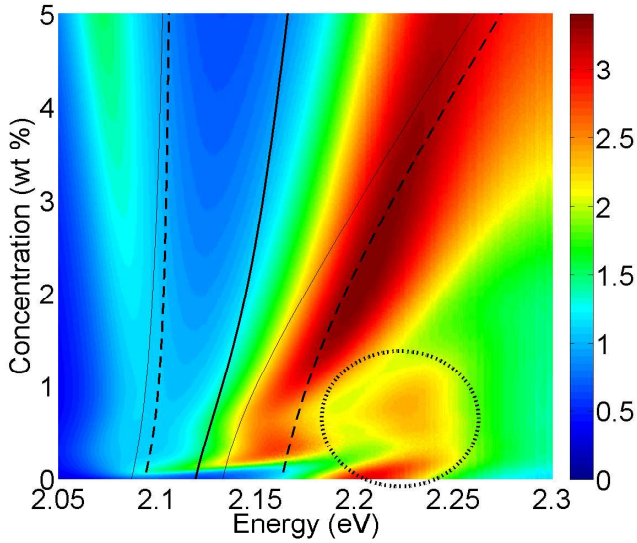


**Figure 5.13:** Mie absorption efficiency spectra (colour plot) as a function of shell dye concentration for a $d = 100\ nm$ 1.46 *wt%* (planar distribution) TDBC:PVA core, and a $t = 10\ nm$ TDBC:PVA shell. Thick lines: quasistatic hybrid mode solutions. Thin solid lines: quasistatic nanoshell solutions. Dotted circle: higher-order feature.

From the two bright modes, it is the mode of the highest energy which dominates the spectra for all concentrations. This mode is close to the solution for the antisymmetric mode of the shell (as indicated on the plot), especially for high dye concentrations in the shell. This finding shows that as the dye concentration of the shell is increased, the shell dominates the response. As this occurs, the modes of the nanoparticle tend towards those of the shell. Considering the mode of highest energy to be the 'antisymmetric' mode as seen for nanoshells, the fact that the antisymmetric mode is the 'brightest' mode echoes the finding for the TDBC@$SiO_2$ nanoparticle in vacuum. As shown above, the relative strength of the symmetric and antisymmetric modes of a nanoshell can be adjusted by embedding the nanoparticle in a medium with a higher refractive index. This redress in the strength of the modes comes at the cost of a reduction in the absorption efficiency of the higher-energy mode. However, in the core-shell geometry there exists an alternative to this approach: replacement of the excitonic core with a metal core, as examined in the following section.

## 5.7 Metal Core, Excitonic Shell

As shown in Sec. 5.6, the PEP of an excitonic core can interact with the two hybrid excitonic polariton modes of an excitonic nanoshell to produce three possible hybrid PEP modes. In this section, the excitonic core of the nanosphere is replaced with a

metal core. Consequently, the metal core can exhibit a PPP mode which may undergo hybridisation with the modes of the excitonic shell to form 'plexciton'[166,181] modes. It is already known that a shift can be induced in the PPP mode of a silver core with the adsorption of a dye-doped shell,[16] and similar nanoparticle systems have seen application within surface-enhanced Raman scattering (SERS)[182]. In this section, the extent to which plexciton modes can be excited and tuned for a TDBC@*Ag* nanosphere is explored.

In order to obtain solutions for resonances in such systems, the master equation in Eq. 5.3 is used in conjunction with the Drude model (Eq. 2.20) for $\varepsilon_1$, and the single-oscillator Lorentz model for $\varepsilon_2$. Re-arrangement of the resultant equation gives a polynomial of the form,

$$\begin{aligned} &c_6\omega^6 + c_4\omega^4 + c_2\omega^2 + c_0 + \\ &i\omega(c_5\omega^4 + c_3\omega^2 + c_1) = 0, \end{aligned} \tag{5.26}$$

from which solutions for $\omega$ can be found. The real part of Eq. 5.26 is a cubic in $\omega^2$, and the imaginary part is a quadratic in $\omega^2$. The real coefficients $c_i$ in Eq. 5.26 are written out in full in App. C.3.

From this point on in this section, the shell material is assumed to be an isotropic material, and aggregates within it are assumed to be distributed in the volume distribution. The concentration of the dye is presumed to be 3.22 *wt%* unless otherwise stated.

### 5.7.1 Shell exciton energy

Adopting a similar approach to the exciton-exciton nanoparticle in Sec. 5.6, the Mie absorption spectra as a function of exciton transition energy in the shell material (labelled here as $\omega_0$) is calculated. Again, potential anti-crossing behaviour is investigated.

In order to gain some basic understanding of what might be expected by varying $\omega_0$, the imaginary part of Eq. 5.26 is taken, and the expressions for the coefficients outlined in App. C.3 are used. This produces a quadratic in $\omega^2$ which when solved takes the following form,

$$\omega^2 = \frac{a_1\omega_0^2 + a_2}{c_5} \pm \sqrt{\frac{(a_1\omega_0^2 + a_2)^2}{4c_5^2} - \frac{(a_3 + a_4\omega_0^2)\omega_0^2}{c_5}}, \tag{5.27}$$

where $a_i$ are real-valued constants. Eq. 5.27 implies two distinct resonant frequencies. In the limit where $\omega_0 \to 0$, one of these solutions vanishes ($\omega = 0$) and the other becomes $\omega = \sqrt{a_2/c_5}$ where,

$$a_2 = 2\gamma(\gamma\gamma_p(\varepsilon_b^2 + \varepsilon_\infty\varepsilon_m) + 2\varepsilon_m\omega_p^2)(1 - x^3) + \varepsilon_b\gamma(\varepsilon_\infty\gamma\gamma_p + 2\omega_p^2)(1 + 2x^3) + (2\varepsilon_b\varepsilon_m\gamma^2\gamma_p)(2 + x^3). \quad (5.28)$$

Since for metals $\{\gamma, \gamma_p\} \ll \omega_p$, $a_2$ becomes,

$$a_2 \to 4\gamma\omega_p^2[(2\varepsilon_m + \varepsilon_b) + 2(\varepsilon_b - \varepsilon_m)x^3]. \quad (5.29)$$

Comparing this expression with the value of $c_5$ in App. C.3, the limiting value of the resonant frequency tends towards $\omega \to \omega_p$, multiplied by a factor close to unity for all aspect ratios, $x$. Symmetry arguments imply the same finding in the limit $\omega_0 \to \infty$. Together, these two findings imply that for large detunings of $\omega_0$ away from $\omega_p$, the dominant mode of the system is expected to be the PPP mode, which may be modified slightly (but not significantly) by the presence of the exciton transition. Therefore, *via* these arguments, a range of exciton transition energies to be investigated in this section is established for which mode hybridisation might be expected to occur: values of $\omega_0$ in the vicinity of $\omega_p$.

As discussed in Ch. 2, silver (unlike gold) has no intraband transitions at optical frequencies; its permittivity can therefore be modelled to a good degree of accuracy with a Drude model, enabling the calculations for the resonant frequencies from Eq. 5.26 to be evaluated against coated Mie theory. Furthermore, as shown in Ch. 4, silver nanospheres when embedded in a $n_m = 1.5$ medium can exhibit PPP modes at optical frequencies (at around 3 $eV$), unlike aluminium. Therefore, a (plasmonic) silver core with an excitonic nanoshell provides the potential for plexciton modes at optical frequencies.

Given that Eq. 5.26 is based upon quasistatic theory, the solutions for $\omega$ are expected to hold best for relatively small metal nanospheres. Therefore, the choice made for the nanoparticle dimensions in this section are a core of $d = 10$ $nm$, and a shell with $t = 2$ $nm$. The material of the shell is fictional, but the parameters used other than that of the exciton transition energy are that of 3.22 *wt%* TDBC:PVA using the four-level quantum model.

Mie absorption efficiency spectra for this system as a function of exciton transition energy in the range $1.2\ eV < \omega_0 < 3.5\ eV$ are visualised in Fig. 5.14 (overleaf). As seen in the figure, absorption occurs at the exciton energy $\omega_0$ (as expected) and the dashed line corresponding to one of the solutions from the real part of Eq. 5.26 follows this peak faithfully. The value of $\varepsilon'$ at $\omega_0$ is too high to permit a polariton mode at this frequency, so this mode is not a polariton mode; merely a feature corresponding to exciton excitation. The two peaks either side of this exciton excitation in Fig. 5.14 arise from the PPP mode of the silver core, split and shifted by the excitonic shell. These peaks are mirrored by both the scattering efficiency spectra (not shown) and by the solutions to the real and imaginary parts of the master equation, as indicated on the plot. These solutions are generally complex, given that the CM condition is unlikely to be fulfilled perfectly, so the solutions obtained from the real and imaginary

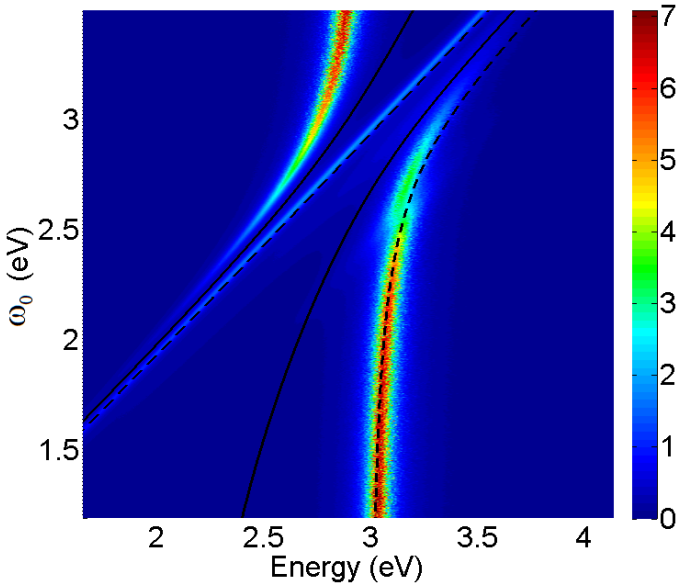


**Figure 5.14:** Mie absorption efficiency spectra for a nanosphere with a $d = 10\ nm$ silver core and a $t = 2\ nm$ 3.22 $wt\%$ excitonic coating in a $n_m = 1.5$ medium as a function of shell exciton energy, $\omega_0$. The black dashed and solid lines are the analytical solutions for the resonances from the real and imaginary parts of the master equation respectively.

parts are expected to differ. The higher-energy peak is best accounted for by another of the solutions from the real part of Eq. 5.26, whereas the lower-energy peak is best accounted for by one of the solutions from the imaginary party of Eq. 5.26. The percentage errors between the mode of higher-energy and the peak from coated Mie theory is within 0.3% for all values of $\omega_0$. The percentage error for the lower-energy mode is within 10%. These two modes exhibit avoided crossing behaviour.

For small values of $\omega_0$ in Fig. 5.14, the strong absorption peak in the visible spectrum tends towards the PPP mode of the bare silver nanosphere in the medium (at 3.0 $eV$). This suggests that an increase in the exciton transition energy of the shell material merely shifts the plasmon mode, as reported elsewhere[16] for adsorption of dyes on silver nanospheres, and as expected from the mathematical arguments above. The mode becomes blueshifted by up to 0.37 $eV$ ($\Delta\lambda = 45\ nm$) at an exciton transition energy of $\omega_0 \approx 2.8\ eV$, beyond which the mode fades in strength with increasing exciton transition energy. For $\omega_0 > 2.5\ eV$, another mode becomes evident, manifested as a 'kink' in the (shifted) PPP mode, which is approximately the same strength as the other PPP mode on the lower energy side of the exciton transition absorption. Given that these two modes mirror each other and their spectral location depends upon the exciton transition energy, it is probable that these two modes are the result of hybridisation with the exciton mode, and are therefore plexciton modes.

The magnitude of the splitting between these two plexciton modes in Fig. 5.14 is dependent upon $\omega_0$, and is minimised when $\omega_0 = 2.97\ eV$, corresponding to the

effective plasma frequency of silver in the medium. For a TDBC coating ($\omega_0 = 2.11\ eV$), the splitting between the two plexciton modes is approximately 1.0 $eV$. The plexciton modes in the absorption and scattering efficiency spectra are both approximately balanced with the exciton transition energy set to $\omega_0 = 2.8\ eV$; these spectra are plotted in Fig. 5.15. Given that there are three peaks in both the absorption

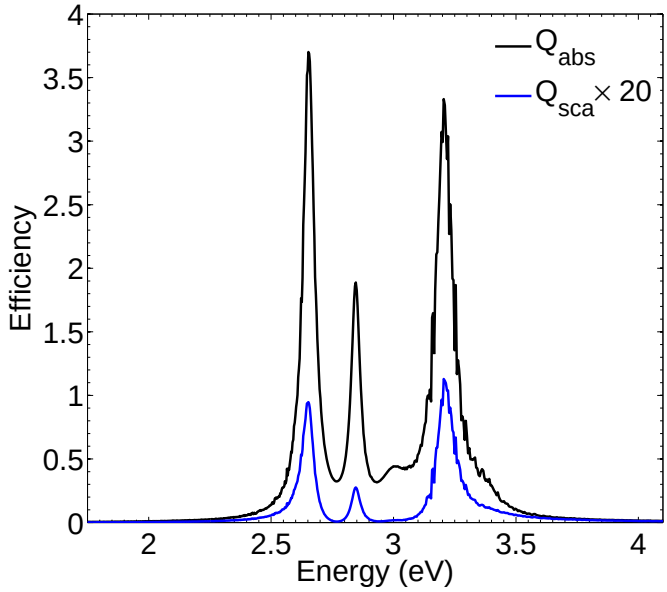


**Figure 5.15:** Mie absorption and scattering (×20) efficiency spectra for a $d = 10\ nm$ silver nanosphere with a $t = 2\ nm$ excitonic coating, with $\omega_0 = 2.8\ eV$ in a $n_m = 1.5$ medium.

and (crucially) the scattering spectra resulting from the splitting of the plasmon mode by the exciton mode, evidence is presented for strong coupling in the system.[183] Strong coupling suggests hybridisation between these two distinct modes, and therefore further evidence for plexciton modes. The quality factors of the peaks corresponding to the low-energy plexciton, exciton, and high-energy plexciton modes in Fig. 5.15 are 63.8, 39.3 and 36.2 respectively. The first of these is comparable to the quality factor of the PEP mode for the TDBC:PVA nanosphere ($Q = 67.7$) examined in Ch. 4. This, coupled with the observation from Fig. 5.14 that the lower-energy plexciton mode can exhibit an absorption efficiency in excess of unity across the energy range $2.30\ eV < E < 2.89\ eV$ ($\Delta\lambda = 110\ nm$) suggests that the spectral location of the plexciton mode can be engineered with a careful choice of dye molecule. The quality factors of the two remaining modes in Fig. 5.15 are not as high as for the lower-energy plexciton mode, but are still approximately four times that of the quality factor associated with the PPP mode of the silver nanosphere, as seen in Ch. 4 (*cf.* Fig. 4.6).

The difference (the splitting) between the two quasistatic solutions for the plexciton modes is plotted in Fig. 5.16 as a function of $\omega_0$, along with the splitting for similar nanoparticles with differing aspect ratios $x$ (as defined in Sec. 5.2). It can be seen that the splitting can be reduced for exciton transition energies near to the effective plasma

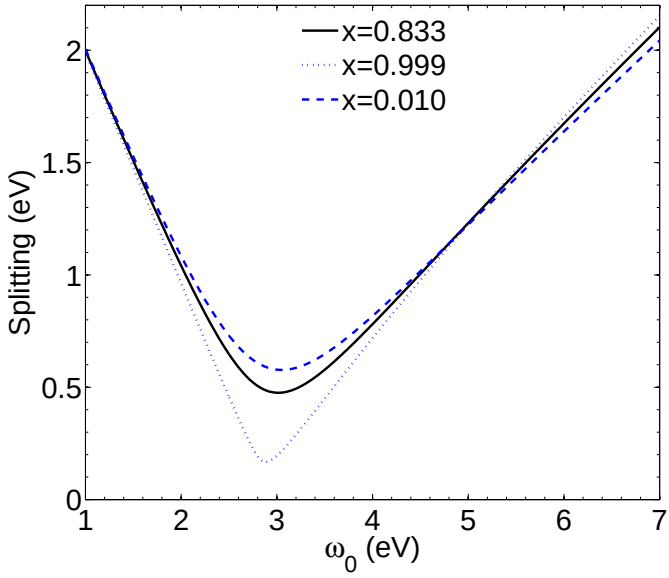


**Figure 5.16:** Plexciton mode splitting for a silver nanosphere with an excitonic coating as a function of exciton energy for thick (blue dashed) and thin (blue dotted) shells. The aspect ratio considered in Fig. 5.14 is indicated with the black line.

frequency for silver in the medium ($\omega_0 \approx 3\ eV$) for thinner shells, and increased for thicker shells. The increase in splitting achievable by adjustment of the shell thickness for TDBC dye ($\omega_0 = 2.11\ eV$) is 0.1 $eV$, which translates to a shift in the resonant energies of $\Delta\lambda = 42\ nm$. These findings demonstrate that the resonances for this system can in principle be tuned with careful design of the nanoparticle aspect ratio *i.e.* the ratio of the core diameter to the overall nanoparticle diameter. For dyes with exciton transitions close to that of the plasma frequency of the silver core, this tuning with aspect ratio is maximised.

### 5.7.2 Shell dye concentration

As seen in the previous section, three modes are present for a nanoparticle with a plasmonic core and an excitonic dye shell. The splitting between the two outermost (plexciton) modes is minimised for exciton transition energies close to the PPP mode of the metal core. In this section, the core material is kept as silver, and the effect of a change in shell dye concentration upon the plexciton splitting is explored, with the exciton transition energy held fixed.

In order to consider mathematically the effect of an increase in dye concentration on the three modes, solutions to the real part of Eq. 5.26 are considered for two cases: first, with the oscillator strength of the dye set to $f = 0$, and second, with $f > 0$. In

either case, the resultant equation is a cubic in $\omega^2$. For $f = 0$, the real part of Eq. 5.26 assumes the form,

$$A_6\omega^6 + A_4\omega^4 + A_2\omega^2 + A_0 = 0, \tag{5.30}$$

where $A_i$ are real positive constants. Keeping the same symbols for $f > 0$, this equation becomes,

$$A_6\omega^6 + (A_4 - B_4 f)\omega^4 + (A_2 + B_2 f + C_2 f^2)\omega^2 + (A_0 + B_0 f) = 0, \tag{5.31}$$

where $B_i$ and $C_2$ are real positive constants. Eq. 5.30 & 5.31 can be solved for the unperturbed and perturbed resonant frequencies, $\omega$ and $\omega'$. The quantity $\Delta\bar{\omega} = \sqrt{\omega^2 - \omega'^2}$ gives a measure for the expected shift in the resonant frequency with an increase in oscillator strength. For the central mode, $\Delta\bar{\omega} = 0$, indicating no shift with an increase in oscillator strength, and hence, no shift with a change in dye concentration. For the other two modes,

$$\Delta\bar{\omega} = \frac{\omega_0}{\sqrt{3}}\sqrt{\frac{B_4}{A_6}}\sqrt{f}, \tag{5.32}$$

where,

$$B_4 = 4\varepsilon_b(1 - x^3) + \varepsilon_\infty(1 + 2x^3) + 2\varepsilon_m(2 + x^3) \tag{5.33}$$

$$A_6 = 2(\varepsilon_b^2 + \varepsilon_\infty\varepsilon_m)(1 - x^3) + \varepsilon_b\varepsilon_\infty(1 + 2x^3) + 2\varepsilon_b\varepsilon_m(2 + x^3). \tag{5.34}$$

Given that oscillator strength and dye concentration are linearly related by $f\omega_0^2 = Ne^2/\varepsilon_0 m$ (see Ch. 2) the splitting of the modes can be written as

$$2\Delta\bar{\omega} = \frac{e}{\sqrt{3}}\sqrt{\frac{B_4 N}{A_6\varepsilon_0 m}}. \tag{5.35}$$

Eq. 5.35 demonstrates symbolically that the splitting of the two plexciton modes in the nanosphere with a metal core and excitonic shell increases with the square root of the dye concentration in the shell, but this splitting is independent of the exciton transition energy. For a dye concentration of zero ($N = 0$), Eq. 5.35 implies that there is only one (dipole) mode present, in accordance with the findings of Sec. 5.4.

These predictions are now examined with the use of Mie absorption calculations. For the sake of keeping the nanoparticle well-represented by the quasistatic calculations above, the chosen geometry of the nanoparticle is $d = 10\ nm$ and $t = 5\ nm$. The exciton transition energy chosen is $\omega_0 = 2.8\ eV$, since for this geometry and value of $\omega_0$, the outer modes are both plexcitonic, their relative strengths are approximately in balance, and the splitting of the plexciton modes is roughly minimised. A reason for

keeping the splitting to a minimum is so that the main features of the spectra can be explored within the visible spectrum, and consideration of modes with equal strengths helps to reduce the complexity of the system. The splitting of the plexciton modes in this case is equal to 0.309 *eV* for a dye concentration of 3.22 *wt%* (as seen from Fig. 5.16).

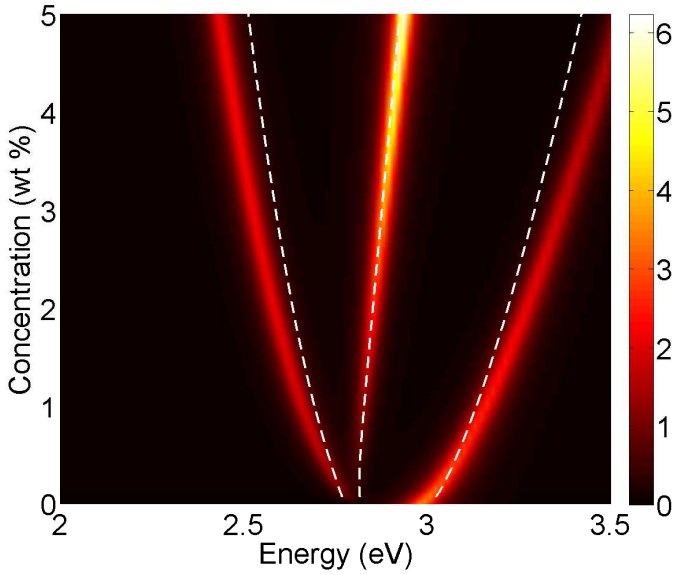


**Figure 5.17:** Mie absorption efficiency spectra as a function of concentration for a nanosphere with a $d = 10\ nm$ silver core and a $t = 5\ nm$ excitonic coating, with $\omega_0 = 2.8\ eV$, together with the quasistatic solutions (dashed lines).

Absorption efficiency spectra from coated Mie theory for the nanosphere are presented in Fig. 5.17, as a function of dye concentration in the shell. The central mode arising from exciton absorption is evident, along with the two plexciton modes, one on either side. The exciton absorption increases with concentration as the probability for exciton excitation in the shell is increased. This mode also blueshifts with an increase in dye concentration in a similar fashion to both the PEP mode of the bare excitonic nanosphere (Eq. 4.10) and the PEP mode of the excitonic nanosphere with an inert shell (Eq. 5.8). However, this blueshift is not as significant as the splitting induced in the plexciton modes by an increase in dye concentration. From inspection, the splitting of the plexciton modes scales with the square root of the dye concentration as expected from Eq. 5.32; this phenomenon has been shown elsewhere.[183]

The Mie calculations in Fig. 5.17 reveal that the strength of the absorption efficiency for the split plexcitonic modes is inversely dependent upon the dye concentration in the shell. Therefore, there exists an optimum concentration at which both the splitting of the plexcitonic modes and the absorption for each are maximised. However, the absorption efficiency is greater than unity at the peaks of the three modes for all concentrations plotted. This finding demonstrates that the plexcitonic modes of this system can be tuned across the range $2.4\ eV < E < 3.5\ eV$ with a change in dye

concentration of the shell. This degree of tunability translates as a wavelength shift of $\Delta\lambda = 159\ nm$; a value exceeding all modal shifts considered so far in this thesis. Given that this shift is independent of exciton transition energy (by Eq. 5.35), this large shift in wavelength is expected to be observed for other choices of $\omega_0$ (and hence other dyes), provided that the plexcitonic modes can be excited.

## 5.8 Conclusions

In this chapter, particle exciton polariton (PEP) modes, hybrid exciton polariton modes and plexciton modes have been demonstrated across a range of coated nanosphere configurations, incorporating excitonic materials.

An excitonic nanosphere with an inert shell can exhibit a PEP mode, the spectral location of which shifts with an increase in shell thickness in a similar way to that of a particle plasmon polariton (PPP) mode for a plasmonic nanosphere with an inert shell. The direction and the magnitude of the shift is dependent upon the difference between the medium index and the index of the shell. The mode is redshifted (blueshifted) if the index of the coating is above (below) that of the medium. A potential application of an inert coating around an excitonic nanosphere is as a stabilising agent, allowing a PEP mode of consistent energy for a change in medium index. While the addition of an inert shell can increase the absorption cross-section of a nanosphere (whether excitonic or plasmonic), the absorption efficiencies of the coated nanospheres examined in this chapter are decreased with the addition of a shell. Under such a circumstance, the particle mode is excited within the core only, and not over the entire nanoparticle volume.

Excitonic nanoshells with inert cores can exhibit hybrid exciton polariton modes. Through Mie calculations it has been shown that the spectral locations of these two modes are predicted well by quasistatic theory for TDBC:PVA nanoshells with a $d = 100\ nm$ core. Thin shells maximise the mode splitting at the cost of a decrease in absorption efficiency, and hence, the field enhancement around the nanoparticle. Increasing the core index causes the higher energy (antisymmetric) mode to become dominant. This is *contra* to the effect of an increase in the medium index, the effect of which is to bring the lower energy (symmetric) mode to greater prominence. In addition, an increase in the medium index causes the antisymmetric mode to redshift slightly. Specifically for the system with a 3.22 *wt%* TDBC:PVA shell and a $SiO_2$ core in vacuum, the symmetric mode dominates. Replacement of the core with the higher-index material $TiO_2$ causes the antisymmetric mode to dominate. These two hybrid modes can be brought into balance by raising the index of the medium to $n_m = 2$. In general, increasing the medium index has the effect of extending the region around the nanoparticle for which electric field enhancement occurs, as predicted with the use of quasistatic arguments in Ch. 4. For either of the two core materials considered for this nanoparticle system, a 3.22 *wt%* TDBC:PVA shell with thickness $t \approx 15\ nm$ is

required to achieve an absorption efficiency in excess of unity for both hybrid modes, a finding which can be used to help inform a future experimental investigation.

An excitonic core within an excitonic nanoshell enables interaction of the two modes of the nanoshell with the PEP mode of the excitonic core: this leads to three possible exciton polariton modes. Through Mie absorption calculations made by varying the exciton transition of the shell, the central mode has been shown to be dark if the exciton transitions of the core and the shell are detuned significantly from each other (large detunings); the two remaining bright modes exhibit splitting, as shown through both quasistatic and Mie calculations. In the case of large detunings, the strongest of these two modes has been shown to lie close to the resonance of the core. The central mode is only bright for small detunings (up to around 35 *meV* for the specific materials considered) and in this case, the mode follows a roughly linear dispersion with a change in shell exciton transition energy.

For the same nanoparticle system, it has been shown analytically that the splitting between the two bright modes increases with the square root of the dye concentration in the shell. It has also been demonstrated that the mean of the two modes blueshifts with an increase in dye concentration in the shell. These two findings have been confirmed through Mie calculations. In addition, it has been found that for higher concentrations, the shell dominates the response; here, the two hybrid modes approach those of the bare nanoshell. Given that the analytical solutions for the resonant energies based on quasistatic theory mirror the peaks in the Mie spectra for the system, evidence is presented for exciton polariton modes in a excitonic-excitonic core-shell nanosphere geometry.

The PPP mode of a silver nanosphere can be split to give three polariton modes with the adsorption of an excitonic coating. This splitting is particularly clear where the exciton transition energy in the shell is close to that of the PPP mode of the core. In this case, the two outermost modes in the spectrum exhibit roughly equal absorption. Under this circumstance, the exciton and plasmon modes of the nanoparticle are strongly coupled and hybridise to form 'plexcitonic' modes. By calculation of Mie absorption spectra for a range of exciton transition energies, the splitting between the plexciton modes has been shown to be minimised for exciton transition energies in the shell close to that of the PPP mode of the core. At this exciton transition energy, the quality factor of one of the plexciton modes for a $t = 2$ *nm* PVA coating doped with an excitonic dye to a concentration of 3.22 *wt%* have been shown to be comparable to that of the PEP mode of a 3.22 *wt%* TDBC:PVA nanosphere. The other two modes have been shown to exhibit quality factors four times that of the silver nanosphere PPP mode. For all exciton transition energies in this system, the mode between the two plexciton modes in the spectrum arises from exciton absorption. For large detunings from the plasmon mode energy, the strong coupling between the plasmonic and excitonic contributions to the two outer modes is weaker, and the plexcitonic nature of the two outer modes is lost. Here, the PPP mode of the core is optically strong and shifted slightly by the exciton transition, as predicted analytically from quasistatic considerations.

In the case of a silver nanosphere with a 3.22 *wt%* TDBC:PVA coating in vacuum, it has been shown that a shift in the plexciton resonances of $\Delta\lambda = 42$ *nm* can be achieved

through a change in shell thickness. This shift exceeds that of the maximum shift achievable for the silver nanosphere with an inert coating in an aqueous environment, as outlined above.

The two plexciton modes can also be tuned with an increase in the dye concentration of the shell. As shown through analytical treatment, the splitting of the two plexciton modes increases with the square root of the dye concentration, and with careful selection of the excitonic dye species, the two modes can be held in balance with each other. For the specific case analysed in this chapter with $\omega_0 = 2.8\ eV$, the shift in resonant wavelength achievable for these plexciton modes is $\Delta\lambda = 159\ nm$; a value which exceeds the shift achievable through a change in shell thickness - and indeed all wavelength shifts so far outlined in this thesis - by a factor close to four. It has been shown that in the quasistatic limit, this tunability is independent of the exciton energy. Therefore, silver nanospheres with excitonic shells provide an exciting prospect for their range of tunability, provided that a suitable species of excitonic dye can be utilised in a coating.

In all, PEP modes offer a consistent resonance with the adsorption of an inert shell. Excitonic nanoshells can exhibit hybrid PEP modes, and metallic-excitonic core-shell nanospheres can exhibit plexcitonic modes. TDBC-silver plexciton modes offer the greatest degree of tunability of all the polariton modes considered in this thesis. With careful nanoparticle design by selection of the most suitable dye, aspect ratio, and dye concentration, high-quality plexcitonic modes can not only be excited in core-shell nanospheres, but can be tuned to accommodate design specification across a relatively broad range of optical wavelengths.

# 6

# SUMMARY

The focus of the work presented in this thesis hinges on the extent to which excitonic nanostructures can be used *in lieu* of plasmonic nanostructures for the purposes of electric field enhancement and electric field confinement. In what follows, the findings from each of the chapters are summarised in order to answer this question.

In Ch. 1, relative permittivity was established as the fundamental quantity which governs the optical response of materials. A Fresnel approach, which utilises the Kramers-Kronig (KK) relations, was outlined in order to find the permittivity of thin films. The excitonic dye molecule TDBC was then introduced, and the permittivity of thin films of poly(vinyl alcohol) (PVA) doped with TDBC was investigated. Provided that the dye concentration in the material is sufficiently high, it was found that the real part of the permittivity for TDBC:PVA is negative in a small range of energies, like a metal (such as gold or silver). This spectral region of negative permittivity is responsible for the metallic visual appearance (and optical properties of) TDBC:PVA, and increases in breadth with an increase in dye concentration. A current limitation of the findings outlined in this chapter is that the response of TDBC:PVA films to photons with wavelengths shorter than 450 *nm* is currently unknown, due to a limitation of the equipment used in experiment. The response to photons with short wavelengths could be the subject of a future investigation in order to obtain improved values for the permittivity of this excitonic material.

The truncated visible spectrum used in order to obtain the permittivities of TDBC:PVA films in Ch. 1 necessitated a theoretical model for the permittivity which could be used to calculate the permittivity for any optical frequency. Therefore, different models used to describe the permittivity of TDBC aggregates were evaluated in Ch. 2. While each monomer can be represented as a two-level quantum system, a single-exciton model for an aggregate has as many energy levels as there are monomers in the aggregate. It has been shown *via* solutions to a nearest-neighbour Hamiltonian for this system that one of the aggregate transition dipole moments dominates the optical response. Therefore, an aggregate (or an ensemble of non-interacting aggregates) can be represented to a reasonable approximation with a two-level quantum system, or to a crude approximation with a single-oscillator Lorentz model. The two-level quantum model has been shown to be the superior of the two models, on account of providing a closer fit to the permittivity obtained from experiment. This is attributed to the variables within the quantum model arising from approximated (Born-Markov) physical processes. However, a quantum model for plasmonic metals (gold and silver) is unnecessary, since the length scales of the nanostructures considered in this thesis

are long enough to permit the macroscopic Drude model (albeit in a modified form for gold) to be used.

Incorporation of a greater number of energy levels in the quantum model for TDBC aggregates permits a more accurate fit to the experimentally-extracted permittivity, as shown in Ch. 2. The highest number of energy levels modelled in this thesis is four, and analytical constraints on the dephasing rates between these levels have been used in order to keep the system physically plausible. No such constraints have yet been encountered for a greater number of energy levels, but limited analysis has suggested that no significant change to the permittivity at optical frequencies can be brought about by consideration of further energy levels of the aggregate than currently considered. Therefore, it has been shown that a four-level quantum model suffices to model the permittivity of TDBC aggregates across optical frequencies. However, the broadening of the tail in the imaginary part of the refractive index - particularly for the 1.46 *wt%* TDBC:PVA film - is left not completely accounted for with the use of the four-level quantum model. Therefore, the contribution of inter-aggregate effects on this broadening provides a topic for future investigation. Another topic for investigation is the effective number of monomers *per* aggregate: this quantity has been shown to reduce to $n = 15$ for high concentrations, and to peak at around $n = 70$ in the concentration range $0.1\ wt\% - 0.2\ wt\%$ (planar distribution). This dependency of monomer number *per* aggregate upon concentration causes low-concentration TDBC:PVA films to exhibit stronger transition dipole moments than expected, and it is for this reason that TDBC:PVA films possess a negative permittivity within a small range of frequencies for concentrations as low as 0.12 *wt%*; possibly lower. The precise concentration at which $n$ peaks is currently unknown. In addition, the question as to whether $n$ is an effective number or a real number remains unanswered.

Thin films of TDBC:PVA have been shown in Ch. 3 to support both bound and quasi-bound surface exciton polariton (SEP) modes. The propagation length and skin depth of these SEP modes are shorter than the same quantities for surface plasmon polariton (SPP) modes in either gold, silver or aluminium; this implies a greater degree of localisation for the SEP modes. These SEP modes rely upon the negative real permittivity of the films originating from the delocalisation of excitons in the aggregates, causing the electrons in the material to behave in a similar way to those of free electrons in plasmonic metals. The SEP modes for TDBC:PVA films have been theorised through the comparison of dispersion diagrams with the calculated absorption for thin films (obtained using the transfer matrix method with the incorporation of the four-level quantum model for the permittivity of TDBC:PVA films outlined in Ch. 2). It has been demonstrated that the colours calculated from the reflectance spectra generated by the transfer matrix method agree with those observed visually for both p and s polarised light, thereby supporting the validity of the reflectance calculations. However, the colours calculated from the transmittance spectra are more blue than the colours of the films observed in reality, implying that transmittance for shorter wavelengths is likely to have been over-estimated. Therefore, measurement of TDBC:PVA films for a wider range of wavelengths together with refinement of both the colour code and the permittivity model is recommended as a future investigation.

Surface modes have also been demonstrated for hyperbolic metamaterials comprising TDBC:PVA with either silver or gold; such metamaterials can exhibit hyperbolic surface modes, as shown in Ch. 3. The dispersion curves of these metamaterials indicate that the hyperbolic modes possess much lower group and phase velocity than either the SEP or SPP modes evidenced by the same nanostructures. In addition, it has been shown that these hyperbolic modes exhibit a greater amount of - and a greater uniformity in - absorption with incident angle. Furthermore, hyperbolic modes have been shown to sharpen SEP modes in the multilayer. The frequency at which the hyperbolic mode occurs is dependent upon the exciton excitation energy within the excitonic material. All-in-all, with suitable design and selection of the correct excitonic dye, hyperbolic surface modes hosted by excitonic-plasmonic metamaterials could be utilised in future applications for which field confinement, uniformity in absorption, or a particularly sharp SEP mode is necessary.

Particle exciton polariton (PEP) modes can be excited in excitonic nanospheres and nanospheroids, as shown in Ch. 4 through the use of both quasistatic and Mie calculations. Quasistatic treatment has shown that a general property of PEP modes is that of electric field enhancement over all solid angles within a region close to the surface of the nanoparticle, accompanied by a peak in absorption efficiency greater than unity - indicative of the nanoparticle acting as a 'magnet for light'. Both of these properties are also exhibited for particle plasmon polariton (PPP) modes. The electric field enhancement and confinement has been shown to be similar for both PEP modes hosted by TDBC:PVA nanospheres and PPP modes hosted by silver and gold nanospheres. However, it has been shown through Mie theory for TDBC:PVA nanospheres that with a sufficient dye concentration, the quality factors of the absorption peaks for PEP modes exhibit much higher quality factors in absorption than their PPP counterparts for nanospheres of the same size. The PEP modes have been shown to redshift with an increase in dye concentration, accompanied by an increase in quality factor.

Field enhancement and confinement have also been demonstrated for ENZ modes of a nanosphere, although unlike the particle polariton modes, the incident power flows around the nanosphere and does not act as a magnet for light.

The PEP mode for the 100 *nm* diameter TDBC:PVA nanosphere has been shown to be tunable with dye concentration in the wavelength range $564\ nm < \lambda < 572\ nm$ in vacuum. The epsilon near zero (ENZ) mode of the nanoparticle has also been shown to be tunable with concentration, over the range $572\ nm < \lambda < 585\ nm$ in vacuum. The PEP modes for the TDBC:PVA nanospheroid have also been shown to be tunable, particularly with the aspect ratio of the nanospheroid. It was determined that in an experiment, the practical range of wavelengths over which the nanospheroidal PEP modes can be tuned is $566\ nm < \lambda < 580\ nm$. Experimental evidence for transverse and longitudinal nanospheroidal PEP modes has been presented for prolate and oblate nanospheroids respectively by calculation of forward extinction efficiency spectra from transmittance measurements through square arrays of nanospheroids. The strongest peak in forward extinction has been shown to arise from the smallest (prolate) TDBC:PVA nanospheroids, in spite of the experimental noise encountered. The forward extinction spectra calculated for the larger nanospheroids suffer from contributions from supporting cylinders upon which the nanospheroids (as fabricated)

sit. Therefore, re-fabrication and experimentation on more TDBC:PVA nanospheroids is encouraged for further confirmation of nanospheroidal PEP modes.

Given that the transverse and longitudinal modes of a nanospheroid are orthogonal modes, it has been suggested that the orientation of a single nanospheroid can determined from its transmittance spectrum. For subwavelength prolate 1.46 *wt%* (planar distribution) TDBC:PVA nanospheroids in vacuum, the colour shift between two orthogonal polarisations in edge-on orientation has been shown to be discernible to the human eye; no such shift is present in the face-on orientation. For oblate excitonic nanospheroids, the longitudinal mode is strongest: this is also the nanospheroid mode for which the quality factor is highest, exceeding that of the nanosphere in the face-on orientation. The high degree of directionality this mode offers may provide a mechanism by which the orientation of a subwavelength oblate nanospheroid can be probed.

In all, calculations in Ch. 4 have demonstrated the validity of PEP modes for TDBC:PVA nanospheres and nanospheroids. These modes are tunable through either a change in dye concentration, medium index or nanospheroid aspect ratio. In principle, other excitonic dyes may offer different (or wider ranges of) energies for which these PEP modes can be excited. Moreover, these findings suggest that in general, excitonic nanoparticles can be used as alternatives to plasmonic nanoparticles for the purposes of field enhancement and confinement.

An inert coating adsorbed onto an excitonic nanosphere acts as a resistive agent to shifts in the absorption peak brought about by changes in the medium index. As shown in Ch. 5, the magnitude of this shift is suppressed with the addition of an inert coating around a TDBC:PVA nanosphere. However, the resonance for a silver nanosphere with the same coating can be shifted more dramatically. Therefore, the PEP mode of an excitonic nanosphere is likely to be present at a stable resonant frequency, making the nanospheres easier to detect than silver nanospheres with the adsorption of a protein or fatty-acid coating in a biosensing context. A subtlety of PEP modes in these coated systems is described in Ch. 5: the PEP mode may be confined within the volume of the nanoparticle if the shell is sufficiently thick, and the PEP mode is not necessarily distributed over the volume of the nanoparticle as a whole, meaning that field enhancement is not necessarily felt over all solid angles of the outer nanoparticle surface.

The inverse of this system *i.e.* an excitonic nanoshell with an inert core, exhibits two modes, borne from hybridisation between the PEP mode of the shell and the cavity exciton polariton mode of the core. The splitting between these two hybrid modes is maximised for thin shells. As shown in Ch. 5, the higher energy (antisymmetric) hybrid mode is strengthened with an increase in core index; with an increase in medium index, the reverse is achieved. Two realistic nanoparticle systems have been suggested for fabrication in order to observe the two modes of an excitonic nanoshell: a $d = 100\ nm$ core of either $SiO_2$ or $TiO_2$ with a $t = 15\ nm$ coating of TDBC:PVA, doped with a concentration of 3.22 *wt%* (volume distribution).

For a coated nanosphere for which both the core and the shell are excitonic, three hybrid exciton-exciton modes are observed. The splitting between the two outermost

of these modes is maximised for high dye concentrations, or for a choice of a shell material for which the exciton transition is far removed from that of the core.

Hybrid modes are also found for nanoparticles with metal cores and excitonic shells, with the hybrid plasmon-exciton modes being termed 'plexciton' modes. In similarity to the exciton-exciton coated nanosphere, the splitting between the two plexciton modes of the coated nanosphere is maximised for high dye concentrations, as well as for a choice of excitonic shell material for which the exciton transition is far removed from that of the effective plasma frequency of the core material. Through Mie calculations of a TDBC:PVA-coated silver nanosphere, it has been demonstrated that the range of tunability in the plexciton modes with a change in shell thickness ($\Delta\lambda = 42\ nm$) or dye concentration ($\Delta\lambda = 159\ nm$) exceeds that of any SEP, PEP or hybrid PEP mode considered in this thesis. This tunability has been shown to be independent of the exciton transition energy, affording a wide scope for the fabrication of suitable plexcitonic nanospheres.

In summary, the negative permittivity brought about by the quasi-free electron behaviour of excitonic materials such as TDBC:PVA permits excitation of SEP and PEP modes within excitonic nanostructures. SEP modes of excitonic films can be hybridised with SPP modes of metallic films to give hyperbolic modes in multilayer stacks. These hyperbolic modes offer low group velocity, low phase velocity and potential sharpening of the quality factor for SEP modes. PEP modes for excitonic nanospheres have been demonstrated as superior in some aspects to PPP modes for metallic nanospheres, and nanospheroidal PEP modes have been demonstrated experimentally. PEP modes can also be excited for nanospheres in a core-shell geometry: these modes can be redshifted with an inert shell coating on an excitonic nanosphere; redshifted through a change in medium index; split by the use of an inert core in an excitonic nanoshell; or hybridised with plasmon modes to produce plexciton modes. These properties enable the tuning of such modes. Given that field enhancement and confinement runs as a common theme through all of these nanostructured configurations, the polariton modes of excitonic nanostructures offer viable alternatives to the use of plasmon modes within plasmonic applications.

# BIBLIOGRAPHY


[1] Ritchie, R. H. *Phys. Rev.* **106**, 874–881 (1957).

[2] Kretschmann, E. and Raether, H. *Z. Naturforsch. A Phys. Sci.* **23**, 2135–2136 (1968).

[3] Swan, J. B., Otto, A., and Fellenzer, H. *Phys. Status Solidi B* **23**, 171–176 (1967).

[4] Ekardt, W. *Phys. Rev. B* **34**, 526–533 (1986).

[5] Le Ru, E. C. and Etchegoin, P. G. *Principles of Surface-Enhanced Raman Spectroscopy and Related Plasmonic Effects*. Elsevier, Oxford, first edition, (2009).

[6] Kreibig, U. and Vollmer, M. *Optical Properties of Metal Clusters*. Springer-Verlag, 1st edition, (1995).

[7] Tanabe, K. *J. Phys. Chem. C* **112**, 15721–15728 (2008).

[8] Sambles, J. and Innes, R. *J. Mod. Opt.* **35**(5), 791–797 (1988).

[9] Kitson, S. C., Barnes, W. L., Sambles, J. R., and Cotter, N. P. K. *J. Mod. Opt.* **43**, 573–582 (1996).

[10] Kitson, S. C., Barnes, W. L., and Sambles, J. R. *Phys. Rev. B* **52**, 11441–11446 (1995).

[11] Chen, Y., Munechika, K., and Ginger, D. S. *Nano Letters* **7**, 690–696 (2007).

[12] Anger, P., Bharadwaj, P., and Novotny, L. *Phys. Rev. Lett.* **96**, 113002 (2006).

[13] Vukusic, P., Bryan-Brown, G., and Sambles, J. *Sensors and Actuators B: Chemical* **8**, 155–160 (1992).

[14] Caruso, F., Jory, M. J., Bradberry, G. W., Sambles, J. R., and Furlong, D. N. *J. Appl. Phys.* **83**, 1023–1028 (1998).

[15] Kelly, K. L., Coronado, E., Zhao, L. L., and Schatz, G. C. *J. Phys. Chem. B* **107**, 668–677 (2003).

[16] Willets, K. A. and Van Duyne, R. P. *Annu. Rev. Phys. Chem.* **58**, 267–97 (2007).

[17] Tittl, A., Yin, X., Giessen, H., Tian, X.-D., Tian, Z.-Q., Kremers, C., Chigrin, D. N., and Liu, N. *Nano Letters* **13**, 1816–1821 (2013).

[18] Haes, A. J., Zou, S. L., Schatz, G. C., and Van Duyne, R. P. *Phys. Chem. B* **108**, 6961–6968 (2004).

[19] Garcia-Parajo, M. F. *Nat. Photonics* **2**, 201–203 (2008).

[20] Isaac, T. H., Barnes, W. L., and Hendry, E. *Appl. Phys. Lett.* **93**, 2008–2010 (2008).

[21] Taylor, R. W., Benz, F., Sigle, D. O., Bowman, R. W., Bao, P., Roth, J. S., Heath, G. R., Evans, S. D., and Baumberg, J. J. *Sci. Rep.* **4**, 1–6 (2014).

[22] Park, D. J., Zhang, C., Ku, J. C., Zhou, Y., Schatz, G. C., and Mirkin, C. A. *Proc. Natl. Acad. Sci. USA* **112**, 977–981 (2015).

[23] Maradudin, A. A. In *Modern Plasmonics,* Maradudin, A. A., Sambles, J. R., and Barnes, W. L., editors, volume 4 of *Handbook of Surface Science*, chapter 1, 1–36. Elsevier, London (2014).

[24] Romero, G., García-Ripoll, J. J., and Solano, E. *Phys. Rev. Lett.* **102**, 173602 (2009).

[25] Li, J., Paraoanu, G. S., Cicak, K., Altomare, F., Park, J. I., Simmonds, R. W., Sillanpää, M. A., and Hakonen, P. J. *Sci. Rep.* **2**, 645 (2012).

[26] Zhao, Y., Engheta, N., and Alú, A. *J. Opt. Soc. Am. B* **28**, 1266–1274 (2011).

[27] Chen, P. Y., Monticone, F., Argyropoulos, C., and Alù, A. In *Modern Plasmonics,* Maradudin, A. A., Sambles, J. R., and Barnes, W. L., editors, volume 4 of *Handbook of Surface Science*, chapter 4, 109–136. Elsevier, London (2014).

[28] Berry, S. J., Campbell, T., Hibbins, A. P., and Sambles, J. R. *Appl. Phys. Lett.* **100**, 101107 (2012).

[29] Brock, E. M. G. and Hibbins, A. P. *Appl. Phys. Lett.* **103**, 111904 (2013).

[30] Constant, T. J., Taphouse, T. S., Rance, H. J., Kitson, S. C., Hibbins, A. P., and Sambles, J. R. *Opt. Express* **20**, 23921–23926 Oct (2012).

[31] Rance, H. J., Constant, T. J., Hibbins, A. P., and Sambles, J. R. *Phys. Rev. B* **86**, 125144 Sep (2012).

[32] Constant, T. J., Vukusic, P., Hibbins, A. P., and Sambles, J. R. *Appl. Phys. Lett.* **106**, 091106 (2015).

[33] Humphrey, A. D. and Barnes, W. L. *Phys. Rev. B* **90**, 075404 (2014).

[34] Heavens, O. S. *Optical Properties of Thin Solid Films*. Butterworth, London, (1955).

[35] Kelly, J. J. *Graduate Mathematical Physics*. Wiley, Weinheim, (2006).

[36] Wood, B., Pendry, J. B., and Tsai, D. P. *Phys. Rev. B* **74**, 115116 Sep (2006).

[37] Maxwell, J. C. *Phil. Mag.* **21**, 281–348 March (1861). Series 4.

[38] Maxwell, J. C. *Phil. Mag.* **23**, 18–24 April (1861). Series 4.

[39] Hecht, E. and Zajac, A. *Optics*. Pearson Higher Education, fourth edition, (2003).

[40] Cole, K. S. and Cole, R. H. *J. Chem. Phys.* **9**, 341–351 (1941).

[41] Afsar, M. N. *IEEE T Instrum Meas.* **IM-36**, 530–536 (1987).

[42] Meurant, G. In *Handbook of Glass Data,* Mazurin, O. V. and Streltsina, M. V., editors, volume 15 of *Physical sciences data*, chapter 1, 1–185. Elsevier, Amsterdam (1983).

[43] Azzam, R. M. A. and Bashara, N. M. *Ellipsometry and polarized light*. North-Holland, 1st edition, (1977).

[44] Phillips, R. T. *J. Phys. D: Appl. Phys.* **16**, 489–497 (1983).

[45] Bednorz, A., Franke, K., and Belzig, W. *New J. Phys.* **15**, 023043 (2013).

[46] Gentile, M. J., Núñez-Sánchez, S., and Barnes, W. L. *Nano Letters* **14**, 2339–2344 (2014).

[47] Khawaja, E. E. *J. Phys. D: Appl. Phys.* **9**, 1939–1943 (1976).

[48] Mageto, M. J., Maghanga, C. M., and Mwamburi, M. *The African Review of Physics* **7**, 95–105 (2012).

[49] Raju, K. M., Raju, M. P., and Mohan, Y. M. *Polym. Int.* **52**, 768–772 (2003).

[50] Theocharous, S., Theocharous, E., and Lehman, J. *Infrared Phys. Techn.* **55**, 299–305 (2012).

[51] Schnapf, J. L., Kraft, T. W., and Baylor, D. A. *Nature* **325**, 439–441 (1987).

[52] Mandel, L. and Wolf, E. *Optical Coherence and Quantum Optics*. Cambridge University Press, Cambridge, (1995).

[53] Bohr, N. *Philos. Mag.* **26**, 1–24 (1913).

[54] De Broglie, L. *Recherches sur la théorie des Quanta*. Phd theses, Migration - université en cours d'affectation, November (1924).

[55] Ziman, J. *Electrons and Phonons*. Oxford University Press, Cavendish Laboratory, Cambridge, (1960).

[56] Meddins, H. and Parrott, J. *J. Phys. C: Solid State Phys.* **9**, 1263–1276 (1976).

[57] Srivastava, G. P. *The Physics of Phonons*. Taylor + Francis, Oxon, (1990).

[58] Balandin, A. and Wang, K. L. *Phys. Rev. B* **58**, 1544–1549 (1998).

[59] Appel, J. *Phys. Rev.* **122**, 1760–1772 (1961).

[60] Goldstein, H., Poole, C., and Safko, J. *Classical Mechanics*. Addison Wesley, San Francisco, third edition, (2001).

[61] Griffiths, D. J. *Introduction to Electrodynamics*. Pearson, Reed College, third edition, (2008).

[62] Stuart, M. R. *J. Appl. Phys.* **26**, 1399–1404 (1955).

[63] Lorentz, H. A. *Theory of Electrons*. Teubner, Leipzig, (1909).

[64] Pockrand, I., Swalen, J. D., Gordon II, J. G., and Philpott, M. R. *J. Chem. Phys* **70**, 3401–3408 (1979).

[65] Bohren, C. F. and Huffman, D. R. *Absorption and Scattering of Light by Small Particles*. Wiley, Pennsylvania State University, first edition, (1983).

[66] Fox, M. *Optical Properties of Solids*. Oxford University Press, Oxford, 2nd edition, (2010).

[67] Lebedev, V. S. *Quant. Electron.* **42**, 701–713 (2012).

[68] Anex, B. G. and Simpson, W. *Rev. Mod. Phys.* **32**, 466 (1960).

[69] Harter, D. J., Narum, P., Raymer, M. G., and Boyd, R. W. *Phys. Rev. Lett.* **46**, 1192–1195 (1981).

[70] Ashcroft, N. W. and Mermin, N. D. *Solid State Physics*. Holt, Rinehart and Winston, London, first edition, (1976).

[71] Johnson, P. B. and Christy, R. W. *Phys. Rev. B* **6**, 4370–4379 (1972).

[72] Lynch, D. W. and Hunter, W. R. *Comments on the Optical Constants of Metals and an Introduction to the Data for Several Metals*. Academic Press, Inc., USA, first edition, (1985).

[73] Sambles, R. J., Bradbury, G. W., and Yang, F. *Contemp. Phys.* **32**, 173–183 (1991).

[74] Schroder, U. *Surf. Sci.* **102**, 118–130 (1981).

[75] Liljenvall, H. G. and Mathewson, A. *J. Phys. C: Solid State Phys.* **3**, S341–S347 (1970).

[76] Etchegoin, P. G., Le Ru, E. C., and Meyer, M. *J. Chem. Phys* **125**, 164–705 (2006).

[77] See, K. C., Spicer, J. B., Brupbacher, J., Zhang, D., and Vargo, T. G. *J. Phys. Chem. B* **109**, 2693–2698 (2005).

[78] Wang, S., Chervy, T., George, J., Hutchison, J. A., Genet, C., and Ebbesen, T. W. *J. Phys. Chem. Lett.* **5**, 1433–1439 (2014).

[79] Rae, A. I. M. *Quantum Mechanics*. Taylor & Francis, fifth edition, (2008).

[80] Rosencher, E. and Vinter, B. *Optoelectronics*. Cambridge University Press, Cambridge, english edition, (2002).

[81] Fox, M. *Quantum Optics An Introduction*. Oxford University Press, University of Sheffield, second edition, (2010).

[82] Foot, C. J. *Atomic Physics*. Oxford University Press, Oxford, (2011).

[83] Kittel, C. *Introduction to Solid State Physics*. Wiley, Hoboken, NJ, eighth edition, (2005).

[84] Schirmer, S. G. and Solomon, A. I. *Phys. Rev. A* **70**, 022107 (2004).

[85] Schaller, G. and Brandes, T. *Phys. Rev. A* **78**, 022106 (2008).

[86] Blum, K. *Density matrix theory and application*. Plenum Press, New York, second edition, (1996).

[87] Breuer, H. P. and Petruccione, F. *The Theory of Open Quantum Systems*. Oxford University Press, New York, (2002).

[88] Frenkel, J. *Phys. Rev.* **37**, 17–44 (1931).

[89] Wannier, G. H. *Phys. Rev.* **52**, 191–197 (1937).

[90] Kerp, H., Donker, H., Koehorst, R., Schaafsma, T., and van Faassen, E. *Chem. Phys. Lett.* **298**, 302–308 (1998).

[91] Skinner, J. L. and Hsu, D. *J. Phys. Chem.* **90**, 4931–4938 (1986).

[92] Abramavicius, D., Butkus, V., and Valkunas, L. In *Quantum Efficiency in Complex Systems, Part II: From Molecular Aggregates to Organic Solar Cells,* Wurfel, U., Thorwart, M., and Weber, E., editors, volume 85 of *Semiconductor and Semimetals*, chapter 1, 3–45. Elsevier, London (2011).

[93] Harris, D. C. and Bertolucci, M. D. *Symmetry and Spectroscopy: an Introduction to Vibrational and Electronic Spectroscopy*. Dover Publications, New York, (1989).

[94] E., D., McCumber, and Sturge, M. D. *J. Appl. Phys.* **34**, 1682 (1963).

[95] Harris, C. B. *J. Chem. Phys.* **67**, 5607 (1977).

[96] Ambrosek, D., Köhn, A., Schulze, J., and Kühn, O. *J. Phys. Chem. A* **116**, 11451–11458 (2012). PMID: 22946964.

[97] Miura, Y. F. and Ikegami, K. In *J-Aggregates,* Kobayashi, T., editor, volume 2, chapter 14, 443–514. World Scientific, London (2012).

[98] Valleau, S., Saikin, S. K., Yung, M., and Guzik, A. A. *J. Chem. Phys* **137**, 034109 (2012).

[99] Spano, F. C. In *J-Aggregates,* Kobayashi, T., editor, volume 2, chapter 2, 49–75. World Scientific, London (2012).

[100] Zhao, Y. S. *Organic Nanophotonics*. Springer, Berlin, (2015).

[101] Parker, S. P. *McGraw-Hill Encyclopaedia of Physics*. McGraw-Hill Companies, New York, (1993).

[102] Knoester, J. In *Proceedings of the International School of Physics*, volume 149, 149–186. IOS Press, (2002).

[103] Chebyshev, P. L. *Mémoires des Savants étrangers présentés à l'Académie de Saint-Pétersbourg* **7**, 539–586 (1854).

[104] Malyshev, V. and Moreno, P. *Phys. Rev. B* **51**, 14587–14593 (1995).

[105] Weisstein, E. W. `http://mathworld.wolfram.com/HypergeometricFunction.html`. Accessed: 2015-09-24.

[106] Hochstrasser, R. M. and Whiteman, J. D. *J. Chem. Phys.* **56**, 5945–5958 (1972).

[107] Kuhn, H. and Kuhn, C. In *J-Aggregates,* Kobayashi, T., editor, chapter 1, 1–40. World Scientific, London (1996).

[108] Kavanaugh, T. C. and Silbey, R. J. *J. Chem. Phys.* **98**, 9444–9454 (1993).

[109] Allen, L. and Eberly, J. H. *Optical Resonance and Two-Level Atoms*. Wiley, New York, (1975).

[110] Dorfman, K. E., Jha, P. K., Voronine, D. V., Genevet, P., Capasso, F., and Scully, M. O. *Phys. Rev. Lett.* **111**, 043601 (2013).

[111] Nakano, M. and Yamaguchi, K. *Phys. Rev. A* **50**, 2989–3004 (1994).

[112] Wang, K. and Chu, S. *J. Chem. Phys.* **86**, 3225–3238 (1986).

[113] Tidström, J., Jänes, P., and Andersson, L. M. *Phys. Rev. A* **75**, 053803 (2007).

[114] Hairer, E. *Journal of the Institute of Mathematics and its Applications* **21**, 47–59 (1978).

[115] van Burgel, M., Wiersma, D. A., and Duppen, K. *J. Chem. Phys* **102**, 20–33 (1995).

[116] Garrett, S. H., Wasey, J. A. E., and Barnes, W. L. *J. Mod. Opt.* **51**, 2287–2295 (2004).

[117] van Burgel, M. and Wiersma, D. *The ultrafast dynamics of aggregate excitons in water*. PhD thesis, University of Groningen, (1999).

[118] Lorentz, H. *Physik. Z.* **11**, 1250 (1910).

[119] Grad, J., Hernandex, G., and Mukamel, S. *Phys. Rev. A* **37**, 3835–3846 (1988).

[120] Misawa, K. and Kobayashi, T. In *J-Aggregates,* Kobayashi, T., editor, chapter 2, 41–66. World Scientific, London (1996).

[121] Hooper, I. and Barnes, W. L. In *Modern Plasmonics,* Maradudin, A. A., Sambles, J. R., and Barnes, W. L., editors, volume 4 of *Handbook of Surface Science*, chapter 2, 37–74. Elsevier, London (2014).

[122] Bharadwaj, P., Bouhelier, A., and Novotny, L. *Phys. Rev. Lett.* **106**, 226802 (2011).

[123] Wood, R. W. *Philos. Mag.* **4**, 396–402 (1902).

[124] Knapp, E. *Chem. Phys.* **85**, 73–82 (1984).

[125] Lagois, J. and Fischer, B. *Phys. Rev. B* **17**, 3814–3824 (1978).

[126] Lei Gu, Livenere, J., Zhu, G., Narimanov, E. E., and Noginov, M. A. *Appl. Phys. Lett.* **103**, 021104 (2013).

[127] Novotny, L. and Hecht, B. *Principle of Nano-Optics*. Cambridge University Press, first edition, (2006).

[128] Geddes, N. J., Sambles, J. R., Jarvis, D. J., Parker, W. G., and Sandman, D. J. *App. Phys. Lett.* **56**, 1916–1918 (1990).

[129] Geddes, N. J., Parker, W. G., Sambles, J. R., and Couch, N. R. *Physics, Fabrication, and Applications of Multilayered Structures*, chapter Electrical Characterisation of Thin Insulating Langmuir Blodgett Films Incorporated in Metal-Insulator-Metal Structures, 377–377. Springer US, Boston, MA (1988).

[130] Zia, R., Selker, M. D., and Brongersma, M. L. *Phys. Rev. B* **71**, 165431 (2005).

[131] Dionne, J. A., Sweatlock, L. A., Atwater, H. A., and Polman, A. *Phys. Rev. B* **72**, 075405 (2005).

[132] Pendry, J. B., Holden, A. J., Stewart, W. J., and Youngs, I. *Phys. Rev. Lett.* **76**, 4773–4776 (1996).

[133] Zhang, J., Zhang, L., and Xu, W. *J. Phys. D: Appl. Phys.* **45**, 113001 (2012).

[134] Wolf, K. B. and Krotzsch, G. *Eur. J. Phys.* **16**, 14–20 (1995).

[135] Pedrotti, F. L. and Pedrotti, L. S. *Introduction to Optics*. Prentice-Hall International, London, 2nd edition, (1993).

[136] Auer, S., Wan, W., Huang, X., Ramirez, A. G., and Cao, H. *App. Phys. Lett.* **99**, 041116 (2011).

[137] Loveday, K. `http://sivirt.utsa.edu/Documents/Kayla%20Lovelady.pdf`, April (2013).

[138] Powell, A. K., Hall, T. J., Iman, H., and Fish, D. A. In *Nonlinear Optics in Signal Processing,* Eason, R. and Miller, A., editors, Engineering Aspects of Lasers, chapter 4. Chapman & Hall, London (1993).

[139] Poddubny, A., Iorsh1, I., Belov, P., and Kivshar, Y. *Nature Photon.* **7**, 958–967 (2013).

[140] Ferrari, L., Wu, C., Lepage, D., Zhang, X., and Liu, Z. *Prog. Quant. Electron.* **40**, 1–40 (2015).

[141] Naik, G., Kim, J., Kinsey, N., and Boltasseva, A. In *Modern Plasmonics,* Maradudin, A. A., Sambles, J. R., and Barnes, W. L., editors, volume 4 of *Handbook of Surface Science*, chapter 6, 189–221. Elsevier, London (2014).

[142] Stiles, P. L., Dieringer, D. J., Shah, N. C., and Van Duyne, R. *Ann. Rev. Anal. Chem.* **1**, 601–626 (2008).

[143] Philpott, M. R., Brillante, A., Pockrand, I., and Swalen, J. D. *Mol. Cryst. Liq. Cryst.* **50**, 139–162 (1979).

[144] Saikin, S. K., Eisfeld, A., Valleau, S., and Aspuru-Guzik, A. *Nanophotonics* **2**, 17 (2013).

[145] Gentile, M. J., Horsley, S. A. R., and Barnes, W. L. *J. Opt.* **18**, 015001 (2016).

[146] Triolo, C., Cacciola, A., Stefano, O. D., Genco, A., Mazzeo, M., Patanè, S., Saija, R., and Savasta, S. *ACS Photonics* **2**, 971–979 (2015).

[147] Hohenau, A., Leitner, A., and Aussenegg, F. R. In *Surface Plasmon Nanophotonics,* Brongersma, M. L. and Kik, P. G., editors, volume 131 of *Optical Sciences*, chapter 2, 11–25. Springer, Atlanta, USA (2007).

[148] Mie, G. *Ann. Phys. (Berlin)* **25**, 377–445 (1908).

[149] Chung, H. Y., Leung, P. T., and Tsai, D. P. *Plasmonics* **7**, 13–18 (2012).

[150] Stewart, M. E., Mack, N. H., Malyarchuk, V., Soares, J. A. N. T., Lee, T., Gray, S. K., Nuzzo, R. G., and Rogers, J. A. *Proc. Natl. Acad. Sci. USA* **103**, 17143–17148 (2006).

[151] Cox, A. J., DeWeerd, A. J., and Linden, J. *Am. J. Phys.* **70**, 620–625 (2002).

[152] Hilbert, D. and Cohn-Vossen, S. *Geometry and the Imagination*, volume 87. AMS Chelsea Pub., (1999).

[153] Prikulis, J. *Optical Imaging and Spectroscopy of Metal Nanostructures*. Phd thesis, Goeteborg University, Goeteborg, Sweden, (2003).

[154] Asano, S. *Appl. Opt.* **18**, 712–723 (1979).

[155] Mishchenko, M. I. *Appl. Opt.* **39**, 1026–1031 (2000).

[156] Michael, D. W. M. and Mishchenko, I. *J. Opt. Soc. Am. A* **13**, 2266–2278 (1996).

[157] Lambert, J. *Photometria sive de mensura et gradibus luminis, colorum et umbrae*. Eberhardt Klett, Augsburg, (1760).

[158] Asano, S. and Yamamoto, G. *Appl. Opt.* **14**, 29–49 (1975).

[159] Waterman, P. C. *Proc. IEEE* **53**(8), 805–812 Aug (1965).

[160] Mishchenko, M. I., Travis, L. D., and Mackowski, D. W. *J. Quant. Spectrosc. RA* **55**, 535–575 (1996).

[161] Núñez-Sánchez, S. "Local exciton resonances in nanospheroid arrays". Four sizes of TDBC:PVA nanospheroids were constructed each with a pitch of 750 nm, and their transmittance measured at normal incidence., October (2014).

[162] Mishchenko, M. I., Travis, L. D., and Mackowski, D. W. `http://www.giss.nasa.gov/staff/mmishchenko/t_matrix.html`, June (2015).

[163] Somerville, W. R. C., Auguié, B., and Ru, E. C. L. "User Guide for smarties: Spheroids Modelled Accurately with a Robust T-matrix Implementation for Electromagnetic Scattering." Preprint article submitted to Elsevier., November (2015).

[164] Kometani, N., Tsubonishi, M., Fujita, T., Asami, K., and Yonezawa, Y. *Langmuir* **17**, 578–580 (2001).

[165] Lekeufack, D. D., Brioude, A., Coleman, A. W., Miele, P., Bellessa, J., Zeng, L. D., and Stadelmann, P. *App. Phys. Lett.* **96**, 253107 (2010).

[166] Fofang, N. T., Park, T.-H., Neumann, O., Mirin, N. A., Nordlander, P., and Halas, N. J. *Nano Letters* **8**, 3481–3487 (2008).

[167] Prodan, E., Radloff, C., Halas, N. J., and Nordlander, P. *Science* **302**, 419–422 (2003).

[168] Prodan, E., Lee, A., and Nordlander, P. *Chem. Phys. Lett.* **360**, 325–332 (2002).

[169] Kaiser, T. and Schweiger, G. *Comput. Phys.* **7**, 682–686 (1993).

[170] Weisstein, E. W. `http://mathworld.wolfram.com/Riccati-BesselFunctions.html`. Accessed: 2016-01-04.

[171] Yurt, A., Daaboul, G. G., Connor, J. H., Goldberg, B. B., and Selim Unlu, M. *Nanoscale* **4**, 715–726 (2012).

[172] Tcherniak, A., Ha, J. W., Dominguez-Medina, S., Slaughter, L. S., and Link, S. *Nano Letters* **10**, 1398–1404 (2010).

[173] Fairbairn, N., Fernandes, R., Carter, R., Elliot, T. J., Kanaras, A. G., and Muskens, O. L. *Proc. SPIE* **8595**, 859501 (2013).

[174] Witzens, J. and Hochberg, M. *Opt. Express* **19**, 7034–7061 (2011).

[175] Murray, W. A., Suckling, J. R., and Barnes, W. L. *Nano Letters* **6**, 1772–1777 (2006).

[176] Gülen, D. *J. Phys. Chem. B* **117**, 11220–11228 (2013).

[177] DeVore, J. R. *J. Opt. Soc. Am.* **41**, 416–419 (1951).

[178] Li, N., Liu, G., Zhen, C., Li, F., Zhang, L., and Cheng, H.-M. *Adv. Funct. Mater.* **21**, 1717–1722 (2011).

[179] Conrady, A. E. *Applied Optics and Optical Design*. Dover, (1960).

[180] Cole, R. M., Baumberg, J. J., de Abajo, F. J. G., Mahajan, S., Abdelsalam, M., and Bartlett, P. N. *Nano Letters* **7**, 2094–2100 May (2007).

[181] Fofang, N. T. *Optical Properties of Strongly Coupled Plasmon-Exciton Hybrid Nanostructures*. Phd thesis, Rice University, Houston, TX, (2011).

[182] Doering, W. E. and Nie, S. *Anal. Chem.* **75**, 6171–6176 (2003).

[183] Antosiewicz, T. J., Apell, S. P., and Shegai, T. *ACS Photonics* **1**, 454–463 (2014).

[184] Fujii, K. `arxiv.org/abs/1301.3585`, January (2013).

[185] Euler, L. *Institutionum Calculi Integralis*, volume II. Imperial, London, (1769).

[186] Charron, E. and Sukharev, M. *J. Chem. Phys* **138** (2013).

[187] Fehlberg, E. *Computing* **6**, 61–71 (1970).

[188] Sun, T. *J. Comput. Appl. Math.* **233**, 1056–1062 (2009).

[189] Kanemitsu, Y. *Acc. Chem. Res.* **46**, 1358–1366 (2013).

[190] *Artis Magnæ, Sive de Regulis Algebraicis Liber Unus*. Girolamo Cardano, (1545).

# A

# Appendix: Code Snippets

All codes in this appendix are written in MATLAB.

## A.1 Colour Perception Code

This function integrates a spectrum over the optical frequencies in order to compute the RGB values (the colour) the human eye would observe. The data files the function requires are available on request: these represent the absorption curves of the opsins in the cone cells. The 'raw' RGB values in lower-case represent the unsaturated colours. The upper-case RGB values represent the saturated values. The colours produced are normalised to white light (flat spectrum); assuming sunlight achieves a similar result (to within 2% of the RGB values calculated).

```
%Title:     ColourPerception_fn.m
%Date:      5-3-15
%Author:    M. Gentile
%Description: This function takes a reflectance or
% transmittance spectrum, calculates the RGB value as seen
% by the human eye and outputs this RGB value beneath a
% graph of the spectrum.
% The data files VLambda.dat, BlueCones.dat, GreenCones.dat
% & RedCones.dat should be included in the same directory as
% this function.
% Lambda: Should be in nanometres.
% T: Can be a reflectance or transmittance spectrum. It is
% normalised within the code.

function result = ColourPerception_fn(Lambda,T)

    lamnmax = max(size(Lambda));

    for i=1:lamnmax
        if Lambda(i)<380 || Lambda(i)>730
            T(:,i)=0;
        end
    end

    [Lambda_w,VLambda]=textread('VLambda.dat','%f\t%f');
```

```
26      [Lambda_b,Cones_b]=textread('BlueCones.dat','%f\t%f');
27      [Lambda_g,Cones_g]=textread('GreenCones.dat','%f\t%f');
28      [Lambda_r,Cones_r]=textread('RedCones.dat','%f\t%f');
29
30      minLambda=min([Lambda_r;Lambda_g;Lambda_b]);
31      maxLambda=max([Lambda_r;Lambda_g;Lambda_b]);
32
33      VLambda_s =abs(spline(Lambda_w,VLambda,Lambda)); %White
34      Cones(1,:)=abs(spline(Lambda_b,Cones_b,Lambda)); %Blue
35      Cones(2,:)=abs(spline(Lambda_g,Cones_g,Lambda)); %Green
36      Cones(3,:)=abs(spline(Lambda_r,Cones_r,Lambda)); %Red
37      VLambda_s = VLambda_s/max(VLambda_s);
38
39      for i = 1:3 %Normalise cone sensitivities
40          Cones(i,:) = Cones(i,:)/max(Cones(i,:));
41      end
42      Cones(1,:)=0.04146649051*Cones(1,:);
43      Cones(2,:)=0.7128272888*Cones(2,:);
44      Cones(3,:)=Cones(3,:);
45
46      %Determine rgb values.
47      %Normalise to (flat spectrum) white light.
48      r = Cones(3,:)*T'*255/124.9521;
49      g = Cones(2,:)*T'*255/73.2213;
50      b = Cones(1,:)*T'*255/3.1633;
51  %     rgb_raw = [r,g,b]; %Unsaturated RGB values.
52
53      a = VLambda_s*T'/(max(T));
54      if a>1, a=1; end
55
56      %Renormalize
57      sum = max([r,b,g])/a; %255
58      b = b/sum;
59      g = g/sum;
60      r = r/sum;
61  %     rgb_norm = [r,g,b]; %Saturated RGB values, in range 0-->1
62
63      R = round(r*255);
64      G = round(g*255);
65      B = round(b*255);
66      RGB = [R,G,B]; %RGB values in range 0-->255
67
68  %     figure %Delete comment as appropriate
69      hold all
70      h1=area(Lambda,T); %Plot the input spectrum
71      set(h1,'facecolor',[r,g,b]) %Colour area under curve with ...
            RGB values
72      xlabel('Wavelength (nm)')
73
74      result = [R,G,B]; %Return the RGB values.
75  end
```

## A.2 Code for Four-Level Quantum Model Permittivity

```
% Title: Optical_Bloch_4level_Jagg_fn.m
% Author: M. Gentile
% Date: 7-1-14 (corrected on 14-9-15)
% Description: This function calculates the permittivity of
% J-aggregated TDBC molecules by solving the optical Bloch
% equations generated by a four-level quantum model in
% conjunction with the rotating wave approximation (RWA).

% Required inputs:
% conc = Concentration (in %),
% w_pr = Ang. freq. (in rad/s).
% Dim = Dimensionality of the space in which the
% aggregates are distributed (1, 2 or 3).
% n_m = Refractive index of embedding medium.

% Outputs:
% eps = Complex permittivity.

function result = Optical_Bloch_4level_Jagg_fn(conc,w_pr,Dim,n_m)

    if Dim < 4 && Dim > 0
    else
        disp('Warning: Dimensionality is non-physical.');
        a = input('Continue?');
    end

    %=======Program parameters===========
    MAX = max(size(w_pr)); %Size of input/output
    MAX_t = 1; %Set to one to save computation time.
    t = 1; %End time (in seconds) of calculation

    no_eig = 16; %Number of eigenvalues for 4-levels.
    coef = zeros(no_eig); %Space for coefficients

    %=========Physical constants in SI=======
    i = sqrt(-1);
    c_0 = 2.9979e8; %Speed of light in free space
    e = 1.602e-19; %Elementary charge
    h = 6.63e-34; %Plank constant
    hbar = h/(2*pi); %hbar
    eps_0 = 8.85e-12; %Permittivity of free space
    u = 1.67e-27; %Atomic mass unit
    Debye = 0.20819434e-10; %The Debye

    %---------TDBC properties----------------
    m_TDBC = 756.627*u; %Molecular weight of TDBC
    m_PVA = 1250; %Density of PVA (kg/m^3)
    N = (m_PVA/m_TDBC)*0.01*conc/(1-0.01*conc); %pc. by wt.

    %----TDBC Transition dipole moments------
    mu_mono = 20*Debye; %Monomer dipole moment
```

```
52      n=15; %Number of monomers per aggregate
53
54      %Aggregate dipole moments
55      d01 = mu_mono*e*cot(pi*0.5/(n+1))*sqrt(2/(n+1))*[1,0,0]/Dim;
56      d03 = mu_mono*e*cot(3*pi*0.5/(n+1))*sqrt(2/(n+1))*[1,0,0]/Dim;
57      d05 = mu_mono*e*cot(5*pi*0.5/(n+1))*sqrt(2/(n+1))*[1,0,0]/Dim;
58      d13 = 0;
59      d15 = 0;
60      d35 = 0;
61
62      P = 1e-3; %Illuminating power, in watts
63      A = pi*(0.5*1.5e-3)^2; %Spot area, in metres
64      E_pr = sqrt(P/(eps_0*c_0*A)); %E-field of a laser, in V/m
65
66      %--------Rabi frequencies----------
67      O01 = E_pr*sqrt(d01*d01')/hbar;
68      O03 = E_pr*sqrt(d03*d03')/hbar;
69      O05 = E_pr*sqrt(d05*d05')/hbar;
70
71      %-----------Energy levels----------
72      J = 0.6665; %nearest neighbour interaction energy (eV)
73      hbarw1 = 3.4174; %Monomer exciton energy (eV)
74
75      %Aggregate exciton energies
76      w5 = (hbarw1-2*J*cos(5*pi/(n+1)))*e/hbar;
77      w3 = (hbarw1-2*J*cos(3*pi/(n+1)))*e/hbar;
78      w1 = (hbarw1-2*J*cos(pi/(n+1)))*e/hbar;
79      w0 = 0; %Ground state
80
81      %----Radiative decay rates-----------
82      g_ph = log(2)*2*pi/(0.6e-12); %Photoluminescent dec.rate
83      g01 = g_ph;
84      g03 = (w3-w0)^3*(d03*d03')/(3*pi*eps_0*hbar*c_0^3);
85      g05 = (w5-w0)^3*(d05*d05')/(3*pi*eps_0*hbar*c_0^3);
86      g10 = hbar*(w1-w0)^3/(pi^2*c_0^3)*g01;
87      g30 = hbar*(w3-w0)^3/(pi^2*c_0^3)*g03;
88      g50 = hbar*(w5-w0)^3/(pi^2*c_0^3)*g05;
89      g13 = (w3-w1)^3*(d13*d13')/(3*pi*eps_0*hbar*c_0^3);
90      g31 = hbar*(w3-w1)^3/(pi^2*c_0^3)*g13;
91      g15 = (w5-w1)^3*(d15*d15')/(3*pi*eps_0*hbar*c_0^3);
92      g51 = hbar*(w5-w1)^3/(pi^2*c_0^3)*g15;
93      g35 = (w5-w3)^3*(d35*d35')/(3*pi*eps_0*hbar*c_0^3);
94      g53 = hbar*(w5-w3)^3/(pi^2*c_0^3)*g35;
95
96      %-------------------Dephasing rates---------------------
97      GDephase = 2.85e13;
98      G_05d = 4*GDephase;
99      G_03d = 4*GDephase;
100     G_01d = GDephase;
101     G_13d = GDephase;
102     G_15d = GDephase;
103     G_35d = GDephase;
104
105     %Check the dephasing rates for physical violations.
106     if (G_03d+G_15d)>(G_03d+G_05d+G_13d+G_35d), disp('Warning: ...
            Gd cond. 1 violated.'); end
107     if (G_05d+G_13d)>(G_01d+G_03d+G_15d+G_35d), disp('Warning: ...
            Gd cond. 2 violated.'); end
```

```
108     if (G_01d+G_35d)>(G_03d+G_05d+G_13d+G_15d), disp('Warning: ...
            Gd cond. 3 violated.'); end
109     if (G_05d+G_13d-G_03d-G_15d)^2>4*G_01d*G_35d, ...
            disp('Warning: Gd cond. 4 violated.'); end
110     if (G_01d+G_35d-G_03d-G_15d)^2>4*G_05d*G_13d, ...
            disp('Warning: Gd cond. 5 violated.'); end
111
112     G05 = G_05d+(g10 + g30 + g50 + g05 + g15 + g35)/2;
113     G03 = G_03d+(g10 + g30 + g50 + g03 + g13 + g53)/2;
114     G01 = G_01d+(g10 + g30 + g50 + g01 + g31 + g51)/2;
115     G13 = G_13d+(g01 + g31 + g51 + g03 + g13 + g53)/2;
116     G15 = G_15d+(g01 + g31 + g51 + g05 + g15 + g35)/2;
117     G35 = G_35d+(g03 + g13 + g53 + g05 + g15 + g35)/2;
118
119     %---Density matrix elements---
120     P00 = zeros(MAX,MAX_t);
121     P11 = zeros(MAX,MAX_t);
122     P01 = zeros(MAX,MAX_t);
123     P10 = zeros(MAX,MAX_t);
124     P33 = zeros(MAX,MAX_t);
125     P03 = zeros(MAX,MAX_t);
126     P30 = zeros(MAX,MAX_t);
127     P13 = zeros(MAX,MAX_t);
128     P31 = zeros(MAX,MAX_t);
129     P55 = zeros(MAX,MAX_t);
130     P05 = zeros(MAX,MAX_t);
131     P50 = zeros(MAX,MAX_t);
132     P15 = zeros(MAX,MAX_t);
133     P51 = zeros(MAX,MAX_t);
134     P35 = zeros(MAX,MAX_t);
135     P53 = zeros(MAX,MAX_t);
136
137     for j2=1:MAX %Loop over energy
138
139         %Optical Bloch equations in matrix form
140         DSLM = [-(g10+g30+g50),g01,i*O01,-i*O01,g03,i*O03,...
141             -i*O03,0,0,g05,i*O05,-i*O05,0,0,0,0;... %p00
142             g10,-(g01+g31+g51),-i*O01,i*O01,g13,0,0,0,0,...
143             g15,0,0,0,0,0,0;... %p11
144             i*O01,-i*O01,i*(w1-w0-w_pr(j2))-G01,0,0,0,0,...
145             0,-i*O03,0,0,0,0,-i*O05,0,0;... %p01
146             -i*O01,i*O01,0,-i*(w1-w0-w_pr(j2))-G01,0,0,...
147             0,i*O03,0,0,0,0,i*O05,0,0,0;... %p10
148             g30,g31,0,0,-(g03+g13+g53),-i*O03,i*O03,0,0,...
149             g35,0,0,0,0,0,0;... %p33
150             i*O03,0,0,0,-i*O03,i*(w3-w0-w_pr(j2))-G03,0,...
151             -i*O01,0,0,0,0,0,0,0,-i*O05;... %p03
152             -i*O03,0,0,0,i*O03,0,-i*(w3-w0-w_pr(j2))-G03,...
153             0,i*O01,0,0,0,0,0,i*O05,0;... %p30
154             0,0,0,i*O03,0,-i*O01,0,i*(w3-w1)-G13,0,0,0,0,...
155             0,0,0,0;... %p13
156             0,0,-i*O03,0,0,0,i*O01,0,-i*(w3-w1)-G13,0,0,...
157             0,0,0,0,0;... %p31
158             g50,g51,0,0,g53,0,0,0,0,-(g05+g15+g35),...
159             -i*O05,i*O05,0,0,0,0;... %p55
160             i*O05,0,0,0,0,0,0,0,0,-i*O05,...
161             i*(w5-w0-w_pr(j2))-G05,0,-i*O01,0,-i*O03,0;... %p05
162             -i*O05,0,0,0,0,0,0,0,0,i*O05,0,...
163             -i*(w5-w0-w_pr(j2))-G05,0,i*O01,0,i*O03;... %p50
```

```
164             0,0,0,i*O05,0,0,0,0,0,0,-i*O01,0,...
165             i*(w5-w1)-G15,0,0,0;... %p15
166             0,0,-i*O05,0,0,0,0,0,0,0,0,i*O01,0,...
167             -i*(w5-w1)-G15,0,0;... %p51
168             0,0,0,0,0,0,0,i*O05,0,0,0,-i*O03,0,0,0,...
169             i*(w5-w3)-G35,0; %p35
170             0,0,0,0,0,-i*O05,0,0,0,0,0,i*O03,0,0,0,...
171             -i*(w5-w3)-G35]; %p53
172
173         %Compute eigenvector & eigenvalues of DSLM
174         MOD = max(max(abs(real(DSLM))));
175         DSLM = DSLM/MOD;
176         [V,D] = eig(DSLM); %Eigenvectors, V
177         l_s = eig(DSLM)*MOD; %Eigenvalues of DSLM
178
179         R=zeros(1,no_eig); %Set IVs of the density matrix.
180         R(1) = 1; %Start in nanoparticle ground state.
181
182         %---find coefficients for density matrix elements---
183         ABCD = V\R'; %Column vector to find coefficents
184         for j3=1:no_eig %Find the coefficients for each mode
185             for j4=1:no_eig
186                 coef(j3,j4) = V(j4,j3)*ABCD(j3);
187             end
188         end
189
190         %--------Compute the density matrix elements----------
191         for j=1:no_eig
192             P00(j2,:) = P00(j2,:) + ...
                    real(coef(j,1)*exp((l_s(j))*t));
193             P11(j2,:) = P11(j2,:) + ...
                    real(coef(j,2)*exp((l_s(j))*t));
194             P33(j2,:) = P33(j2,:) + ...
                    real(coef(j,5)*exp((l_s(j))*t));
195             P55(j2,:) = P55(j2,:) + ...
                    real(coef(j,10)*exp((l_s(j))*t));
196             P01(j2,:) = P01(j2,:) + coef(j,3)*exp((l_s(j))*t);
197             P10(j2,:) = P10(j2,:) + coef(j,4)*exp((l_s(j))*t);
198             P03(j2,:) = P03(j2,:) + coef(j,6)*exp((l_s(j))*t);
199             P30(j2,:) = P30(j2,:) + coef(j,7)*exp((l_s(j))*t);
200             P13(j2,:) = P13(j2,:) + coef(j,8)*exp((l_s(j))*t);
201             P31(j2,:) = P31(j2,:) + coef(j,9)*exp((l_s(j))*t);
202             P05(j2,:) = P05(j2,:) + coef(j,11)*exp((l_s(j))*t);
203             P50(j2,:) = P50(j2,:) + coef(j,12)*exp((l_s(j))*t);
204             P15(j2,:) = P15(j2,:) + coef(j,13)*exp((l_s(j))*t);
205             P51(j2,:) = P51(j2,:) + coef(j,14)*exp((l_s(j))*t);
206             P35(j2,:) = P35(j2,:) + coef(j,15)*exp((l_s(j))*t);
207             P53(j2,:) = P53(j2,:) + coef(j,16)*exp((l_s(j))*t);
208         end
209     end
210
211     %==Evaluate susceptibility (chi) & permittivity (eps)==
212     Chi = n_m^2-2*N/(eps_0*E_pr)*( (P10*sqrt(d01*d01'))+...
213         (P30*sqrt(d03*d03'))+(P50*sqrt(d05*d05')) );
214     eps = real(Chi(:,MAX_t)) + sqrt(-1)*imag(Chi(:,MAX_t));
215
216     result = eps;
217 end
```

# B

# Appendix: Methods and Derivations

## B.1 Orientationally-Averaged Dipole Moment

The dipole moment $\boldsymbol{d}_{0m}$ discussed in Ch. 2 is that of a single, on-axis aggregate. A realistic nanostructure composed of these aggregates (such as a film or a nanoparticle) contains randomly-orientated aggregates. It is presumed that these are non-interacting. In this section, a relationship is derived to relate the on-axis dipole moment with that of the orientationally-averaged dipole moment.

For a collection of $N = n/V$ identical dipoles per unit volume induced by an electric field with dipole moments $\boldsymbol{d}_i$ each with tensor polarizability $\bar{\alpha}_i(\omega)$, the polarisation per unit volume ($\boldsymbol{P}$) is given by,

$$\begin{aligned}\boldsymbol{P} &= \frac{1}{V}\sum_{i=1}^{n}\boldsymbol{d}_i \\ &= N\left\langle\bar{\alpha}(\omega)\right\rangle\cdot\boldsymbol{E} \\ &= \boldsymbol{\chi}(\omega)\cdot\boldsymbol{E}.\end{aligned} \tag{B.1}$$

It is assumed above that the electric field is uniform over the volume $V$. The average value of the polarizability is defined as,

$$\left\langle\bar{\alpha}(\omega)\right\rangle = \frac{1}{N}\sum_{i}\bar{\alpha}_i(\omega). \tag{B.2}$$

By making the assumption that the dipoles are identical, the polarizabilities $\bar{\alpha}_i(\omega)$ have the same magnitude $\alpha(\omega)$, and are only different in their dipole orientation $\hat{\boldsymbol{n}}_i$. For a collection of such dipoles distributed in a $\mathcal{D}$ dimensional space,

$$\langle \bar{\alpha}(\omega) \rangle = \alpha(\omega) \langle \hat{\boldsymbol{n}} \otimes \hat{\boldsymbol{n}} \rangle. \tag{B.3}$$

Recognising that $\langle n_i n_j \rangle = \delta_{ij} n_i n_j$ gives,

$$\langle \bar{\alpha}(\omega) \rangle = \alpha(\omega) \left( \langle n_x^2 \rangle \hat{\boldsymbol{x}} \otimes \hat{\boldsymbol{x}} + \langle n_y^2 \rangle \hat{\boldsymbol{y}} \otimes \hat{\boldsymbol{y}} + \dots \right). \tag{B.4}$$

Using $\langle n_i^2 \rangle = \langle n_j^2 \rangle$ along with the normalisation condition of unit vectors $\hat{\boldsymbol{n}}_i \cdot \hat{\boldsymbol{n}}_i = 1$ gives $\sum_i^{\mathcal{D}} \langle n_i^2 \rangle = \mathcal{D} \langle n_i^2 \rangle = 1$, which enables Eq. B.4 to be re-written as,

$$\langle \bar{\alpha}(\omega) \rangle = \frac{\alpha(\omega)}{\mathcal{D}} \left( \hat{\boldsymbol{x}} \otimes \hat{\boldsymbol{x}} + \hat{\boldsymbol{y}} \otimes \hat{\boldsymbol{y}} + \dots \right). \tag{B.5}$$

Combining Eq. B.1 & B.5, one can find the macroscopic isotropic permittivity $\varepsilon$ to be equal to,

$$\boxed{\varepsilon(\omega) = \varepsilon_b + \frac{N\alpha(\omega)}{\mathcal{D}}}, \tag{B.6}$$

where $\varepsilon_b$ is the permittivity of the embedding medium. For a planar sample, $\mathcal{D} = 2$ and for a bulk sample, $\mathcal{D} = 3$.

## B.2 Solving the Optical Bloch Equations

As stated in Sec. 2.3.3, the Optical Bloch Equations (OBEs) derived from the Liouville-von Neumann equation can be written in the compact form as,

$$\dot{\boldsymbol{\rho}}_V = \overline{L} \boldsymbol{\rho}_V, \tag{B.7}$$

where $\boldsymbol{\rho}_V$ is a vector of the density matrix elements. One may solve the OBEs by application of the rotating wave approximation (RWA)[110] with subsequent use of a matrix inversion method, or numerically by way of a Runge-Kutta method, such as the RK10(8) method.[114] In this section, both of these approaches are detailed, evaluated, and shown to be equivalent for an ensemble illuminated with a cosine potential.

### B.2.1 Matrix inversion method

The matrix-inversion method relies on application of the RWA[184] to the perturbing potential, which enables one to write $\overline{L}(t,\omega)$ as a time-independent matrix, $\overline{L}(\omega)$. In this case, solutions for the density matrix elements can be written in the following form,

$$\rho_{mn}(t,\omega) = \sum_i c_{mn,i} e^{i\omega_i t}, \tag{B.8}$$

using the principle of superposition. The coefficients $c_{mn,i}$ are determined from initial conditions and from the eigenvectors of $\overline{L}(\omega)$. The angular frequencies $\omega_i$ are related to the eigenvalues $\lambda_i$ of the matrix $\overline{L}(\omega)$ by $i\omega_i = \lambda_i$. $\lambda_i$ is complex with a negative real part in order to conserve probability. The RWA may be applied to a cosine potential, $G = \boldsymbol{d}\cdot\boldsymbol{E}_0\ \cos(\omega t)$. An advantage of this method is that computation time is very short and weak fields may be considered easily.

A restriction on the RWA is that only a field of one frequency may impinge upon the system in this method, since the time-independence of $\overline{L}$ must be preserved. In order to solve the OBEs for circumstances including a frequency-spread pulse, a numerical approach must be used instead, as outlined below.

### B.2.2 Explicit Runge-Kutta methods

For the general case where $\overline{L}$ cannot be written as time-independent *e.g.* when the system is subjected to a pulse, a numerical method must be used to solve the OBEs. The OBEs have the general form $\dot{y} = f(t,y)$ which has a general solution written in discretised form,

$$y_{n+1} = y_n + h_n \sum_{i=1}^{n} b_i k_i, \tag{B.9}$$

where,

$$k_i = f\left(t_n + h_n a_i, y_n + h_n \sum_{j=1}^{j=i-1} C_{ij} k_j\right). \tag{B.10}$$

The estimated error at each step is evaluated as,

$$e_{n+1} \propto y_{n+1} - y^*_{n+1}. \tag{B.11}$$

The values $a_i$, $b_i$ and $C_{ij}$ all depend upon the specific method involved. The original 1st-order algorithm using this general method is the Euler method,[185] but a much more accurate method is the Runge-Kutta (RK4) method, which has been used previously to probe the dynamics of two-level systems.[186] This method suffers from being non-adaptive, in the sense that the step size is always taken to be constant. This makes numerical solutions for rapidly-changing behaviour unreliable. An improved approach is to dynamically allocate the step size between each iteration through a comparison of the estimated local error between the 4$^{th}$ and 5$^{th}$-order solutions at each point. The yields the Runge-Kutta-Fehlberg (RK4(5)) method.[187] The advantage of an adaptive numerical method such as the RK4(5) method over a non-adaptive method such as the RK4 method is that rapidly-changing behaviour can be modelled with greater accuracy. Local errors are also minimized and the resultant solution that one determines is numerically smoother.[188] However, for weak fields, the RK4(5) method is insufficient to produce numerically stable solutions. During the course of this thesis being written, the RK10(8) method (a 10$^{th}$-order Runge-Kutta method with in-built error estimation by comparison to the 8$^{th}$ order)[114] was tested and found to produce smoother output for insignificantly more computing time than that of the RK4(5) method.

The main advantage of a Runge-Kutta method over the RWA is that no terms in the Hamiltonian are neglected. As a result, any arbitrary potential can be modelled, not just a cosine potential. However, the main drawback of any Runge-Kutta method is that the computation time for the process is many times longer than using the RWA with matrix inversion. This longer timescale is sometimes prohibitive depending on the parameters involved. A further drawback is that for weak fields the solutions to the OBEs become stiff in time and numerical instability is encountered. This can be seen from the fact that with the calculations for TDBC illuminated with a 1 $mW$

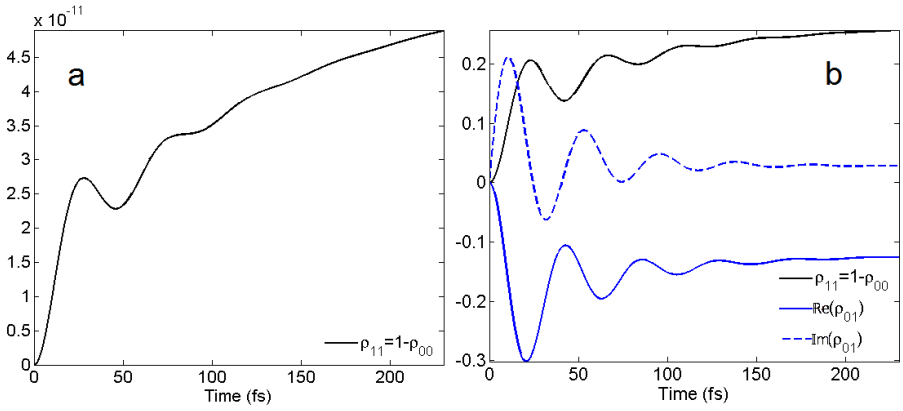


**Figure B.1:** (a) The relative occupancy of the excited state $\rho_{11}$, for a 1 $mW$ laser potential with spot size 1.5 $mm$. (b) The relative occupancy of the excited state $\rho_{11}$, together with the coherence $\rho_{01}$ (real and imaginary parts shown) for a 10 $MW$ laser with the same spot size.

cosine potential with spot size 1.5 *mm*, the relative occupancy of the excited state $\rho_{11}$ does not exceed one part in $10^{10}$, so $\rho_{00}$ remains more-or-less constant in time with value $\rho_{00} \approx 1$ as shown in Fig. B.1 (conversely, the coherences oscillate in time at the applied frequency and are of order $10^{-6}$). Therefore, the populations are incredibly stiff and this is where explicit numerical methods fail. One way to avoid the resultant numerical instability is to confine this procedure to solving OBEs with strong fields. To achieve physically meaningful solutions in this circumstance, one would need to introduce other effects such as multi-exciton recombination[189] and nonlinear effects.[112] By neglecting these effects, similar solutions can be obtained to those of weak fields for the coherences, provided the field does not induce significant population inversion. As an alternative to this compromise, one can use an implicit Runge-Kutta method to solve stiff equations. However, the computation time for implicit Runge-Kutta methods was found to exceed that of the explicit methods by at least a factor of ten, making this approach ungainly.

In summary, the procedure for solving the OBEs is as follows: for weak fields the RWA is used. Solutions derived using this method are supported by the solutions obtained using the RK10(8) method for strong fields with multi-exciton and nonlinear effects neglected. It is concluded that by careful use of the RWA, realistic behaviour can be simulated subject to the condition that the system is illuminated by a monochromatic field. For slowly time-varying strong fields or for two strong lasers, an explicit Runge-Kutta method may be used, but for time-varying weak fields an implicit Runge-Kutta method may be implemented successfully.

## B.3 Transmittance Through Array of Nanospheres

The Beer-Lambert law[157] (p. 391) states that the intensity of light through an absorbing medium decreases with distance through the medium,

$$dI = -\kappa I dz. \tag{B.12}$$

When integrated, the following expression is obtained,

$$\begin{aligned} \int \frac{dI}{I} &= -\int \kappa dz \\ \ln|I| &= -\kappa z + \ln|I_0|, \end{aligned} \tag{B.13}$$

which can be re-arranged as follows,

$$\frac{I}{I_0} = e^{-\kappa z}, \tag{B.14}$$

where $I_0$ is the intensity of the light entering the medium. $\kappa$ is the coefficient representing the length over which the fraction $1/e$ of the light undergoes extinction. For an array of nanospheres this can be represented as,

$$\kappa = N\sigma_{\text{ext}}, \tag{B.15}$$

where $\sigma_{\text{ext}}$ is the extinction cross-section of a single nanosphere. For a two-dimensional square array of nanospheres, the number density of nanospheres in the sample ($N$) is related to the nanosphere spacing ($\mu$) by $N = 1/\mu^2 z$. Therefore, the far-field intensity transmitted through the array is,

$$\begin{aligned} I &= I_0 e^{-\sigma_{\text{ext}} z/\mu^2 z} \\ &= I_0 e^{-\sigma_{\text{ext}}/\mu^2}. \end{aligned} \tag{B.16}$$

Identifying that $T = I/I_0$, the following equation for the transmitted light through the array is obtained,

$$\boxed{T = e^{-\sigma_{\text{ext}}/\mu^2}}. \tag{B.17}$$

This result is identical to that obtained with more thorough treatment.[65]

## B.4 Transmittance Through a Quasistatic Nanospheroid

As outlined in Ch. 4, the starting point for the transmittance through quasistatic nanospheroids is the potentials for the two dipole modes induced in the nanospheroid,

$$\Phi_x = \frac{|\boldsymbol{p}_x| \cos\phi}{4\pi\varepsilon_0 r^2} \tag{B.18}$$

$$\Phi_z = \frac{|\boldsymbol{p}_z| \cos\theta}{4\pi\varepsilon_0 r^2}. \tag{B.19}$$

Using $\boldsymbol{E} = -\nabla\Phi$ (and denoting $\beta = 1/4\pi\varepsilon_0$), the following expression for the dipole electric fields can be found,

$$\boldsymbol{E}_{dx} = E_0\alpha_{xx}\beta\left(2\cos\phi\,\hat{\boldsymbol{r}} - \frac{\sin\phi}{\sin\theta}\,\hat{\boldsymbol{\phi}}\right) \tag{B.20}$$

$$\boldsymbol{E}_{dz} = E_0\alpha_{zz}\beta\left(2\cos\theta\,\hat{\boldsymbol{r}} - \sin\theta\,\hat{\boldsymbol{\theta}}\right), \tag{B.21}$$

where $|\boldsymbol{p}_i| = \alpha_{ii}E_0$ has been used. The incident (unpolarised) light is assumed to be incident along the positive y-axis. This gives the following expression for the incident electric field,

$$\begin{aligned}\boldsymbol{E}_i &= E_0(\hat{x} + \hat{z}) \\ &= E_0\left((\sin\theta\cos\phi + \cos\theta)\hat{\boldsymbol{r}} + (\cos\theta\cos\phi - \sin\theta)\hat{\boldsymbol{\theta}} - \sin\phi\hat{\boldsymbol{\phi}}\right).\end{aligned} \tag{B.22}$$

These expressions are combined to obtain the total field,

$$\begin{aligned}\frac{\boldsymbol{E}}{E_0} = &\left[\left(\sin\theta + \frac{2\beta}{r^3}\alpha_{xx}\right)\cos\phi + \left(1 + \frac{2\beta}{r^3}\alpha_{zz}\right)\cos\theta\right]\hat{\boldsymbol{r}} + \\ &\left[\cos\theta\cos\phi + \left(\frac{\beta\alpha_{zz}}{r^3} - 1\right)\sin\theta\right]\hat{\boldsymbol{\theta}} + \\ &\left[\frac{\beta\alpha_{xx}}{r^3}\frac{\sin\phi}{\sin\theta} - \sin\phi\right]\hat{\boldsymbol{\phi}}.\end{aligned} \tag{B.23}$$

For a point along the y-axis, $\theta = \phi = \pi/2$, and Eq. B.23 reduces to,

$$\frac{\boldsymbol{E}}{E_0} = \left(\frac{\beta\alpha_{zz}}{r^3} - 1\right)\hat{\boldsymbol{\theta}} + \left(\frac{\beta\alpha_{xx}}{r^3} - 1\right)\hat{\boldsymbol{\phi}}. \tag{B.24}$$

For points along the y-axis with $x = z = 0$, $y = r$ and the unit vectors $\hat{\boldsymbol{\theta}}$ and $\hat{\boldsymbol{\phi}}$ become $-\hat{\boldsymbol{z}}$ and $-\hat{\boldsymbol{x}}$ respectively. This leads to,

$$\frac{\boldsymbol{E}}{E_0} = -\left(\frac{\beta\alpha_{xx}}{y^3} - 1\right)\hat{\boldsymbol{x}} - \left(\frac{\beta\alpha_{zz}}{y^3} - 1\right)\hat{\boldsymbol{z}}. \tag{B.25}$$

Now the field intensity for points along the y-axis is calculated. This quantity is equivalent to the transmittance coefficient, $T$, and is dependent upon polarisation as shown,

$$\left(\frac{\boldsymbol{E}}{E_0}\right)^2 = \boldsymbol{T} = \left[\frac{\beta^2|\alpha_{xx}|^2}{y^6} - \frac{2\beta\alpha'_{xx}}{y^3} + 1\right]\hat{\boldsymbol{x}} + \left[\frac{\beta^2|\alpha_{zz}|^2}{y^6} - \frac{2\beta\alpha'_{zz}}{y^3} + 1\right]\hat{\boldsymbol{z}}. \tag{B.26}$$

In the limit where $y \to \infty$, $|\boldsymbol{T}| \to 1$ as the contribution from the dipole fields becomes negligible with respect to the incident field. In the (relatively) near-field limit, field enhancement is possible owing to the $1/y^6$ dependency in transmission.

# C

# Appendix: Coefficients To Hybrid Nanoparticle Equations

## C.1 Inert Core, Lorentz Oscillator Shell

As outlined in Sec. 5.5, a more precise equation than Eq. 5.11 can be constructed for the resonant energies $\omega$ of a nanosphere with an inert core and a Lorentz oscillator shell. This equation takes the form,

$$c_4\omega^4 + c_2\omega^2 + c_0 = 0, \tag{C.1}$$

and can be solved using the quadratic formula. The coefficients have the following values,

$c_4 = \varepsilon_1\varepsilon_b(2x^3 + 1) + 2(\varepsilon_1\varepsilon_m + \varepsilon_b^2)(1 - x^3) + 2\varepsilon_b\varepsilon_m(x^3 + 2)$

$c_2 = -\varepsilon_1(\varepsilon_b(\gamma^2 + 2\omega_0^2) + f\omega_0^2)(2x^3 + 1) - 2\varepsilon_b\varepsilon_m(\gamma^2 + 2\omega_0^2(1 - \varepsilon_m f))(x^3 + 2) + 2(\varepsilon_1\varepsilon_m(\gamma^2 + 2\omega_0^2) + \varepsilon_b^2\gamma^2 + 4\varepsilon_b\omega_0^2(\varepsilon_b + f))(x^3 - 1)$

$c_0 = \varepsilon_1\omega_0^4(\varepsilon_b + f)(2x^3 + 1) + 2\omega_0^4(\varepsilon_1\varepsilon_m + \varepsilon_b^2 + 2\varepsilon_b f + f^2)(1 - x^3) + 2\varepsilon_m\omega_0^4(\varepsilon_b + f)(x^3 + 2).$

## C.2 Lorentz Oscillator Core and Shell

The resonant frequencies of the exciton-exciton nanoparticle geometry outlined in Sec. 5.6 satisfy an equation of the form,

$$(c_5\omega^4 + c_3\omega^2 + c_1)\omega i + (c_6\omega^6 + c_4\omega^4 + c_2\omega^2 + c_0) = 0. \tag{C.2}$$

The coefficients to this equation written out in full are,

$$c_6 = \varepsilon_{\infty 1}\varepsilon_{\infty 2}(1+2x^3) + 2(\varepsilon_{\infty 1}\varepsilon_m + \varepsilon_{\infty 2}^2)(1-x^3) + 2\varepsilon_{\infty 2}\varepsilon_m(2+x^3)$$

$$c_5 = [\varepsilon_{\infty 1}\varepsilon_{\infty 2}(1+2x^3) + 2\varepsilon_{\infty 2}\varepsilon_m(2+x^3) + 2(\varepsilon_{\infty 1}\varepsilon_m + \varepsilon_{\infty 2}^2)(1-x^3)](\gamma_1 + 2\gamma_2)$$

$$c_4 = -2[2(\varepsilon_{\infty 2}^2 + \varepsilon_{\infty 1}\varepsilon_m)\gamma_1\gamma_2(\gamma_1+\gamma_2) + 2\omega_{02}^2(\varepsilon_{\infty 1}\varepsilon_m + \varepsilon_{\infty 2}^2 + \varepsilon_{\infty 2}f_2)(2\gamma_1+\gamma_2) + \omega_{01}^2(2(\varepsilon_{\infty 2}^2 + \varepsilon_{\infty 1}\varepsilon_m) + \varepsilon_m f_1)(\gamma_1+2\gamma_2)](1-x^3) - 2\varepsilon_m[2\varepsilon_{\infty 2}\omega_{01}^2(\gamma_1+2\gamma_2) + (2\varepsilon_{\infty 2} + f_2)\omega_{02}^2(2\gamma_1+\gamma_2) + 2\varepsilon_{\infty 2}\gamma_1\gamma_2(\gamma_1+\gamma_2)](2+x^3) - [\varepsilon_{\infty 2}f_1\omega_{01}^2(\gamma_1+2\gamma_2) + \varepsilon_{\infty 1}f_2\omega_{02}^2(2\gamma_1+\gamma_2) + 2\varepsilon_{\infty 1}\varepsilon_{\infty 2}\gamma_1\gamma_2(\gamma_1+\gamma_2) + 2\varepsilon_{\infty 1}\varepsilon_{\infty 2}\omega_{01}^2(\gamma_1+2\gamma_2) + 2\varepsilon_{\infty 1}\varepsilon_{\infty 2}\omega_{02}^2(2\gamma_1+\gamma_2)](1+2x^3),$$

$$c_2 = 2f_2^2\omega_{02}^4(\gamma_1(1-2x^3)-1) + (f_1f_2\omega_{01}^2\omega_{02}^2(\gamma_1+\gamma_2) + 2\varepsilon_{\infty 1}\varepsilon_{\infty 2}[\omega_{01}^2\gamma_2(\omega_{01}^2 + \gamma_1\gamma_2) + \omega_{02}^2\gamma_1(\omega_{02}^2 + \gamma_1\gamma_2) + 2\omega_{01}^2\omega_{02}^2(\gamma_1+\gamma_2)] + \varepsilon_{\infty 2}f_1\omega_{01}^2[(2\omega_{01}^2 + \gamma_1\gamma_2)\gamma_2 + 2\omega_{02}^2(\gamma_1+\gamma_2)] + \varepsilon_{\infty 1}f_2\omega_{02}^2[(2\omega_{02}^2 + \gamma_1\gamma_2)\gamma_1 + 2\omega_{01}^2(\gamma_1+\gamma_2)])(1+2x^3) + (4\varepsilon_m f_2\gamma_1\omega_{02}^4 + 4\varepsilon_m f_2\gamma_2\omega_{01}^2\omega_{02}^2 + 4\varepsilon_{\infty 2}\varepsilon_m\gamma_1\omega_{02}^4 + 8\varepsilon_{\infty 2}\varepsilon_m\gamma_2\omega_{01}^2\omega_{02}^2 + 4\varepsilon_{\infty 2}\varepsilon_m\gamma_1^2\gamma_2\omega_{02}^2 + 4\varepsilon_{\infty 2}\varepsilon_m\gamma_1\gamma_2^2\omega_{01}^2 + 8\varepsilon_{\infty 2}\varepsilon_m\gamma_1\omega_{01}^2\omega_{02}^2 + 2\varepsilon_m f_2\gamma_1^2\gamma_2\omega_{02}^2 + 4\varepsilon_m f_2\gamma_1\omega_{01}^2\omega_{02}^2 + 4\varepsilon_{\infty 2}\varepsilon_m\gamma_2\omega_{01}^4)(2+x^3) + (2\varepsilon_m f_1\omega_{01}^2[2\omega_{02}^2(\gamma_1+\gamma_2) + \gamma_2(\omega_{01}^2 + \gamma_1\gamma_2)] + 4\varepsilon_{\infty 1}\varepsilon_m[\gamma_2\omega_{01}^2(\gamma_1\gamma_2 + \omega_{01}^2) + \gamma_1\omega_{02}^2(\gamma_1\gamma_2 + \omega_{02}^2) + 2\omega_{01}^2\omega_{02}^2(\gamma_1+\gamma_2)] + 4\varepsilon_{\infty 2}^2[2\omega_{01}^2\omega_{02}^2(\gamma_1+\gamma_2) + \omega_{01}^2\gamma_2(\omega_{01}^2+\gamma_1\gamma_2) + \omega_{02}^2\gamma_1(\omega_{02}^2+\gamma_1\gamma_2)] + 4\varepsilon_{\infty 2}f_2[\omega_{02}^2\gamma_1(2\omega_{02}^2 + \gamma_1\gamma_2) + 2\omega_{01}^2\omega_{02}^2(\gamma_1+\gamma_2)])(1-x^3),$$

$$c_0 = -[(2\varepsilon_{\infty 1}\varepsilon_{\infty 2}\omega_{01}^2\omega_{02}^2 + f_1f_2\omega_{01}^2\omega_{02}^2)(\gamma_1\omega_{02}^2 + \gamma_2\omega_{01}^2) + \varepsilon_{\infty 1}f_2\omega_{01}^2\omega_{02}^2(2\gamma_1\omega_{02}^2 + \gamma_2\omega_{01}^2) + \varepsilon_{\infty 2}f_1\omega_{01}^2\omega_{02}^2(\gamma_1\omega_{02}^2 + 2\gamma_2\omega_{01}^2)](1+2x^3) - [(+4\varepsilon_{\infty 1}\varepsilon_m\omega_{01}^2\omega_{02}^2 + 2\varepsilon_m f_1\omega_{01}^2\omega_{02}^2)(\gamma_1\omega_{02}^2 + 2\gamma_2\omega_{01}^2) + 4\varepsilon_{\infty 2}\omega_{01}^2\omega_{02}^2(f_2(\gamma_2\omega_{01}^2 + 2\gamma_1\omega_{02}^2) + \varepsilon_{\infty 2}(\gamma_2\omega_{01}^2 + \gamma_1\omega_{02}^2))](1-x^3) - 2\varepsilon_m\omega_{01}^2\omega_{02}^2[+f_2(2\gamma_1\omega_{02}^2 + \gamma_2\omega_{01}^2) + 2\varepsilon_{\infty 2}(\gamma_1\omega_{02}^2 + \gamma_2\omega_{01}^2)](2+x^3) - 4f_2^2\gamma_1\omega_{01}^2\omega_{02}^4.$$

Solutions for $\omega$ can be found using Cardano's cubic polynomial formula,[190]

$$x_i = -\frac{1}{3a}\left(b + u_i C + \frac{\Delta_0}{u_i C}\right), \tag{C.3}$$

where $u_i$ are the three cube roots of unity and,

$$C = \left(\frac{\Delta_1 + \sqrt{\Delta_1^2 - 4\Delta_0^3}}{2}\right)^{1/3}, \tag{C.4}$$

where,

$$\Delta_0 = c_4^2 - 3c_6c_2 \tag{C.5}$$

$$\Delta_1 = 2c_4^3 - 9c_6c_4c_2 + 27c_6^2c_0. \tag{C.6}$$

## C.3 Metal Core, Lorentz Shell

The solutions for the nanoparticle geometry with a metal core and excitonic shell as outlined in Sec. 5.7 satisfy an equation of the form,

$$c_6\omega^6 + c_4\omega^4 + c_2\omega^2 + c_0 + i(c_5\omega^4 + c_3\omega^2 + c_1)\omega = 0.$$

The real part of this equation can be solved with the cubic formula above, and the coefficients have the values,

$$c_6 = 2(\varepsilon_b^2 + \varepsilon_\infty\varepsilon_m)(1 - x^3) + \varepsilon_b\varepsilon_\infty(1 + 2x^3) + 2\varepsilon_b\varepsilon_m(2 + x^3)$$

$$c_4 = -2(\gamma(\varepsilon_b^2+\varepsilon_\infty\varepsilon_m)(\gamma+2\gamma_p)+2\omega_0^2(\varepsilon_b(\varepsilon_b+f)+\varepsilon_\infty\varepsilon_m)+\varepsilon_\infty\varepsilon_m\omega_p^2)(1-x^3)-\varepsilon_\infty(\varepsilon_b\gamma(\gamma+2\gamma_p) + (2\omega_0^2 + \omega_p^2)\varepsilon_b + f\omega_0^2)(1 + 2x^3) - 2\varepsilon_m(\gamma\varepsilon_b(\gamma + 2\gamma_p) + (2\varepsilon_b + f)\omega_0^2)(2 + x^3)$$

$$c_2 = 2(\varepsilon_b\omega_0^2(2\gamma\gamma_p(f + \varepsilon_b) + (2f + \varepsilon_b)\omega_0^2) + \varepsilon_\infty\varepsilon_m(\gamma^2\omega_p^2 + 2\gamma\gamma_p\omega_0^2 + \omega_0^4 + 2\omega_0^2\omega_p^2) + f^2\omega_0^4)(1 - x^3) + \varepsilon_\infty(\varepsilon_b\gamma^2\omega_p^2 + (2\gamma\gamma_p + \omega_0^2 + 2\omega_p^2)\varepsilon_b\omega_0^2 + f\gamma\gamma_p\omega_0^2 + f\omega_0^4 + f\omega_0^2\omega_p^2)(1 + 2x^3) + 2\varepsilon_m\omega_0^2[(2\varepsilon_b + f)\gamma\gamma_p + (\varepsilon_b + f)\omega_0^2](2 + x^3)$$

$$c_0 = -\varepsilon_\infty\omega_0^4\omega_p^2[(\varepsilon_b + f)(1 + 2x^3) + 2\varepsilon_m(1 - x^3)]$$

The imaginary part of the equation can be solved with the quadratic formula, and the values of the coefficients are,

$$c_5 = [(2\varepsilon_m + \varepsilon_b)(\varepsilon_\infty + 2\varepsilon_b) + 2(\varepsilon_\infty - \varepsilon_b)(\varepsilon_b - \varepsilon_m)x^3](\gamma_p + 2\gamma)$$

$$c_3 = -2[(\gamma^2\gamma_p+2(\gamma+\gamma_p))(\varepsilon_b^2+\varepsilon_\infty\varepsilon_m)+2(\gamma+\gamma_p)\varepsilon_b f\omega_0^2+2\varepsilon_\infty\varepsilon_m\gamma\omega_p^2](1-x^3)-\varepsilon_\infty[(\gamma+\gamma_p)(f+2\varepsilon_b)\omega_0^2+\varepsilon_b\gamma(2\omega_p^2+\gamma\gamma_p)](1+2x^3)-2\varepsilon_m[(\gamma+\gamma_p)(f+2\varepsilon_b)\omega_0^2+\varepsilon_b\gamma^2\gamma_p](2+x^3)$$

$$c_1 = 2\omega_0^2[\omega_0^2\gamma_p((\varepsilon_b + 2f)\varepsilon_b + \varepsilon_\infty\varepsilon_m + f^2) + 2\varepsilon_\infty\varepsilon_m\gamma\omega_p^2](1 - x^3) + \varepsilon_\infty\omega_0^2[(f + \varepsilon_b)\gamma_p\omega_0^2 + (2\varepsilon_b + f)\gamma\omega_p^2](1 + 2x^3) + 2\varepsilon_m\omega_0^4\gamma_p(f + \varepsilon_b)(2 + x^3).$$

# Publications

## Journal Articles in Print

*Optical Field-Enhancement and Subwavelength Field-Confinement Using Excitonic Nanostructures*, M. J. Gentile, S. Núñez-Sánchez and W. L. Barnes, Nano Letters, **14**, 2339–2344 (2014)

*Localized exciton-polariton modes in dye-doped nanospheres: a quantum approach*, M. J. Gentile, S. A. R. Horsley and W. L. Barnes, J. Opt., **18**, 015001 (2016)

## Journal Articles to Appear

*Excitonic surface lattice resonances*, A. D. Humphrey, M. J. Gentile and W. L. Barnes, J. Opt., (2016). Accepted 24$^{th}$ May 2016.

## Journal Articles in Preparation

*Hybridized Exciton-Polariton Resonances in a Core-Shell Geometry*, M. J. Gentile, W. L. Barnes (2016)

## Poster Presentations

*Transient Particle Exciton Polariton modes in Dye-Doped Polymer Nanoparticles*, M. J. Gentile and W. L. Barnes, Quantum Optics Meets Non-Linear Spectroscopy, FRIAS, Freiburg, Germany. (October 2014)

*Transient plasmon-like modes in multi-level quantum emitter systems*, M. J. Gentile and W. L. Barnes, Optics and Photonics 2014, San Diego, California, USA. (August 2014)

*Optical Field-Enhancement and Subwavelength Field-Confinement Using Excitonic Nanostructures*, M. J. Gentile, S. Núñez-Sánchez and W. L. Barnes, PND@10 Future Directions for Plasmonics, University of Exeter, Exeter, UK. (May 2014)

## Future Publications

*Exciton Polaritons for Nanophotonics*, S. Núñez-Sánchez, M. J. Gentile, A. D. Humphrey and W. L. Barnes

# INDEX